# GEODYNAMIC INVERSION TO CONSTRAIN THE RHEOLOGY OF THE LITHOSPHERE

DISSERTATION

zur Erlangung des akademischen Grades

DOKTOR DER NATURWISSENSCHAFTEN
(DR. RER. NAT.)

vorgelegt dem Fachbereich Chemie, Pharmazie und Geowissenschaften
der Johannes Gutenberg Universität Mainz

von

DIPL.-GEOPHYS. TOBIAS SAMUEL BAUMANN

geboren in Freiburg im Breisgau

JG|U

JOHANNES GUTENBERG
UNIVERSITÄT MAINZ

Mainz – Januar 2016

Die vorliegende Arbeit wurde an der Johannes Gutenberg-Universität Mainz angefertigt (D77).

Für Paul Oskar und Eva.

# CONTENTS

# 1 INTRODUCTION

During the past twenty years, numerical modelling of lithospheric deformation has developed as a new branch of geosciences. Growing computer power has increased both model resolution and complexity, such that numerical models are now widely regarded as the first method of choice to understand geological deformation processes on multiple scales by verifying results of laboratory experiments or observations from the field (e.g., Burov et al., 2014; Burov, 2007). In this context, the title of the thesis '*Geodynamic inversion to constrain the rheology of the lithosphere*' is proposing a new direction in the field of lithosphere geodynamics. *Inversion* is something that has already become well-established in other geoscientific disciplines such as seismology. The term implies to systematically turn observations into models that are consistent with physical conditions and observational constraints. This is usually done by minimising an error that describes the misfit between model predictions and observations. Yet, lithospheric-scale models have so far not been combined with data in an inverse modelling sense, which is the topic of this thesis.

We link inversion techniques with dynamic models of lithospheric deformation to constrain material properties of the lithosphere. The aim is to better understand and to verify the underlying material parameters that control lithospheric deformation with an independent approach that does not rely on extrapolating laboratory measurements to geological conditions. The following sections provide a general introduction to the subject, as well as an overview of the chapter contents.

## RHEOLOGY OF THE LITHOSPHERE

About the same time when Alfred Wegener published his ideas on plate tectonics (Wegener, 1912), the concept of *lithosphere* and *asthenosphere* as outer shells of the Earth was introduced. This goes back to the work of Joseph Barrell (e.g., Barrell, 1914a,b), who showed, based on gravity measurements, that stresses first increase and then decrease with depth – confirming the existence of a strong outer layer (lithosphere) that overlies another weak layer (asthenosphere) beneath (Watts, 2007). Whereas at that time the denotation was still imprecise (e.g., Love, 1911) and Andrija Mohorovičić just discovered (1910) the homonymous seismic P-wave discontinuity (Moho) that marks a sudden change in material properties and the transition from crust to mantle (e.g., Prodehl et al., 2013), we nowadays understand the lithosphere as a strong layer that also comprises parts of the upper mantle and supports stresses (e.g., Anderson, 2007). Compared to the Moho discontinuity, the transition from lithosphere to asthenosphere is less clear and although a couple of physical properties such as density and temperature are discriminative, the drop in seismic velocity is

most frequently equated with the lithosphere asthenosphere boundary (LAB, Kind et al., 2012). Gutenberg (1926) was the first who identified this seismic discontinuity (Gutenberg discontinuity) below the Moho from analysing P-waves (Kind & Li, 2015). Today, the LAB is mostly constrained through surface wave dispersion or receiver function experiments (Kind et al., 2012). However, the LAB is still vaguely determined and other quantities, such as thermal or chemical and elastic (see below) definitions are used to describe the spatial extends of the lithosphere (e.g., Anderson, 2007).

In general, the strength of the lithosphere depends on its structure and rheological properties (Burov, 2007). The term *rheology* describes the deformation and flow behaviour of solid materials. The expression was firstly designated by the colloid chemist E. C. Bingham after Heraclitus' παντα ρει (Ancient Greek: panta rhei), which means 'everything flows' (Reiner, 1964). This leads to the question of how a solid can flow, and stresses the relation of rheology to the time of observation, or to the length of time for which stress is applied to the solid (Lowrie, 2007). In this context, Reiner (1964) defines the Deborah number D, which states the difference between solids and fluids:

$$D = \frac{\text{Time of relaxation}}{\text{Time of observation}}. \tag{1.1}$$

On the one hand, it implies that rocks behave as solids when the time of observation is short compared to the time of material relaxation ($D \to \infty$), and, on the other hand, that rocks can also behave as fluids for small relaxation times, i.e. $D \to 0$. This point of view also applies to the multifaceted deformation behaviour of rocks within the lithosphere, which can be described with multiple theoretical relationships. Depending on the time of observation and the magnitude of applied stresses, the dominant deformation behaviour of rocks can be either elastic, plastic, or viscous.

*Deformation and strength of the lithosphere*

By definition, elastic deformation is fully recoverable as long as the elastic limit (yield stress) is not exceeded (e.g., Lowrie, 2007). Elastic properties of the lithosphere arise on different scales of time, as response to short-lasting stresses due to seismic waves, and on a long-term basis through loading and unloading events due to seamounts or ice shields (glacial rebound). These observations suggest that the lithosphere behaves as a rigid plate that has a flexural rigidity and is able to deform elastically, also on long-term time scales (10 ka to 1 Ma, Watts, 2007). For example, a plate of thickness $T_e$ has a flexural rigidity

$$D = \frac{E}{12\,(1-\nu^2)}\,T_e^3, \tag{1.2}$$

that is a function of Young's modulus $E$ and Poisson's ratio $\nu$ (e.g., Watts, 2001). It was demonstrated that the concept of elastic thickness is applicable to oceanic lithosphere, where a relation between lithospheric age and $T_e$ was observed, which suggests that oceanic lithosphere becomes stronger with age $t$, i.e. (Watts, 1978):

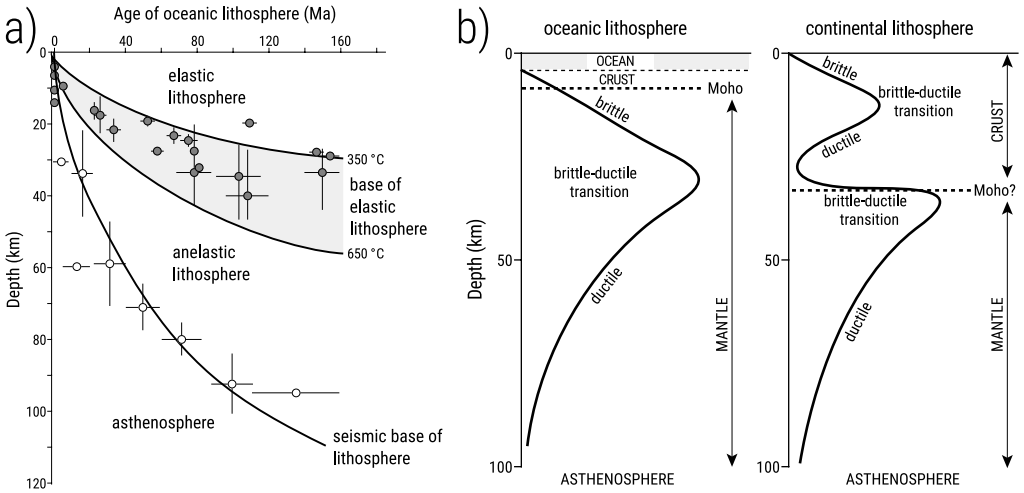


Figure 1.1: Lithospheric thickness and maximum strength profilesof the lithosphere. **a)** Elastic ($T_e$) and seismic thickness of oceanic lithosphere as a function of lithospheric age (modified from Lowrie, 2007; Watts et al., 1980). Differences in thickness reflect the fact that only the upper part of the lithosphere behaves elastically under loading at long time scales, which is approximately confined by the $300 - 600°C$ oceanic isotherms. **b)** Hypothetical profiles of lithospheric strength and brittle–ductile regimes of oceanic (left) and continental (right) lithosphere. Original version of Molnar (1988), modified after Lowrie (2007).

$$T_e = (3.0 \pm 1.5)\ t^{0.5}, \tag{1.3}$$

where $T_e$ is usually smaller than 50 km (Burov, 2007). Also the seismic thickness, which refers to the LAB, increases with the age of the lithosphere. However, the thickness obtained from seismic observations is usually two to three times larger (Fig. 1.1a), which reflects the fact that only the upper part of the lithosphere behaves elastically (Lowrie, 2007).

In the late 1970s, the concept of yield strength envelopes (YSE, Fig.1.1b) was developed to describe an upper limit for the strength of the lithosphere as a function of depth (Kohlstedt et al., 1995). YSEs are constitutive relationships that are empirically determined from rock deformation experiments in the laboratory and scaled to lithospheric conditions (e.g., Brace & Kohlstedt, 1980; Goetze & Evans, 1979).

In the shallow lithosphere the total strength is limited by plastic yield criteria. More precisely, it is generally agreed that frictional resistance along faults is the limiting factor of strength in the uppermost part of the lithosphere, as the stress required for frictional sliding is much smaller than the stress required for fracturing (Kohlstedt et al., 1995). Byerlee (1978) demonstrated that, under conditions of low pressure and temperature, most rock types have similar frictional strength that can be described consistently to the Mohr–Coulomb failure criterion in terms of shear ($\tau$) and normal ($\sigma_n$) stress:

$$\tau = \mu_f \sigma_n + C_f, \tag{1.4}$$

where $\mu_f$ is the coefficient of friction and $C_f$ the frictional cohesive strength. $\mu_f$ varies between $0.6 - 0.85$ and $C_f$ between $0 - 60\,\mathrm{MPa}$, depending on $\sigma_n$, which is approximately equivalent to lithospheric pressure and increases linearly with depth, such that, in the brittle regime, the YSE increases approximately linearly with depth (Fig.1.1b) and is relatively insensitive to temperature (Kohlstedt et al., 1995). Direct evidence for this comes from drilling experiments, for example at KTB in Southern Germany up to a depth of about 9 km (Brudy et al., 1997).

At larger depths, with higher pressures and temperatures, Byerlee's law is no longer applicable and viscous yield strength becomes dominant. Semi-brittle regimes build a transition to ductile regimes, where the total strength is bounded by viscous strength that decays exponentially with depth. A variety of ductile (creep) deformation mechanisms can take place on an atomic scale (e.g., Ranalli, 1995; Karato, 2008). The term 'ductile' is often associated with strain rate dependent rock properties (Burov, 2007), but creep mechanisms depend on multiple conditions. For example, the regime diagram in Fig.1.2a illustrates the stress and temperature conditions under which the most common creep mechanisms are dominant. Whereas Peirl's creep (low-temperature plastic flow, Goetze & Evans, 1979) is relevant for large differential stresses, experimental data from a wide range of conditions fit the general form of constitutive relationship (e.g., Bürgmann & Dresen, 2008):

$$\dot{\varepsilon} \propto A\,(\sigma_3 - \sigma_1)^n \exp\left(\frac{E + P\,V}{RT}\right), \tag{1.5}$$

which is used to describe dislocation and diffusion creep deformation mechanisms, such that differential stress of YSE is given as a function of strain-rate $\dot{\varepsilon}\,[s^{-1}]$, material parameters $A$, stress exponent $n\,[1]$, temperature $T\,[K]$ and pressure $P\,[Pa]$. Activation volume $V\,[m^3\,mol^{-1}]$ and energy $E\,[J\,mol^{-1}]$ are material properties that control pressure and temperature dependence, and $R\,[J\,mol^{-1}\,K^{-1}]$ is the gas constant. However, multiple parameters such as water content or grain size have additional control on the deformation regime. For example, Fig. 1.2b shows a regime diagram of wet olivine as a function of grain size that is also temperature and pressure dependent.

*Jelly sandwich or Crème brûlée?*

The concept of elastic thickness works well to describe the integrated strength of oceanic lithosphere (e.g., Watts, 2001). Observations of $T_e$ are in agreement with YSEs that are estimated from laboratory experiments (Burov, 2007). On the other hand, it has been shown that the same concept applied to continental lithosphere leaves a number of open questions (Burov & Diament, 1995). Whereas it is generally accepted that continental lithosphere can be described as rheologically stratified medium (e.g., Burov, 2007), the thickness and strength of the layers are part of an ongoing discussion. The prevailing view of strength profiles of continental lithosphere is commonly referred to as the 'Jelly sandwich' model, suggesting a weak lower crust sandwiched between a strong upper crust and mantle lithosphere (Fig. 1.3a). For this model, significant parts

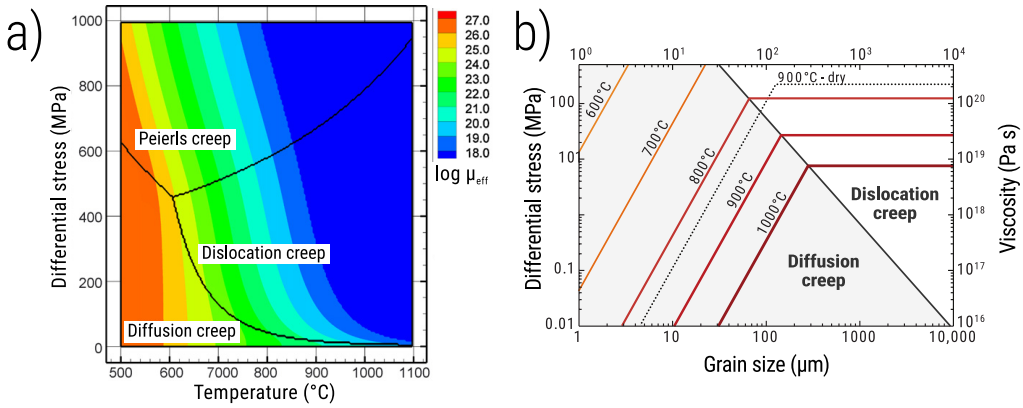


Figure 1.2: Ductile deformation (creep) regimes and effective viscosity of olivine; **a)** as a function of differential stress and temperature (valid for dry olivine, from Popov & Sobolev, 2008). **b)** Example of a water saturated sample, i.e. wet olivine; effective viscosity and creep regime as a function of differential stress, grain size and temperature (modified from Bürgmann & Dresen, 2008). Original data from Hirth & Kohlstedt (2003).

of the integrative strength resides in the lithospheric mantle (Afonso & Ranalli, 2004). However, conflicting observations of elastic thickness ($T_e$) and depth distributions of earthquakes (Jackson, 2002; Maggi et al., 2000b,a) provoked an ongoing discussion about the 'Jelly sandwich' model (Burov & Watts, 2006) and an alternative model with a strong upper crust and a weak mantle lithosphere (Fig. 1.3b, Jackson, 2002), later dubbed as 'Crème brûlée model' (Burov & Watts, 2006). In contrast to the Jelly sandwich model, the integrated strength of the 'Crème brûlée model' entirely resides within the crust, inferring a close correlation of elastic thickness and seismogenic layer (Bürgmann & Dresen, 2008; Burov & Watts, 2006).

Although the debate is ongoing (Jackson et al., 2008; Burov, 2007), it is now understood that there is not only a single type of YSE that is characteristic for all continental lithosphere (Burov & Watts, 2006) and it is rather a limit criterion with a number of simplifications. This illustrates the necessity of alternative approaches, independent from $T_e$ estimations (Burov et al., 2014), which a-priori assume the lithosphere to be an elastic plate floating on a viscous mantle.

## CONSTRAINING RHEOLOGICAL PROPERTIES OF THE EARTH

### *State of the art*

The elastic thickness $T_e$ is one of the key quantities to describe the strength of the lithosphere. However, $T_e$ is a proxy to describe the lithosphere's first order rheology with strictly simplifying assumptions (Watts, 2001). It is physically more consistent to estimate effective viscosity as it directly participates in constitutive relationships that link conservation of mass and momentum when considering continuum mechanics. There are a number of different approaches to directly estimate viscosities of the lithosphere and lithospheric rocks. Each

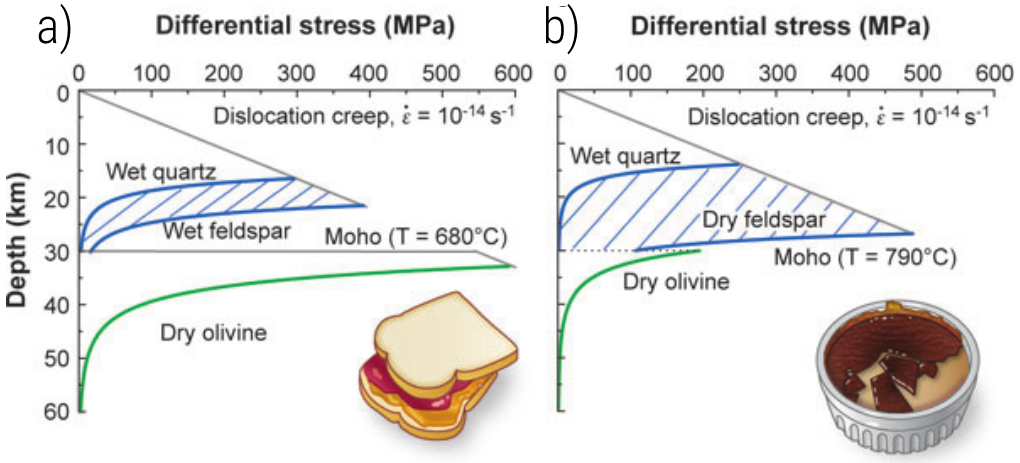


Figure 1.3: Schematic models of continental lithospheric 'strength' (from Bürgmann & Dresen, 2008) that describe the ongoing discussions. **a)** The 'Jelly-Sandwich' model with weak lower crust sandwiched between a moderately strong upper crust and mantle lithosphere (e.g., Burov & Diament, 1995; Burov & Watts, 2006). **b)** Alternative 'Crème brûlée model with a very strong crust and without significant contribution of the lithopsheric mantle to total strength (e.g., Jackson, 2002; Maggi et al., 2000b,a).

methodology has its own limitations and sensitivity to certain scales of time and space. The following paragraphs give a complementary picture of the state of the art methods.

*Rock mechanics experiments*

More than 30 years ago, Goetze & Evans (1979) were the first to draw inferences on lithospheric long-term rheology from rock mechanics experiments. Since then, a lot of progress has been made in terms of experimental design and accuracy to study the deformation behaviour of rocks (e.g., Karato, 2008; Hirth & Kohlstedt, 2003; Ranalli, 1995). Whereas elastic properties and Byerlee's brittle parameters for large scale deformation can be well constrained with rock mechanics experiments up to a satisfying accuracy of $\pm 10 - 30\%$, ductile properties remain uncertain (Burov, 2007).

Burov (2007) summarises a number of sources for the uncertainties regarding experimentally derived estimates of the ductile long-term rheology: The main difficulty in determining robust quantities is the need for extrapolation, from laboratory to geological conditions. Experimental strain rates are on the order of $10^{-8} - 10^{-4}\,s^{-1}$, which implies a difference of 10 orders of magnitude compared to strain rates under geological conditions ($10^{-18} - 10^{-14\,-1}$). Besides, experimental design can only approximate geological conditions. Thus, most experiments are realised as uniaxial or torque deformation tests of small rock samples or monophase minerals under different pressure and temperature conditions. Whereas different water contents can be included in the experiments, the effect of macro structures in rocks and varying strain rates are difficult to determine. Although experimental results of dry olivine fit to $T_e$ observations

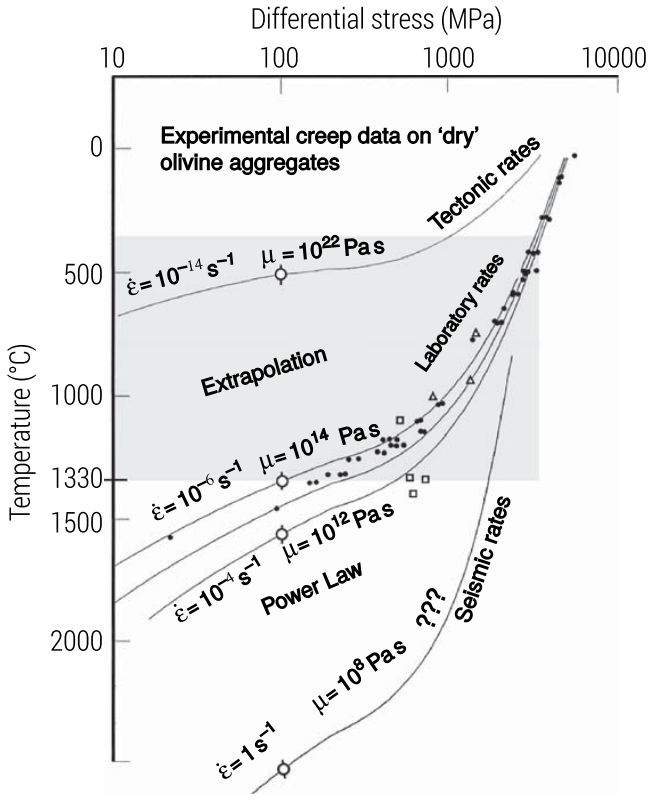


Figure 1.4: Proportions of scale differences between typical flow law experiments in the laboratory and correspondent observations in nature, which implies an extrapolation over 10 orders of magnitude in strain rate to scale experimental results to geological conditions. After Burov (2007).

of oceanic lithosphere (e.g., Watts, 2001), rock mechanics data needs validation with real-scale observations and models (Burov, 2011). Fig. 1.4 illustrates the different scales of laboratory and tectonic conditions (strain rate, temperature, differential stress) and gives an impression of the order of extrapolation that is required to scale rock mechanics experiments to geological conditions. It also implies that geological estimates of viscosity are time dependent.

*Geophysical observations*

Several geological loading and unloading processes can be analysed to infer viscosities of the lithosphere and asthenosphere. For example, large earthquakes are followed by elastic relaxation processes (*postseismic relaxation*) that can be observed geodetically (c.f. review in Bürgmann & Dresen, 2008). Similar relaxation processes, but on a larger time scale, are (un-)loading events, for example of retreating iceshields or glaciers, which is referred to as *postglacial rebound*. Inferring mantle viscosity from glacial rebound observations goes back to the pioneer work of Haskell (1935), who provided first direct evidence of viscous mantle deformation (Bürgmann & Dresen, 2008). His viscosity estimate ($10^{21}$ Pa s) still matches the order of magnitude of more recent observations (see for example a study by Milne et al. (2001) as shown in Fig. 1.5). From inversion of GPS data

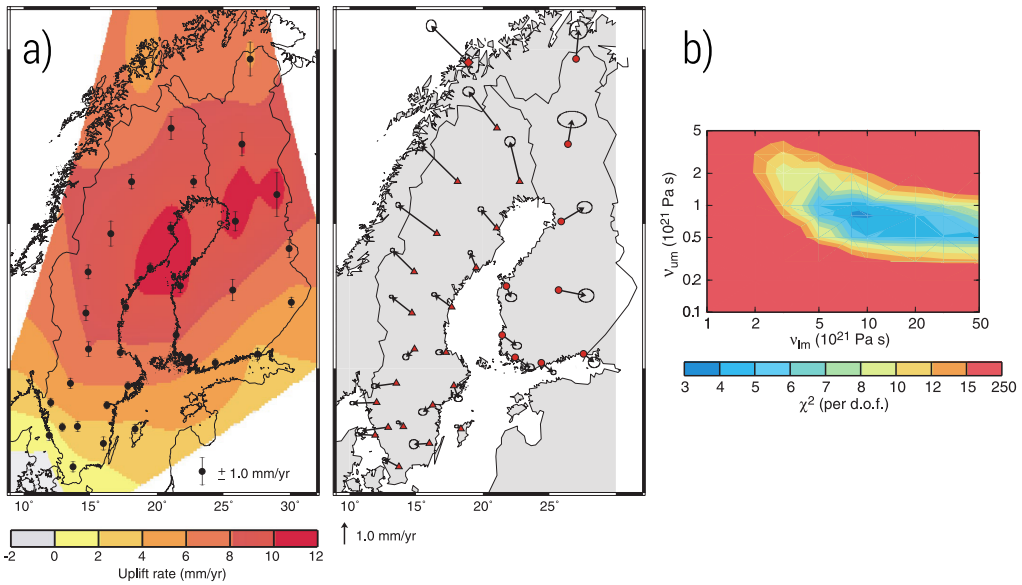


Figure 1.5: Viscosity estimates from post glacial rebound observations in Fennoscandia (modified from Milne et al., 2001). **a)** 3D velocity observations with GPS indicate dome alike uplift. **b)** Grid-search 'inversion' using a viscoelastic model reveals correlated viscosity parameters of upper and lower mantle.

(a), they estimate viscosities (b) of the asthenosphere ($5 - 10 \times 10^{20}$ Pa s) below a fixed elastic lithosphere.

Related to these relaxation observations, the time dependence is an important aspect, because the viscosity estimates of postseismic relaxation and postglacial rebound observations differ by one to two orders of magnitude. This can be explained by different deformation physics acting on different time scales, i.e. deformation mechanisms, that are activated at seismic strain rates are independent of those activated at geodynamic strain rates (Fig.1.4, Burov, 2011). Differences can also occur because non-tectonic loading events are usually observed far away from active faults, whereas for observations of postseismic deformation the opposite is the case (Bürgmann & Dresen, 2008). Therefore, viscosity estimates from postseismic observations are not compatible to the long-term rheology of the lithosphere, i.e. $T_e$ estimations, which can be up to six orders of magnitude higher (Burov, 2007).

Whereas postglacial rebound data can only provide regional viscosity estimates of the asthenosphere, global estimates of the Earth's entire mantle viscosity became a subject of very active research in the late 1970's (Hager & O'Connell, 1979, 1981), alongside with inferences on mantle flow from geodetic and gravity (geoid) data (e.g., Forte & Peltier, 1987; Ricard et al., 1984; Richards & Hager, 1984). In these studies, semi-analytical instantaneous mantle flow models are used to constrain radial viscosity, but even today, the resolution power is limited. Hence, the method is used to focus on viscosity variations deep in the mantle (Rudolph et al., 2015), but not on small radial scales close to the surface where a lot of lateral variation is expected. However, the advantage of the general approach is obvious: Despite limited resolution and other limitations,

the underlying model is physically consistent and can be linked with arbitrary inversion algorithms (e.g., Rudolph et al., 2015; Soldati et al., 2009; Simmons et al., 2006; Ricard et al., 1989) to infer constitutive model properties from independent data, such as plate velocities, gravity and geoid anomalies.

*A new approach using numerical models of lithospheric deformation*

As described above, the general idea of using an inversion algorithm to constrain rheological properties of the Earth directly from geophysical observations is not new. It is also not new to incorporate data acquired from rock mechanics experiments, such as extrapolated strength profiles, into physically consistent, state-of-the-art numerical models of lithospheric temporal and spatial scale to verify the rheology of the lithosphere through systematic forward modelling (e.g., Burov, 2007; Burov et al., 1999).

However, the aim of this thesis is to link both, an inversion approach and physically consistent numerical models of lithospheric deformation to infer rheological properties of the lithosphere directly from geophysical observations at the Earth's surface. Experimental results can be incorporated as prior knowledge with large uncertainties such that the method of *geodynamic inversion* is complementary to rock deformation experiments and denotes an independent approach to verify geodynamic and geological concepts.

As the rheological properties of the lithosphere are non-linear and also geophysical data is known to be non-unique, ambiguous inversion results are expected, which is the motivation to use a probabilistic, i.e. Bayesian inversion approach (e.g., Tarantola, 2005) in this context. This might not always be feasible as probabilistic inversion methods are computationally demanding and require many forward models depending on the nature of the inverse problem and on how many unknowns are involved (Sambridge & Mosegaard, 2002). Consequently, two inversion methods are used within this thesis, a Bayesian approach and a deterministic method (Nelder-Mead downhill-simplex algorithm Nelder & Mead, 1965), to respond to the different settings.

## STRUCTURE AND ABSTRACT OF THE THESIS

The thesis is a cumulative work with chapters being composed as mostly independent papers that have already been published in peer reviewed journals, submitted or are prepared for submission. The thesis contains six chapters including this introductory chapter and a final chapter with conclusions and outlook. My contributions to each chapter are listed in separate tables.

CHAPTER 2: This chapter corresponds to the first publication '*Constraining effective rheologies through parallel joint geodynamic inversion*' (Baumann et al., 2014, authors' contributions are listed in Tab. 1.1) and basically covers the first attempts of constraining effective viscosities and densities through joint inversion of gravity and surface velocity data. The study is divided into two parts, a theoretical part, where the benefits of a joint inversion of gravity and velocity are

| AUTHOR | CONTRIBUTION |
|---|---|
| Baumann, T.S. | Main author. Wrote the publication. Fully conducted the analytical part of the study. Implemented the parallel gravity code and objective function into LaMEM[1]. Main developer of NAplus[2]. Created all figures. Fully conducted all simulation and inversion runs. Evaluated the study results. |
| Kaus B.J.P. | Co-author. Main PI of superordinated project. Provided original Stokes-flow code (LaMEM[1]) including erosion and sedimentation algorithms to generate forward models. Gave advice in planning and constructing the publication. Modified written contents for clarification and corrected language and spelling mistakes. |
| Popov A.A. | Co-author. Co-developer of NAplus[2]: Gave advice regarding the parallel MPI[3] development. Corrected language and spelling mistakes of the publication. |

Table 1.1: Authors and their contributions to chapter 2: '*Constraining effective rheologies through parallel joint geodynamic inversion*'. [1]LaMEM: Lithospheric And Mantle Evolution Model. [2]NAplus: Optimised parallel version of the Neighbourhood Algorithm (original, sequential version from Sambridge, 1999a). [3]MPI: Message Passing Interface.

analytically demonstrated, and a synthetic case study to demonstrate the feasibility of Bayesian-type inversions in the context of numerical geodynamics. In the analytical part, we use the example of a rising sphere, which is a first-order approximation of a rising plume or salt-diapir model (Schmeling et al., 1988). In terms of gravity, a spherical anomaly model has a well-known, but non-unique solution when inverting its gravity signal to find the density contrast and volume of the spherical body. On the other hand, inverting the velocity signal of a rising sphere also results in an ambiguous solution. However, these trade-offs are different and involve the viscosity of the surrounding material, such that a joint inversion of gravity and velocity results in a unique solution in terms of for geometry, density contrast and viscosity. A joint velocity and gravity inversion with geodynamic models must not result in unique solutions in general, but it reduces the ambiguities, because the model is physically consistent. This is also revealed in the second part, where densities and viscosities of three dimensional salt-tectonics model can be constrained as long as the geological units contribute to the dynamics of the model. From a technical point of view, a well established direct-search algorithm (Neighbourhood Algorithm (NA), Sambridge, 1999a), was rewritten and reorganised in terms of MPI (Message Passing interface) layout and memory management for an efficient usage with parallelised geodynamic forward models on massively parallel computers (NAplus, Baumann & Popov, 2014).

CHAPTER 3: In this chapter, which is published as '*Geodynamic inversion to constrain the non-linear rheology of the lithosphere*' (Baumann & Kaus, 2015, authors' contributions in Tab. 1.2), the methodology is improved and applied to the full scale of the lithosphere. It covers a theoretical resetting of the technique including the implementation of Bayesian priors. A synthetic study is conducted to test the methodology for the use with non-linear rheologies, which naturally involves a lot more of unknowns, but also the number of independent constraints is increased, as topography and vertical surface velocity are included beside gravity and horizontal surface velocity. Tests with a known and a parameterised temperature structure reveal the effect of temperature on the inversion results and show that the effective non-linear viscosity structure can be estimated within the uncertainty limits. As our model has a free topography, a technical part of the paper addresses the question of when a dynamic model has to be stopped to catch the present-day dynamics that should be compared with the observations. Beside the synthetical models, the major part of the paper deals with a 2D profile through the India-Asia collision system whose geometry is constructed from multiple seismological constraints. Assuming the geometry

| AUTHOR | CONTRIBUTION |
|---|---|
| Baumann, T.S. | Main author. Wrote the publication. Planned and conducted the entire inversion procedure. Implemented the objective function, the gravity forward modelling code, the stopping criterion and the interfaces to NAplus[1]. Improved Sambridge's MCMC code (Sambridge, 1999b) for 'ensemble appraisals' with the Metropolis-rule to make use of non-uniform priors. Compiled all geophysical data to construct the model setup. Pre-processed geophysical data that were used as observational constraints (interpolation, filtering, computation of Bouguer anomaly, etc.). Created all figures. Fully conducted all simulation and inversion runs. Interpreted results. |
| Kaus B.J.P. | Co-author. Main PI of superordinated project. Main developer of Milamin-VEP2, the 2D MATLAB based Stokes code that is used to perform dynamic forward modelling. Provided the idea of using an India-Asia cross section as application in the study. Gave advice in conducting the synthetic tests. Helped to interpret the synthetic inversion results. Partly modified written contents for clarification and corrected language and spelling mistakes. |

Table 1.2: Authors and their contributions to chapter 3: '*Geodynamic inversion to constrain the non-linear rheology of the lithosphere*'. [1]NAplus: Optimised parallel version of the Neighbourhood Algorithm (original, sequential version from Sambridge, 1999a).

is constrained, we conduct a two level approach, i. e. to reduce the parameter space, a gravity-only inversion is performed prior to the full geodynamic inversion. We find a posterior distribution, which is defined in a 19 dimensional parameter space, confining the complete non-linear rheology within the 2D cross section. In this respect, the results are not unique and multiple end-member models coexist. However, there are stable features that most of the acceptable models have in common, for example a strong, i.e. high-viscosity, lithospheric mantle of India.

CHAPTER 4: As the application in chapter 3 involves about 1.9 million forward models, in '*Appraisal of non-unique geodynamic inversion results: A data mining approach*' (submitted), the question of how to appraise such large model ensemble in a geological context is reposed. The appraisal is conducted with a two-level approach that involves a well established unsupervised machine learning technique (Self-Organizing Map, Kohonen, 1990) and additional clustering. The analysis enables a successful classification of all models into 4 end-member categories, which are mainly confined through the existence of a few key characteristics. The end-member models either have a weak Asian mantle lithosphere or a weak Tibetan lower crust and are distinguished through the presence of a distinctive viscosity power-law behaviour of the Indian mantle lithosphere. The classification also reveals what causes the non-uniqueness of the inversion results in terms of observational constraints and demonstrates that more accurate GPS observations of the uplift velocities will exclude end-member models, and therefore help to massively improve the results on lithospheric rheology.

CHAPTER 5: '*The present-day geodynamics of the India-Asia collision system: Consolidating structural and dynamic constraints to estimate rheological properties*' (Authors' contributions are given in Tab. 1.3) focusses on the India-Asia collision system as well, but from a 3D perspective. The aim of this study is twofold and involves (i) a compilation of multiple seismological data into a 3D geometry of the present-day India-Asia collision, and (ii) inversion approach to constrain a best-fit effective viscosity structure by minimising the misfit to the observed horizontal GPS velocity field. For the construction process of the 3D geometry, seismic tomography, P-/S receiver functions, focal mechanisms and other data are jointly interpreted on horizontal and vertical cross sections and transferred into 3D volumes. For the model compilation, a new MATLAB toolbox, '*geomIO*' (Geometry I/O, Bauville & Baumann, 2015), was collaboratively developed. The optimisation is realised with a Nelder-Mead Downhill Simplex method (NMDS, Nelder & Mead, 1965) and the 'best-fit' model found by optimisation reproduces the observed velocity field reasonably well such that several key issues can be answered. For example, the analysis demonstrates that an interplay of strike-slip faults, a low-viscous lower crust and lateral heterogeneities, i.e. cratonic blocks, such as the Sichuan basin, are crucial to reproduce the characteristic flow field, observed in the Eastern Himalayian syntaxis.

| AUTHOR | CONTRIBUTION |
|---|---|
| Baumann, T.S. | Main author. Wrote the paper. Planned the entire study and conducted the inversion process. Linked NMDS-algorithm[1] with LaMEM[2]. Implemented the objective function. Performed all geophysical interpretations to construct the model geometry. Planned and constructed the model setup, including geographical settings and coordinate transformations. Developer of geomIO[3]. Performed the entire data preprocessing. Evaluated and discussed the results. |
| Kaus B.J.P. | Co-author. Main PI of superordinated project. Gave advice in constructing the boundary conditions. Corrected language and spelling mistakes. |
| Popov A.A. | Co-author. Main developer of LaMEM[2]. Helped to find appropriate options for iterative solvers. |
| Bauville A. | Co-author. Developer of geomIO[3]. |

Table 1.3: Authors and their contributions to chapter 5: '*The present-day geodynamics of the India-Asia collision system: Consolidating structural and dynamic constraints to estimate rheological properties*'. [1]NMDS-algorithm: Nelder-Mead Downhill Simplex algorithm (Nelder & Mead, 1965). [2]LaMEM: Lithospheric And Mantle Evolution Model - revised version. [3]geomIO: Geometry I/O (Bauville & Baumann, 2015).

## REFERENCES

Afonso, J. C. & Ranalli, G., 2004. Crustal and mantle strengths in continental lithosphere: is the jelly sandwich model obsolete?, *Tectonophysics*, **394**(3-4), 221–232.

Anderson, D. L., 2007. *New theory of the Earth*, Cambridge University Press.

Barrell, J., 1914a. The Strength of the Earth's Crust Part I: Geologic Tests of the Limits of Strength, *J. Geol.*, **95**(6), 28–48.

Barrell, J., 1914b. The Strength of the Earth's Crust Part VII: Variations of strength with depth as shown by the nature of departures from isostasy, *J. Geol.*, **22**(8), 729–741.

Baumann, T. S. & Kaus, B. J. P., 2015. Geodynamic inversion to constrain the non-linear rheology of the lithosphere, *Geophys. J. Int.*, **202**(2), 1289–1316.

Baumann, T. S. & Popov, A. A., 2014. NAplus: An efficient parallel version of the Neighourhood Algorithm, https://bitbucket.org/tosaba/naplus/.

Baumann, T. S., Kaus, B. J. P., & Popov, A. A., 2014. Constraining effective rheology through parallel joint geodynamic inversion, *Tectonophysics*.

Bauville, A. & Baumann, T. S., 2015. Geometry I/O: A library for geoscientists to transfer 2D interpretations into 3D geometries, https://geomio.bitbucket.org/.

Brace, W. F. & Kohlstedt, D. L., 1980. Limits on lithospheric stress imposed by laboratory experiments, *J. Geophys. Res.*, **85**(B11), 6248.

Brudy, M., Zoback, M. D., Fuchs, K., Rummel, F., & Baumgartner, J., 1997. Estimation of the complete stress tensor to 8 km depth in the KTB scientific drill holes: Implications for crustal strength, *J. Geophys. Res. - Solid Earth*, **102**(B8), 18453–18475.

Bürgmann, R. & Dresen, G., 2008. Rheology of the Lower Crust and Upper Mantle: Evidence from Rock Mechanics, Geodesy, and Field Observations, *Annu. Rev. Earth Planet. Sci.*, **36**(1), 531–567.

Burov, E., Podladchkov, Y., Grandjean, G., & Burg, J. P., 1999. Thermomechanical approach to validation of deep crustal and lithospheric structures inferred from multidisciplinary data: Application to the Western and Northern Alps, *Terra Nov.*, **11**(2-3), 124–131.

Burov, E., Watts, T., Podladchikov, Y., & Evans, B., 2014. Observational and modeling perspectives on the mechanical properties of the lithosphere, *Tectonophysics*, **631**, 1–3.

Burov, E. B., 2007. Crust and Lithosphere Dynamics: Plate Rheology and Mechanics, in *Treatise Geophys.*, vol. 6, chap. 3, pp. 99–151, ed. Watts, A. B., Elsevier.

Burov, E. B., 2011. Lithosphere, mechanical properties, in *Encycl. Solid Earth Geophys.*, pp. 693–701, ed. Harsh K. Gupta, Springer.

Burov, E. B. & Diament, M., 1995. The effective elastic thickness (Te) of continental lithosphere: What does it really mean?, *J. Geophys. Res.*, **100**, 3905–3927.

Burov, E. B. & Watts, A. B., 2006. The long-term strength of continental lithosphere : 'jelly sandwich' or 'crème brûlée'?, *GSA today*, **16**(1), 4–10.

Byerlee, J., 1978. Friction of rocks, *Pure Appl. Geophys.*, **116**(4-5), 615–626.

Forte, A. M. & Peltier, W. R., 1987. Plate tectonics and aspherical earth structure: The Importance of poloidal-toroidal coupling, *J. Geophys. Res.*, **92**(B5), 3645–3679.

Goetze, C. & Evans, B., 1979. Stress and temperature in the bending lithosphere as constrained by experimental rock mechanics, *Geophys. J. Int.*, **59**(3), 463–478.

Gutenberg, B., 1926. Untersuchungen zur Frage, bis zu welcher Tiefe die Erde kristallin ist, *Zeitschrift für Geophys.*, **2**, 24–29.

Hager, B. H. & O'Connell, R. J., 1979. Kinematic models of large-scale flow in the Earth's mantle, *J. Geophys. Res.*, **84**(B3), 1031–1048.

Hager, B. H. & O'Connell, R. J., 1981. A simple global model of plate dynamics and mantle convection, *J. Geophys. Res.*, **86**(B6), 4843–4867.

Haskell, N. A., 1935. The Motion of a Viscous Fluid Under a Surface Load, *Physics (College. Park. Md).*, **6**(8), 265–269.

Hirth, G. & Kohlstedt, D., 2003. Rheology of the Upper Mantle and the Mantle Wedge: A View from the Experimentalists, *Geophys. Monogr. Ser.*, **138**(4), 83–105.

Jackson, J., 2002. Strength of the continental lithosphere: Time to abandon the jelly sandwich?, *GSA today*, **12**(9), 4–9.

Jackson, J., McKenzie, D., Priestley, K., & Emmerson, B., 2008. New views on the structure and rheology of the lithosphere, *J. Geol. Soc. London.*, **165**(2), 453–465.

Karato, S., 2008. *Deformation of earth materials: an introduction to the rheology of solid earth*, Cambridge University Press.

Kind, R. & Li, X., 2015. Deep Earth Seismology: Deep earth structure-transition zone and mantle discontinuities, in *Treatise Geophys.*, chap. 1, pp. 655–682, eds Dziewonski, A. M. & Romanowicz, B. A., Elsevier.

Kind, R., Yuan, X., & Kumar, P., 2012. Seismic receiver functions and the lithosphere-asthenosphere boundary.

Kohlstedt, D. L., Evans, B., & Mackwell, S. J., 1995. Strength of the lithosphere: Constraints imposed by laboratory experiments.

Kohonen, T., 1990. The self-organizing map, *Proc. IEEE*.

Love, A. E. H., 1911. Chapter I: The distribution of land and water, in *Some Probl. Geodyn.*, no. Xii, pp. 1–5, Cornell University Library.

Lowrie, W., 2007. *Fundamentals of Geophysics*, Cambridge University Press.

Maggi, A., Jackson, J. A., McKenzie, D., & Priestley, K., 2000a. Earthquake focal depths, effective elastic thickness, and the strength of the continental lithosphere, *Geology*, **28**, 495–498.

Maggi, A., Jackson, J. A., Priestley, K., & Baker, C., 2000b. A re-assessment of focal depth distributions in southern Iran, the Tien Shan and northern India: Do earthquakes really occur in the continental mantle?, *Geophys. J. Int.*, **143**(3), 629–661.

Milne, G. A., Davis, J. L., Mitrovica, J. X., Scherneck, H.-G., Johansson, J. M., Vermeer, M., & Koivula, H., 2001. Space-geodetic constraints on glacial isostatic adjustment in Fennoscandia, *Science*, **291**(5512), 2381–2385.

Molnar, P., 1988. Continental tectonics in the aftermath of plate tectonics, *Nature*, **335**(6186), 131–137.

Nelder, J. A. & Mead, R., 1965. A simplex method for function minimization, *Comput. J.*, **7**(4), 308–313.

Popov, A. & Sobolev, S., 2008. SLIM3D: A tool for three-dimensional thermomechanical modeling of lithospheric deformation with elasto-visco-plastic rheology, *Phys. Earth Planet. Inter.*, **171**(1-4), 55–75.

Prodehl, C., Kennett, B., Artemieva, I. M., & Thybo, H., 2013. 100 years of seismic research on the Moho, *Tectonophysics*, **609**, 9–44.

Ranalli, G., 1995. *Rheology of the Earth*, Springer.

Reiner, M., 1964. The Deborah Number, *Phys. Today*, **17**(1), 62.

Ricard, Y., Fleitout, L., & Froidevaux, C., 1984. Geoid heights and lithospheric stresses for a dynamic Earth, *Ann. Geophys.*, **2**(3), 267–286.

Ricard, Y., Vigny, C., & Froidevaux, C., 1989. Mantle heterogeneities, geoid, and plate motion: A Monte Carlo inversion, *J. Geophys. Res. Solid Earth*, **94**(B10), 13739–13754.

Richards, M. A. & Hager, B. H., 1984. Geoid anomalies in a dynamic Earth, *J. Geophys. Res.*, **89**(B7), 5987–6002.

Rudolph, M. L., Leki, V., & Lithgow-bertelloni, C., 2015. Viscosity jump in Earth' s mid-mantle, *Science*, **350**(6266), 1349–1352.

Sambridge, M., 1999a. Geophysical inversion with a neighbourhood algorithm–I. Searching a parameter space, *Geophys. J. Int.*, **138**(2), 479–494.

Sambridge, M., 1999b. Geophysical inversion with a neighbourhood algorithm–II. Appraising the ensemble, *Geophys. J. Int.*, **138**(3), 727–746.

Sambridge, M. & Mosegaard, K., 2002. Monte Carlo methods in geophysical inverse problems, *Rev. Geophys.*, **40**(3), 1–3.

Schmeling, H., Cruden, A. R., & Marquart, G., 1988. Finite deformation in and around a fluid sphere moving through a viscous medium: implications for diapiric ascent, *Tectonophysics*, **149**(1-2), 17–34.

Simmons, N., Forte, A., & Grand, S., 2006. Constraining mantle flow with seismic and geodynamic data: A joint approach, *Earth Planet. Sci. Lett.*, **246**(1-2), 109–124.

Soldati, G., Boschi, L., Deschamps, F., & Giardini, D., 2009. Inferring radial models of mantle viscosity from gravity (GRACE) data and an evolutionary algorithm, *Phys. Earth Planet. Inter.*, **176**(1), 19–32.

Tarantola, A., 2005. *Inverse Problem Theory and Methods for Model Parameter Estimation*, Society for Industrial & Applied Mathematics.

Watts, A. B., 1978. An analysis of isostasy in the world's oceans: 1. Hawaiian-Emperor Seamount Chain, *J. Geophys. Res.*, **83**(B12), 5989–6004.

Watts, A. B., 2001. *Isostasy and Flexure of the Lithosphere*, Cambridge University Press.

Watts, A. B., 2007. Crust and Lithosphere Dynamics: An Overview, in *Treatise Geophys.*, vol. 6, chap. 1, pp. 1–48, ed. Watts, A. B., Elsevier.

Watts, A. B., Bodine, J. H., & Steckler, M. S., 1980. Observations of flexure and the state of stress in the oceanic lithosphere, *J. Geophys. Res. Solid Earth*, **85**(B11), 6369–6376.

Wegener, A., 1912. Die Entstehung der Kontinente, *Geol. Rundschau*, **3**(4), 276–292.

# 2

# CONSTRAINING EFFECTIVE RHEOLOGY THROUGH PARALLEL JOINT GEODYNAMIC INVERSION

**This chapter has been published in:**
Baumann, T. S., Kaus, B. J., & Popov, A. A. (2014). Constraining effective rheology through parallel joint geodynamic inversion. Tectonophysics, 631, 197-211.

**Abstract**

The dynamics of crust and lithosphere is to a large extent controlled by its effective viscosity. Unfortunately, extrapolation of laboratory experiments indicates that viscosity is likely to vary over many orders of magnitude. Additional methods are thus required to constrain the effective viscosity of the present-day lithosphere using more direct geophysical observations.

Here we discuss a method, which couples 3D geodynamic models with observations (surface velocities and gravity anomalies) and with a Bayesian inversion scheme on massively parallel high performance computers.

We illustrate that the basic principle of a joint geodynamic and gravity inversion works well with a simple analytical example. In a next step, we test our approach using a synthetic 3D model of salt tectonics with erosion and sedimentation, and check how much noise conditions, model resolution, and sparse data coverage affect the resolving power of the method. Results show that it is possible to constrain the effective viscosity and density of layers that contribute to the large-scale dynamics, provided that those layers are numerically well resolved. The properties of thin layers that do not contribute much to the overall dynamics cannot be constrained, but noise or sparse data sampling does not significantly affect the inversion results.

This thus illustrates that a joint geodynamic and gravity inversion is a potentially powerful method to constrain the dynamics of the crust and lithosphere. Having better constraints on the structure of the present-day crust and lithosphere will help to narrow the parameter space for models that aim to unravel lithosphere dynamics on a geological time scale.

## INTRODUCTION

Arguably, one of the most uncertain parameters in geodynamic models is the rheology that is employed in the models (e.g., Burov, 2007). Typically, rheological parameters are estimated from laboratory experiments on small sample sizes which results in creeplaws that have to be extrapolated over ten orders of magnitude to geological conditions. Whether this is correct or not is questionable and given that laboratory-based viscosity estimates vary widely between

different rock types, it is desirable to have additional independent methods to constrain the viscosity of the Earth or parts of it.

Doing this is not new, and one of the first to look at the problem was Haskell (1935), who estimated the viscosity of the asthenosphere to be around $10^{21}$ Pas based on postglacial rebound data. More recently, semi-analytical instantaneous mantle flow models were developed in which surface plate motions were imposed as boundary conditions with the aim to find appropriate radial viscosity distributions by comparing model predictions against observations such as stresses associated with post-glacial rebound (Hager & O'Connell, 1979, 1981). For a given a priori knowledge of mantle density distributions (e.g. seismic tomography), these geodynamic models were extended to also fit the geoid (Ricard et al., 1984; Richards & Hager, 1984; Forte & Peltier, 1987), which can be seen as the most reliable constraint on mass heterogeneities of the mantle apart from seismic tomography (Thoraval & Richards, 1997).

On a global scale, several authors explicitly performed inversions of a number of different observations (e.g. plate motions, geoid undulations, global free air gravity, seismic tomography, body wave traveltimes, post glacial rebound data and mineral physics) to constrain radial viscosity profiles. A variety of inversion methods has been applied, including Monte Carlo (Ricard et al., 1989), probabilistic approaches (Ricard & Wuming, 1991; Forte et al., 1991), evolutionary (Soldati et al., 2009) and more specific genetic algorithms (King, 1995), simplex methods (Steinberger & Calderwood, 2006) and Occam inversion approaches (Simmons et al., 2006; Moucha et al., 2007). The authors of these studies use spectral, semi-analytical codes, which efficiently solve the instantaneous mantle flow problem for a limited resolution, and in the case that there are no lateral viscosity variations. A slightly different approach that theoretically allows much higher resolution was followed by Bunge et al. (2003) (excluding lateral viscosity variations) and Liu & Gurnis (2008) (temperature-dependent viscosity structure) who use a fully numerical finite element mantle convection method in conjunction with the adjoint method (Tarantola, 1984; Talagrand & Courtier, 1987).

All of the geodynamic inverse approaches discussed so far focus on constraining the rheology of the mantle using flow models and large-scale first-order observations. Many of these models assume: (i) that the Earth is radially symmetric, meaning that viscosity only varies with depth and lateral viscosity variations are ignored (e.g. King, 1995; Simmons et al., 2006; Steinberger & Calderwood, 2006; Soldati et al., 2009). (ii) that the Earth's surface has a prescribed horizontal plate-motion and no vertical motion, or that it is a free-slip boundary condition. Whereas these assumptions may hold for mantle scale convection models, where lateral variations in viscosity have a minor influence on the geoid (Moucha et al., 2007), it is questionable whether they are still correct for inferring upper mantle and lithospheric viscosity (Thoraval & Richards, 1997). This is supported by the results of Becker & Boschi (2002), who find minor agreement between seismic tomography and semi-analytic geodynamic models for intermediate wavelengths, mainly because subducting slabs are not resolved. Subducting slabs are, however, the major driving-force of plate-tectonics

(Lithgow Bertelloni & Richards, 1998; Bercovici, 2003) even though the dynamics and the rheology of slabs are not perfectly understood (Becker & Faccenna, 2009). Recent findings also show that subduction dynamics is strongly affected by the type of upper boundary condition (e.g. Kaus et al., 2010), and Crameri et al. (2012b) demonstrate that a free surface boundary condition in combination with a sufficiently large viscosity contrast between slab and surrounding mantle are required to obtain asymmetric subducting plates in self-consistent spherical models of mantle convection. On a lithosperic-scale a free surface provides a potential driving force of tectonic processes, through lateral variations in the gravitational potential energy, and many numerical codes of lithosphere dynamics therefore include this effect (e.g. Popov & Sobolev, 2008; Kaus et al., 2008; Gerya & Yuen, 2007; Fullsack, 1995).

Compared to global mantle flow models with a radial viscosity variation only, the presence of strong lateral variations in viscosity and a free surface strongly increases the computational demands of the forward models. Yet, on a lithospheric scale, the above mentioned complexities are likely to be important. Therefore, fully three dimensional models of forward models of lithospheric deformation have only appeared very recently, and nearly all studies perform parameter studies by manually changing input parameters to get some insights in the physics of the system (Li et al., 2013; Popov et al., 2012) or to constrain the rheology of slabs (e.g. Moresi & Gurnis, 1996; Alisic et al., 2010).

There are a few numerical studies on lithospheric or crustal scale which aim to infer best-fit rheologies. Burov et al. (1999) used a 2D numerical model to distinguish which rheological and density structures are dynamically most feasible for a cross-section through the Alps. Kaus et al. (2009) made an attempt to fit 2D models to observed GPS data and earthquake focal mechanisms in southern Taiwan. Yet, both studies changed model parameters manually. Boschetti & Moresi (2001) and Wijns et al. (2003) partly automatise this approach, by using a genetic algorithm to vary the model parameters, but they evaluate the mismatch of the models interactively.

Guiding the parameter search in a subjective manner is a possibility to reduce the number of required geodynamic forward models, but it might become infeasible for an increasing complexity of the model, i.e. a larger parameter space. Progress in computing power and in software to model 3D lithospheric deformation has been quite significant in recent years such that tackling the inverse approach, in which we determine optimal model parameters in an automated fashion, is now becoming feasible. Recently, Afonso et al. (2013b,a) used such an automated probabilistic inverse approach with a number of geophysical observables as constraints and thermal, seismological and petrological models as forward models, but they employed kinematic rather than dynamic models.

In fact, a large number of inverse modelling approaches exist and many of the sub-disciplines in geophysics routinely use, for example, descend-based algorithms. The problem with those algorithms is that they can be trapped in local minima in the parameter space, and that they give no information about the uncertainty of the "best-fit" model parameters which is arguably at least as interesting as the optimal parameters themselves. For that reason, we use a

Monte Carlo based approach which was initially introduced in geophysics by Keilis Borok & Yanovskaja (1967) and Press (1968, 1970) for seismological inversion procedures and is still widely used in seismology. Particularly, the Neighbourhood algorithm (NA, Sambridge, 1999a) is a popular method. It combines the geometrical concepts of Voronoi diagrams (Voronoï, 1908) with a Monte Carlo ensemble-based search approach (Sambridge, 1999a). The search process is self-adaptive depending on the properties of all previously created models (Sambridge, 1999a). Similar to genetic algorithms the sampling can be focused on multiple regions of the parameter space and can therefore account for ambiguities and local minima, but also in high dimensional parameter spaces (Sambridge & Mosegaard, 2002).

Although the NA can be used as a global optimisation algorithm (Mosegaard & Sambridge, 2002), it was developed to efficiently sample a parameter space. As Sambridge (1999b) shows, the resulting model ensemble, i.e. all evaluations of the forward problem, can be used to estimate the posterior probability density function (PPD) as function a of model parameters. The combined approach can therefore be seen as an Bayesian approach (e.g. Tarantola & Valette, 1982a) to solve high-dimensional nonlinear inverse problems.

Despite the fact that the Stokes problem is a computationally demanding task and seem to be not feasible for a largely integrated probabilistic approach, we do expect a complex nonlinear relationship between rheological model parameters and data, and we can not be sure that a single global minima exist. Moreover, the dimension of the parameter space grows rapidly with the number of geological units of the model and at least some non-uniqueness is likely to exist as the gravity problem is a well know non-unique problem. A Monte Carlo based approach thus seems a natural choice to perform geodynamic inverse approach, although the major drawback of the method is that it require a large amount of forward models.

We employ the NA as it is more efficient than a standard Monte Carlo approach and as it suits itself well for parallelisation (Rickwood & Sambridge, 2006). Yet in order to perform parallel inversions in combination with parallel forward models (in which the solution time of different forward models can vary dramatically), it was necessary to develop a completely new parallel layout for the NA including a fully non-blocking architecture and explicit MPI-buffer (Message Passing Interface) management.

In this paper we aim to demonstrate the potential of joint geodynamic inversions to constrain effective rheologies. We show that a Monte Carlo based, probabilistic inversion is a feasible method to approach geodynamic inverse problems with numerical three-dimensional models, which are computed in parallel. In general, this approach is scalable and applicable to either small scale dynamics or lithosphere scales. However, involving the entire lithosphere requires power-law rheology, and thus a large parameter space. Here, we focus on synthetic models with Newtonian rheology, for which we choose a salt-tectonics model scenario to keep the number of model parameters limited, although it has geometric complexities to benchmark the inverse approach.

In the following sections, we first discuss an analytical experiment to demonstrate that theoretically, performing an inversion with a geodynamic model helps to reduce ambiguities of the inverse problem. Next, the general methodology is described including the forward problems that have to be solved. Finally, we employ synthetic three-dimensional salt-tectonics models to conduct a detailed feasibility study of the methodology, which includes how model resolution, model geometry and different constraints on the data affect the inversion results. Details on the new parallel implementation of the NA and derivations for the analytical experiment are described in the appendix.

## GEODYNAMIC INVERSION - AN ANALYTICAL EXPERIMENT

We employ a simple geodynamic model to illustrate the basic features of a joint geodynamic-gravity inversion. The model setup consists of a solid, buried sphere of radius R that is emplaced at a depth h below a horizontal free-slip interface and has a lower density than its surroundings, which have linear viscous rheology (see Fig. 2.1 and Table 2.1). The gravity problem has a well-known analytical solution, and the geodynamic problem is similar to that of a Stokes sphere with the difference that it rises in the vicinity of a free slip boundary (for which an approximate solution exists).

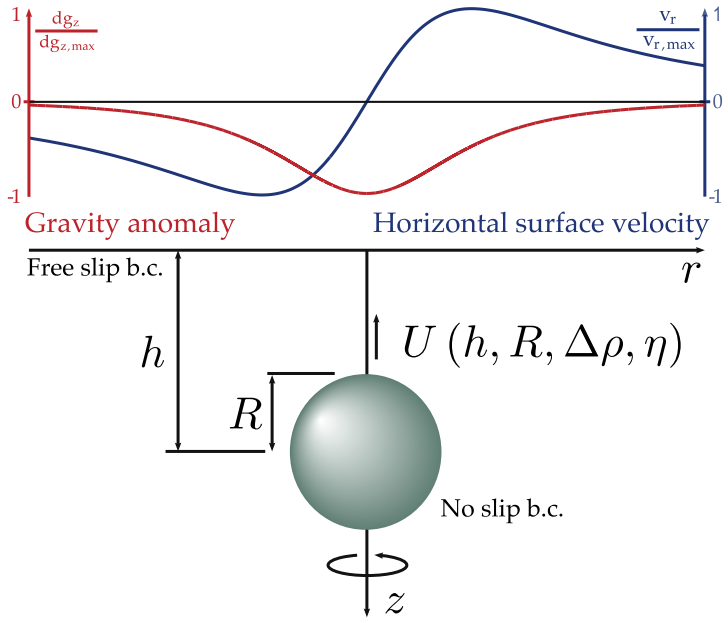


Figure 2.1: Analytical model setup, which consists of a solid, low density sphere that is surrounded by a linear viscous material and emplaced at depth h beneath a free-slip horizontal interface. Two sorts of data are used for inversions: (i) the gravity anomaly and (ii) the horizontal surface velocity.

| Name | Symbol | Value |
|---|---|---|
| Radius | $R$ | 4 km |
| Depth | $h$ | 8 km |
| Density of sphere | $\rho_{sphere}$ | 2000 kg/m$^3$ |
| Density of half-space | $\rho$ | 2600 kg/m$^3$ |
| Viscosity of half-space | $\eta$ | $10^{21}$ Pa s |

Table 2.1: True model parameters of the analytical model in Fig. 2.1

*Analytical solutions*

The lower density of the sphere will result in a variation of the vertical gravity component $dg_z$ along the horizontal surface $r$, that is given by (e.g. Jacoby & Smilde, 2009; Turcotte & Schubert, 2002):

$$dg_z(r) = \frac{4}{3}\pi G \frac{h}{(r^2+h^2)^{3/2}} \Delta\rho R^3, \tag{2.1}$$

where $G$ is the gravitational constant, $\Delta\rho$ the density difference between the sphere and surrounding material, $h$ the depth of the sphere and $r$ the horizontal distance to the sphere's center.

The horizontal surface velocity at the surface can be found by combining the results of Brenner (1961), Stimson & Jeffery (1926) and Pasol et al. (2005). In bipolar coordinates $(\xi, \mu)$, the velocity along the top (free-slip) boundary $(\xi = 0)$ is:

$$\begin{aligned} v(\mu)_{\xi=0} &= \frac{(1-\cos(\mu))^{1/2}}{c^2 \sin(\mu)} \\ &\quad \cdot \sum_{n=1}^{\infty} \left( B_n \left(n - \frac{1}{2}\right) + D_n \left(n - \frac{3}{2}\right) \right) \cdot V_n(\cos\mu), \text{ with} \end{aligned} \tag{2.2}$$

$$V_n(\cos\mu) = P_{n-1}(\cos\mu) - P_{n+1}(\cos\mu), \tag{2.3}$$

where $P_n(x)$ are Legendre polynomials. Along the top boundary of the model $\mu_{\xi=0}$ is equivalent to $r$. $B_n(R, h, \Delta\rho, \eta)$ and $D_n(R, h, \Delta\rho, \eta)$ are constants derived by Brenner (1961) which depend on the geometry, density contrast $\Delta\rho$ and viscosity $\eta$ (see appendix A for a detailed derivation).

*Inversion results*

The half-width $w$ of the gravity anomaly (e.g. Jacoby & Smilde, 2009) can be used to constrain the depth of the sphere, which is $h = {}^1/_2 \left(4^{1/3} - 1\right)^{-1/2} w \approx {}^2/_3 w$. Yet, at a given depth, the gravity signal is identical as long as the mass

of the sphere remains constant. Let $\widehat{dg_z}(x)$ be the observed gravity anomaly at the surface, in which case the density difference is (from eq. 2.1):

$$\Delta\rho(R) = \underbrace{\frac{3}{4\pi G} \cdot \frac{\widehat{dg_z}(r) \cdot (r^2 + h^2)^{3/2}}{h}}_{\text{const.}} \cdot \frac{1}{R^3} \tag{2.4}$$

The first part of this equation is constant for a given location r, which shows that a nonlinear trade-off exists between density and radius ($\Delta\rho \propto {}^{1}/_{R^3}$), which is clearly visible if we plot misfit as a function of density and radius (Fig. 2.2c), using a grid-search approach.

Now, we perform a grid-search inversion for the Stokes problem, using the horizontal surface velocity as input data. Since the Stokes velocity also depends on the viscosity of the half-space, $\eta$, the parameter space is increased by one dimension. If the viscosity of the surrounding media is known, results show that a single minima exists in the parameter space (e.g. Fig. 2.2a, b). Yet, if the viscosity is unknown, an infinite number of radii give equally good misfits. Interestingly, however, the radius of the sphere is uniquely determined. The Stokes problem in itself is thus also a non-unique problem, but since the trade-offs between density and radius are different for the gravity and the Stokes problem, we can combine them in a joint inversion to obtain a uniquely determined solution (Fig. 2.2d).

This illustrates that the benefits of performing an inversion with geodynamic models are two-fold. First it is obvious that we gain insights about the dynamical properties, i.e. the rheology of model. Second, it also helps to reduce ambiguities, despite the fact that the dimension of the parameter space increases. This implies that more forward models will need to be performed to find a (better) solution, but the pay-off is that this solution also gives insights into the physics or dynamics of the model opposed to pure gravity inversions. Yet, the model we studied here is a very simple one and it is thus desirable to tests this with more complex (3D) models.

### JOINT GEODYNAMIC INVERSION - GENERAL METHODOLOGY

The method involves three parts, namely (i) numerically solving three-dimensional forward problems for given input parameters many times, (ii) controlling the forward modeling with an optimisation technique that changes the input parameters with the aim to better fit surface observations and (iii) quantitatively interpreting the resulting model misfits. In our approach we combined the two first steps into a single massively parallel application, which we will discuss in more detail before we test the methodology with synthetic data.

#### *Forward problems*

Similar to what we used for the analytical experiment in section 2.2, we assume that observations of the gravity field and the surface velocity field are available,

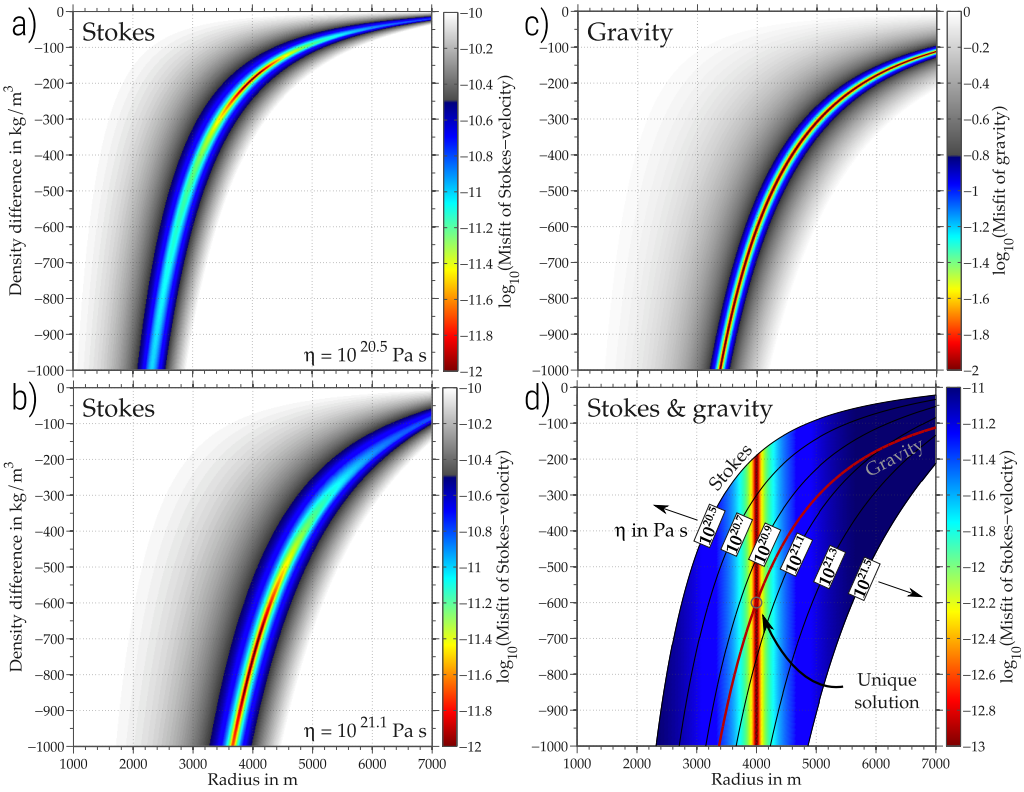


Figure 2.2: Model misfit versus radius and density difference. **a,b)** Only the Stokes problem is considered under the assumption that depth is known from gravity observations. For a given viscosity, a unique solution exist. **c)** Only gravity is used in the inversion, which results in an infinite number of solutions. **d)** Inversions are done for the Stokes problem for a viscosity range of $\eta = 10^{20.5} - 10^{21.5}$ Pa s. There is a clear trade-off between radius R and viscosity $\eta$. If this result is however combined with the gravity inversion result (red line), we can uniquely determine all model parameters.

and that we have knowledge of the 3D geometry of the problem, which arguably is the case for many places on earth were GPS observations and gravity data are available. As forward models we use a 3D viscous Stokes code and a 3D gravity code.

*Forward model (A): Variable viscosity Stokes*

The governing equations are the conservation of mass for incompressible fluids and the conservation of momentum, assuming a Newtonian viscous (but variable) viscosity:

$$\frac{\partial \sigma'_{ij}}{\partial x_j} - \frac{\partial P}{\partial x_i} + \rho g_i = 0 \tag{2.5}$$

$$\frac{\partial v_i}{\partial x_i} = 0 \tag{2.6}$$

$$\sigma'_{ij} = 2\eta\, \dot{\epsilon}_{ij}, \tag{2.7}$$

where $\sigma'_{ij}$ is the deviatoric stress tensor, P pressure and $v_i$ the velocity field. $\sigma_{ij}$ is linearly related to the strain rate tensor $\dot{\epsilon}_{ij} = {}^1/_2 \left( \frac{\partial v_i}{\partial x_j} + \frac{\partial v_j}{\partial x_i} \right)$, where $\eta$ is the effective viscosity. The discretized equations (2.5 - 2.7) form a coupled system of equations that can be expressed in a block form:

$$\begin{pmatrix} \mathbf{K} & \mathbf{G}^T \\ \mathbf{G} & \mathbf{0} \end{pmatrix} \begin{pmatrix} \mathbf{v} \\ \mathbf{p} \end{pmatrix} = \begin{pmatrix} \mathbf{f} \\ \mathbf{0} \end{pmatrix}, \tag{2.8}$$

where the solution vector $(\mathbf{v}, \mathbf{p})^T$ containing velocity and pressure solutions is coupled to the right hand side $(\mathbf{f}, \mathbf{0})^T$ that incorporates body and boundary forces with the Jacobian matrix. The jacobian contains the stiffness operator $\mathbf{K}$ with the discrete rheology of the model, the discrete divergence operator $\mathbf{G}$ and the discrete gradient operator $\mathbf{G}^T$.

We employ a staggered grid finite differences scheme to numerically evaluate the system of algebraic equations in (2.8). The Stokes problem is implemented and parallelised with the PETSc toolkit (Balay et al., 2012b,a, 1997), which allows running massively parallel forward simulations using a range of iterative solvers and algebraic multigrid preconditioners. The code is highly scalable and has been tested on over 16'000 cores with more than 2 billion degrees of freedom, although the runs performed here are done with significantly lower resolution, to allow many runs to be performed simultaneously during the inversion process. Material properties are stored on markers, and an internal free surface is implemented using the 'sticky air' approach (Crameri et al., 2012a), which is implemented as a low viscosity layer at the top of the domain. A fast erosion and sedimentation algorithm is implemented which adds sediments at a given, constant, rate to the model domain, which is important for modelling salt diapirs formed by down-building. The fast erosion is implemented after Kaus (2005) and Burg et al. (2004), where the average surface height is the controlling parameter. Material that was transported above the average surface height is eroded, for other areas that are below, sediments are deposited up to this level. This process is performed for every time step of the Stokes forward model.

*Forward model (B): Gravity*

In addition to the Stokes problem, we also have to solve the gravity forward problem. The density anomaly is given as the resulting density distribution of the Stokes problem. As we employ finite differences for the Stokes problem, we deal with discrete densities that are constant over the cubic volumes of each finite difference cell in the entire domain ($N_x \times N_y \times N_z$). There are different ways to perform the gravity forward problem. A solution can either be found by solving the gravitational potential equation or by explicitly evaluating the gravitational attraction of solid bodies in combination with the superposition principle. May & Knepley (2011) compared several approaches for computing gravity anomalies in terms of parallel performance and conclude that, besides the more advanced fast multipole technique, a classical summation technique

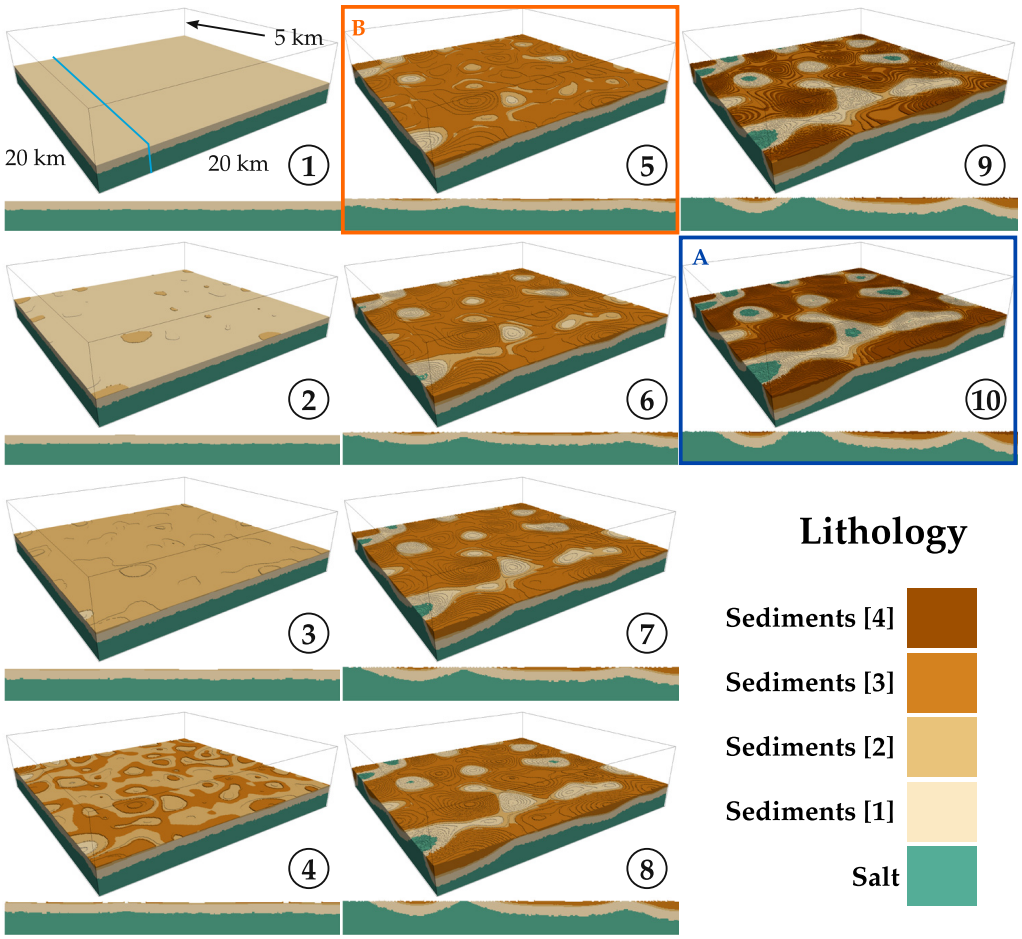


Figure 2.3: Forward simulation of salt tectonics, which involves both sedimentation and erosion, and results in various salt domes. Two snapshots of this simulation are taken as reference geometries for the inversion setups. Geometry A (number 10) is a case in which salt reached the surface, whereas geometry B is an intermediate evolution step where the salt has not reached the surface yet. For the inversion tests described in sections 2.4.1 and 2.4.2 model geometry A is employed only. Model geometries A and B are used for a comparative inversion test in section 2.4.3.

shows comparably good performance in accuracy, computation time and parallel scalability. As this summation approach is much more straightforward to implement, we employ it here. In general, the vertical gravitational contribution of a three dimensional body at a survey point $\mathbf{s}(\xi, \eta, \zeta)$ is given as:

$$g_z(\mathbf{s}) = G \int\int\int \rho(x, y, z) \cdot \frac{\zeta - z}{[(\xi - x)^2 + (\eta - y)^2 + (\zeta - z)^2]^{3/2}} \, dx \, dy \, dz, \tag{2.9}$$

where G is the gravitational constant and $\rho(x, y, z)$ is the discrete density in the model. The classical summation technique numerically evaluates the integral in eq. (2.9) by using a two point gauss quadrature scheme in each coordinate direction for each of the finite difference cells. We compute the gravity anom-

aly of the entire domain by superposing all contributions. As calculating each single contribution is an independent task, it can be parallelised in a straightforward manner without need for parallel MPI communication. We only need to perform a single global MPI reduction at the end of the calculations. As long as decomposing the domain into equally sized sub domains is possible, this procedure is highly scalable (May & Knepley, 2011). Having a parallel forward gravity code is necessary as the gravity computation otherwise becomes the bottleneck of the forward simulations.

*Inversion technique*

The inversion procedure is a two stage approach. First, a direct-search method is applied, which involves solving the forward problems described in section 2.3.1 and the computation of misfits based on observational data sets. The direct-search method results in a discrete representation of the misfit function in the parameter space. In a next step, this data set (model parameters and respective misfit values) is analysed to estimate acceptable parameter ranges, i.e. the posterior probability density function (PPD).

*Direct-search approach*

We use the Neighbourhood Algorithm (NA) by Sambridge (1999a), which combines a Monte Carlo direct-search method with geometric concepts for partitioning the parameter space. This allows searching a high-dimensional parameter space in a very efficient manner compared to the classical Monte Carlo methods, which is very important if the forward problem is computationally expensive as in our case. Moreover, because the NA is a Monte Carlo like inversion algorithm, it is especially suitable when dealing with nonlinear inverse problems and expected non-uniqueness. A parallel version of the NA was published by Rickwood & Sambridge (2006). We found this version unsuited for our problem as (i) we have forward models that have to be performed in parallel and (ii) we typically have large run time differences between the individual forward models, which depends on the viscosity contrast and geometry of the Stokes forward model. In the original parallel version of the NA, a synchronisation barrier was been implemented after the initial sampling stage. This implied that all processors had to wait until all initial forward models were finished before they could continue the main sampling stage. On large scale computers, this significantly degrades the parallel performance of the code. We therefore developed a new parallel layout (NAplus) that explicitly allows parallel forward models and avoids synchronisation bottlenecks. In particular, we also employ `C++` containers to explicitly handle the MPI message buffer to avoid memory problems. A detailed description of our new implementation is given in B.

| Layer | Density $\rho$ [kg/m$^3$] | Viscosity $\eta$ [Pa s] |
|---|---|---|
| Salt | 2200 | $10^{18.0}$ |
| Sediments [1] | 2810 | $10^{19.1}$ |
| Sediments [2] | 2790 | $10^{19.3}$ |
| Sediments [3] | 2750 | $10^{19.2}$ |
| Sediments [4]* | 2800 | $10^{19.5}$ |
| Sticky-air* | 0 | $10^{16.0}$ |

Table 2.2: Rheology of the reference model. The rheology of the reference model is similar to the rheology of the forward evolution simulation in Fig. 2.3. This is also the 'target' rheology for the inversion tests. We do not invert for the rheology of sediment layer [4] and the rheology of the sticky-air layer.
*(*) Layer is not part of the inversion.*

The inversion is based on minimising an objective function in a weighted least squares manner:

$$\begin{aligned} \chi^2 &= \frac{1}{\nu} \sum_{i=1}^{N_{obs}} \left( \frac{\phi_i^{obs} - \phi_i^{pred}}{\sigma_i} \right)^2, \\ \nu &= N_{obs} - M_{mod} \end{aligned} \tag{2.10}$$

where $\nu$ is the number of degrees of freedom, which is the difference between the number of observations $N_{obs}$ and the number of model parameters $M_{mod}$. $\phi_i^{obs}$ describes the observations and $\phi_i^{pred}$ the predictions of the model respectively. The residual is normalized with the standard deviation $\sigma_i$, computed from the data.

*Estimation of acceptable parameter ranges*

The resulting data set of the direct-search procedure contains a collection of model-misfits depending on the respective model parameters. We follow Sambridge (1999b) who proposed a resampling technique to estimate Bayesian integrals (i.e. marginal PPD). In this method, a Gibbs sampler (Geman & Geman, 1984) is used to importance sample an approximation of the PPD, which can be estimated from the resulting ensemble of models of the direct-search process. Additionally, this method provides estimates (potential scale reduction, PSR values) that show whether the Gibbs sampler has converged, which is also a good indicator on whether sufficient forward models have been performed.

*Case study model geometry: Salt-tectonics*

As test case, we use a forward model that simulates the formation of salt domes under a sedimentary overburden of increasing thickness (Fig. 2.3), which is a

synthetic scenario that is nevertheless not totally unrealistic and comes with a certain geometric complexity.

The forward problem uses a box of $20 \times 20 \times 5$ km with a numerical resolution of $128 \times 128 \times 32$ finite-difference cells. The model consists of a basal layer of low density salt that is overlain by a sedimentary layer that increases in thickness with time due to (i) a constant sedimentation rate (1 mm/yr) to introduce a sedimentary layering and (ii) a constant erosion process. Besides the upwelling of the salt, this adds a down-building effect to the dynamic system, which also controls the spacing and shape of the salt domes. Gaussian random noise of maximum amplitude 190 m is initially added at the salt-sediment interface.

We start the simulation with a flat salt layer of 1.25 km thickness, whereas the initial sedimentary overburden consists of a single, 500 m thick layer (sediments [1]). The remaining part of the domain is initially filled with sticky air. During the sedimentation process the properties (or phase number) of the sedimented material change every 100 kyrs to ensure a change in lithology, where each layer is given a particular density and viscosity, as listed in Table 2.2.

For the inversion, we use two different snapshots of the forward simulation; Geometry A, describes a stage in the development where a few salt-diapirs reached the free surface and the sedimentation of the fourth sedimentary layer has just started. Geometry B, involves an earlier stage in which the salt does not yet extrude to the surface. During the inversions, we only focus on the geometry and the model output at the center of the model domain to minimize the model bias due the free slip boundaries (see Fig. 2.4).

### INVERSION TEST RESULTS

During the inversion runs we assume that the 3D geometry is perfectly well-known, which is reasonable for salt-structures due to the availability of high-resolution 3D seismic data in many sedimentary areas, and we seek the optimal model parameters. Within these assumptions, we have eight unknown parameters, which are the densities and effective viscosities of the salt layer and the sedimentary layers [1-3], which we will refer to as the 'true' model parameters. We exclude sediment layer four from the inversion targets because it is not present in geometry B and is very thin in geometry A. Using the true model parameters we create a synthetic set of surface observations, which is the gravity anomaly and the horizontal and vertical surface velocities. For all inversion tests, we at least add 5% of Gaussian noise to the data, which corresponds to a signal-to-noise-ratio (SNR) of 20.

We investigate the robustness of the inverse approach with three different tests. In a first test, we perform the inversion with models that have the same numerical resolution as the original forward model. These results are compared with inversion results of models that are performed at a lower numerical resolution, and that are thus computationally cheaper. In a second test, we test the sensitivity of the results to changes in the noise-level and incomplete data coverage of the surface observables. Finally, we check the sensitivity of the inversion results to the input geometry. Uncertainties in geometry (for example in

| Name | Cells | Grid spacing |
|---|---|---|
| High resolution (HR) | $128 \times 128 \times 32$ | 156.25 m |
| Intermediate resolution (IR) | $96 \times 96 \times 24$ | 208.33 m |
| Low resolution (LR) | $80 \times 80 \times 20$ | 250.00 m |
| Low lateral & high vertical resolution (MR) | $80 \times 80 \times 32$ | 250.00 m<br>156.25 m |

Table 2.3: Model properties for performing resolution tests. The aspect ratio of the FD cells is 1 for all models except the mixed resolution (MR) model where the aspect ratio is 1.6. The dimension of domain is kept at a constant size of $20 \times 20 \times 5$ km.

layer thickness) can in principle also be taken into account during the inversion, which would simply increase the number of unknowns. Here, we study the effect of differences in geometry by considering two geometrical end-member models.

*Inversion for different model resolutions*

We use a setup with fully developed salt-diapirs (geometry A in Fig. 2.3), and perform inversions using four different model resolutions (Table 2.3), with HR being the high resolution model that is the same as that used for the forward evolution simulation. The geometry of the salt-tectonics scenario is stored as a field of markers with a corresponding lithological phase information. For the inversions, the marker field of the high resolution model is also used for the models of reduced resolution as geometry. Moreover, the data quality (SNR $=$ 20) is the same for all inversion runs. However, since we work with different lateral resolutions of the model, the velocity data has to be interpolated to a grid that corresponds to the currently used model resolution.

For this experiment, about 38'000 forward models have been calculated for every inversion. We started NAplus with 4000 randomly chosen initial models, and the controlling parameters of the algorithm were adjusted to act more explorative than directive, which means 1500 new samples are generated to resample 500 cells of lowest misfit (Sambridge, 1999a). We used 16384 CPUs in total, and 16 CPUs for every forward model, which implies that 1024 forward models were running simultaneously during the inversion. The overall runtime of the inversion was approximately four hours for the high-resolution case.

The $\chi^2$ misfit values of all forward models of the HR inversion case are plotted for all possible parameter combinations on Fig. 2.5, where each dot represents a simulation result and the true model values are marked as grey circles. The inversion algorithm focusses on regions with a low misfit and the number of models that are performed for a certain parameter range therefore gives a first indication on the optimal parameters (histograms in Fig. 2.5).

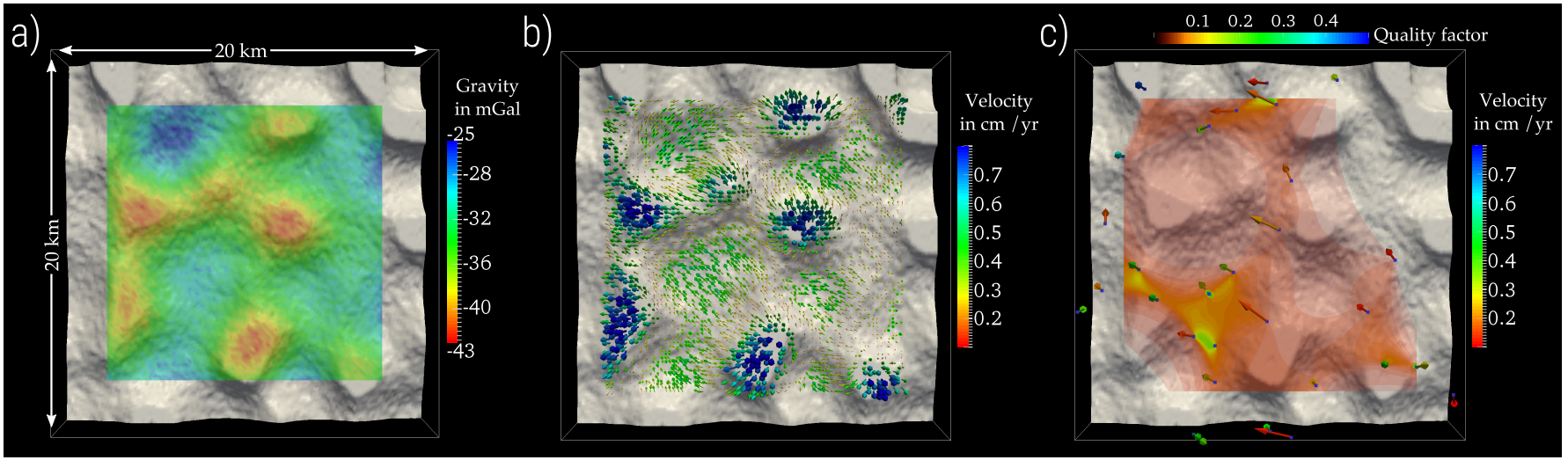


Figure 2.4: Synthetic surface observations computed with the high resolution model for geometry A. To minimize boundary effects, we only interpret results in the center of the model (at 2.5 km distance from the boundaries). **a)** Gravity anomaly with added Gaussian noise (SNR = 20). A clear correlation exists between gravity lows and the interface between salt-sediment interface (gray). **b)** Surface velocity field with noise (SNR = 20), computed with the high resolution model but interpolated to the intermediate resolution (IR) grid. **c)** Velocity constraints used for the inversion test in section 2.4.2, in which the number of surface data points is limited to 30, and data is interpolated to a regular grid using a natural neighbour interpolation. A quality factor is computed as a function of data sparsity, which is taken into account during the inversions.

The results show that a clear (single) misfit minima exists for the density and viscosity of the salt layer ($\rho_0$, $\eta_0$) as well as that of the first sedimentary layer ($\rho_1$, $\eta_1$), and that this misfit is in good agreement with the true model parameters. For other parameter combinations, such as ($\rho_2$, $\eta_2$) numerous misfit minima are present, and the parameters of the third sedimentary layer ($\rho_3$, $\eta_3$) are not as well constrained as those of the salt- and first sedimentary layer.

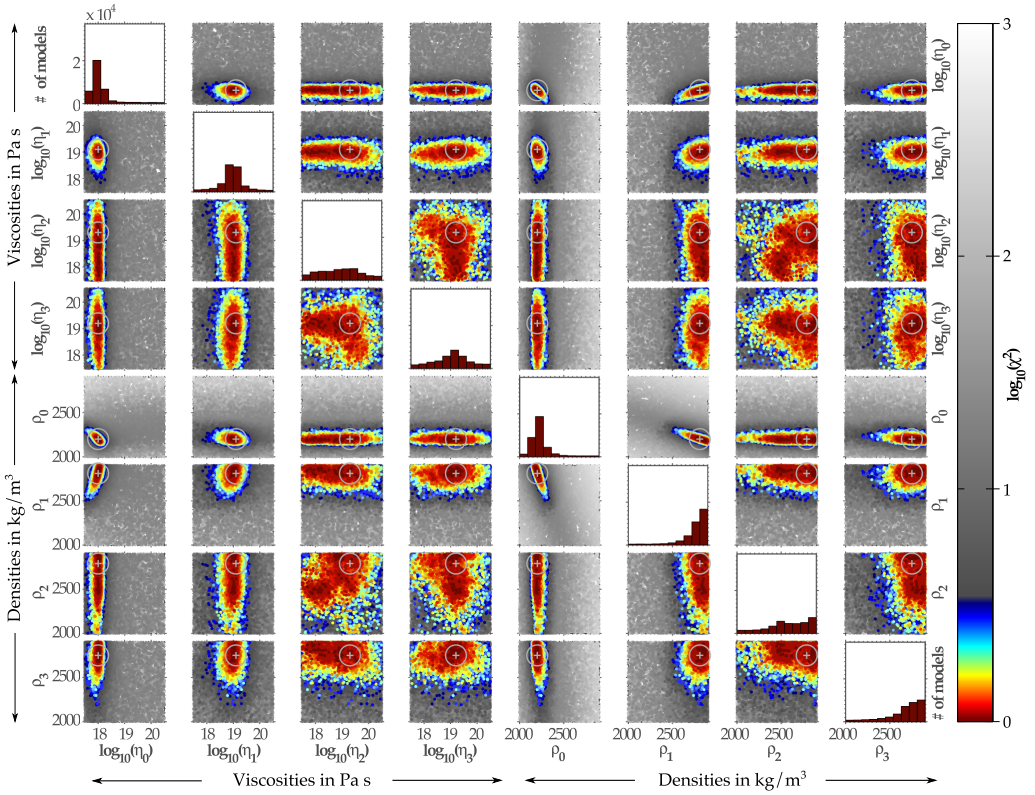


Figure 2.5: $\chi^2$ misfit as a function of model parameters after the first (direct-search) stage of the inversion procedure for the high resolution (HR) inversion case. Parameter indices correspond to respective layers, with 0 being the salt layer. Grey markers indicate true model values, and every dot represents a single 3D forward model. Histograms indicate how many models have been performed for certain material parameters. The true model parameters can be well recovered for most layers.

Misfit as a function of density of the layers [0] and [1] is given in Fig. 2.6, where we can observe a clear trade-off between the parameters, which is linear in this case and correlates well with the true model value in this component-plane of the parameter space. It also illustrates a basic feature of the NA, which samples more models in 'promising' regions of the parameter space.

However, the results at this stage of the inversion procedure, the direct-search results, only give a first overview of the variety of possibly acceptable models in the parameter space. In order to get quantitative estimates, we follow Sambridge (1999b) and estimate marginal PPDs in a Bayesian approach (section 2.3.2.2), for which a Gibbs sampler performs 100 random walks with 100 steps each, starting from the best 100 model locations. For all computations of the

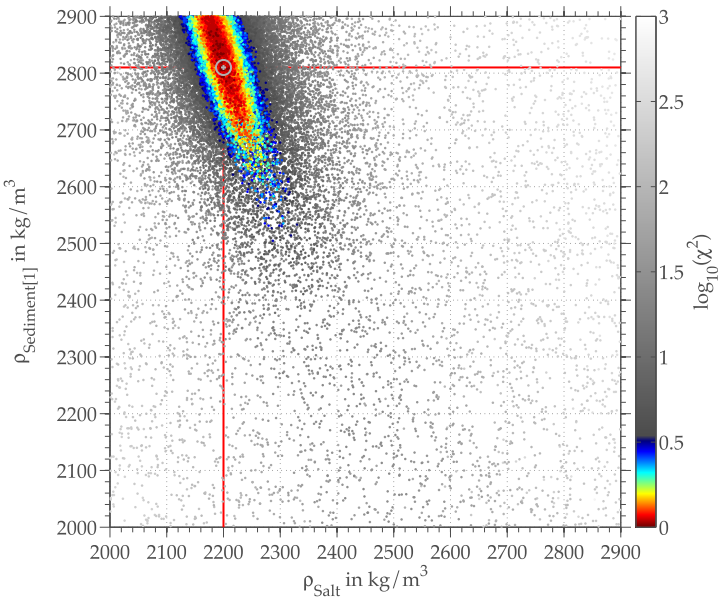


Figure 2.6: Misfit of the high resolution model as a function of density of the salt and first sedimentary layer. Every dot represents one forward model. A nearly linear trade-off exists between the two parameters. Low misfit models are located in the vicinity of the true model parameters, which are indicated with a grey marker and the red lines.

marginal PPDs, the prior distributions are uniform between the boundaries of the parameter space.

The results of this comparison can be visualized as 1D marginal PPDs for each of the model parameters, with the peak corresponding to its most likely value and the width of the peak to the uncertainty of the parameter (see Fig. 2.7, where red lines indicate the true model parameters). Results for the HR inversion (blue line) show that the parameters of the basal salt layer as well as those of the first sedimentary layer are very well constrained and almost 'Gaussian' shaped. On the other hand, the marginal distributions of the parameters of sedimentary layer [3] are not as clear, and exhibit two distinct maxima for the density and three for viscosity. The marginal PPD of layer [2] shows several maxima over a wide range, suggesting that we cannot constrain its parameters very well. A cross-section of model geometry A (Fig. 2.3) reveals that this layer is very thin and it is thus likely that it doesn't contribute much to the overall dynamics of the model, which is why an inversion will not be able to correctly retrieve its properties.

If we compare the marginal PPDs of the high resolution model with those at lower resolutions, we can see that the IR-model is fairly similar to that of the HR-model, although the PPD amplitudes are slightly smaller and the results look 'smoother'.

The resulting distributions of the low resolution model (red) for the salt layer have a clearly defined peak which is however offset from the true model parameters, and we can thus no longer reliably retrieve model parameters. In order to understand whether this is mainly due to limited horizontal or vertical res-

olution, we performed an inversion with a 'mixed' (MR) resolution model that is highly resolved in vertical direction, but laterally low resolved. Its marginal PPD in green correlates very well with the HR and IR results, which suggests that it is mainly the vertical resolution of the model that matters in this particular setup. This result is expected because the material properties mainly vary in vertical direction, which directly affects the down-building. Besides the upwelling of the salt, this is the second of the two main driving processes in the model.

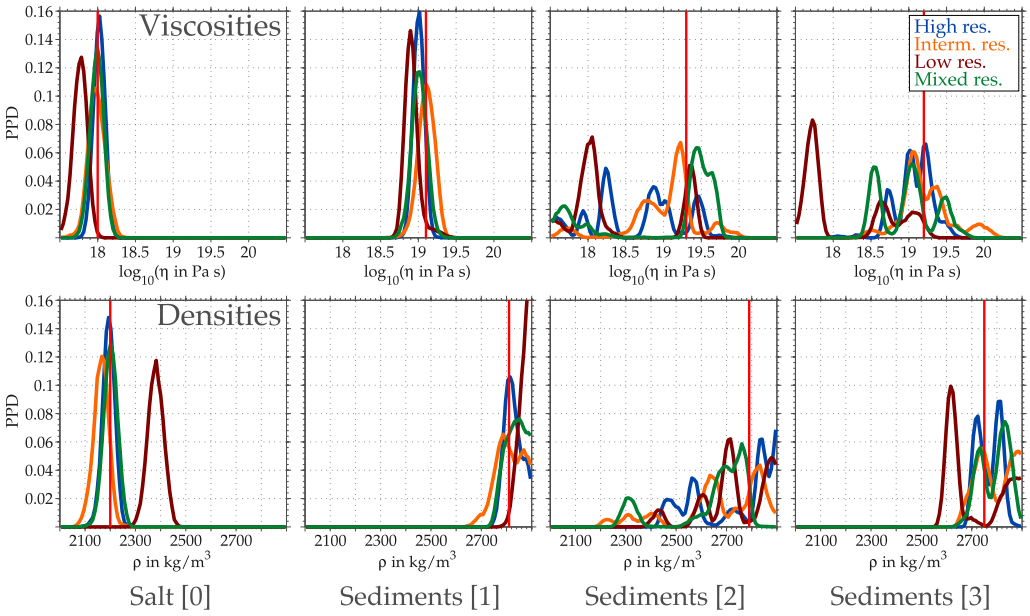


Figure 2.7: 1D marginal PPDs for different model resolutions for each of the model parameters. 'True' model values are shown with red lines. The marginals of the high resolution model in blue can be seen as reference.

*Surface constraints*

Next, we study the influence of noise and data coverage of the surface constraints on the inversion results. All test were performed with the intermediate resolution model, and we added 5% (SNR = 20) and 10% (SNR = 10) noise to the data. Results show that we can retrieve the true model parameters in both cases, even though the viscosity parameters are slightly better recovered if there is less noise (Fig. 2.8). Thin layers, such as layer [2], cannot be constrained in either case.

In the previous tests, we assumed homogeneous data coverage. In reality this will rarely be the case and GPS stations are often more sparsely located. To test the effect of this, we performed an inversion in which we use only 30 randomly chosen velocity vectors of the reference data set for the inversion and added Gaussian noise (SNR 20) to them. The velocity vectors were interpolated on the free surface grid points of the finite-difference grid using natural neighbour interpolation (Sibson, 1981), which uses a Voronoi tessellation of the lateral

positions of the velocity observations. The inverse of the area of a Voronoi cell represents the point density at any particular position, and we use this value (which can be easily computed from the location of GPS sensors) as a quality factor to evaluate the velocity vector as illustrated in Fig. 2.4c. The quality factor is low for regions with low data coverage, such as in the top-right part, whereas regions with a high point have a higher quality factor as can be seen in the lower left corner. For the misfit computation, the quality factor is used as a linear weighting factor for the velocity error at that particular position.

Inversion results show that the viscosities of the salt and sediment layer [1] can still be retrieved, even though they are less well constrained as in the case of homogeneous data coverage (red lines in Fig. 2.8), but as previously, we cannot constrain the viscosities of the second and third sedimentary layer very well. The results for the densities are not strongly affected by the reduction in velocity constraints which is expected, because viscosity is only part of the Stokes forward problem, whereas density is involved in the gravity and the Stokes forward problem. We thus expect a reduction in velocity constraints to have a first order effect on the viscosities results, but only a reduced effect on the density results.

Introducing the quality factor for the velocity data helps to balance this impact. In order to get a better understanding on how strongly the randomness of the velocity constraints affects the viscosity PPDs, we repeated the inversion five times, each run having 30 randomly chosen velocity constraints. We plot the resulting marginal PPDs as a mean PPD and variance of marginal PPDs in Fig. 2.9. The variance of the density PPDs is relatively small compared to the variance of viscosity PPDs. This means that the density results are relatively robust, also if only a limited number of velocity measurements is available. The results also show that viscosities of important layers such as salt and first sediment layer can be resolved within the error limits. Nevertheless, the variations can be quite significant depending on where velocity is measured on the surface.

The result also gives a hint how the velocity data quality affects the determination of the density contrast, as the noise of the gravity field was kept the same for all five independent inversions. Whereas for the salt layer, the variance in density is almost not noticeable, there is an increase in variance for the density PPDs of other layers. The uncertainty in density, which originates from the distribution of the velocity measurements can be as high as $\Delta\rho \approx \pm 50\,\mathrm{kg/m^3}$ for the layer [3] density.

*Effect of model geometry*

In a next step, we test the effect of changing the model geometry. As the forward simulation was done with a constant density and viscosity for each of the layers, we should ideally be able to retrieve these values irrespective of the geometry of the setup. Yet, the model dynamics and velocity fields of the forward model change quite drastically once the salt extrudes to the free surface and it is thus interesting to compare the stage after extrusion (geometry A, which we

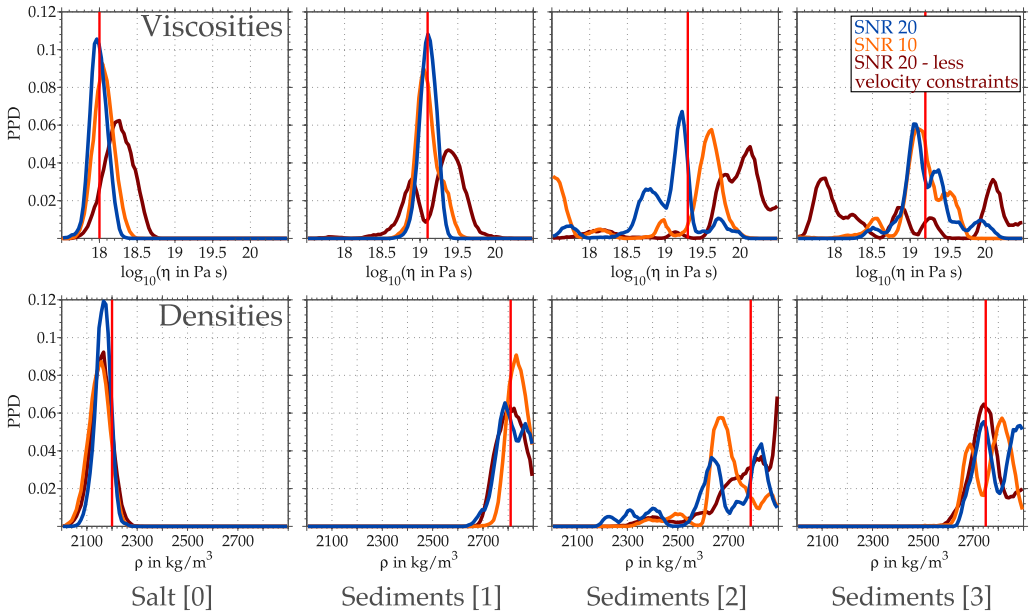


Figure 2.8: Comparison of 1D marginal PPDs for different noise conditions added on top of out synthetic data set. Results are shown for an inversion results with SNR = 20, SNR = 10 and a third case in which we only used 30 velocity constraints and additional quality weighting based on the sparsity of the velocity data.

considered so far), with the stage prior to that (geometry B). We use HR models and added 5 % of noise (SNR 20). The results (Fig. 2.10) show that we can retrieve the true model parameters in both cases, but that the rheology of the salt layer is less constrained for model geometry B. For both viscosity and density the peak-amplitude is smaller and the peak-width (or uncertainty range) is larger.

These results might be due to the fact that the salt structures are less evolved and as a result, the velocity magnitudes and gravity anomalies are smaller for geometry B. Strong differences are found for the parameters of sediment layer [3], although it should be kept in mind that this layer is not fully developed in geometry B (see Fig. 2.3), which implies that it has less impact on the overall model dynamics. Contrary to the previous results, the relative thickness of layer [2] is increased as the layer [3] thickness is smaller for model B. This increases the impact of layer [2] on the entire dynamics of the system, which results in a better fit of its viscosity. However, the layer [1] and [2] densities show trade-offs, which is likely due to the fact that the two consecutive layers are less deformed at this stage.

### DISCUSSION

As with any model, the quality of the result of a geodynamic inverse problem depends on the choice of the model, i.e. the expert knowledge, which is implemented in terms of physics, geometry, boundary conditions, scaling and resolution of the model. Together with a suitable parametrisation, this is part of the

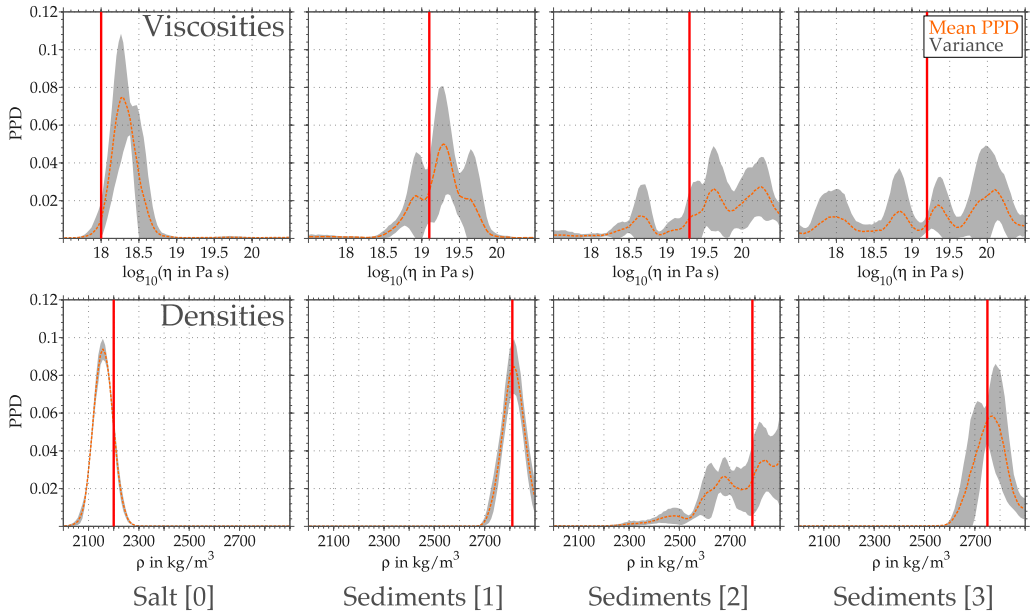


Figure 2.9: Mean PPD and variance of marginal PPDs as result of five independent inversions. For each inversion a different set of 30 surface velocity constraints is employed. This test demonstrates the robustness of the inversion with respect to a limited number of surface velocity measurements available.

a priori assumptions. In this respect, defining appropriate prior distributions is essential in a probabilistic inversion approach (e.g. Mosegaard & Tarantola, 1995). In our case, we assume that the prior is uniform between the boundaries of all model parameters, which is a reasonable choice for our synthetic model. For real world cases (with a larger parameter space) the parameter boundaries have to be chosen more carefully, and it has to be evaluated whether a uniform distribution is the right choice for the prior, because it directly affects the PPD. Moreover, it is up to the scientist to decide which sort of observed data can be represented by the model, and how to appropriately pre-process the data with selections, corrections and filters and how this affects the error of the data. Finally, the quality of the inversion results also depends on the choice of the inversion algorithm.

In our case, we assume that we have knowledge on the model geometry, which is a strong simplification, but in terms of salt-tectonics probably a reasonable one. On a larger, lithospheric scale, this can be more problematic. Yet, in many mountain belts (such as the Himalaya or Alps) quite a bit of geophysical information is available already and in most cases at least the location of the Moho has been determined to high precision. In addition, seismic tomography models have been developed for most mountain belts and whereas the tomographic models are not always necessarily in agreement with each other, they can at least be used to derive end-member geometries for which a geodynamic inversion can be performed. By comparing the inversion results for the different end member models we get some idea on the sensitivity of the most likely lithospheric rheologies to the model geometry and, ideally, which geometry is most consistent with available data. Directly linking the tomography

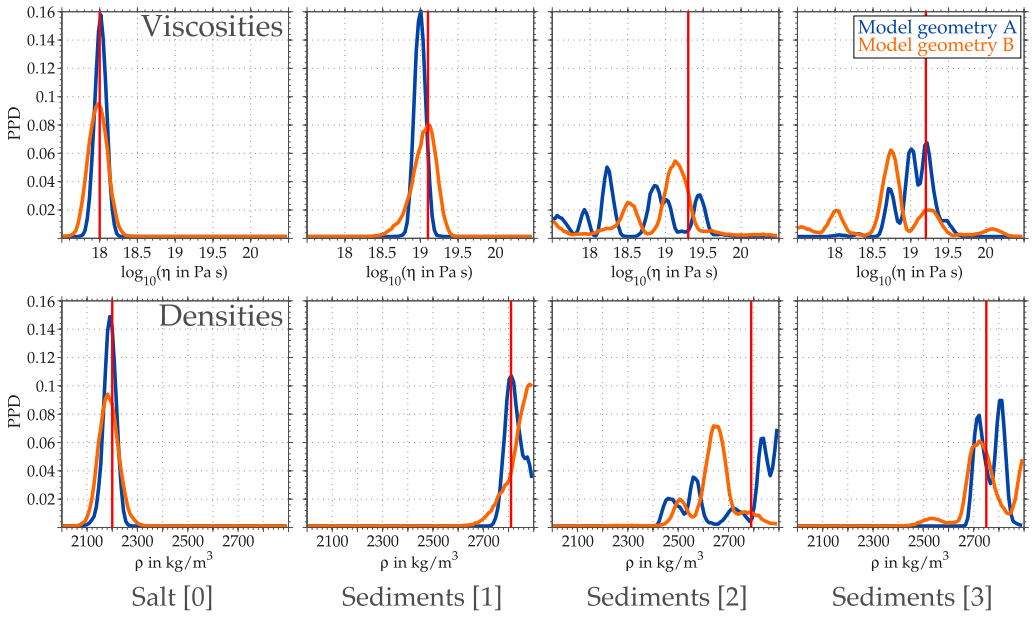


Figure 2.10: Comparison of marginal PPDs for two different model geometries (see Fig. 2.3). Geometry A is a model with almost fully developed salt diapirs, whereas model B is at an intermediate stage, when salt does not yet extrude at the surface.

inverse problem with the geodynamic inverse problem in a joint-multiphysics inversion is certainly an ambitious task and has potential for future approaches. However, there is a lot of uncertainty how seismic velocities, attenuation and other seismological quantities are linked with the temperature distribution and geological units that are geodynamically relevant. For the moment, geological interpretation is required to use this data. Other seismological observations such as Moho depths derived from receiver functions are more precise and should be tested in the first place.

Another assumption we made implicitly in our inversion is that homogeneously observed gravity data is available (which is the case for much of the planet thanks to recent satellite missions, although their quality varies with scale) and that measured surface velocities are representative of lithospheric deformation on a geological time-scale. This latter assumption has been discussed quite vigorously in the literature. One location where it can be tested is the western US, where a large amount of GPS stations have been installed in recent years. Platt & Becker (2010) performed such a comparison with recent data and found that GPS-derived slip rates compare well with geological estimates which suggests that present-day velocity field is representative of long-term motions. Even if this is not perfectly satisfied, performing a geodynamic inversion give still important insights as it will excluded models that result in total unrealistic velocities.

Another important limiting factor is how the physics is incorporated and discretised in the forward model. In our synthetic inversion tests, we experimented with four distinct lithological units, each of which had only two effective parameters: a constant linear viscosity and density. This was mainly done to restrict

the number of free parameters in the model and make the inverse model feasible. Yet, real rocks are more likely to have a nonlinear or even plastic rheology. As these rheologies do not have a memory, it is technically possible to take these complexities into account during the inversion procedure. Yet, it will of course increase the dimension of the parameter space, and as temperature of the lithosphere is often imprecisely known, it will also require a viscosity parametrisation that does not depend on temperature.

This emphasises the need for an 'intelligent' sampling strategy that reliably works in high dimensional parameter spaces. The neighbourhood algorithm is a well-tested and frequently applied algorithm, which allows to efficient and reliably sample a multidimensional space. However, in our experience a scalable parallelisation without blocking communication strategies is crucial in order to effectively deal with geodynamic forward models of different run-times. Nevertheless, the inversion approach is a Monte Carlo type approach, which is in fact the worst method to choose in terms of computational efficiency. On the other hand, a Monte Carlo type approach is easy to parallelise and scalable. The obviously nonlinear geodynamic inverse problem must not be linearised, neither additional efforts must be undertaken to account for ambiguities. Future projects of this kind must not disregard other approaches. In particular, it would be interesting to compare with other inverse approaches (such as the adjoint method) in terms of inversion results and computational efficiency.

In our approach, we limited the number of observables to the gravity field and the surface velocities. In reality, many more (reliable) datasets exists for many places on Earth, such as topography, lithospheric stresses, seismicity (which might be a proximity to the plastic or brittle part of the lithosphere), or seismic anisotropy. Adding these additional constraints to the inversion algorithm is rather straightforward as long as we have a forward model to predict each data set from a synthetic model, and having more constraints will likely help to reduce the ambiguities (Afonso et al., 2013b,a). Here, we demonstrate that performing the Stokes forward model within such a Monte Carlo type inverse approach is possible if a highly scalable parallel implementation is used, which shows the great potential of the Stokes forward problem being used as a complementary part of a multi-observable probabilistic inversion.

The usual way to compute the strength (or effective parameters) of the lithosphere is through estimating the effective elastic thickness (EET) of the lithosphere from the coherence of the gravity and topography (e.g., Burov, 2007; Watts, 2001). The disadvantage of that method is that it assumes a priori that the lithosphere is a thin elastic plate floating on a viscous mantle. Whereas this might be an appropriate simplification for oceanic lithosphere (where estimates of EET between various groups largely agree), it is certainly incorrect for many active mountain belts where estimates of the EET between various authors vary dramatically. In those locations, we typically have many additional geophysical data-sets available, and it is thus important to take this data into account in order to better understand which rheologies are consistent with the given data. The results here are a first step in this direction and show that geodynamic

inversion is feasible even with 3D models, although more work is required to understand how rheological complexities can be resolved.

## CONCLUSIONS

We describe a new method to constrain the rheology of the lithosphere which combines surface observations (gravity and surface velocity) with forward models of lithospheric deformation and a Bayesian inversion approach.

The advantages of using such a geodynamic inversion method are illustrated with a simple example of a rising low density sphere for which analytical results exist. Whereas a gravity inversion alone gives non-unique results, a joint gravity and geodynamic inversion increases the parameter space but gives a uniquely constrained result.

In order to study more complicated cases, we developed a massively parallel inversion method that combines a frequently used Monte Carlo direct-search approach, the Neighbourhood algorithm, with parallel, three dimensional geodynamic forward models. The parallel layout of the Neighbourhood algorithm was rewritten to robustly and optimally perform the inverse approach with parallel geodynamic Stokes and parallel gravity forward models runs on over 16'000 cores.

To test the inverse method we perform a 3D forward simulation that simulates the formation of salt diapirs under sedimentation and fast erosion. Snapshots of this model are taken as an input for the inversion algorithm and results show that we can reliably retrieve the true model parameters even if noise is present in the data, as long as the layers (i) contribute to the overall, large scale dynamics of the model and (ii) are numerically sufficiently well resolved.

This thus suggests that a joint geodynamic inversion is a potentially powerful technique that links geophysical observables with the dynamics of the crust and lithosphere.

## ACKNOWLEDGMENTS

This project was fully supported by the European Research Council under the European Community Seventh Framework Program (FP7/2007-2013) with ERC Starting Grant agreement #258830. We thank M. Sambridge for sharing his Neighbourhood Algorithm code. Numerical computations have been performed on JUQUEEN of the Jülich high-performance computing centre. Two anonymous reviewers are acknowledged for their critical and detailed reviews. We also thank the Editor-in-Chief L. Jolivet and the Managing-Editor E. Burov for their editorial handling of the manuscript.

## REFERENCES

Afonso, J., Fullea, J., Yang, Y., Connolly, J., & Jones, A., 2013a. 3-d multi-observable probabilistic inversion for the compositional and thermal struc-

ture of the lithosphere and upper mantle. ii: General methodology and resolution analysis, *J. Geophys. Res. Solid Earth*, **118**(4), 1650–1676.

Afonso, J. C., Fullea, J., Griffin, W. L., Yang, Y., Jones, A. G., D. Connolly, J. A., & O'Reilly, S. Y., 2013b. 3-d multiobservable probabilistic inversion for the compositional and thermal structure of the lithosphere and upper mantle. i: a priori petrological information and geophysical observables, *J. Geophys. Res. Solid Earth*, **118**(5), 2586–2617.

Alisic, L., Gurnis, M., Stadler, G., Burstedde, C., Wilcox, L. C., & Ghattas, O., 2010. Slab stress and strain rate as constraints on global mantle flow, *Geophys. Res. Lett.*, **37**(22), L22308.

Balay, S., Gropp, W. D., McInnes, L. C., & Smith, B. F., 1997. Efficient management of parallelism in object oriented numerical software libraries, in *Modern Software Tools in Scientific Computing*, pp. 163–202, Birkhäuser Press.

Balay, S., Brown, J., , Buschelman, K., Eijkhout, V., Gropp, W. D., Kaushik, D., Knepley, M. G., McInnes, L. C., Smith, B. F., & Zhang, H., 2012a. PETSc users manual, Tech. Rep. ANL-95/11 - Revision 3.3, Argonne National Laboratory.

Balay, S., Brown, J., Buschelman, K., Gropp, W. D., Kaushik, D., Knepley, M. G., McInnes, L. C., Smith, B. F., & Zhang, H., 2012b. PETSc Web page, http://www.mcs.anl.gov/petsc.

Becker, T. W. & Boschi, L., 2002. A comparison of tomographic and geodynamic mantle models, *Geochem. Geophys. Geosyst.*, **3**(1).

Becker, T. W. & Faccenna, C., 2009. A review of the role of subduction dynamics for regional and global plate motions, in *Front. Earth Sci.*, pp. 3–34, Springer.

Bercovici, D., 2003. The generation of plate tectonics from mantle convection, *Earth Planet. Sci. Lett.*, **205**(3), 107–121.

Boschetti, F. & Moresi, L., 2001. Interactive inversion in geosciences, *Geophysics*, **66**(4), 1226–1234.

Brenner, H., 1961. The Slow Motion of a Sphere Through a Viscous Fluid Towards a Plane Surface, *Chem. Eng. Sci.*, **16**, 242–251.

Bunge, H. P., Hagelberg, C. R., & Travis, B. J., 2003. Mantle circulation models with variational data assimilation: inferring past mantle flow and structure from plate motion histories and seismic tomography, *Geophys. J. Int.*, **152**(2), 280–301.

Burg, J.-P., Kaus, B. J., & Podladchikov, Y. Y., 2004. Dome structures in collision orogens: Mechanical investigation of the gravity/compression interplay, *Special papers - Geological Society of America*, **-**, 47–66.

Burov, E., 2007. Plate Rheology and Mechanics, in *Treatise on Geophysics*, vol. 6, Crust and Lithosphere Dynamics, pp. 99–151, ed. Schubert, G., Elsevier.

Burov, E., Podladchkov, Y., Grandjean, G., & Burg, J. P., 1999. Thermomechanical approach to validation of deep crustal and lithospheric structures inferred from multidisciplinary data: application to the Western and Northern Alps, *Terra Nov.*, **11**(2-3), 124–131.

Crameri, F., Schmeling, H., Golabek, G. J., Duretz, T., Orendt, R., Buiter, S., May, D. A., Kaus, B., Gerya, T. V., & Tackley, P. J., 2012a. A comparison of numerical surface topography calculations in geodynamic modelling: An evaluation of the 'sticky air'method, *Geophys. J. Int.*, **189**(1), 38–54.

Crameri, F., Tackley, P. J., Meilick, I., Gerya, T. V., & Kaus, B., 2012b. A free plate surface and weak oceanic crust produce singl-sided subduction on Earth, *Geophys. Res. Lett.*, **39**(3), L03306.

Forte, A. M. & Peltier, W. R., 1987. Plate tectonics and aspherical earth structure: The Importance of poloidal-toroidal coupling, *J. Geophys. Res.*, **92**(B5), 3645–3679.

Forte, A. M., Peltier, W. R., & Dziewonski, A. M., 1991. Inferences of mantle viscosity from tectonic plate velocities, *Geophys. Res. Lett.*, **18**(9), 1747–1750.

Fullsack, P., 1995. An arbitrary Lagrangian-Eulerian formulation for creeping flows and its application in tectonic models, *Geophys. J. Int.*, **120**(1), 1–23.

Geman, S. & Geman, D., 1984. Stochastic relaxation, gibbs distributions, and the bayesian restoration of images, *IEEE Trans. Pattern Anal. Mach. Intell.*, **6**, 721–741.

Gerya, T. V. & Yuen, D. A., 2007. Robust characteristics method for modelling multiphase visco-elasto-plastic thermo-mechanical problems, *Phys. Earth Planet. In.*, **163**, 83–105.

Hager, B. H. & O'Connell, R. J., 1979. Kinematic models of large-scale flow in the Earth's mantle, *J. Geophys. Res.*, **84**(B3), 1031–1048.

Hager, B. H. & O'Connell, R. J., 1981. A simple global model of plate dynamics and mantle convection, *J. Geophys. Res.*, **86**(B6), 4843–4867.

Haskell, N. A., 1935. The Motion of a Viscous Fluid Under a Surface Load, *Physics*, **6**(8), 265–269.

Jacoby, W. & Smilde, P. L., 2009. *Gravity interpretation: fundamentals and application of gravity inversion and geological interpretation*, Springer.

Kaus, B., Steedman, C., & Becker, T. W., 2008. From passive continental margin to mountain belt: Insights from analytical and numerical models and application to Taiwan, *Phys. Earth Planet. In.*, **171**(1-4), 235–251.

Kaus, B., Liu, Y., Becker, T. W., Yuen, D. A., & Shi, Y., 2009. Lithospheric stress-states predicted from long-term tectonic models: Influence of rheology and possible application to Taiwan, *J. Asian Earth Sci.*, **36**(1), 119–134.

Kaus, B., Mühlhaus, H., & May, D. A., 2010. A stabilization algorithm for geodynamic numerical simulations with a free surface, *Phys. Earth Planet. In.*, **181**, 12–20.

Kaus, B. J., 2005. *Modelling approaches to geodynamics processes*, Ph.D. thesis, ETH Zuerich.

Keilis Borok, V. I. & Yanovskaja, T. B., 1967. Inverse problems of seismology (structural review), *Geophys. J. Int.*, **13**(1-3), 223–234.

King, S. D., 1995. Radial models of mantle viscosity: results from a genetic algorithm, *Geophys. J. Int.*, **122**(3), 725–734.

Li, Z.-H., Xu, Z., Gerya, T., & Burg, J.-P., 2013. Collision of continental corner from 3-D numerical modeling, *Earth Planet. Sci. Lett.*, **380**(C), 98–111.

Lithgow Bertelloni, C. & Richards, M. A., 1998. The dynamics of Cenozoic and Mesozoic plate motions, *Rev. Geophys.*, **36**(1), 27–78.

Liu, L. & Gurnis, M., 2008. Simultaneous inversion of mantle properties and initial conditions using an adjoint of mantle convection, *J. Geophys. Res.*, **113**(B8), B08405.

May, D. A. & Knepley, M. G., 2011. Optimal, scalable forward models for computing gravity anomalies, *Geophys. J. Int.*, **187**(1), 161–177.

Moresi, L. & Gurnis, M., 1996. Constraints on the lateral strength of slabs from three-dimensional dynamic flow models, *Earth Planet. Sci. Lett.*, **138**(1), 15–28.

Mosegaard, K. & Sambridge, M., 2002. Monte Carlo analysis of inverse problems, *Inverse Probl.*, **18**(3), R29–R57.

Mosegaard, K. & Tarantola, A., 1995. Monte carlo sampling of solutions to inverse problems, *J. Geophys. Res. Solid Earth (1978–2012)*, **100**(B7), 12431–12447.

Moucha, R., Forte, A. M., Mitrovica, J. X., & Daradich, A., 2007. Lateral variations in mantle rheology: implications for convection related surface observables and inferred viscosity models, *Geophys. J. Int.*, **169**(1), 113–135.

Pasol, L., Chaoui, M., Yahiaoui, S., & Feuillebois, F., 2005. Analytical solutions for a spherical particle near a wall in axisymmetrical polynomial creeping flows, *Phys. Fluids*, **17**(7), 073602.

Platt, J. P. & Becker, T. W., 2010. Where is the real transform boundary in California?, *Geochem. Geophys. Geosyst.*, **11**(6), Q06012.

Popov, A. & Sobolev, S., 2008. Slim3d: A tool for three-dimensional thermomechanical modeling of lithospheric deformation with elasto-visco-plastic rheology, *Phys. Earth Planet. In.*, **171**(1), 55–75.

Popov, A. A., Sobolev, S. V., & Zoback, M. D., 2012. Modeling evolution of the San Andreas Fault system in northern and central California, *Geochem. Geophys. Geosyst.*, **13**, Q08016.

Press, F., 1968. Earth models obtained by Monte Carlo inversion, *J. Geophys. Res. Solid Earth (1978–2012)*, **73**(16), 5223–5234.

Press, F., 1970. Earth models consistent with geophysical data, *Phys. Earth Planet. In.*, **3**, 3–22.

Ricard, Y. & Wuming, B., 1991. Inferring the viscosity and the 3-D density structure of the mantle from geoid, topography and plate velocities, *Geophys. J. Int.*, **105**(3), 561–571.

Ricard, Y., Fleitout, L., & Froidevaux, C., 1984. Geoid heights and lithospheric stresses for a dynamic Earth, *Ann. Geophys.*, **2**(3), 267–286.

Ricard, Y., Vigny, C., & Froidevaux, C., 1989. Mantle heterogeneities, geoid, and plate motion: A Monte Carlo inversion, *J. Geophys. Res. Solid Earth (1978–2012)*, **94**(B10), 13739–13754.

Richards, M. A. & Hager, B. H., 1984. Geoid anomalies in a dynamic Earth, *J. Geophys. Res.*, **89**(B7), 5987–6002.

Rickwood, P. & Sambridge, M., 2006. Efficient parallel inversion using the Neighbourhood Algorithm, *Geochem. Geophys. Geosyst.*, **7**(11), Q11001.

Sambridge, M., 1999a. Geophysical inversion with a neighbourhood algorithm - I. Searching a parameter space, *Geophys. J. Int.*, **138**(2), 479–494.

Sambridge, M., 1999b. Geophysical inversion with a neighbourhood algorithm - II. Appraising the ensemble, *Geophys. J. Int.*, **138**(3), 727–746.

Sambridge, M. & Mosegaard, K., 2002. Monte Carlo methods in geophysical inverse problems, *Rev. Geophys.*, **40**, 3.1–3.29.

Sibson, R., 1981. A brief description of natural neighbour interpolation, *Interpreting multivariate data*, **21**.

Simmons, N., Forte, A., & Grand, S., 2006. Constraining mantle flow with seismic and geodynamic data: A joint approach, *Earth Planet. Sci. Lett.*, **246**(1-2), 109–124.

Soldati, G., Boschi, L., Deschamps, F., & Giardini, D., 2009. Inferring radial models of mantle viscosity from gravity (GRACE) data and an evolutionary algorithm, *Phys. Earth Planet. In.*, **176**(1), 19–32.

Steinberger, B. & Calderwood, A. R., 2006. Models of large-scale viscous flow in the Earth's mantle with constraints from mineral physics and surface observations, *Geophys. J. Int.*, **167**(3), 1461–1481.

Stimson, M. & Jeffery, G., 1926. The motion of two spheres in a viscous fluid, *P. R. Soc. London. Series A*, **111**(757), 110–116.

Talagrand, O. & Courtier, P., 1987. Variational Assimilation of Meteorological Observations With the Adjoint Vorticity Equation. I: Theory, *Q. J. Roy. Meteor. Soc.*, **113**(478), 1311–1328.

Tarantola, A., 1984. Inversion of seismic reflection data in the acoustic approximation, *Geophysics*, **49**(8), 1259–1266.

Tarantola, A. & Valette, B., 1982a. Inverse problems= quest for information, *J. geophys*, **50**(3), 150–170.

Thoraval, C. & Richards, M. A., 1997. The geoid constraint in global geodynamics: viscosity structure, mantle heterogeneity models and boundary conditions, *Geophys. J. Int.*, **131**(1), 1–8.

Turcotte, D. L. & Schubert, G., 2002. *Geodynamics*, Second Edition, Cambridge University Press.

Voronoï, G., 1908. Nouvelles applications des paramètres continus à la théorie des formes quadratiques. deuxième mémoire. recherches sur les parallélloèdres primitifs., *J. Reine Angew. Math.*, **134**, 198–287.

Watts, A., 2001. *Isostasy and flexure of the lithosphere*, Cambridge University Press.

Wijns, C., Boschetti, F., & Moresi, L., 2003. Inverse modelling in geology by interactive evolutionary computation, *J. Struct. Geol.*, **25**(10), 1615–1621.

## APPENDIX

### *The surface velocity signal of a rising sphere*

The analytical inverse problem described in section 2.2 has a kinematic component, as the low density sphere will want to rise through the surrounding viscous material. For very slow motions and sufficient small times the set-up can be simplified with a non-deformable sphere embedded in an infinite large half-space of a viscous fluid which mimics the properties of the sediments. Thus, the problem can be described with the simplified Navier-Stokes equations for low Reynolds numbers, the Stokes equations:

$$\nabla p = \kappa \nabla^2 \vec{v}. \tag{2.11}$$

In addition, there is the continuity equation for an incompressible fluid

$$\nabla \cdot \vec{v} = 0 \tag{2.12}$$

where $p$ is the pressure and $\vec{v}$ the velocity field of the fluid. The problem can be written in terms of a stream function $\Psi$:

$$\nabla^4 \Psi = 0. \tag{2.13}$$

Stimson & Jeffery (1926) provide a general solution for the stream function in bipolar coordinates that satisfies equation 2.13:

$$\begin{aligned}\Psi(\xi,\eta) &= \frac{c^2}{(\cosh\xi-\mu)^{3/2}}\sum_{n=1}^{\infty} U_n(\xi)\cdot V_n(\mu), \text{ with}\\ \mu &= \cos(\eta)\\ c &= b\cdot\sinh(\alpha)\\ \alpha &= \cosh^{-1}\left(\frac{h}{b}\right),\end{aligned} \tag{2.14}$$

where $h$ is the normal distance of sphere's centre to the plane surface and $b$ the radius of the sphere. Moreover,

$$V_n(\eta) = P_{n-1}(\mu) - P_{n+1}(\mu) \tag{2.15}$$

with Legendre polynomials $P_n(\mu)$ and

$$\begin{aligned}U_n(\xi) = {} & A_n\cosh\left(n-\frac{1}{2}\right)\xi + B_n\sinh\left(n-\frac{1}{2}\right)\xi +\\ & C_n\cosh\left(n+\frac{3}{2}\right)\xi + D_n\sinh\left(n+\frac{3}{2}\right)\xi.\end{aligned} \tag{2.16}$$

The expressions $A_n,\cdots,D_n$ must be derived in order to fulfill the boundary conditions. Brenner (1961) derived a solution for no-slip boundary conditions on the surface of the sphere and free-slip boundary conditions at the plane surface. He found

$$A_n = C_n = 0, \text{ and} \tag{2.17}$$

$$\begin{aligned}B_n = {} & \frac{b^2\sinh^2(\alpha\, U\, n(n+1))}{\sqrt{2}\,(2n-1)}\cdot\\ & \left[\frac{4\cosh^2(n+\frac{1}{2})\alpha + 2(2n+1)\sinh^2\alpha}{2\sinh(2n+1)\alpha-(2n+1)\sinh(2\alpha)} - 1\right]\end{aligned} \tag{2.18}$$

$$\begin{aligned}D_n = {} & \frac{b^2\sinh^2(\alpha\, U\, n(n+1))}{\sqrt{2}\,(2n+3)}\cdot\\ & \left[1 - \frac{4\cosh^2(n+\frac{1}{2})\alpha - 2(2n+1)\sinh^2\alpha}{2\sinh(2n+1)\alpha-(2n+1)\sinh(2\alpha)}\right]\end{aligned} \tag{2.19}$$

$B_n$ and $D_n$ depend on $U$, the constant rising-velocity of the sphere. By setting up a force balance of drag-force and buoyancy-force, it can be shown that $U$ is a function of $\Delta\rho$ and $b$:

$$\begin{aligned}F_{\text{drag}} &= 6\pi\cdot\kappa\cdot b\cdot U\cdot\beta\\ F_{\text{buoyancy}} &= \frac{4}{3}\pi\cdot b^3\cdot g\cdot\Delta\rho\\ U &= \frac{2}{9}\cdot\frac{b^2\cdot\Delta\rho}{\kappa\cdot\beta}.\end{aligned} \tag{2.20}$$

where $\beta$ is a correction factor of Stokes' law. Brenner (1961) derived $\beta$ that satisfy the boundary conditions:

$$\begin{aligned}\beta &= \frac{4}{3}\sinh\alpha\sum_{n=1}^{\infty}\frac{n(n+1)}{(2n-1)(2n+3)}\cdot \\ &\left[\frac{4\cosh^2(n+\frac{1}{2})\alpha+2(2n+1)^2\sinh^2\alpha}{2\sinh(2n+1)\alpha-(2n+1)\sinh(2\alpha)}\right].\end{aligned} \tag{2.21}$$

Pasol et al. (2005) show the velocity components in bipolar coordinates are dependent on the solution for the stream function (eq. 2.13)

$$v_\xi = \frac{(\cosh\xi-\mu)^2}{c^2\sin(\eta)}\frac{\partial\Psi}{\partial\mu} \tag{2.22}$$

$$v_\eta = \frac{(\cosh\xi-\mu)^2}{c^2}\frac{\partial\Psi}{\partial\xi} \tag{2.23}$$

$$\begin{aligned}\frac{\partial\Psi}{\partial\xi} &= \sum_{n=1}^{\infty}\frac{\partial U_n(\xi)}{\partial\xi}\cdot V_n(\eta) \\ &= \sum_{n=1}^{\infty}\frac{B_n\cosh(\xi(n-\frac{1}{2}))(n-\frac{1}{2})+D_n\cosh(\xi(n-\frac{3}{2}))(n-\frac{3}{2})}{(\cosh(\xi)-\mu)^{3/2}} \\ &\quad -\frac{3\cdot\sinh(\xi)\cdot(B_n\sinh(\xi(n-\frac{1}{2}))+D_n\sinh(\xi(n+\frac{1}{2}))}{2(\cosh(\xi)-\mu)^{5/2}} \\ &\quad \cdot V_n(\eta).\end{aligned} \tag{2.24}$$

At the surface ($\xi=0$) $v_{\eta=0}=0$ and

$$\begin{aligned}v_{\xi=0} &= \frac{(1-\cos(\eta))^{1/2}}{c^2\sin(\eta)}\cdot\sum_{n=1}^{\infty}\left(B_n\left(n-\frac{1}{2}\right)+\right. \\ &\quad \left.D_n\left(n-\frac{3}{2}\right)\right)\cdot V_n(\eta).\end{aligned} \tag{2.25}$$

$$\begin{aligned}v_{\xi=0} &= \frac{(1-\cos(\mu))^{1/2}}{c^2\sin(\mu)}\cdot\sum_{n=1}^{\infty}\left(B_n\left(h,R,\Delta\rho,\eta\right)\left(n-\frac{1}{2}\right)+\right. \\ &\quad \left.D_n\left(h,R,\Delta\rho,\eta\right)\left(n-\frac{3}{2}\right)\right)\cdot V_n\left(\cos\left(\mu\right)\right).\end{aligned} \tag{2.26}$$

*Highly scalable implementation of the Neighbourhood algorithm*

In order to have a highly scalable algorithm on massively parallel computers, it is important to allow for parallel forward models and to avoid `MPI` synchronization calls (e.g. `MPI_Allreduce`) within the code, which required us to redesign the parallel layout of the NA algorithm. Our implementation scheme is shown in Fig. 2.11. One of the basic additional features is a grouping procedure which creates processor groups, as illustrated in Fig. 2.11a. The forward modeling tasks are assigned to these CPU-groups during the optimisation. Each group

has a leading processor, which is responsible for the optimisation, which means that only this CPU shoulders the workload of the optimisation routine. The rest of the group processors wait for instructions of the leading CPU (LCPU). We embedded the core of the original NA routine into a new parallel layout (NAplus, Fig. 2.11b). As for the original NA, the workflow can be broken down into two major parts: (i) an initial parameter search and (ii) a main parameter search controlled by the NA. In our framework, this is implemented by mainly changing the subroutine in stage (4) (Fig. 2.11b). Generally, the method to compute the initial set of model parameters is arbitrary. Similar to the original NA implementation we use a pseudo-random or quasi-random number generator to compute a uniformly distributed set of initial parameters. For the parallelisation, this set of precomputed model parameters is redundantly provided as look-up table, and is partitioned into as many subsets as LCPUs are available. Usually, the size of the look-up table should be larger than the number of initial models required by the user to account for run-time differences of the forward models and imbalances between CPUs. Each LCPU is keeping record of the globally computed number of models, which allows to switch from initial stage to the main stage as soon as the required number of initial models is reached. To illustrate the new parallel layout, we begin at step (4) of the process, where new model parameters are assigned to the LCPU, either by the precomputed set of model parameters (initial sampling) or by the NA based on the previous model history. In a second step, the LCPU informs its own group to start performing new forward models (5). As soon as the forward modeling is finished, the new model and model misfit is sent to all other LPUS (1) and is attached to the own model history (3). In general, none of the other LCPUs is immediately available to receive this information. Therefore, we explicitly implemented a sending routine that combines `MPI_Isend` and `MPI_Test` with a `C++` a container object that works as a message buffer (2). This construct allows a completely asynchronous communication. All messages stay in the message buffer until the sending operation is terminated, meaning the model was received by the destination LCPU or the message was copied to the internal `MPI` system buffer. As soon as the sending process is terminated, respective models can be removed from the dynamic message buffer, which is important to avoid memory problems. To complete the asynchronous communication, models and respective misfit values of other processes have to be received and added to the own model history (3). Based on the model history, the new model parameters are either chosen with the NA (main stage) or they are taken from the look-up table (initial stage).

The parallel layout is completely written in `C++`, but there is a large freedom in what language the forward model should be implemented. For this study we have implemented an interface to a forward modeling code written in `C` with `PETSc` support. The code also supports other (sequential) forward modeling codes written in `fortran90` and `MATLAB`.

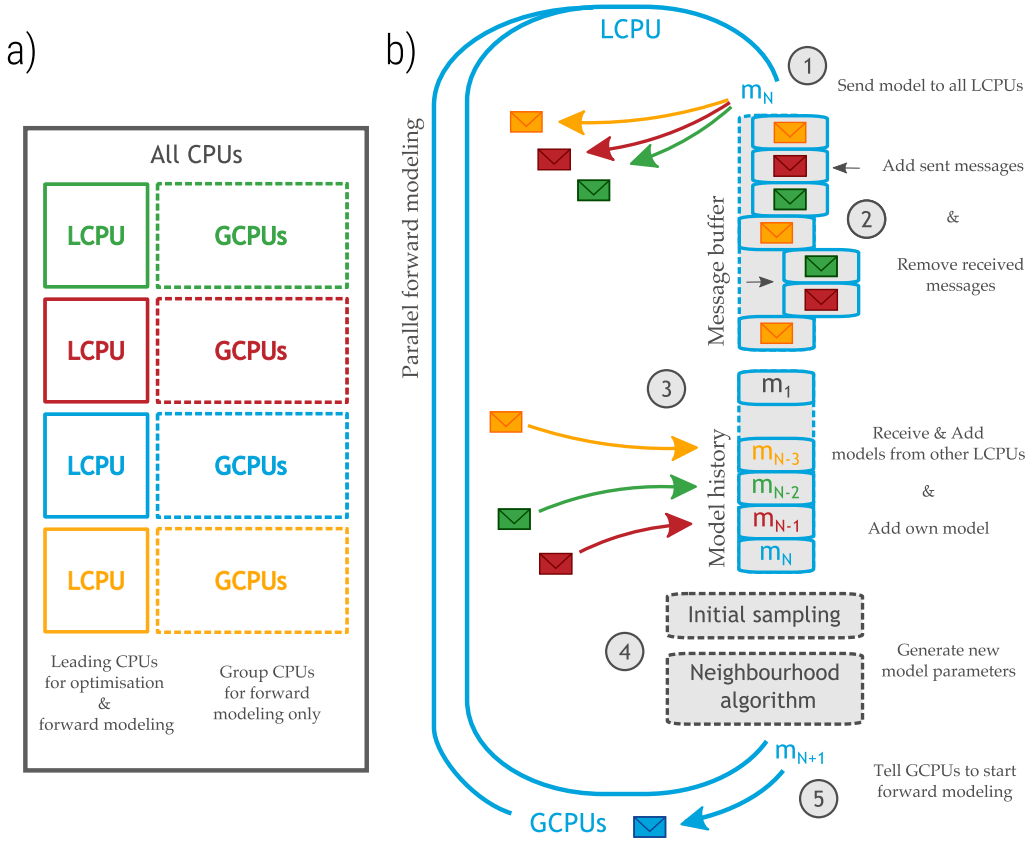


Figure 2.11: Parallel layout and workflow of NAplus. **a)** The available CPUs are partitioned into groups, here illustrated with colors. In each group, one CPU is assigned as leading CPU (LCPU), whereas all others are denoted as group CPUs (GCPUs). The LCPUs are integrated in another MPI-communicator, in which the parallel NA workflow is performed. **b)** The workflow is shown for a particular LCPU.

# 3

# GEODYNAMIC INVERSION TO CONSTRAIN THE NON-LINEAR RHEOLOGY OF THE LITHOSPHERE

**This chapter has been published in:**
Baumann, T. S. & Kaus, B. J. (2015). Geodynamic inversion to constrain the non-linear rheology of the lithosphere. Geophysical Journal International, 202(2), 1289-1316.

**Abstract**

One of the main methods to determine the strength of the lithosphere is by estimating its effective elastic thickness. This method assumes that the lithosphere is a thin elastic plate that floats on the mantle and uses both topography and gravity anomalies to estimate the plate thickness. Whereas this seems to work well for oceanic plates, it has given controversial results in continental collision zones. For most of these locations, additional geophysical datasets such as receiver functions and seismic tomography exist that constrain the geometry of the lithosphere and often show that it is rather complex. Yet, lithospheric geometry by itself is insufficient to understand the dynamics of the lithosphere as this also requires knowledge of the rheology of the lithosphere. Laboratory experiments suggest that rocks deform in a viscous manner if temperatures are high and stresses low, or in a plastic/brittle manner if the yield stress is exceeded. Yet, the experimental results show significant variability between various rock types and there are large uncertainties in extrapolating laboratory values to nature, which leaves room for speculation.

An independent method is thus required to better understand the rheology and dynamics of the lithosphere in collision zones. The goal of this paper is to discuss such an approach. Our method relies on performing numerical thermo-mechanical forward models of the present-day lithosphere with an initial geometry that is constructed from geophysical datasets. We employ experimentally determined creep laws for the various parts of the lithosphere, but assume that the parameters of these creep-laws as well as the temperature structure of the lithosphere are uncertain. This is used as a priori information to formulate a Bayesian inverse problem that employs topography, gravity, horizontal and vertical surface velocities to invert for the unknown material parameters and temperature structure.

In order to test the general methodology, we first perform a geodynamic inversion of a synthetic forward model of intra-oceanic subduction with known parameters. This requires solving an inverse problem with $14-16$ parameters, depending on whether temperature is assumed to be known or not. With the help of a massively parallel direct-search combined with a Markov Chain Monte Carlo method, solving the inverse problem becomes feasible. Results show that the rheological parameters and particularly the effective viscosity structure of the lithosphere can be reconstructed in a probabilistic sense. This also holds, with somewhat larger uncertainties, for the case where the temperature distribution is parameterised.

Lastly, we apply the method to a cross-section of the India-Asia collision system. In this case, the number of parameters is larger, which requires solving around $1.9 \times 10^6$ forward models. The resulting models fit the data within their respective uncertainty bounds, and show that the Indian mantle lithosphere must have a high viscosity. Results for the Tibetan plateau are less clear, and both models with a weak Asian mantle lithosphere and with a weak Asian lower crust fit the data nearly equally well.

## INTRODUCTION

The effective elastic thickness model has been successfully applied to estimate the strength of the lithosphere (e.g., Burov, 2007; Watts, 2001). The underlying assumptions are strict in that they assume the lithosphere to be a thin elastic plate floating on a linear viscous (or inviscid) mantle and, although the distribution of seismicity is sometimes used for additional argumentation (e.g. Maggi et al., 2000), the only input data are gravity and topography. Whereas the model is widely accepted to work well for oceanic lithosphere, its application to the continental lithosphere is controversially discussed (Burov & Diament, 1995), with some authors favouring small values of elastic thickness (e.g. Jackson, 2002) and others much larger values (e.g. Burov & Watts, 2006). That is unfortunate as these collision zones are impressive witnesses of the collision of tectonic plates, and their formation has intrigued geoscientists since centuries.

Thankfully, for many places on Earth, a large number of other geophysical datasets exist that give additional insights into the deformation and geometry of the crust and lithosphere. Ideally, we would like to incorporate these data in a dynamic model and in this manner learn more about the rheology of the lithosphere. On a laboratory scale, the rheological properties of minerals and rock samples are well understood for relevant pressure and temperature conditions of the lithosphere and upper mantle (e.g. Ranalli, 1995; Hirth & Kohlstedt, 2003; Karato, 2008). These results, however, suffer from intrinsic scaling problems in terms of geological time spans and spatial scales (Burov, 2007). Moreover, there is significant variability between the experiments, depending on which laboratory performed the experiments and on factors such as the chemistry or water content of the deformed rock samples. Thus, independent validations are required to better understand their reliability. Ideally, we would like to link the rheology relations known from laboratory experiments with independent geophysical data in a joint, physically consistent approach.

A possibility to fill this gap can be provided with the help of geodynamic deformation models that incorporate the rheological relations, but can also be used for the forward modelling of geophysical observations. The idea of doing this is not new, and has been developed before in the context of mantle flow models (e.g. Ricard et al., 1989; Ricard & Wuming, 1991; Forte et al., 1991; Bunge et al., 2003; Liu & Gurnis, 2008). These previous approaches focused on global scales and have underlying simplifications such as lateral homogeneous material properties, and linear viscosities. In a recent study, we focussed on a 3D crustal-scale problem with multiple geological units (Baumann et al., 2014)

and demonstrated that a Bayesian inversion strategy with numerical 3D Stokes-flow models can be conducted on massively parallel computers to constrain the linear viscosities from surface observations. We also demonstrated analytically that a joint geodynamic inversion of gravity and velocity data gives unique results in terms of density and viscosity, as opposed to a gravity inversion only which is known to be non-unique (Baumann et al., 2014). Yet, a drawback of our previous work is that it was limited to linear viscous rheologies. Here, we further extend the approach and test its applicability for more complex nonlinear rheologies known from laboratory experiments that are widely applied to lithospheric scale 2D models.

The paper is composed into four parts. First, we describe the inversion method and the physics underlying the forward models. In the following part, we apply the inversion method to a synthetic case to test its ability to constrain nonlinear rheologies of a typical geodynamic model scenario. Here, we also investigate the role of a unknown temperature distribution and its impact on the rheology-inversion results. We conduct two inversions, one for which we assume a known temperature distribution and another one with a parameterised temperature, with 14 and 16 inversion parameters respectively. Part three is dedicated to a real world example of our methodology. We construct a 2D model of the India-Asia collision system from seismological data. Compared to the synthetic cases, the model complexity is larger, which is why we encounter the inverse problem with an increased number of inversion parameters (19). Finally, we discuss the advantages and the current limitations of the methodology and elaborate possible modifications and future applications.

## METHODS

### *Geodynamic inversion*

Whereas in our previous approach (Baumann et al., 2014), we directly followed Sambridge (1999a,b) in tackling the inverse problem, we here establish our approach into a more fundamental Bayesian framework, which also includes the use of non-uniform parameter priors. In the subsequent sections we give a theoretical introduction into the theory of Bayesian inversion and we outline our technical implementation focusing on the geodynamic forward problem.

### *Bayesian inversion*

From a Bayesian viewpoint, the solution of the inverse problem is the posterior probability density function (pdf) $\sigma(\mathbf{d}, \mathbf{m})$, which is, in the most general case, a joint distribution in the model parameter space M and the data space D. We use the terminology of Tarantola (2005, chapter 1.4 to 1.5) to introduce how the posterior is defined in this paper. Starting with the most general formulation of the posterior pdf (Tarantola & Valette, 1982a) in the joint model and data space

$$\sigma(\mathbf{d}, \mathbf{m}) = \frac{\rho(\mathbf{d}, \mathbf{m})\,\theta(\mathbf{d}, \mathbf{m})}{\mu(\mathbf{d}, \mathbf{m})}, \tag{3.1}$$

it becomes clear that the inverse problem is composed of three parts. $\theta(\mathbf{d},\mathbf{m})$ represents the possible correlations between the model $\mathbf{m}$ and the observations $\mathbf{d}$, which describes the theoretical uncertainties in the forward modelling process. A reasonable approximation $\theta(\mathbf{d},\mathbf{m}) = \theta(\mathbf{d}|\mathbf{m})\,\mu_m(\mathbf{m})$ is obtained when it expresses no information about $\mathbf{m}$ (Mosegaard, 2011). The a priori information on data and model parameters can be decomposed as $\rho(\mathbf{d},\mathbf{m}) = \rho_d(\mathbf{d})\,\rho_m(\mathbf{m})$ provided the prior information on model parameters is independent of data. From this it directly follows that the homogeneous probability density $\mu(\mathbf{d},\mathbf{m}) = \mu_d(\mathbf{d})\,\mu_m(\mathbf{m})$ can be decomposed in a similar manner. When incorporating these assumptions, the a posteriori information in the model space can be computed as a marginal distribution

$$\sigma_m(\mathbf{m}|\mathbf{d}) = k\,\rho_m(\mathbf{m}) \int_D \frac{\rho_d(\mathbf{d})\,\theta(\mathbf{d}|\mathbf{m})}{\mu_d(\mathbf{d})}\,d\mathbf{d}, \tag{3.2}$$

$$\sigma_m(\mathbf{m}|\mathbf{d}) = k\,\rho_m(\mathbf{m})\,L(\mathbf{m}), \tag{3.3}$$

where $k$ is a constant. The integral over the data is referred to as likelihood $L(\mathbf{m})$ and expresses the model fit to the observations. If we employ Gaussian error statistics, the likelihood can be written as

$$L(\mathbf{m}) = k \exp\left(-\frac{1}{2}(\mathbf{d}-\mathbf{g}(\mathbf{m}))^T \left(C_d^{-1} + C_T^{-1}\right)(\mathbf{d}-\mathbf{g}(\mathbf{m}))\right), \tag{3.4}$$

where

$$C_D^{-1} = C_d^{-1} + C_T^{-1}, \tag{3.5}$$

denotes theoretical and measurement uncertainties, both expressed in terms of covariance matrices and $g(\mathbf{m})$ denotes the model predictions. Here, we neglect the theoretical uncertainties ($C_T$) because the distribution of data uncertainty and theoretical uncertainty is hardly known. When assuming Gaussian statistics, the likelihood is associated with the well-known least-squares misfit if data correlations are neglected as well

$$\chi^2(\mathbf{m}) = (\mathbf{d}-\mathbf{g}(\mathbf{m}))^T\, C_D^{-1}\,(\mathbf{d}-\mathbf{g}(\mathbf{m})). \tag{3.6}$$

In the same manner, the uncertainties of the model parameters can also be Gaussian, such that the model prior probability can be written as

$$\rho_m(\mathbf{m}) = k \exp\left(-\frac{1}{2}(\mathbf{m}-\langle\mathbf{m}\rangle)^T\, C_M^{-1}\,(\mathbf{m}-\langle\mathbf{m}\rangle)\right), \tag{3.7}$$

with $\langle\mathbf{m}\rangle$ being the arithmetic mean of the model vectors and $C_M^{-1}$ the model covariance matrix.

This completes the mathematical formulation of the inversion result, including the uncertainties for both, observations and model parameters, and we can now turn to the practical implementation and computation.

*Implementation of the Bayesian approach*

The key challenge of solving the inverse problem with a Bayesian approach is to solve many thousands or even millions of forward models, which can be seen as samples of the posterior distribution (eq. 3.2 and eq. 3.3). Obviously, for computationally demanding, geodynamic forward models, the emphasis is on optimizing the sampling strategy as much as possible without underestimating the non-unique and nonlinear character of the geodynamic inversion problem.

Markov Chain Monte Carlo (MCMC) methods are frequently used to directly sample the posterior (eq .3.3, e.g. Tarantola, 2005; Mosegaard & Tarantola, 1995; Sambridge & Mosegaard, 2002; Mosegaard & Sambridge, 2002). A modified (two-step) approach to sample the posterior is described by Sambridge (1999a,b). The method is separated into an optimised direct-search (Neighbourhood algorithm, NA, Sambridge, 1999a) and a Bayesian evaluation of the direct-search models (Sambridge, 1999b), where the likelihood function (eq. 3.4) is approximated and a Gibbs sampler (Geman & Geman, 1984) is employed to create samples of the posterior distribution. A new evaluation of forward models is not required during this appraisal stage. As our forward models are computationally demanding, this is a crucial argument in favour of using Sambridge's approach rather than directly performing the MCMC. Moreover, the parallelisation of Markov chains that is required in the classical MCMC method can be an issue, especially if poor mixing and long burn-in times exist (Wilkinson, 2006). In contrast, the NA can efficiently be parallelised and optimized for the usage with geodynamic forward models (NAplus, Baumann et al., 2014). A summary of the optimized parallel implementation (NAplus) is given in appendix A.

Considering complex rheologies for a geodynamic inversion strongly increases the number of inversion parameters. Even in the simplest case, that will be discussed in the next section, the number of unknown inversion parameters increased by almost a factor of two compared to our previous synthetic tests with constant Newtonian rheology (Baumann et al., 2014). Obviously, an increase in the number of inversion parameters causes an increase in volume of the parameter space and a reasonable initial sampling is required before the direct-search stage with the NA. Therefore, the aim of the initial sampling stage is to sample the parameter space as uniformly as possible (Sambridge & Mosegaard, 2002). Pseudo random sampling as in our previous study can no longer be a method of choice. Instead, quasi-random sampling can be applied, but their correlation effects in higher dimensions can not be reliably controlled, which is why our strategy is to conduct the initial sampling on a regular, predefined grid to ensure a minimum distance between forward models and to handle the increased volume of the parameter space. For details we refer to the appendix B, where we also address a few technical obstacles that have to be resolved, including the question how independent random numbers can be reliably created in a parallel programming environment (appendix C) and how many direct-search samples (forward models) are needed for a N-D problem (appendix D).

In Sambridge (1999b) the prior distribution (eq. 3.7) is assumed to be uniform, and the sampling of the posterior is approximated with the neighbour-

hood approximation of the likelihood function. Yet, priors are informative in general and are eventually required to regularise a high dimensional inverse problem. We therefore decided to slightly adapt the way the random walk is performed in Sambridge (1999b). Instead of using the proposed rejection rule (Press et al., 1992) and a uniform prior distribution, we implemented the Metropolis rule suggested by Mosegaard & Tarantola (1995) to draw deviates from an arbitrary prior distribution. Hereafter, the random step $m_i \rightarrow m_j$ according to the a-priori probability $\rho_m$, is modified with an acceptance rule. For example, the random walk may start at the location of maximum prior probability $m_{i,max.prior}$, then the transition $i \rightarrow j$ to the proposed location is only accepted if the condition $L(m_i) \leqslant L(m_j)$ is achieved for the likelihoods $L(m_i)$ at the current and $L(m_j)$ at the proposed location. Alternatively, if $L(m_i) > L(m_j)$, the proposed step is accepted with the probability ${}^{L(m_j)}/_{L(m_i)}$. The proposed step will always be accepted for a uniform likelihood. In this case, the resulting distribution is equal to the prior probability distribution.

### *Geodynamic forward modelling*

#### *Governing equations*

On a geological time-scale, the deformation of rocks can be approximated with Stokes flow and a nonlinear rheology. The governing equations

$$\rho c_p \left( \frac{\partial T}{\partial t} + v_i \frac{\partial T}{\partial x_i} \right) = \frac{\partial}{\partial x_i} \left( k \frac{\partial T}{\partial x_i} \right) + H_r \tag{3.8}$$

$$\frac{\partial P}{\partial x_i} - \frac{\partial \tau_{ij}}{\partial x_j} = \rho g_i \tag{3.9}$$

$$\frac{\partial v_i}{\partial x_i} = 0 \tag{3.10}$$

form a coupled system and describe the conservation of energy, momentum and mass for incompressible fluids, where the Boussinesq approximation is employed.

The conservation equation of energy assembles with a convective term depending on density $\rho$, temperature $T$, the heat capacity $c_p$, as well as the spatial coordinates $x_i$, velocities $v_i$, and a time component $t$. The right hand side indicates a conduction term with the conductivity $k$ and a source term due to radioactive $H_r$ heating.

Focussing on the momentum equation (eq. 3.9), $g_i$ and $\rho$ denote a gravity component and density respectively. $\tau_{ij}$ is the deviatoric stress tensor related to the stress tensor $\sigma_{ij}$ as $\tau_{ij} = \sigma_{ij} + P$, where the pressure is defined as $P = -\frac{\sigma_{ii}}{3}$.

The system is of equations (eq. 3.8-3.10) is coupled with a constitutive relationship that relates the deviatoric stress tensor $\tau_{ij}$ with the strainrate tensor

$$\dot{\epsilon}_{ij} = \dot{\epsilon}_{ij}^{viscous} + \dot{\epsilon}_{ij}^{plastic} = \frac{1}{2\mu_{eff}} \tau_{ij} + \dot{\lambda} \frac{\partial Q}{\partial \sigma_{ij}}. \tag{3.11}$$

The strainrate tensor is a function of velocities $\dot{\varepsilon}_{ij} = \frac{1}{2}\left(\frac{\partial v_i}{\partial x_j} + \frac{\partial v_j}{\partial x_i}\right)$ and describes the viscous ($\dot{\varepsilon}_{ij}^{viscous}$) and plastic ($\dot{\varepsilon}_{ij}^{plastic}$) deformation behaviour of the continuum. $\mu_{eff}$, the effective viscosity indicates a viscous, strainrate-dependent power-law rheology. The latter term in eq. (3.11) describes the influence of plasticity with the plastic flow potential Q and the plastic multiplier $\dot{\lambda}$ (Moresi et al., 2007; Popov & Sobolev, 2008; Kaus, 2010). A more detailed description of the viscous and plastic deformation behaviour is given below.

*Numerics*

To perform geodynamic forward models, we employ a finite element based Stokes code (MVEP2, a further development of MILAMIN_VEP, e.g. Kaus, 2010; Thielmann & Kaus, 2012), which employs the efficient MATLAB based finite element library MILAMIN to speed up the matrix assembly (Dabrowski et al., 2008).

The code includes several quadrilateral and triangular elements types (Kaus, 2010). Here we employ a $Q_1P_0$ element with a constant shape function for pressure and bilinear (4-nodes) shape functions for velocities. The argument of not using an higher order element type with larger accuracy (e.g. $Q_2P_{-1}$) is the massive trade-off between accuracy and computational requirements, as we will compute $10^5 - 10^6$ forward models with rather small time steps.

MVEP2 is employed in an arbitrary Lagrangian-Eulerian manner, where the mesh undergoes remeshing after every time step. The material properties are tracked with markers, which are used to transfer the properties from the old to the deformed mesh (Thielmann & Kaus, 2012). To avoid numerical instabilities, the effective viscosity is limited by an upper and lower threshold of $10^{18}\,\mathrm{Pa\,s} \leqslant \mu_{eff} \leqslant 10^{25}\,\mathrm{Pa\,s}$. Other instabilities can result from a free surface that is implemented as a self-consistent stress-free boundary. Nonetheless, modelling the free surface of the Earth is of major importance as in this study, model surface signals (topography ad surface velocities) are directly compared with observations. Moreover it is known from benchmarks that a free surface influences the slab dynamics (Schmeling et al., 2008). We therefore employ a free-surface stabilization algorithm (FSSA) that allows us to take larger time steps than in normal free surface models (Kaus et al., 2010).

Although the FSSA is employed, large surface velocities can occur due to the automatised parameter setting with the direct-search method. This eventually results in density and viscosity distributions, which cause an isostatic imbalance in the model and consequently triggers a period of isostatic compensation. As this a model-dependent effect, we are required to separate this motion from the motion resulting from dynamic effects, which is the model result we want to compared with observations. We found an empirical criterion based on the dynamic model topography to determine the end of the isostatic compensation to which we refer to as stopping criterion. A detailed description is given in the appendix, section E.

*Rheology implementation*

*Dislocation creep*

To describe the effective viscosity, we implement a dislocation creep viscosity, which is an exponential power law relationship:

$$\mu_{eff} = \mu_0 \cdot \left(\frac{\dot{\epsilon}_{II}}{\epsilon_0}\right)^{(1/n-1)} \cdot \exp\left(\frac{E + P \cdot V}{n \cdot R \cdot T}\right). \tag{3.12}$$

The exponential function is both temperature and pressure-dependent, where the influence of temperature and pressure by itself is adjusted by the activation energy $E$ and activation volume $V$ respectively. The power-law behaviour of $\mu_{eff}$ is additionally controlled by a power-law exponent $n$, which also controls the dependency on the second invariant of the strain rate tensor $\dot{\epsilon}_{II}$ that is scaled with the reference strain rate of the model $\epsilon_0$. The entire expression is linearly adjusted with a constant pre-factor $\mu_0$. For us, $\mu_0$ is the effective viscosity at a reference strain rate $\dot{\epsilon}_0 = 10^{-15}\,s^{-1}$.

In many cases (eq. 3.12) is formulated differently. Here, we construct (eq. 3.12) from a parameterised relationship sometimes referred to as flow-law, where $A_D$ is a material constant and independent of stress and grain size (see e.g. Gerya, 2009):

$$\dot{\gamma} = A_D \cdot \sigma_d^n \cdot \exp\left(\frac{E + P \cdot V}{R \cdot T}\right), \tag{3.13}$$

$$\dot{\gamma} = \begin{cases} \frac{2}{\sqrt{3}}\dot{\epsilon}_{II} & \text{(uni-axial compression)} \\ 2\dot{\epsilon}_{II} & \text{(simple shear)} \end{cases} \tag{3.14}$$

$$\sigma_d = \begin{cases} \sqrt{3}\sigma_{II} & \text{(uni-axial compression)} \\ 2\sigma_{II} & \text{(simple shear).} \end{cases} \tag{3.15}$$

Substituting (eq. 3.14) into (eq. 3.13) and solving for the effective viscosity $\mu_{eff} = \frac{\sigma_{II}}{2\dot{\epsilon}_{II}}$ gives

$$\mu_0 = F_2 \cdot A_D^{-1/n} \cdot (\dot{\epsilon}_0)^{(1/n-1)}, \tag{3.16}$$

$$F_2 = \begin{cases} \frac{1}{2^{(n-1)n}\,3^{(n+1)/2n}} & \text{(uni-axial compression)} \\ \frac{1}{2^{(2n-1)/n}} & \text{(simple shear).} \end{cases} \tag{3.17}$$

In order to understand over which ranges these parameters vary, we compiled a non-comprehensive summary of viscous power-law creep parameter that are commonly used in geodynamic modelling (Fig. 3.1). Many of these parameters are taken from studies that described the corresponding laboratory experiments, whereas others are frequently employed values in geodynamic modelling studies. We notice that the parameters are distributed over a wide range, which we use to define upper and lower bounds for each of the inversion parameters.

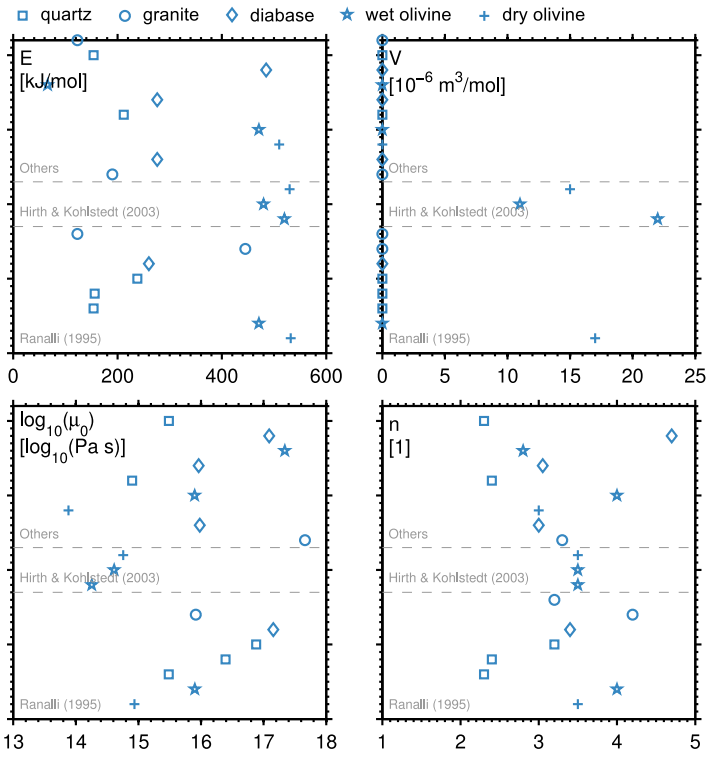


Figure 3.1: Power-law dislocation creep viscosity parameters: A (incomplete) literature review of what is regularly used in geodynamic modelling (e.g. Ranalli, 1995; Hirth & Kohlstedt, 2003; Burg & Schmalholz, 2008; Schmalholz et al., 2009). The variation of the parameters is the underlying basis of our inversion parameter bounds and the prior assumptions.

*Drucker-Prager plasticity*

Brittle or plastic deformation in MVEP2 is a Drucker-Prager model implemented after Vermeer & De Borst (1984) as follows (Kaus, 2010):

$$F = \tau^* - \sigma^* \sin(\phi) - C\cos(\phi) \tag{3.18}$$

$$Q = \tau^* \tag{3.19}$$

with $\phi$ and $C$ being friction angle and cohesion respectively, $\sigma^* = -\frac{(\sigma_{xx}+\sigma_{zz})}{2}$ and $\tau^* = \sqrt{0.25\,(\sigma_{xx}-\sigma_{zz})^2 - \sigma_{xz}^2}$ denoting the radius of the Mohr circle. In this, we assume a zero dilation angle which thus results in a non-associated and pressure-dependent plasticity model for friction angles larger than zero. In general, plasticity only occurs for stresses higher than the yield stress, which is defined with the conditions $\dot{\lambda} \geqslant 0, \quad F \leqslant 0, \quad \dot{\lambda}F = 0$.

*Temperature-dependent density*

The density in (eq. 3.9) is implemented as temperature-dependent density

$$\rho(T) = \rho_0\,(1 - \alpha\,(T - T_0))\,, \tag{3.20}$$

where $\alpha$ denotes the thermal expansion coefficient. $\rho_0$ and $T_0$ are the reference values of density and temperature respectively. We note that realistic rock

densities vary as a function of pressure, temperature and composition, and can be computed for real rock compositions through Gibbs-energy minimisation (Kaus et al., 2005). For reasons of simplicity we ignore this here, but in future studies this could be taken into account (even as an inversion parameter).

*Gravity forward modelling*

Similar to our synthetic 3D application in Baumann et al. (2014), we solve the gravity forward problem in an explicit manner as a summation of the gravitational contributions of all discrete control volumes within the computational domain. The gravitational contributions can be computed numerically using Gaussian quadrature rules, or analytically, which is more precise and to be preferred if the computational costs are not prohibitive. As we deal with $Q_1P_0$ elements, we have to integrate over a possibly distorted quadrilateral element volume, which is a four sided polygon in 2D space that can be solved analytically. We implemented the solution suggested by Won & Bevis (1987).

To focus the sensitivity of the gravity field on heterogeneities within the crust and lithosphere, one typically considers the Bouguer anomaly, as it is not correlated with short wavelength topography such as the free-air anomaly. Instead, it is dominated by the long wavelength signal of the crustal root of the mountain range (e.g. Blakely, 1996). The Bouguer anomaly reflects the density differences with respect to a reference model (e.g. Ebbing et al., 2001). Typically the reference model is laterally homogeneous and is subtracted from the absolute densities stored in the finite element mesh. In the application part of this paper (section 3.4), we use the PREM model (Dziewonski & Anderson, 1981) as a reference, but replace the upper-most density with $2670\,kg/m^3$ as this is the density that is typically used to perform topographic corrections (e.g. Blakely, 1996). For finite sized models, the gravity signal is overlain by the artificial long-wavelength signal of the computational domain, which is sometimes referred to as edge effect (Ebbing et al., 2001). This effect is largely reduced when relative densities (Bouguer anomaly) are used. It can further be attenuated by padding additional largely scaled elements to the sides of the domain (Fullea et al., 2009). As the grid of our model is refined towards the center, we extend the model with about 50 copies of the largest elements at the boundaries. In addition, the densities in these elements are gradually decreased towards zero, which helps to smooth out the effect of the box-domain.

## SYNTHETIC TESTS: INTRA-OCEANIC SUBDUCTION

To test whether the described approach is applicable for complex rheologies, we start with conducting a synthetic study. Thus, we extract a reference model from a geodynamic forward evolution simulation of intra-oceanic subduction and compute a set of synthetic observations. Under the assumption that we know the model geometry, we perform two geodynamic inversions to reconstruct the effective rheology of the reference model from the surface observations. To test the effect of temperature on the inversion results, we conduct a

first inversion with the full knowledge of the temperature field and perform a second inversion, where the unknown temperature field is parameterised with two half-space cooling profiles.

*Reference model and uncertainties*

The reference model is created from a snapshot of the subduction evolution arbitrarily chosen at approximately 8.6 Myrs (see Fig. 3.2 and 3.16). Additional information of the subduction simulation such as initial conditions and numerical model parameters are provided in appendix F. Fig. 3.2 A shows the 'known' model geometry which is composed of a mantle, mantle lithosphere, a serpentinized harzburgite layer and an oceanic crust. The subduction channel, which was treated as a separate phase during the forward model is now merged with the subducting oceanic crust. Each of the geological units is associated to a particular set of rheology model parameters that are listed in Table 3.1, which can be seen as the 'true' model parameters that we are trying to constrain with the inversion. We use the evolved model geometry and temperature field of that time step as a synthetic 'present-day' situation and compute a set of surface expressions, i.e. the topography, the Bouguer anomaly and the velocity field in vertical and horizontal direction respectively. The data signals are filtered with a second order, zero-phase low-pass filter of $\lambda = 30\,\text{km}$ and we refer to these data as synthetic observations. Later on, during the direct-search process, we also apply the same filter to the model data. The filtering is necessary to avoid spikes, mainly in the velocity fields, that are caused by local, short-term, localized plastic zones. In addition to the synthetic observations, we need reasonable uncertainties in our synthetic data in order to compute the covariance matrix $C_D$. One possibility to achieve this, is to compute a certain number of model realisations, but with noisy input parameters (e.g. Afonso et al., 2013b). We perform 300 realisations of the reference model. The noise, which is added to the input parameters, is assumed to be Gaussian and is defined by standard deviations that correspond to 10 % of the parameter ranges configured for the synthetic inversions (Table 3.2). We furthermore compute the variances of the model surface observations and determine their average. For simplicity, we neglect any correlations within the data and only consider the variances, i.e. the trace of the covariance matrix. To reduce the effect of the model boundaries on the inversion, we limit our synthetic surveys to $\|x\| \lesssim \pm 520\,\text{km}$.

*Geodynamic inversion with known temperature*

As the temperature distribution of subduction zones is usually only poorly constrained, it would ideally be required to model the full evolution of the temperature within the subducting slab (e.g. Sobolev et al., 2006). Another possibility is to infer temperature from seismic velocities (e.g. Sobolev & Babeyko, 1994). However, in this section, we want to exclude the effect of an unknown temperature on the inversion results, and we assume a known temperature distribution in addition to the known geometry, which is thus an idealised 'best-case' scen-

| Name | Viscosity | | | | Plasticity | | Density | |
|---|---|---|---|---|---|---|---|---|
| Parameterisation | Dislocation creep | | | | Drucker-Prager | | T-dependent | |
| Parameter | $\mu_0$ | $n$ | $E$ | $V$ | $\phi$ | $C$ | $\alpha$ | $\rho_0$ |
| Unit | $[\log_{10}(\mathrm{Pa\,s})]$ | [1] | [kJ/mol] | $[10^{-6}\mathrm{m^3/mol}]$ | [°] | [MPa] | [1/K] | $[\mathrm{kg/m^3}]$ |
| Upper overriding oceanic crust (wet Olivine) | 14.61 | 3.5 | 480 | 0 | 2 | 5 | $3.0 \cdot 10^{-5}$ | 3100 |
| Upper subducting oceanic crust (wet Olivine) | 14.61 | 3.5 | 480 | 0 | 30 | 20 | $3.0 \cdot 10^{-5}$ | 3100 |
| Serpetinized Harzburgite (wet Olivine) | 14.61 | 3.5 | 480 | 0 | 30 | 20 | $3.0 \cdot 10^{-5}$ | 3250 |
| Mantle lithosphere (dry Olivine) | 14.76 | 3.5 | 530 | 15 | 30 | 20 | $3.0 \cdot 10^{-5}$ | 3200 |
| Upper mantle (dry Olivine) | 14.76 | 3.5 | 530 | 15 | 30 | 20 | $3.0 \cdot 10^{-5}$ | 3200 |
| Subduction channel* | $\mu_{\mathrm{eff}} = 10^{19}\,\mathrm{Pa\,s}$ | | | | 0 | 5 | $3.0 \cdot 10^{-5}$ | 3100 |

Table 3.1: Initial model parameters, which are used to create the reference model of intra-oceanic subduction (section 3.3.1) for synthetic geodynamic inversions (section 3.3.2 and 3.3.3). (*) The subduction channel is only present in the forward evolution model. During the inversion, we merge the subduction channel and the subducting oceanic crust into a single geological unit.

| Name | Viscosity | | | | Plasticity | | Density | Temperature* |
|---|---|---|---|---|---|---|---|---|
| Parameterisation | Dislocation creep | | | | Drucker-Prager | | T-dependent | Half-space cooling |
| Parameter | $\mu_0$ | $n$ | $E$ | $V$ | $\phi$ | $C$ | $\rho_0$ | $t_{age}$ |
| Units | $[\log_{10}(\mathrm{Pa\,s})]$ | [1] | [kJ/mol] | $[10^{-6}\mathrm{m^3/mol}]$ | [°] | [MPa] | [kg/m³] | [Myrs] |
| **Left model part** | | | | | | | | |
| Overriding upper oceanic crust | 13–18(1) | 1–5(3) | 50–600(5) | – | 0–40(9) | 1–50(11) | 3000–3150(12) | 10–40(15) |
| Serpentinized Harzburgite | | | | | | | 3150–3280(13) | |
| Mantle lithosphere | 13–18(2) | 1–5(4) | 50–600(6) | 0–25(7) | | | 3180–3220(14) | |
| **Right model part** | | | | | | | | |
| Subducting upper oceanic crust | 13–18(1) | 1–5(3) | 50–600(5) | – | 0–40(8) | 1–50(10) | 3000–3150(12) | 40–70(16) |
| Serpentinized Harzburgite | | | | | 0–40(9) | 1–50(11) | 3150–3280(13) | |
| Mantle lithosphere | 13–18(2) | 1–5(4) | 50–600(6) | 0–25(7) | | | 3180–3220(14) | |
| Upper mantle | 13–18(2) | 1–5(4) | 50–600(6) | 0–25(7) | | | 3180–3220(14) | |

Table 3.2: Parameter limits of synthetic inversions used in section 3.3.2 and 3.3.3. Lithospheric ages are only varied for the latter case, for which the temperature is not known a priori. Labels (1–14, 16) indicate inversion parameter numbers.

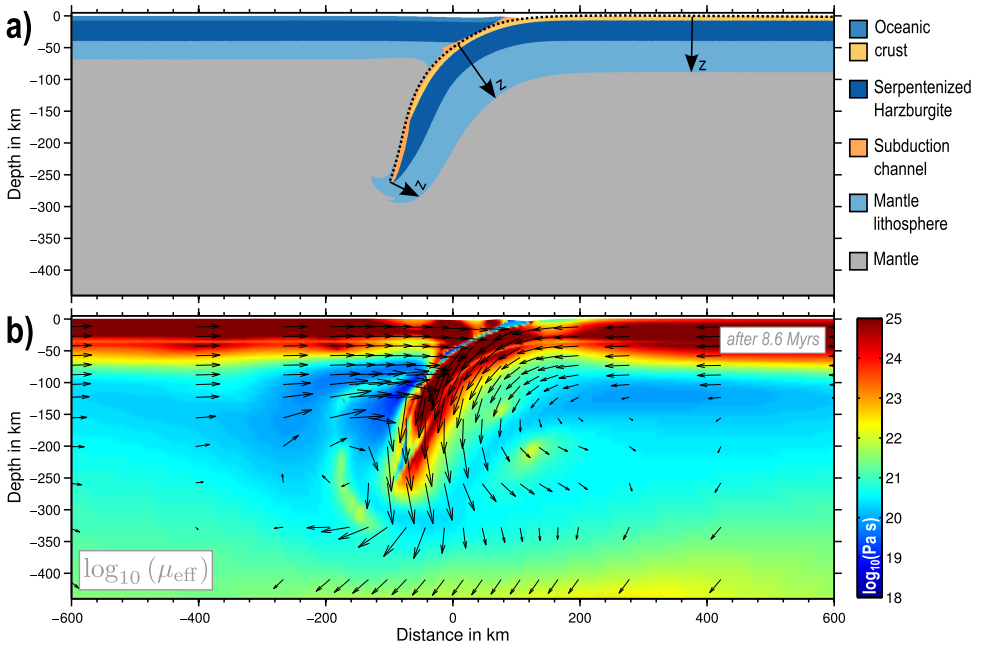


Figure 3.2: A snapshot of intra-oceanic subduction, which serves as a 'present-day' reference model. **a)** The geometry prior information of the synthetic inversions. In the case of an inversion with unknown temperature (section 3.3.3), a half-space cooling model is assumed to parameterise the temperature field within the lithosphere. For the subducted part of the lithosphere, we discretised the Benioff-zone, and define $z$ within the half-space cooling equation (eq. 3.26) as the distance to the closest point on the surface, which is either the Benioff-zone or the sea floor. **b)** The effective viscosity structure of the reference model used to compute the surface observation.

ario. Nevertheless, we aim to constrain 14 parameters of the reference model that represent the nonlinear rheology (dislocation creep and plasticity) and the density structure of the model (Table 3.1). Table 3.2 contains the parameter ranges that are used during the direct-search. Labels show the parameter number and also indicate which parameters are representative for multiple phases. For example, the overriding and the subducting crust share the same inversion parameters except of the friction angle and the cohesion parameter.

The technical details of this inversion are summarised in Table 3.3. About 120'000 forward models were initially sampled on a regular grid with 50 grid points along each parameter axis. The main sampling, performed with NAplus and the number of CPU used for this inversion was mainly driven by the characteristics of the computational hardware. As one computational node on the cluster we used had 64 CPUs, a computation with a multiple of 64 is preferred over other CPU configurations. Due to the run time limitation of 5 hours, the direct-search process was separated into several parts, for which the resampling parameter could be adapted to the current sampling results. Fig. 3.3 illustrates the direct-search results for a particular parameter combination. Each point represents one forward model, where their color represents the misfit (eq. 3.6). Here, the models are plotted for the pre-factor of the viscosity power-law (eq.

| Sampling | Resampling parameter | Cumulative number of models | Number of processors |
|---|---|---|---|
| Initial | – | 120571 | 1024 |
| Main | 1200 | 162201 | 768 |
| Main | 900 | 247107 | 768 |
| Main | 600 | 341859 | 768 |
| Main | 300 | 726445 | 768 |

Table 3.3: Numerical parameters and technical details of the direct-search part of the inversion. Values are referred to the geodynamic inversion with full temperature knowledge (14 dimensions, section 3.3.2). The direct-search is separated into several parts, because of the wall time limits of the cluster we used (5 hrs). The resampling parameter was adapted after visual inspection of the sampling distribution.

3.13) of the crust and the respective activation energy. For visualisation purposes, the models are sorted and plotted according to their misfit value, with models with a low misfit on top of the distribution. Two local minima for this parameter combination are detected by the direct-search. The one associated with a smaller pre-factor correlates with the reference model that is indicated with the black marker. The direct-search results with NAplus (Fig. 3.3) can only provide a first visual impression of the misfit function. As discussed in sections 3.2.1.1 and 3.2.1.2, we want to determine the posterior distribution of the model parameters, which is achieved with the appraisal technique in a Markov Chain Monte Carlo manner after Sambridge (1999b). Our priors are defined to be Gaussian, centred at the midpoints of the parameter ranges given in Table 3.2. The standard deviation are adapted to 75 % of the parameter ranges to give models closer to the centre a slightly higher priority. The appraisal was performed on 128 CPUs, with 508 independent random walks and 2000 steps each, where 1000 steps were assigned for the burn-in phases, such that 508000 random steps were realised in total.

An example is given in Fig. 3.4. In A, we show the 1D marginal distributions of the cohesion of the subducting crust ($C\,(sc)$) in combination with the power-law exponent of the mantle lithosphere ($n\,(ml/um)$). The joint distribution forms a 2D marginal distribution, which is illustrated in terms of samples per bin (with 200 bins per parameter axis). A sample denotes one random step after the burn-in phase. We also show confidence intervals of 20, 40, 60, 80 and 95% respectively. They are constructed in the following manner. All bins are sorted according to the related number of samples, then we compute the cumulative sum of samples for each bin and normalise it with the total number of samples.

In the context of $n\,(ml/um)$, we observe a single maximum of the posterior pdf unlike the two local extrema of the scatter plot example of Fig. 3.3. Also the other parameter ($C\,(sc)$) shows a single maximum, but its peak is wider.

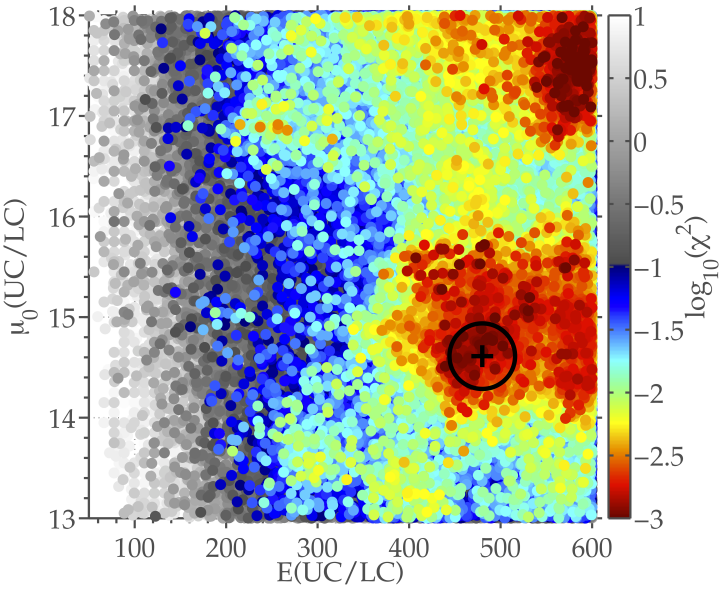


Figure 3.3: Direct-search results for the case of full temperature knowledge (section 3.3.2). Each point represents one forward model, the color indicates the misfit of the models respectively. The models are plotted for two viscosity parameters of the upper and lower crust, the power law pre factor and the activation energy. We observe two local minima, where the one with a smaller pre-factor correlates with the true solution that is denoted with the black marker.

Obviously, the impact of $n\,(ml/um)$ on the dynamics is more significant, which causes the parameter to be better constrained. However, both parameters fit the true solution well. The other example (Fig. 3.4b) illustrates the marginal posterior distribution of the activation energy of the crust ($E\,(c)$) and friction angle of the subducting crust ($\phi\,(sc)$). Although a minor local maximum exist at $E \approx 150\,kJ/mol$ and $\phi \approx 12°$, it shows a clear single global maximum of the posterior that correlates well with the reference model. Both model parameters thus seem to play an important role in the dynamics and only show minor trade-offs. An activation energy of the crust ($E\,(c)$) that is larger than 300 kJ/mol is clearly preferred, which indicates that the crust needs to have a certain strength in order to reproduce the surface observations. The same applies to the friction angle, which needs to be sufficiently small to prevent the subducting crust from locking and hence buckling.

A representation of the entire parameter space of this kind is provided in Fig. 3.18 of appendix section H. It can be seen that most of the marginal distributions of non-viscosity parameters are very closely correlated with the reference model. On the other hand, there are a few viscosity parameters that show trade-offs. For these parameters, the maximum posterior probability does not always correlate with the reference model, but show a certain offset. However, we want to stress that the reference model is in most cases related to the trade-offs and that the effective viscosity that results from these parameter combinations along the trade-offs can be rather similar. We will describe the effective viscosity structure resulting from this geodynamic inversion in section 3.3.4.

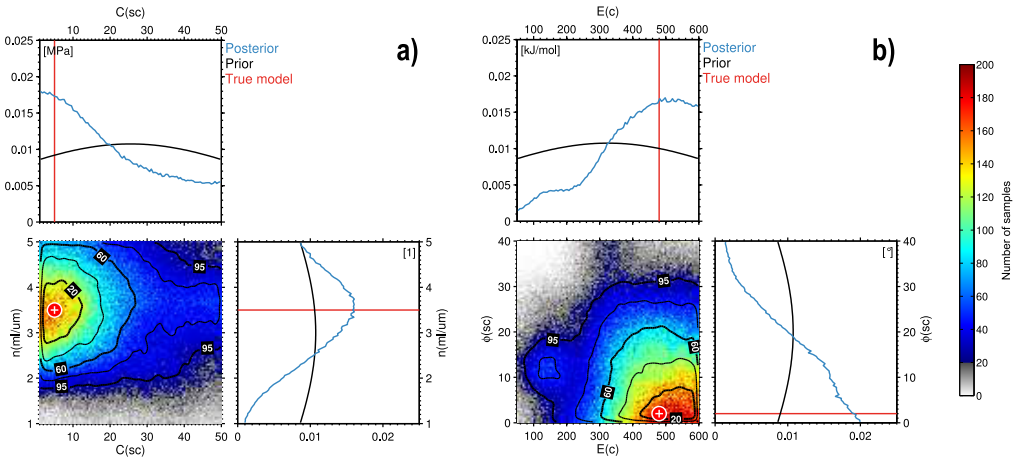


Figure 3.4: 1D and 2D marginal distributions of the posterior probability for two parameter combinations. We used 508 random walks with 2000 steps each (508000 MCMC samples) to determine the posterior. The 2D marginal distributions are illustrated in terms of samples per bin, which is denoted with color. The black lines show the associated confidence intervals with a step-width of 20 % and the red markers indicate the true model values. **a)** This is an example of the cohesion of the subducting crust and the power-law exponent of the mantle lithosphere/upper mantle. Here, as opposed to the scatter plot of Fig. 3.3, we find a global maximum, where the true model is associated with a location within the 20 % confidence area. We can also see that $n\,(\mathrm{ml/um})$ has a higher sensitivity. **b)** In this case the friction angle of the subducting crust is plotted against the activation energy of the crust. We have a clear maximum, which is also well correlated with the true solution. An overview of all marginal distributions of the posterior is provided in the appendix section H.

*Geodynamic inversion with estimated temperature*

In order to estimate the temperature distribution within the lithosphere we have various methods from mineralogy, seismology (i.e. $v_p/v_s$ ratios) and heat flow measurements. These constraints are either sparse (mineralogy), ambiguous (seismology), or, can vary dramatically due to local conditions (heat flow), which is why a precise temperature distribution within the lithosphere is usually not known. As we deal with a oceanic intra oceanic subduction scenario, a reasonable description of the temperature field is the analytical half-space cooling model (eq. 3.26, Turcotte & Schubert, 2002), which was also used to create an initial temperature field for the evolution modelling (see appendix F). If we have a constant (known) thermal diffusivity and a nearly-constant mantle temperature, we have only one free parameter, the lithospheric age, that controls the temperature, which only depends on the depth. However, as the lithosphere is laterally not homogeneous, we define the depth as the lot-distance (normal-distance) to the closest surface. This is either the sea floor, or the slab surface, which approximately coincides with the Benioff-zone (see Fig. 3.2a). This approximation of course lacks generality, but we will demonstrate that it is first order accurate. Towards the nose of the subducting slab the error of

| Sampling | Resampling parameter | Cumulative number of models | Number of processors |
|---|---|---|---|
| Initial | – | 120038 | 1600 |
| Main | 1200 | 209565 | 768 |
| Main | 900 | 311861 | 768 |
| Main | 600 | 554690 | 768 |
| Main | 300 | 820816 | 768 |

Table 3.4: Direct-search parameters of direct search with synthetic model of parameterised temperature structure (16 inversion parameters).

this temperature approximation increases as heat conduction took place during the subduction process, which can not be taken into account accurately. Also towards the surface of the slab the error of the approximation increases, as it is difficult to determine the exact location of the slab surface. With the lithospheric ages of the overriding part (left) and the subducting part (right) of the model, we increase the parameter space by two dimensions and perform an inversion with 16 parameters indicated in Table 3.2. Consequently, we need more forward models to sample the additional space. Table 3.4 summarises the technical parameters, but the procedure of the direct-search and the appraisal procedure is analogue to what was described in the previous section. Fig. 3.5 illustrates the same parameter combinations as described for the case of full temperature knowledge. We observe that the relative importance of the parameters controlling the plasticity increased at the expense of the parameters controlling the power-law viscosity. In particular the friction angle of the subducting crust is now much better constrained, but also the cohesion shows a clear maximum, which seems to be a clear effect of the less constrained temperature distribution. We observe similar trends for other parameter combinations (see appendix H, Fig. 3.19). Furthermore, we observe more extended trade-offs as in the previous case and that the correlations with the reference model parameters are less pronounced. For both examples shown here, the true solution is, however, still within the 40 % confidence interval.

For a broader perspective, we also need to consider the two additional temperature parameters that are shown in Fig. 3.6. The colorscale for all examples is the same, such that we can directly see that their relative importance is large compared to other viscosity parameters and approximately equally important as the friction angle. The lithospheric age of the left part of the model (overriding plate) is very well constrained. This is not surprising, as the overriding lithosphere is not very much deformed. On the other hand, the posterior of the lithospheric age of the subducting part of the model shows a clear trend towards the lower parameter boundary - a younger age is preferred in general. This implies that the lithosphere would be warmer, which causes an adjustment of other viscosity parameters and explains why the reference values do not fit as well as in the previous case. In addition, it also correlates with the plate age

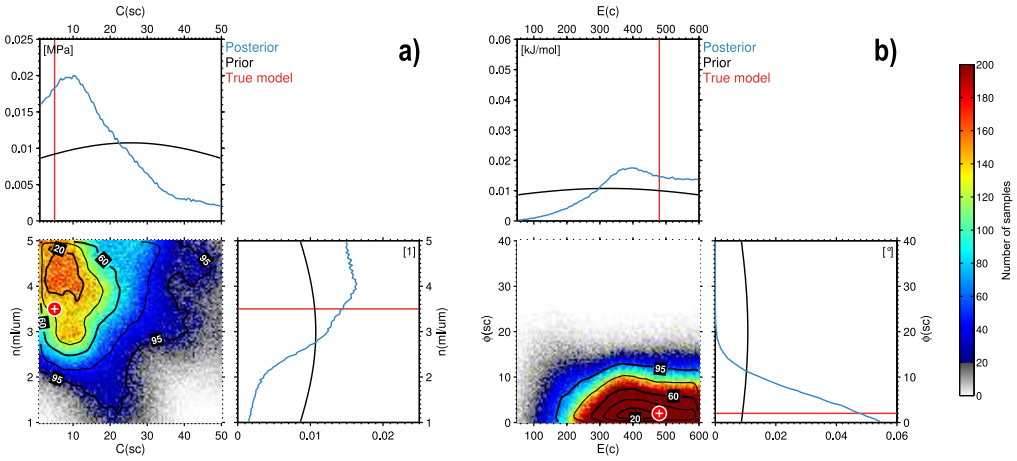


Figure 3.5: Inversion results of the intra-oceanic subduction model with parameterised temperature. Marginals of the posterior are given for the same parameter combinations as in Fig. 3.4. Plasticity parameters become more important and get, relatively seen, better constraint. **a)** The true solution does not correlate with the maximum pdf, but is correlated with the trade-off and the 40 % confidence interval. **b)** The friction angle is now much better constrained as it is apparently more relevant for reproducing similar surface observations. Nevertheless, the subducting crust still needs be to sufficiently strong. The posterior for all other parameter combinations is shown in appendix H, Fig. 3.19.

of the overriding lithosphere. We see that as the subducting plate gets younger (warmer), the overriding plate is required to be younger as well. The younger plate age of the subducting lithosphere is caused by our crude approximation of the lithospheric temperature. For example, lateral temperature changes along the slab surface are not incorporated. At this point we want to emphasis that it is not our aim to prescribe a very precise temperature model, we rather want to estimate the influence of a first order accurate temperature approximation, because in many real world scenarios precise information on temperature is simply not available. To summarise the observations, we can state that the inaccuracies of the temperature within the subducting slab cause an adjustment of other parameters. We will demonstrate with the following analysis that this is mainly an compensation effect, which results in very similar structures of effective viscosity.

*Summary of synthetic geodynamic inversion results*

Although many model parameters are involved in describing the rheology, most of them directly influence the effective viscosity structure in one way or the other (eq. 3.13). Thus, many very similar viscosity structures, constructed from different parameters, can coexist and explain the geodynamic surface observations approximately equally well. In order to identify major 'stable' features, but also the uncertainties of the effective viscosity structure, we determine arithmetically averaged viscosity structures and their standard deviations,

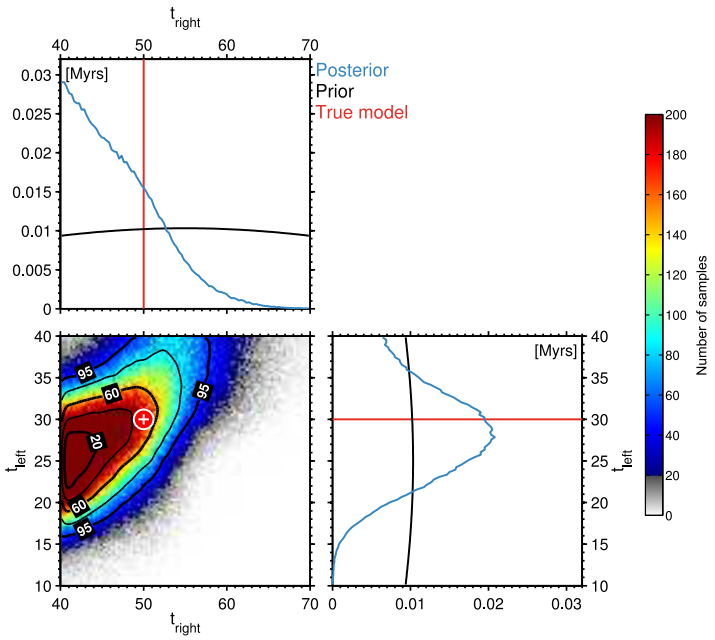


Figure 3.6: Marginals of the posteriors controlling the temperature parameterisation of the model (section 3.3.3). The lithospheric ages of the reference model are denoted with red lines and the marker. Referring to the posterior, younger lithospheric ages are preferred. However, a trade-off exist, which correlates with the true solution. Younger ages are related with lower temperatures, which results in higher viscosities.

resulting from inverted parameters in a weighted manner. We also directly compare the results of the two synthetic inversions, to better understand the resolving power of the inversion approach. The averaging is performed in the following manner. First, we identify forward models and their associated Voronoi cells ('nearest neighbour' regions in which the particular model is the closest model in the parameter space) that contain samples of the resampling with the MCMC appraisal approach (Sambridge, 1999b). In other words, these are the forward models that came in touch with one of the random walks. Many of the Voronoi cells will never be affected by the random walks because of the low associated likelihood, and for a growing dimension of the parameter space, the number of Voronoi cells that were 'visited' by at least one of the random walks decreases. However, we can come up with a ranking of the Voronoi cells that were 'visited' and with how many steps (samples) of the random walks they are associated. These values are used to weight the viscosity structures that are associated with the Voronoi cells respectively, and to compute their arithmetic average. In a similar manner, we compute the weighted standard deviations. The result is shown in Fig. 3.7. The top row shows the weighted arithmetic averages $\bar{\mu}_{\text{eff}}$ of the effective viscosity for the cases with and without temperature information. Below, we estimate the uncertainty limits by plotting the average effective viscosity with two times the standard deviation ($\bar{\mu}_{\text{eff}} \pm 2\sigma_{\mu_{\text{eff}}}$). We gain further insights by computing the residual viscosity structures, which are shown in the bottom row, which are the differences with the true model. The reference structure is

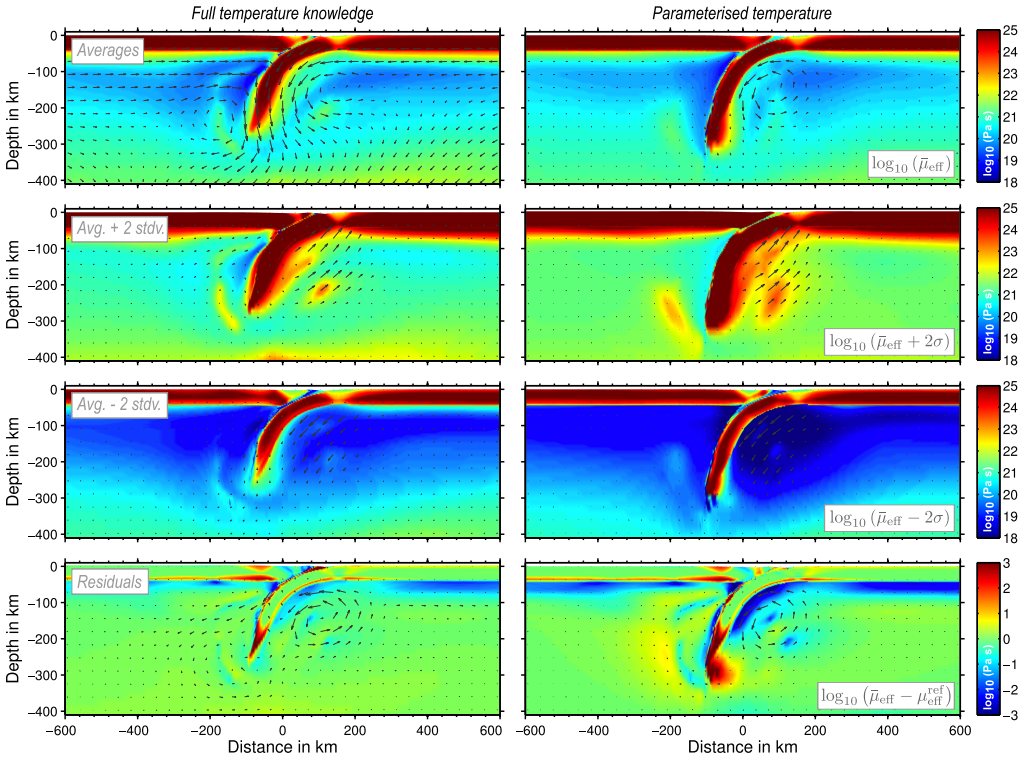


Figure 3.7: Comparison of the final inversion results. Arithmetically averaged viscosity structures for both synthetic inversions described in the text (sections 3.3.2 and 3.3.3). The averaging is a weighted averaging according to the posteriors probabilities. The residuals are computed as the difference of the weighted average viscosity and effective viscosity structure of the reference model (Fig. 3.2b).

given in Fig. 3.2b. The most striking similarity between the results is the effective viscosity of the crust. This is a very stable feature that is consistent within the uncertainty limits. Even the small plastically weakened zones at $x \approx 20\,\text{km}$ (overriding plate) and $x \approx 150\,\text{km}$ (subducting plate) are consistently present in both results. Moreover, the former subduction channel subduction (now regular subducting crust), to which a particular friction angle is attributed, consistently shows a low effective viscosity. This can be explained by the fact that this is one of the main requirements to reproduce the horizontal velocity field. If the friction angle would be too high, the model would lock and folding would take place and the topography would be deformed accordingly. The most obvious mismatch is recognisable at the nose of the subduction slab, where the estimated effective viscosity is consistently higher $\left(\log_{10}(\Delta\mu_{\text{eff}}) > 3\log_{10}(\text{Pa s})\right)$ in both cases. Other areas of obvious mismatch are the boundary between geological units, such as the Moho or the Benioff zone. All of the named regions are often correlated with higher strain rates, which also goes into the equation of effective viscosity, which can explain the larger uncertainties in those areas. In the lithosphere, similarities occur in terms of a consistent power-law behaviour, which is also present for the upper uncertainty limits. However, the model with parameterised temperature does not show this feature at the lower uncertainty

limit, which is confirmed by the residual plot. The effective viscosity of the subducting slab is underestimated, but this seems to be not only an effect of the inaccurate temperature approximation as the model with full temperature knowledge shows a similar trend towards too low viscosities. Another inconsistency is the viscosity towards the nose of the slab, which is overestimated. This is a clear effect of the inaccuracy of the temperature approximation.

To obtain an impression of the match of the model data with the synthetic observations, we compare the $\pm 2\sigma$ variations of the model data selected by the MCMC appraisal with the reference data in Fig. 3.8. The MCMC walk selected 6992 and 4022 models regarding the inversion with and without full temperature knowledge respectively. The variation in the model data (gray band with dashed boundaries) is plotted as $\mu_{\text{arithm}} \pm 2\sigma$. The selected models show a good fit and have only very small variations with regard to topography and Bouguer anomaly, but much larger variations in terms of velocities. Whereas the horizontal velocities are well-fitted at the left and right side of the signal, they have larger variations towards the convergence zone even though the reference signal still overlaps with the $\pm 2\sigma$ interval. The majority of the selected models is, however, associated with larger velocities of the subducting slab close to the convergence zone ($x \approx 100\,\text{km}$). Probably this is also reflected in the effective viscosity, as the viscosity of the upper crust is, on average, slightly larger and slightly lower for the weak channel. This is less clear in the parameterised temperature inversion. Here, the vertical velocity has the largest variation and is not limited to the region around the conversion zone, but rather more equally distributed over the profile, which probably reflects bending effects of the lithosphere. This can be caused by multiple reasons. Most likely, a high friction angle in the subduction channel is involved in many cases. The largest variations are observed towards the convergent margin. Here, the observation is not fully reflected by the variation of the selected model data for the case with parameterised temperature. As the vertical velocity has the largest uncertainties, it is possible that the selected models do not reflect the entire interval of variation at this part of the profile.

### REAL CASE SCENARIO: INDIA-ASIA COLLISION

In this section we apply the inverse approach to the India-Asia continental collision. The collision of the Indian and Asian continent resulted in the highest mountains on Earth (Molnar & Tapponnier, 1975; Fielding et al., 1994; Hatzfeld & Molnar, 2010), which is one of the reasons that the Himalayas and the Tibetan plateau are scientifically interesting. Particularly dense GPS-velocity data are available (e.g. Zhang et al., 2004; Gan et al., 2007; Liang et al., 2013; Zubovich et al., 2010) that show a high convergence rate of India of up to $40 - 55\,\text{mm/yr}$ (DeMets et al., 1990). Despite the fact that there are many observations, the rheology and the temperature distribution within the collision zone are heavily disputed, with some claiming that the Indian mantle lithosphere has a low effective viscosity (e.g., Jackson, 2002), whereas others suggest that the viscosity is large (e.g., Burov, 2007; Watts, 2001). These questions are closely related to

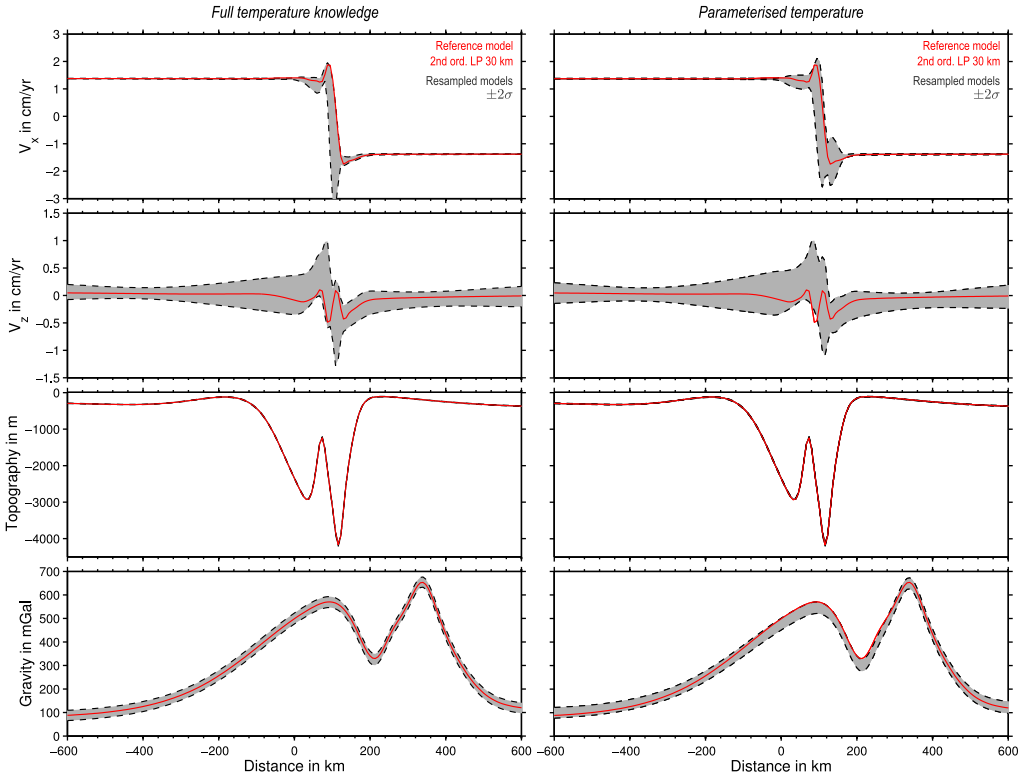


Figure 3.8: Representation of model and reference data for both synthetic inversions respectively (section 3.3.2 and 3.3.3). The reference data in red is low-pass filtered. The same filter was applied to the model data, its variation is illustrated in terms of the 95% confidence interval ($\mu_{arithm} \pm 2\sigma$). To compute the interval, only models selected by the MCMC-appraisal are taken into account. The collection consists of 6992 and 4022 models for the cases with and without full temperature knowledge.

the question about the manner and mechanisms by which the Indian crust and lithosphere underthrusts Tibet and how this results in the development of a mountain-belt and high elevation continental plateau.

To obtain additional insights in this question, we here apply our new inversion method to a cross-section through the collision zone as indicated in Fig. 3.9. Along this cross-section, we combine the results from several nearby regional geophysical studies to create a model setup (shown in Fig. 3.10). The location and orientation of our profile are chosen to match and combine the information of profiles from other studies and was partly inspired by the structural interpretation of Klemperer et al. (2013). The 3401 km long cross section with a strike of 35° is centred at 79.05° E/33.28° N on the Karakorum fault (KKF), which is thought to be one of the possible separators of Indian and Asian crust in the western Himalayas (Klemperer et al., 2013; Nabelek et al., 2009).

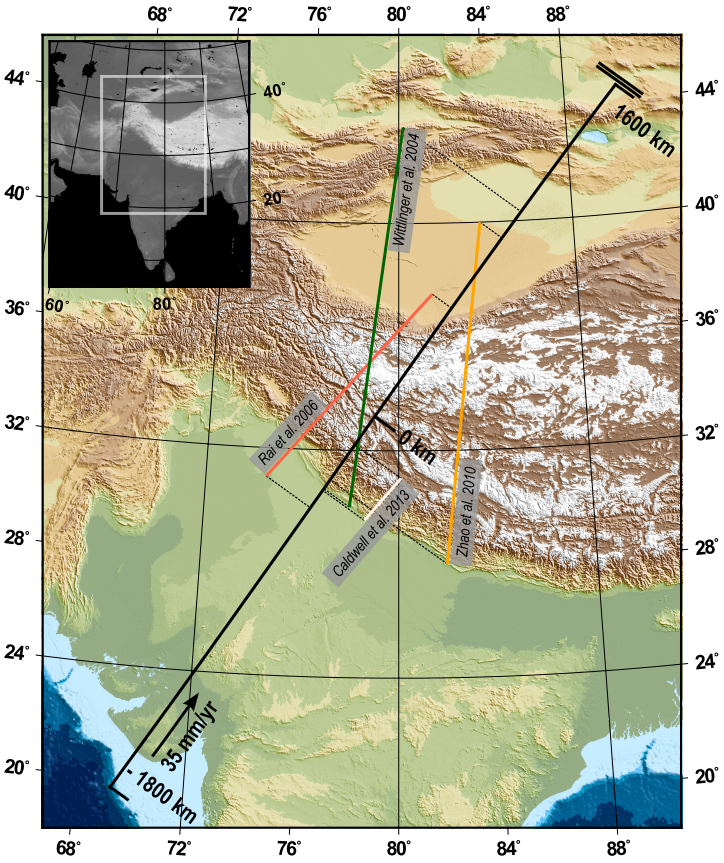


Figure 3.9: Geographic configuration of the 2D model geometry described in section 3.4.1. The cross-section is 3401 km long, and intersects with the Indian shield, the Himalayas, the Tibetan plateau and the Tarim basin in a SW-NE (strike: 35°) orientation, approximately perpendicular to the Main Boundary Thrust (MBT). The profile is centred at the Karakorum fault at 79.05° E/33.28° N as a cross section through the Himalaya the Tibetan plateau. The profiles of studies that were used to construct the geometry are marked with same colors as in Fig. 3.10. The underlying map projection is a conic projection with the origin at 80° E/31° N and the two standard parallels at 23° N and 40° N.

*Model geometry*

Our model geometry is based on various sources. As a coarse crustal model geometry, we take the global crustal model CRUST 1.0 (Laske et al., 2013), which we refine with regional receiver function studies (Fig. 3.9 & 3.10). Rai et al. (2006) determined the Moho location, in a profile that is approximately parallel to ours with an average lateral offset of about 200 km, which is why we consider their Moho signal as a strong constraint for our model geometry. After projecting their Moho signal to our profile, we aligned their interpretation at the Main Frontal Thrust (MFT). We also project and align the results of Caldwell et al. (2013) on our profile, who focused on localising the main Himalayan Thrust (MHT). In comparison with the data of Rai et al. (2006) we interpret their Moho signal as the upper crust/lower crust interface. To further estimate the

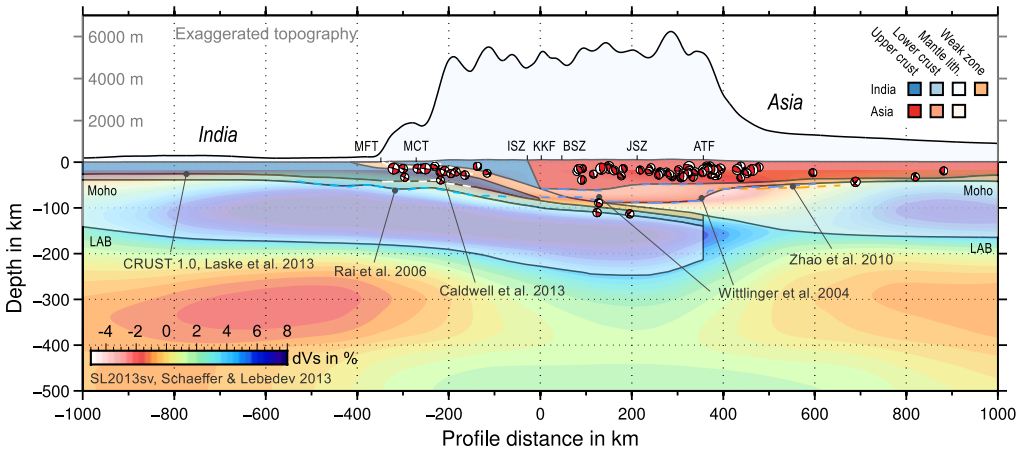


Figure 3.10: Our interpreted cross section of the profile in Fig. 3.9, used as a model geometry for the forward simulations. The structure of the Indian and Asian lithosphere is based on the recent S-wave tomography model (SL2013sv) by Schaeffer & Lebedev (2013). The crustal structures and interfaces are interpreted from projected profiles of several receiver function studies. The respective profiles are indicated with same the colors as in the mapview perspective of Fig. 3.9. Additional crustal geometry is inferred from CRUST 1.0 (Laske et al., 2013). Focal mechanisms of the CMT catalogue (1976–2014 Dziewoński et al., 1981; Ekström et al., 2012) with a maximum perpendicular displacement of $\pm 100$ km with respect to the profile, were used to construct the weak zone of the model.

location of the MHT, we use the focal mechanisms of the CMT catalogue (1976–2014 Dziewoński et al., 1981; Ekström et al., 2012). The MHT is constructed as a wide plastic weak zone that incorporates the MFT, MBT and MCT (Main Boundary and Central Thrust) due to resolution limitations of our model. We further extend the weak zone through the entire upper crust up to the KKF and treat it as a thin crustal layer on top of the Indian lithosphere that has different plastic parameters than the surrounding units, consistent with it being a heavily deformed mylonitic shear zone. Towards the northern end of the profile we use the interpretations of Wittlinger et al. (2004). As the MFT, the KKF and the Altyn Tagh (ATF) fault diverge towards East, we align their Moho and upper crust/lower crust boundary with the location of the ATF on our profile. Zhao et al. (2010) provide an additional constraint of the Moho in that region, but with a profile to the east of ours. The projected Moho horizon correlates well with the results of Wittlinger et al. (2004). To construct the LAB of the Indian and Asian continents, we based our interpretations mainly on the S-wave tomography model (SL2013sv) by Schaeffer & Lebedev (2013). The Indian shield is clearly visible as a high velocity anomaly, which suggests a northern extend of the Indian lithosphere up to the ATF. The vertical upper limit of the anomaly also correlates well with deep earthquakes at $150 \leqslant x \leqslant 200$ km, which are plotted with their focal mechanisms in Fig. 3.10. In addition, the LAB depth estimates by Zhao et al. (2010) are employed suggesting a depth of $d_{LAB} \approx 150$ km under the Tarim basin and an offset of about 50 km to the Indian LAB at larger depth. The distance between both profiles towards the southern end is admit-

tedly large and it is known that the Indian lithosphere varies in depth and is underthrusting Tibet in a shallower angle towards the western Himalayan syntax (Zhao et al., 2010), which is why we do not employ their LAB interpretation in that part of our profile.

*Surface constraints*

To estimate the likelihood function we compute the misfit against a set of four different observations. In this section, we describe the details of the preprocessing of these data. Fig. 3.11 shows the original, unfiltered data (blue), the associated uncertainties ($\pm 2\sigma$, black dashed lines) together with the processed data (red), which are used to compare with the estimated model data. To minimise the effect of the model boundaries and the part of the model where we impose the velocities, we limit the Bouguer anomaly and remaining observations to $-500\,\mathrm{km} \leqslant x \leqslant 750\,\mathrm{km}$ and $-1000\,\mathrm{km} \leqslant x \leqslant 900\,\mathrm{km}$ respectively. In addition, we do not consider correlations between the data sets, and therefore only the trace of the covariance matrix is non-zero.

*Topography*

The surface topography is probably the most accurate data that exists for the region. We use ETOPO1 data (Amante & Eakins, 2009), which has a resolution of 1 arc-minute. The data is filtered with a 4th order Butterworth low pass filter and with a corner wave number of $k = {}^{1}/_{100\,\mathrm{km}}$. The associated error is estimated to be $\sigma_{\mathrm{topo}} = 50\,\mathrm{m}$, based on the difference between the filtered and unfiltered signal.

*Gravity*

For the gravity anomaly, we take the Bouguer anomaly as it is mostly correlated with density differences between the crust and lithosphere and is less sensitive to short-wavelength topographic effects. Therefore, the gravity model EGM2008 (Pavlis et al., 2012) that provides the free-air anomaly is taken as input data for the software FA2BOUG by Fullea et al. (2008) to compute the Bouguer anomaly. The software is able to compute simplified Bouguer slab-anomalies and terrain corrected Bouguer anomalies. As our region has strong variations in topography, a simple Bouguer slab-correction is inaccurate and a terrain correction with high resolution topography is required (e.g. Blakely, 1996). We use the lower resolution ETOPO1 (including water) and the high resolution topography shuttle radar data (SRTM data, Jarvis et al., 2008) as input input for FA2BOUG. Both are provided for the entire map (Fig. 3.9). To correct for topographic masses $\rho_{\mathrm{topo}} = 2670\,\mathrm{kg/m^3}$ and $\rho_{\mathrm{water}} = 1030,\mathrm{kg/m^3}$ are used. Moreover, the parameters $D_{ri} = 20\,\mathrm{m}$ and $D_{rd} = 167\,\mathrm{m}$ required for a proper terrain correction are chosen as suggested by Fullea et al. (2008). Similar to the topography pre-processing, we lowpass-filter the resulting 2D Bouguer anomaly with a 4th order low pass filter. As we are not able to resolve crustal details we take a lower corner wave number of $k = {}^{1}/_{200\,\mathrm{km}}$. The standard deviation is

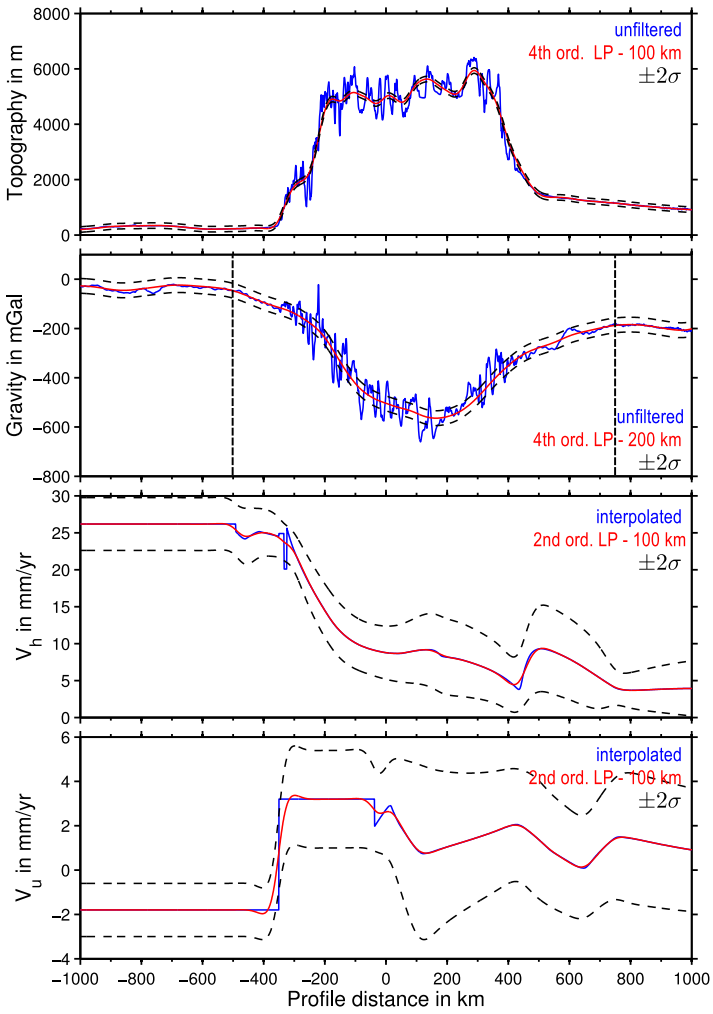


Figure 3.11: Surface constraints and uncertainties used for the geodynamic inversion described in section 3.4. Blue signals show the extracted or interpolated data. Red signals denote the filtered data, which we employ in the inversions. The uncertainties are illustrated as black dashed lines. In case of the Bouguer anomaly and topography, the uncertainties are estimated as constant standard deviations. The velocity uncertainties are in accordance with the measurements. Vertical dashed lines mark the part of the gravity profile that is taken into account ($-500\,\text{km} \leqslant x \leqslant 750\,\text{km}$). For the remaining signals, we choose the following limits: $-1000\,\text{km} \leqslant x \leqslant 900\,\text{km}$. Due to the limited extend of the model, the horizontal velocity is normalised with the magnitude at the northern end of the profile ($x = 1600\,\text{km}$).

estimated in the same manner, based on the difference of filtered and unfiltered signal and is $\sigma_{\text{boug}} = 15\,\text{mGal}$.

*3D surface velocities*

The surface velocity data that we use is a combined data set of several GPS measurement campaigns. The horizontal data are provided by several authors (Zhang et al., 2004; Gan et al., 2007; Liang et al., 2013) whereas the vertical

velocity data of Fig. 3.11 is only provided by Liang et al. (2013). For the processing, we separated the velocity data into two parts, an Indian and an Asian dataset, which are separated by the MBT, which is also prescribed in the model geometry. To geographically divide the data set, we used the MBT geometry provided by the fault data base of Styron et al. (2010). For each part, we construct a triangulation of the irregularly located measurements and interpolate the data on the regularly spaced profile using a natural and nearest neighbour interpolation from which we extract the three components of the velocity field (east, north, vertical) along the profile. The horizontal components are then projected on a Cartesian reference frame ($v_x$, $v_y$) from which we compute the component in profile direction ($v_h$), where positive values correspond to northwards directed velocities. The associated errors of the velocity field are processed in the same manner. The velocity data is provided with respect to a fixed Eurasian reference frame, but as our 2D model is limited in northern direction with a vertical free-slip boundary condition, we normalise the magnitude of horizontal velocity to the northern end of the profile.

*Model parametrisation*

*Numerics*

The model domain, which is 3401 km wide and spread up to a depth of 660 km, is discretised with $209 \times 69$ $Q_1P_0$ elements. We use a no-stress (free-surface) top boundary and free-slip boundaries at the sides and a no-slip boundary at the bottom, which is justified by the 660 km discontinuity, which serves as a barrier for subducting slabs (e.g. Fukao et al., 2009; Ringwood, 1994; Tackley et al., 1993). The energy boundary conditions are insulating at the sides and isothermal at the top (20 °C) and bottom ($T_{660km} = 1531$ °C) of the domain. The bottom temperature is based on an adiabatic temperature profile with a potential mantle temperature of $T_{pot} = 1300$ °C and an adiabatic gradient of $\gamma = 0.35$ K/km. We employ an internal horizontal pushing boundary condition in which we prescribe the horizontal velocity between $x = -1600$ km and $x = -1300$ km and above a depth of 100 km.

For the inversion, to remain numerically feasible, we have to limit the number of inversion parameters to no more than around 20. This implies that we cannot leave all model parameters free, but have to combine several units into a single one. Below, we discuss our choices. An overview of all inversion parameters used here is given in Table 3.5.

*Densities*

The density model is temperature-dependent (eq. 3.20) and parametrised according to the model geometry. Each unit is associated with a particular $\rho_0$, but the absolute density changes with temperature. In addition, we also refine the density structure by adding three sub-regions in the model geometry. Hence, the variation is attributed with three scalar factors. Below 20 km, the crustal densities of (i) India and (ii) Asia are free to increase up to 25% and (iii) we also

| Name | Viscosity | | | | Plasticity | Density | Temperature |
|---|---|---|---|---|---|---|---|
| Parameterisation | Dislocation creep | | | | Drucker-Prager | T-dependent | Step-wise linear |
| Parameter | $\mu_0$ | $n$ | $E$ | $V$ | $\phi$ | $\rho_0$ | $T_i$ |
| Units | $[\log_{10}(\mathrm{Pa\,s})]$ | [1] | [kJ/mol] | [$m^3$/mol] | [°] | [kg/$m^3$] | [°C] |
| **India** | | | | | | | |
| Weak zone | 13–18(1) | 1–5(5) | 50–600(2) | | 0–40(14) | $-0.478\,1/°C \cdot T_i + 2889$ | 300–600(17) |
| Upper crust | | | | | | | |
| Lower crust | | | 50–600(3) | | 0–40(15) | $-11.954 \cdot \rho_0(\mathrm{Iml}) + 44632.721$ | |
| Mantle lithosphere | | 1–5(6) | 50–600(4) | | | 3490–3515(19) | |
| **Asia** | | | | | | | |
| Upper crust | 13–18(7) | 1–5(11) | 50–600(8) | | 0–40(16) | $-8.103 \cdot \rho_0(\mathrm{Aml}) + 30923.926$ | 300–800(18) |
| Lower crust | | | 50–600(9) | | | $0.072\,°C^{-1} \cdot T_i + 3367$ | |
| Mantle lithosphere | | 1–5(12) | 50–600(10) | | | $0.061\,°C^{-1} \cdot T_i + 3451$ | |
| Upper mantle | | prescribed* | | 0–25(13) | – | 3502** | prescribed *** |

Table 3.5: Summary of inversion parameters for India Asia inversion described in sec 3.4. The labels (1–19) indicate the numbers (IDs) of the inversion parameters and the values denote the limits applied during the direct-search. (*) We prescribe the viscosity parameters with a rheology of dry olivine determined by Hirth & Kohlstedt (2003), but add a degree of freedom to allow for a variable activation volume. (**) The reference density of the upper mantle is prescribed, and is uniquely constrained by the gravity inversion (section 3.4.4.1). (***) The mantle temperature is prescribed to increase adiabatically with depth according to the relation $1300°C + z \cdot 0.35\,K/km$.

account for an additional density increase of up to 15 % due to eclogitisation of the Indian crust north of the KKF. Eclogitisation as a mechanism to increase the density of the Indian crust has been proposed by several authors to match the gravity anomaly (Hetényi et al., 2007; Nabelek et al., 2009).

The entire density parametrisation is listed in Table 3.6. In order to test our density model (11 parameters) we first perform a computationally cheaper gravity-only inversion to find trade-offs between density model parameters. For the joint geodynamic inversion, we then use these parameter relationship to reduce the number of free model parameters, as there is little point to run a full mechanical inversion if the density structure does not fit the gravity field.

*Rheology & plasticity*

Viscosity and plasticity are parameterised with 13 and 3 parameters respectively. The Indian crust and mantle lithosphere have the same power-law viscosity pre-factor $\mu_0(I)$ and effective friction coefficient $\phi(I)$. However, they differ in terms of the viscous power-law exponent ($n(Ic)$ and $n(Iml)$). Moreover, individual activation energy values are given for each part, upper, lower crust and mantle lithosphere. To enable the weak channel to behave differently than the Indian crust, we add an individual effective friction angle for the channel. In total, we use 8 parameters to describe the rheology of the Indian shield, and we apply the same rule to parameterise the Asian crust and lithosphere (7 parameters). The rheology of the mantle is mostly prescribed with the values for dry olivine found by Hirth & Kohlstedt (2003). We impose activation energy, pre-factor and power-law exponent, but take the activation volume $V(M)$ into account as an inversion parameter as this might result in a significant viscosity variations with depth.

*Temperature*

Viscosity has a strong, exponential dependence on temperature (eq. 3.12). An accurate temperature model is therefore required in an ideal case. However, the continental geotherms are usually only poorly constraint. Especially for mountainous regions heatflow measurements can be highly inaccurate (Jaupart & Mareschal, 2011). Using xenolith data, we at least have indirect methods to quantify geotherms for various regions (Priestley et al., 2008).

For our model setup, we do not rely on direct temperature constraints but rather use approximate geotherms for the Indian and Asian lithosphere part of the model. The geotherms are constructed as step-wise linear approximations that are fully defined with two free parameters, that are used as inversion parameters. A detailed description of our approximation can be found in appendix G. For this model, the geotherms are controlled by (i) the local depth of the lithosphere asthenosphere boundary (LAB) and (ii) the temperature at the boundary of upper and lower crust, to which we will refer to as interface temperature.

Potentially, the LAB can be parameterised with certain degrees of freedom, e.g. locally varying depths. We decided to prescribe the location of the LAB.

However, due to the power-law character of the mantle lithosphere's viscosity and the related degrees of freedom, the strength of the lithosphere is sufficiently parameterised.

In order to apply this temperature approximation, we have to make a few addition assumptions. We assume that the temperature within the upper mantle only varies adiabatically with a known adiabatic temperature gradient of $\gamma_{adb} = 0.35\,K/km$, and that the potential temperature of the mantle $T_{pot.,mantle} = 1300°C$. Moreover, we assume a constant surface temperature of $T_{surface} = 20°C$.

The final temperature model has two variables that are modified during the inversion process, which are the interface temperatures ($T_i(I)$ and $T_i(A)$) at the upper crust lower crust boundary of India and Asia. It is expected that the Indian shield is relatively cold compared to the Tibetan lower crust and mantle lithosphere. We therefore allow its interface temperature to vary between $300°C \leqslant T_i(I) \leqslant 600°C$. For the Asian part of the model, higher crustal temperatures are expected due to the presence of local volcanism (e.g. Kulun Volcanic Group), which is why we extend the upper limit in this case, $300°C \leqslant T_i(A) \leqslant 800°C$.

*Inversion results*

The inversion procedure is separated into two separate inversions, a gravity-only inversion (11 parameters, see Table 3.6) to reduce the number of free model parameters, and a full, joint geodynamic inversion (19 parameters, see Table 3.5). For the latter, we use linear combinations of correlated parameters that were found from the pure gravity inversion to describe the full parameterisation. This two step procedure is justified, because the computation of a gravity forward model is relatively cheap and only takes about 10% of the computation time of a combined gravity-geodynamic forward model. In addition, gravity data are potential field data, which is well-known to be non-unique. We therefore expect parameter trade-offs, which would unnecessarily expand the low misfit regions of the joint inversion.

*Gravity-only inversion*

We computed 621532 gravity forward models in the direct-search manner with NAplus. The forward models performed for the gravity inversion are illustrated with respect to two model parameters in Fig. 3.12, where the model misfit is color coded. Linear correlations clearly exist between the Asian crustal interface temperature $T_i(A)$ and the density pre-factor $\rho_0(Aml)$.

Assuming linear correlations only, a principal component analysis can be applied to find the orientation of the correlation axes. This was done by computing eigenvalues and eigenvectors for a subset of 'best-fit' model parameters respectively (Fig. 3.13). We find that $\rho_0$ of Asian lower crust and mantle lithosphere are directly correlated with the temperature at the interface between upper and lower crust ($T_i(A)$). Correlation also exist between $\rho_0$ of the upper crust and $T_i(A)$, but its correlation with $\rho_0(Aml)$ is much more pronounced. In this manner, the density parameters of Asia can be directly or indirectly described with

| Name | Density | | Temperature |
|---|---|---|---|
| Parameterisation | T-dependent | Dens. | Step-wise linear |
| Parameter | $\rho_0$ | factor | $T_i$ |
| Units | [kg/m$^3$] | [1] | [°C] |
| **India** | | | |
| Weak zone | | | |
| Upper crust | 2600–2800 (3) | | |
| Deep upper crust* | | 1.0–1.25 (10) | |
| Sub. upper crust** | | 1.0–1.15 (9) | 300–600 (2) |
| Lower crust | | | |
| Deep lower crust* | 2650–3100 (4) | 1.0–1.25 (10) | |
| Sub. lower crust** | | 1.0–1.15 (9) | |
| Mantle lithosphere | 3490–3550 (5) | | |
| **Asia** | | | |
| Upper crust | 2600–2800 (6) | | |
| Deep upper crust* | | 1.0–1.25 (11) | 300–800 (1) |
| Lower crust | 2800–3400 (7) | | |
| Mantle lithosphere | 3490–3550 (8) | | |

Table 3.6: Gravity inversion parameter boundaries.
(*) The crust has an additional degree of freedom (densification factor) to increase $\rho_0$ by up to 25 %. (**) The subducted Indian crust north of the KKF is allowed to get even denser, according to an additional factor to account for the effect of eclogitisation. Labels (1–11) indicate the inversion parameter numbers (IDs).

the interface temperature $T_i(A)$. For the geological units of the Indian shield, we do not observe equally strong correlations with the interface temperature $T_i(I)$, but find a correlation of the lower crustal $\rho_0(\mathrm{Ilc})$ with $\rho_0(\mathrm{Iml})$. For the entire parametrisation, we found that 7 out of 11 parameters are linearly correlated. One parameter, the densification factor due to eclogitisation is uniquely constrained ($f_{\mathrm{eclogite}} = 1.015$), suggesting that the effect of eclogitisation seems to be rather weak. However, this part of the Indian crust is also affected by another densification parameter (Fig. 3.13 right), which is determined to vary between $1.14 \lesssim f_{\mathrm{depth}} \lesssim 1.24$. This results in an increase of $\rho_0$ between $\sim 16\%$ and 26% for the model regions where eclogitisation is expected. As a result of the pure gravity inversion, we keep the two temperature parameters and $\rho_0$ of the Indian mantle lithosphere as free parameters of the joint geodynamic inversion. Other parameters are described with linear combinations of these parameters (see Table 3.7).

| Parameter | Linear combination |
|---|---|
| $\rho_0(\mathrm{Iuc})$ | $-0.48\,°\mathrm{C}^{-1} \cdot T_i(\mathrm{I}) + 2888.85\,\mathrm{kg/m^3}$ |
| $\rho_0(\mathrm{Ilc})$ | $-11.95 \cdot \rho_0(\mathrm{Iml}) + 44632.72\,\mathrm{kg/m^3}$ |
| $\rho_0(\mathrm{Aml})$ | $0.061\,°\mathrm{C}^{-1} \cdot T_i(\mathrm{I}) + 3451.40\,\mathrm{kg/m^3}$ |
| $\rho_0(\mathrm{Alc})$ | $0.073\,°\mathrm{C}^{-1} \cdot T_i(\mathrm{A}) + 3367.25\,\mathrm{kg/m^3}$ |
| $\rho_0(\mathrm{Auc})$ | $-8.10 \cdot \rho_0(\mathrm{Aml}) + 30923.93\,\mathrm{kg/m^3}$ |
| $f_{\mathrm{depth}}(\mathrm{I})$ | $-4.86 \cdot 10^{-4}\,\mathrm{m^3/kg} \cdot \rho_0(\mathrm{Iuc}) + 2.50$ |
| $f_{\mathrm{depth}}(\mathrm{A})$ | $-6.33 \cdot 10^{-4}\,\mathrm{m^3/kg} \cdot \rho_0(\mathrm{Auc}) + 2.86$ |
| $f_{\mathrm{eclogite}}$ | 1.015 |

Table 3.7: Resulting linear combinations for correlated parameters of the gravity-only inversion. The linear combinations are found with a principal component analysis applied to a 'best-fit' subset of the direct-search forward models. The linear combinations are used in the joint geodynamic inversion to reduce the dimensionality of the parameter space.

*Full geodynamic inversion*

A total number of about $1.9 \times 10^6$ forward models were computed during the direct-search process using NAplus (Table 3.8 for technical details). Despite the fact that the dimensions of the parameter space increased by three additional parameters (now 19, see Table 3.5), we do not increase the number of initial samples much compared to the earlier synthetic examples (sections 3.3.2 & 3.3.3). We, however, coarsen the discrete grid to 20 instead of 30 (50) values per parameter direction to account for the increased dimensionality. In addition, the main sampling is tuned to be very explorative at the beginning of the NA-sampling. As for the synthetic cases, the wall-time limits for the cluster are prescribed to 5 hours and restarts are required, which is why the sampling is separated into smaller blocks.

The appraisal of the direct-search ensemble is performed with 128 CPUs. We conduct 635 random walks with 2000 steps each (again, 1000 steps are attributed as burn-in period), starting from the 635 'best-fit' models. The priors are adjusted such that models towards the center of the parameter bounds are preferred over models close to the boundaries. As before, we therefore formulate the priors as Gaussians, centred between the parameter limits and spread with standard deviations that are equivalent to 75 % of the total parameter ranges.

The entire set of marginal distributions of the posterior are provided in the appendix H (Fig. 3.20). However, analysing the appraisal results more carefully reveals that 815 Voronoi cells are selected by the MCMC walks.

As the models are occasionally very different in terms of viscosity structure, we do not compute average structures from all selected models, but instead try to identify classes of models that have distinct viscosity structures. As it is infeasible and possibly imprecise to do this manually, we use a neural network

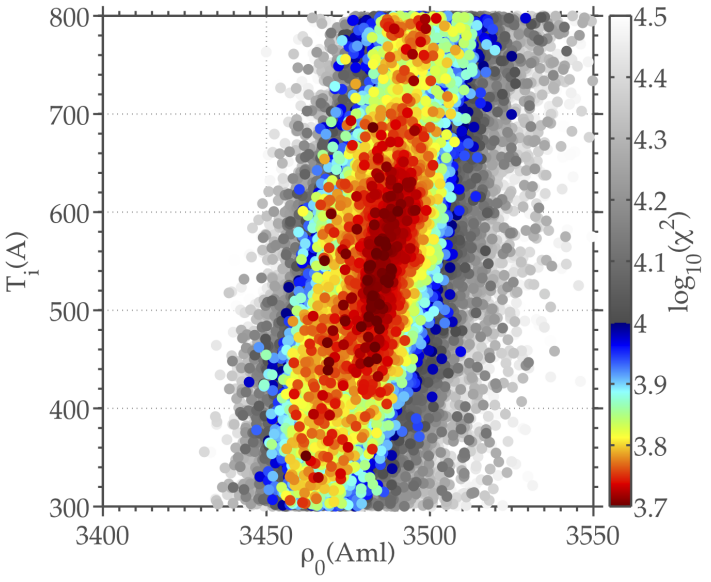


Figure 3.12: Direct-search examples of the pure gravity inversion, where each point represents a forward model, color-coded by its misfit value. The density pre-factor of the Asian mantle lithosphere $\rho_0(Aml)$ is plotted versus the Asian interface temperature ($T_i(A)$), and clear linear correlation can be observed.

approach to identify the end-member model classes. A detailed description of this post-processing step is described in Baumann (2016). In a nutshell, we extract three characteristic viscosity profiles of the model, for India, Tibet and the Tarim region. These profiles are then used to construct feature vectors as input for the neural network. The algorithm pre-sorts the models and a standard clustering algorithm, such as *k*-means can be used to summarise the models even further. In Fig. 3.14, we illustrate the inversion results in terms of the 'best-fit' representatives of the identified classes. Two examples classes are shown together with the 'best-fit' model found by the direct-search.

To interpret the inversion results, we first focus on the viscosity structures. There are a few very robust features that exist in all model classes. For all of them, we find that the Indian lithosphere must be strong under all circumstances. Very often, as represented here, the Indian lithosphere is additionally characterised by a strong power-law behaviour of the viscosity. On the other hand, the Indian crust is dominated by plastic yielding. This correlates with a well constrained $T_i(I)$ that suggests temperatures of the order of $\sim 500\,^{\circ}C$ at the inner crustal boundary. The corresponding temperature of the Asian model part is consistently higher, its marginal posterior distribution is centred at $\sim 600\,^{\circ}C$. This temperature can cause a weakened lower crust in Tibet, where the lower crust is thicker. It also suggests that partial melting would occur for some of the end-member models, which is, however, not taken into account in our forward models. Focussing on the Asian part of the model, we notice that most model classes except the 'yellow' class have a significant strong Asian lithosphere, which resembles a craton like behaviour. In addition, we observe that for these models, the interaction of temperature and effective power-law

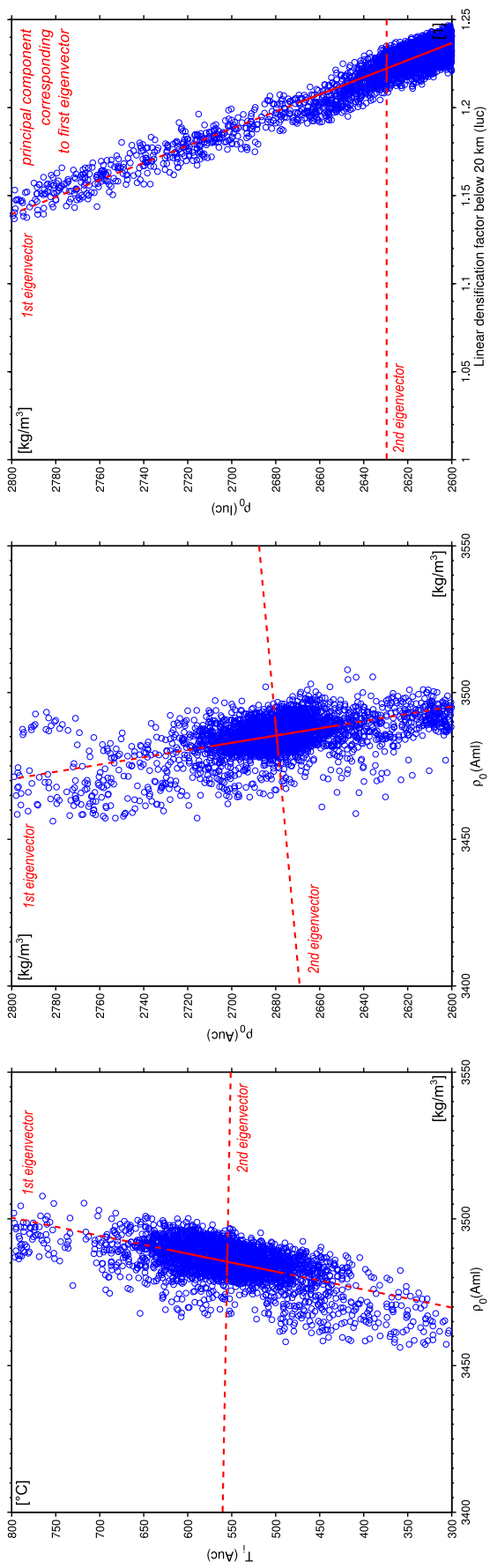


Figure 3.13: Principal component analysis of a 'best-fit' subset of the model ensemble of the gravity inversion. This is an efficient method to detect linearly correlated model parameters and to reduce the number of free parameters of the full geodynamic inversion. The 'best-fit' model subset and first and second eigenvector are shown for three cases. For example, $\rho_0$ of the Asian mantle lithosphere is a linear function of the temperature approximation, which is also linearly correlated with the upper crustal $\rho_0$. Moreover, the densification factor of the Indian upper crust is linearly related to $\rho_0$ of the Indian upper crust. In a similar manner, 7 out of 11 parameters that were used in the gravity inversion can be approximated by linear correlations. The entire system can therefore be described with only three parameters, which are kept during the joint geodynamic inversion.

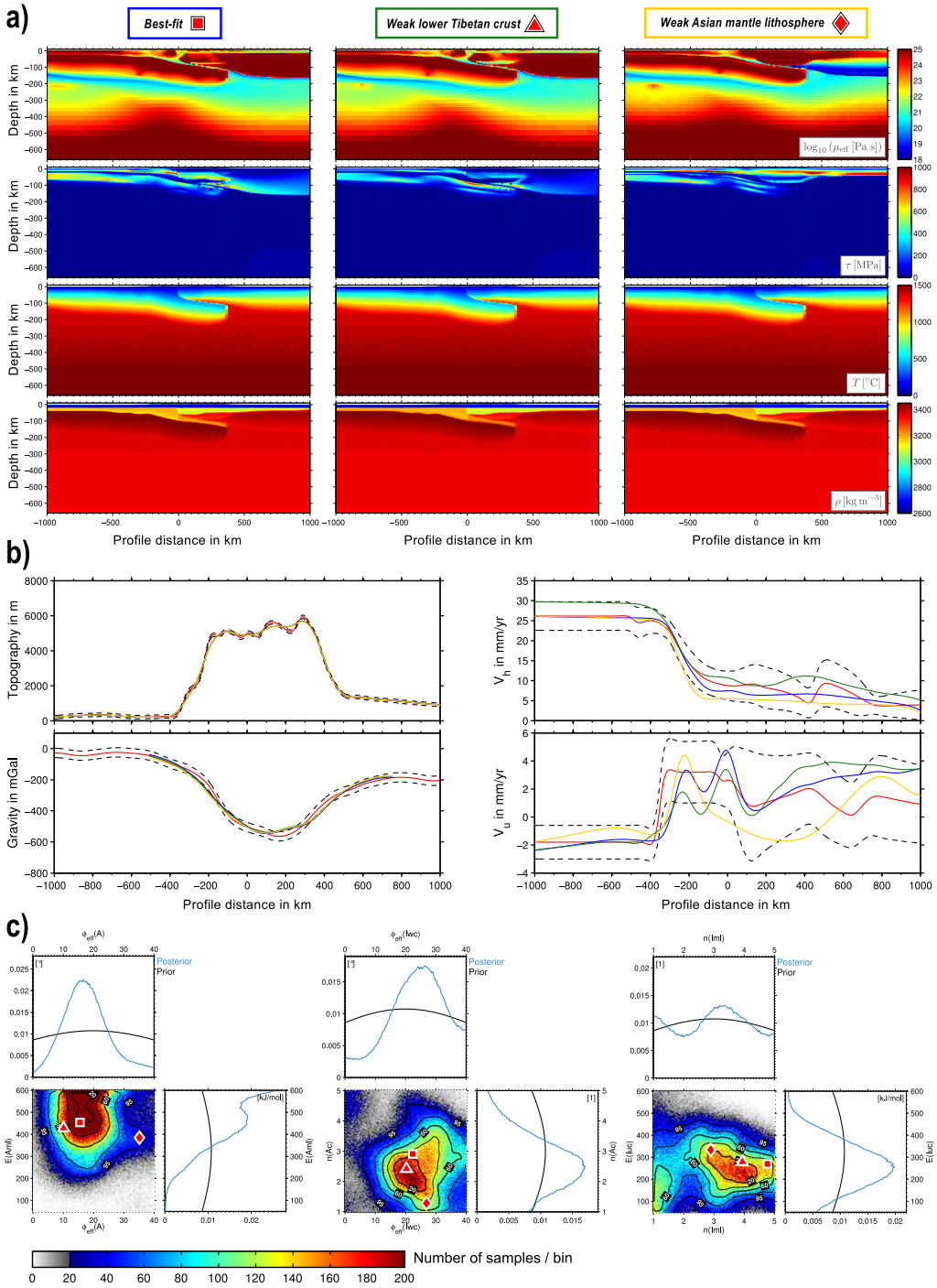


Figure 3.14: Summary of inversion results in section 3.4.4.2. Six model classes were identified that represent distinct viscosity distributions and result in approximately similar misfit values. **a)** Best fit model and representative models of two characteristic classes with a weak Tibetan lower crust and weak Asian mantle lithosphere. Results are shown in terms of effective viscosity, stress, temperature and density distribution. **b)** Observations (red) and model data of identified classes. Colours indicate the models shown above. Dashed lines show uncertainty limits. **c)** Examples of marginal distributions of the posterior. Markers indicate the models shown above.

| Sampling | Resampling parameter | Cumulative number of models | Number of processors | Runtime [hrs] |
|---|---|---|---|---|
| Initial | – | 297919 | 3456 | 5 |
| Main | 15000 | 400660 | 640 | 5 |
| Main | 7500 | 501799 | 640 | 5 |
| Main | 3500 | 604897 | 640 | 5 |
| Main | 1500 | 710159 | 640 | 5 |
| Main | 750 | 816357 | 640 | 5 |
| Main | 500 | 924241 | 640 | 5 |
| Main | 350 | 1250171 | 640 | 15 |
| Main | 500 | 1472277 | 640 | 10 |
| Main | 350 | 1886896 | 640 | 25 |

Table 3.8: Direct-search characteristics of the India-Asia collision example (section 3.4.4.2). Wall-time limitations of the cluster require restarts after 5 hours. Instead of an extensive initial sampling, a large resampling parameter was chosen at the beginning of the main sampling to compensate for the increased dimensionality of the parameter space. Visualizing intermediate sampling results helps to adjust the resampling parameter.

viscosity parameters forms a weakened layer at intermediate depths in the upper crust. This 'Christmas tree' pattern of the effective viscosity does not exist if the strong Asian lithosphere is missing as for the yellow class models. Here, a very strong upper and lower Asian crust are required to resist the Indian indentor and to maintain the topographic loading. At this point, it is useful to have a more detailed look at the corresponding model data. The Bouguer anomaly and particularly the topography are very well represented by all selected models (Fig. 3.14B). Only models associated with a very large misfit value show significant discrepancies with these data because of the small variances in the data covariance matrix. The models differ mainly in terms of vertical and horizontal velocity. Focussing on $v_h$, we observe only very little variation for the Indian part of the profile, whereas the shape of the drop in velocity at the convergence zone and north of the MBT has larger variations as the uncertainty bounds increase. If the Asian mantle lithosphere is weak, the $v_h$ signal shows a sharper step at the convergence zone and varies less north of KKF due to the very strong crust. The main differences in terms of surface expressions are, however, observed in the $v_v$ signal. The variation for the Indian part of the profile is, again, rather minor. The jump of $\sim 4\,\mathrm{mm/yr}$ from $-2\,\mathrm{mm/yr}$ to $2-3\,\mathrm{mm/yr}$ at $x = -400\,\mathrm{km}$ is represented by all models shown here. If a strong Asian lithosphere exists, the plateau like feature between $-400\,\mathrm{km} \lesssim x \lesssim 150\,\mathrm{km}$ seems to be present. On the other hand, a weak Asian lithosphere correlates with decreased uplift or even subsidence between $-200\,\mathrm{km} \lesssim x \lesssim 800\,\mathrm{km}$. We

attribute this behaviour with the buckling example of a thin plate under axial compression that is deflected downwards. For the Indian part of the model, we can observe the same effect, but less pronounced and reversely directed. This is a good example, where high effective friction parameters are dominating the deformation behaviour. Compared to the other models, the $\phi_{\text{eff}}$ parameter are highest for this model (see Fig. 3.14c left and center).

The deformation behaviour is also well reflected in terms of the stress patterns of the various end-member models (Fig. 3.14a). For the latter case, most stresses accumulate in the upper crust and close to the Tibetan Moho and bending stresses occur in the Indian lithosphere. On the other hand, the stresses are very differently distributed for the cases without weak Asian lithosphere. Both models have rather low stresses in the Indian and Tibetan lower crust, but the stresses appear at the lower upper crust and in the Tibetan mantle lithosphere. Bending stress patterns can be observed in the Indian lithosphere, which correlates with deep normal fault earthquakes (Fig. 3.10) at $x \approx 100$ km. The remaining seismicity pattern in Tibet is in better agreement with the stress pattern of the 'yellow' model with a weak Asian mantle lithosphere. At this point we want to emphasis that the Tarim basin is not taken into account as a separate geological unit in our inversion. Having a separated Tarim lithospheric block might allow for a lower viscosity of the Tibetan lithosphere, which could result in larger effective viscosities and correspondingly higher stresses in the Tibetan upper crust.

So far, we have focused on lithospheric properties of the model, but also the effective viscosity of the upper mantle shows very little variation between the models and results in relatively high viscosities below 400 km. The effective viscosity of the upper mantle is mainly controlled by the activation volume as the other parameters (activation energy, power-law exponent and prefactor) are prescribed with typical (laboratory) values of dry olivine (Table 3.5). Although its prior is relatively weak as we find a large variation in literature ($0 \lesssim V \lesssim 25 \cdot 10^{-6}\text{m}^3/\text{mol}$), the activation volume is one of the best constrained inversion parameters in our models, suggesting $V \gtrsim 15 \cdot 10^{-6}\text{m}^3/\text{mol}$ (appendix H, Fig. 3.20).

In Fig. 3.14c, we demonstrate a few examples of the marginal posterior distributions, which are provided for the entire parameter space in appendix H (Fig. 3.20). As we already analysed the effective viscosity structures of the models, we can easily explain the relative euclidean distances between the model locations in the parameter space. The triangle (green class) is always in the vicinity of the square (blue class model), whereas the yellow class, represented by the diamond, represents a distinct region of the parameter space. For example, the posterior of the effective friction angle of Asia (Fig. 3.14c left) is dominated by the blue and green class models. The yellow class, however, causes a certain shift in the marginal distribution towards higher friction angles (stronger crust). At the same time, the yellow class has a lower activation energy of the Asian mantle lithosphere. It seems that $\mathtt{E(Aml)}$ of the yellow class is not much lower, but the weakening effect is amplified due to high temperatures.

The effective friction angles of the weak channel (Fig. 3.14c, center) are concentrated in a small range ($20\,^\circ - 30\,^\circ$), although the yellow class friction angle is still slightly increased. As discussed, this correlates well with the vertical velocity signal. It also correlates with a low power-law exponent ($n(Ac) \approx 1$), which implies a homogeneous and stable Asian crust. The other models have a power-law exponent of $n(Ac) \approx 3$, which explains the 'Christmas tree' structure in the effective viscosity that has been discussed.

The consistent power-law behaviour within the Indian lithosphere is illustrated in Fig. 3.14c, where all model examples share the same local maximum of the marginal distribution of the power-law exponent ($n(Iml) \approx 2.5 - 5$). In addition, they also have very similar crustal activation energies ($E(Iuc) \approx 300\,\mathrm{kJ/mol}$), consistent with the similarities of the effective viscosity patterns.

## DISCUSSION

We separate the discussions into two parts. First, we evaluate our approach in general and discuss possible improvements. Then, as the arguments are more specific, we discuss the application of the presented method to the India-Asia collision with all its regional characteristics.

### *General aspects*

One of the main assumptions we make in our inversion method is that we know the geometry of the lithosphere reasonably well. This is admittedly a very strong assumption, but one could very easily attribute several degrees of freedom to the geometry as part of an inversion. For example, the LAB, which is only first order accurate, could be parameterised with a variable depth. Another possibility for oceanic subduction scenarios would be to vary the subduction angle or the width of the weak channel. Related to the India Asia collision, one could vary the northern extend of the Indian shield as different studies suggest different locations (see for example an overview by Klemperer et al., 2013). Nonetheless, adding new parameters to describe the geometry quickly increases the parameter space. For many subduction zones the slab surfaces are well constrained as 2D cross sections or 3D contours from analysing Wadati-Benioff zones (local seismicity distribution) and moment tensor solutions (Hayes et al., 2012; Syracuse & Abers, 2006). In general, this also applies to continental collision, albeit with more uncertainty as there is usually much less deep seismicity. Nevertheless, as we showed, the existing seismicity distribution, CMT solutions, tomographic models and Moho-signals from receiver function studies are usually well constrained, together with LAB estimates, which can be used in a joint approach to construct geological end-member models for the further usage in geodynamic inversions. Moreover, by performing a similar inversion for another geometrical end-member model at the same cross-section gives additional insights in the sensitivity of the inversion output to changes in the model geometry.

The first argument is closely related with another crucial question, which is how many model parameters can be used for this approach in practice, as well as a related question namely how many forward models are required to address the inverse problem with a NA-search. In general, the base of the NA, the computation of the Voronoi cells can in principle be performed for many dimensions (Sambridge, 1999a). Thus, the limiting factor is how many forward models can be computed in a reasonable amount of time. In appendix section D we provide a benchmark problem that is symmetric for infinite dimensions and is characterised by one global minimum and many local minima. We use this test function as a benchmark to address the question of limiting dimensionality and to estimate the number of forward models needed. Of course, the actual misfit topology can be very different and it is rather unlikely that as many local extrema exist. A good initial sampling strategy thus becomes much more important for higher dimensions. We employ a pseudo random sampling on a regular, predefined grid (section B that can be coarsened for higher dimensions, which has a clear advantage over other methods such as Quasi Monte Carlo sampling in that it can be used with random numbers initialized on many CPUs (which is an issue for many other methods).

The temperature parameterisation within our approach is another important factor. Temperature affects the effective viscosity in an exponential manner as well as the densities of the forward model. The way we parameterised the temperature for the synthetic model is admittedly a very rough approximation and might be too inaccurate for other scenarios. Especially close to the slab surface and towards the deeper parts of the slab, we clearly introduce errors. We, however, showed that this effect is at least partly compensated for the effective viscosity by other viscosity parameters. Nonetheless, we believe that there is some room for improvements. In particular cases, a good prior knowledge may exist from numerical forward modelling of the temperature evolution and could lead to more realistic temperatures within subducting slabs. On the other hand, one should consider that this also requires many assumptions (material properties and boundary conditions) as well (Syracuse et al., 2010; Sobolev et al., 2006). Integrated instantaneous forward modelling approaches (Fullea et al., 2009) might be more appropriate in this respect as many different data sets are combined to compute temperature estimates. For example, temperature can be estimated from seismic velocities (tomographies) (Sobolev et al., 1997; Sobolev & Babeyko, 1994), compositional as well as electromagnetic data (Vozar et al., 2014), which could in principle be combined with our geodynamic inversion approach, although it would further increase the parameter space (Afonso et al., 2013a,b). However, a two step approach with a precursory thermo-compositional inversion to construct a reasonable a priori temperature (and compositional) parameterisation, would significantly reduce the parameter space of a geodynamic inversion (with more computationally expensive) Stokes forward models. Exemplary, the gravity-only inversion applied for the India-Asia scenario (section 3.4.4.1) demonstrated that a precursory inversion with fast forward models can be efficient in identifying correlations. A

dimensionality reduction with a PCA can be applied to estimate linear correlations.

In principle, estimating more sophisticated relations and a priori distributions can be a non-trivial task (Mosegaard & Tarantola, 1995). In this study, we only used Gaussian priors with large standard deviations to relax the parameter ranges, which are in principle rather weak priors and might not be the best choice. On the other hand, Fig. 3.1 shows that we have only very little statistically independent data, which would justify the usage of stronger, non-Gaussian priors. Here, we just slightly prefer parameters in the center of the domain towards parameter combinations close to the parameter boundaries. Related to this, it is also unclear whether the empirical parameters found by laboratory experiments are directly applicable for geodynamic models or whether there are implicit scaling errors in going from the laboratory to natural conditions. Moreover, is it correct to summarise the parameters of several geological units (i.e. same power law exponent for upper and lower crust)? This can only be addressed, if we apply the geodynamic inversion for several real-world scenarios on Earth.

Compared to other lithospheric-scale inversions and forward models, the geodynamic inversion has an intrinsic time component. Two time-dependent processes are involved in the dynamics. At the beginning of the forward modelling, the motion is dominated by isostatic effects, which cause strong artificial motions. The resulting model surface observations are biased. As soon as the model is isostatically equilibrated, the surface motions are dominated by the stress-strain distribution in the lithosphere and asthenosphere, hence the effective viscosity structure. The question is than how long a forward model needs to be run until it can be compared with geodynamic data (topography and velocity). We addressed this with an empirical stopping criterion, where a statistical property of a quasi-dynamic topography (elevation based on a pressure difference at a compensation depth) signal is analysed (see section E for details). The empirical criterion only serves as an approximation and is not a definite proof that all isostatic motions have ended. Further work is required to find automatic model stopping criteria. At the same time, it is also unclear whether an investigated region is isostatically or dynamically compensated.

So far, we discussed the limitations of the forward model itself and the implications on the inversion results. Moreover, the inversion result depends on the data we use, the data pre-processing and probably even more on how the data covariance matrix is constructed (how the data is relatively weighted). In this study, we neglected correlations in the data. Although the long wavelength of the topography is anti-correlated with the Bouguer anomaly signal, we neglect it because both quantities clearly originate from physically distinct sources (Afonso et al., 2013b).

Regarding the pre-processing, we always low-pass filter the data to assure that data that can not be represented with the current model resolution is not part of the reference data. As the wavelength is chosen subjectively, there is always a certain risk that important data is missing that influence the inversion result. Another issue is the handling of interpolations because the lithosphere

is heterogeneous. This mainly affects the surface velocities, because faults in the crust should be accounted for during the interpolation process. In terms of the application of the India Asia collision, we therefore separated the interpolation of the velocity field for both continents. Other major faults in this area are not taken into account as only the MHT is represented in the model. This probably leads to small inaccuracies. However, for this approach, including smaller faults into the model is not feasible resolution-wise and because of the large uncertainties of GPS data. Even if the velocity field is only first order accurate, it will be possible to neglect many models with velocity fields that are far off.

Another open question refers to the applicability of GPS data for a geodynamic inversion in general, or whether the present-day velocity field can be interpreted in terms of long-term motions. Platt & Becker (2010) looked at the San Andreas fault and suggest that GPS data are consistent with long-term geological motion of the lithosphere, suggesting that GPS data can indeed be used in combination with geodynamic models.

In this respect, it has to be tested if replacing the surface velocities with their spatial derivatives (strainrates) improves the inversion results, as strainrates might be more sensitive to the model rheology. Using a similar argument, future studies could consider to incorporate gravity gradients instead of Bouguer anomalies, as these data are available from the newest satellite missions (GOCE) and have a certain potential for lithospheric scale modelling (Bouman et al., 2015).

*Application to India-Asia*

Besides the discussed possibility to introduce geometrical parameters, which also applies to this model, our end-member model geometry is simplified because the Tarim basin is not treated as a separate geological unit as suggested by some authors (e.g. Cook & Royden, 2008). Although the presented model classes partially show a weakened lower crust of Tibet, the Asian lithosphere which is treated as a whole block, is possibly too strongly represented in these models. Having a separated Tarim basin and attributing a distinct rheology to this unit, might change the effective viscosity pattern.

Regarding the Indian lithosphere, it is not entirely clear whether a connection to old oceanic lithosphere exist. Whereas in Eastern Tibet a subducting Indian lithosphere is clearly observed (e.g. Kosarev, 1999; Agius & Lebedev, 2013), it becomes more diffuse along the convergence zone towards the Western syntax where many tomographic modes suggest India underthrusting Tibet (Agius & Lebedev, 2013; Li et al., 2008). The high seismic velocity suggest low temperatures, which corresponds well to our inversion results. In the upper mantle, the cross-section of the SL2013sv model (Schaeffer & Lebedev, 2013) in Fig. 3.10 shows a decreased velocity anomaly at $0 \leqslant x \leqslant 400\,\mathrm{km}$, probably reflecting a low temperature anomaly which is possibly correlated with subducted oceanic lithosphere. This is an observation that we did not account for in our model because the temperature distribution is limited parameter-wise, as the temperature in the mantle does not change laterally, and only varies adiabatically.

Related to temperature, tomographic models also show anomalous low shear wave speed for Tibetan middle crust, suggesting high temperatures or even partial melting (e.g. Agius & Lebedev, 2014), which is also supported by electromagnetic studies for southern Tibet (Nelson et al., 1996). Here, the interpreted partially molten parts are rather shallow (~ 15 km). In terms of effective viscosity our end-member models partly correspond to these observations, as we have shallow weak zones in Asia, and a weakened lower Tibetan crust. Our inverted temperatures for Asia are rather large (~ 600 °C at the upper crust lower crust boundary). This implies that partial melting can occur in the lower crust, which would cause an additional weakening effect on viscosity.

For the mantle part of the model, we observed a relatively high effective viscosity below 400 km, which correlates with a high activation volume. Models that do not have these high effective viscosities do not fit the data equally well. Additional inversions, also for different locations on Earth, are required to investigate whether such high activation volumes are a global feature of upper mantle rheologies.

## CONCLUSIONS

We demonstrated that it is possible to combine numerical geodynamic models with geophysical observations and use massively parallel inversions in a Bayesian sense to fit the observed data (which are gravity, topography and GPS velocities in our case). Synthetic results demonstrate that this joint inversion approach can indeed be used to retrieve the rheology of the models as well as their uncertainties and parameter trade-offs, even if this rheology is nonlinear. Models with a parameterised temperature have larger uncertainties than models in which the thermal structure is well known.

We also apply our method to a cross-section of the India-Asia collision system. The resulting models fit the data within their respective uncertainty bounds, but the results also show that different classes of models are found that fit the data nearly equally well. Whereas the Indian mantle lithosphere must have a high effective viscosity to fit the observations, the mechanical structure of the Tibetan lithosphere is less well constrained.

We conclude that geodynamic inversion is a powerful, but computationally expensive, new method to constrain the rheology and dynamics of the lithosphere. In the future, additional datasets could be taken into account during the inversions which is likely to reduce the number of required forward models.

## ACKNOWLEDGMENTS

This project was fully supported by the European Research Council under the European Community under the Seventh Framework Program (FP7/2007-2013) with ERC Starting Grant agreement #258830. We thank M. Sambridge for sharing his Neighbourhood algorithm. We also thank T. Gerya and T. Bodin for constructive remarks. Numerical computations have been performed on MOGON,

deployed by Johannes Gutenberg University, Mainz. We thank M. Tacke and the HPC-support team for their assistance. Figures were partly created using the Generic Mapping Tools (GMT) software (Wessel et al., 2013).

## REFERENCES

Afonso, J., Fullea, J., Griffin, W., Yang, Y., Jones, A., D Connolly, J., & O'Reilly, S., 2013a. 3-D multiobservable probabilistic inversion for the compositional and thermal structure of the lithosphere and upper mantle. I: A priori petrological information and geophysical observables, *J. Geophys. Res.: Solid Earth*, **118**(5), 2586–2617.

Afonso, J. C., Fullea, J., Yang, Y., Connolly, J. A. D., & Jones, A. G., 2013b. 3-D multi-observable probabilistic inversion for the compositional and thermal structure of the lithosphere and upper mantle. II: General methodology and resolution analysis, *J. Geophys. Res.: Solid Earth*, **118**(4), 1650–1676.

Agius, M. R. & Lebedev, S., 2013. Tibetan and Indian lithospheres in the upper mantle beneath Tibet: Evidence from broadband surface-wave dispersion, *Geochem. Geophys. Geosyst.*, **14**(10), 4260–4281.

Agius, M. R. & Lebedev, S., 2014. Shear-velocity structure, radial anisotropy and dynamics of the Tibetan crust, *Geophys. J. Int.*, **199**(3), 1395–1415.

Amante, C. & Eakins, B. W., 2009. *ETOPO1 1 arc-minute global relief model: procedures, data sources and analysis*, US Department of Commerce, National Oceanic and Atmospheric Administration, National Environmental Satellite, Data, and Information Service, National Geophysical Data Center, Marine Geology and Geophysics Division.

Balay, S., Abhyankar, S., Adams, M., Brown, J., Brune, P., Buschelman, K., Eijkhout, V., Gropp, W., Kaushik, D., Knepley, M., et al., 2014. Petsc users manual revision 3.5.

Baumann, T. S., 2016. Appraisal of geodynamic inversion results: A data mining approach, *submitted*.

Baumann, T. S., Kaus, B. J., & Popov, A. A., 2014. Constraining effective rheology through parallel joint geodynamic inversion, *Tectonophysics*, **631**, 197–211.

Blakely, R. J., 1996. *Potential theory in gravity and magnetic applications*, Cambridge University Press.

Bouman, J., Ebbing, J., Meekes, S., Fattah, R. A., Fuchs, M., Gradmann, S., Haagmans, R., Lieb, V., Schmidt, M., Dettmering, D., et al., 2015. Goce gravity gradient data for lithospheric modeling, *Int. J. Appl. Earth Obs.*, **35**, 16–30.

Bunge, H. P., Hagelberg, C. R., & Travis, B. J., 2003. Mantle circulation models with variational data assimilation: inferring past mantle flow and structure

from plate motion histories and seismic tomography, *Geophys. J. Int.*, **152**(2), 280–301.

Burg, J.-P. & Schmalholz, S., 2008. Viscous heating allows thrusting to overcome crustal-scale buckling: Numerical investigation with application to the himalayan syntaxes, *Earth Planet. Sci. Lett.*, **274**(1), 189–203.

Burov, E. & Watts, A. B., 2006. The long-term strength of continental lithosphere:" jelly sandwich" or" crème brûlée"?, *GSA today*, **16**(1), 4.

Burov, E. B., 2007. Crust and Lithosphere Dynamics: Plate Rheology and Mechanics, in *Treatise Geophys.*, vol. 6, chap. 3, pp. 99–151, ed. Watts, A. B., Elsevier.

Caflisch, R. E., 1998. Monte carlo and quasi-monte carlo methods, *Acta numer.*, **7**, 1–49.

Caldwell, W. B., Klemperer, S. L., Lawrence, J. F., Rai, S. S., & Ashish, 2013. Characterizing the Main Himalayan Thrust in the Garhwal Himalaya, India with receiver function CCP stacking, *Earth Planet. Sci. Lett.*, **367**, 15–27.

Cook, K. L. & Royden, L. H., 2008. The role of crustal strength variations in shaping orogenic plateaus, with application to tibet, *J. Geophys. Res.: Solid Earth*, **113**(B8).

Dabrowski, M., Krotkiewski, M., & Schmid, D., 2008. Milamin: Matlab-based finite element method solver for large problems, *Geochem. Geophys. Geosyst.*, **9**(4).

DeMets, C., Gordon, R. G., Argus, D. F., & Stein, S., 1990. Current plate motions, *Geophys. J. Int.*, **101**(2), 425–478.

Dziewoński, A., Chou, T.-A., & Woodhouse, J., 1981. Determination of earthquake source parameters from waveform data for studies of global and regional seismicity, *J. Geophys. Res.: Solid Earth*, **86**(B4), 2825–2852.

Dziewonski, A. M. & Anderson, D. L., 1981. Preliminary reference earth model, *Phys. Earth Planet. In.*, **25**(4), 297–356.

Ebbing, J., Braitenberg, C., & Götze, H.-J., 2001. Forward and inverse modelling of gravity revealing insight into crustal structures of the eastern alps, *Tectonophysics*, **337**(3), 191–208.

Ekström, G., Nettles, M., & Dziewoński, A., 2012. The global cmt project 2004–2010: centroid-moment tensors for 13,017 earthquakes, *Phys. Earth Planet. In.*, **200**, 1–9.

Fielding, E., Isacks, B., Barazangi, M., & Duncan, C., 1994. How flat is Tibet?, *Geology*, **22**(2), 163–167.

Forte, A. M., Peltier, W. R., & Dziewonski, A. M., 1991. Inferences of mantle viscosity from tectonic plate velocities, *Geophys. Res. Lett.*, **18**(9), 1747–1750.

Fukao, Y., Obayashi, M., & Nakakuki, T., 2009. Stagnant slab: a review, *Annu. Rev. Earth Planet. Sci.*, **37**, 19–46.

Fullea, J., Fernández, M., & Zeyen, H., 2008. FA2BOUG - A FORTRAN 90 code to compute Bouguer gravity anomalies from gridded free-air anomalies: Application to the Atlantic-Mediterranean transition zone, *Comput. Geosci.*, **34**(12), 1665–1681.

Fullea, J., Afonso, J. C., Connolly, J. a. D., Fernàndez, M., García-Castellanos, D., & Zeyen, H., 2009. LitMod3D: An interactive 3-D software to model the thermal, compositional, density, seismological, and rheological structure of the lithosphere and sublithospheric upper mantle, *Geochem. Geophys. Geosyst.*, **10**(8).

Gan, W., Zhang, P., Shen, Z.-K., Niu, Z., Wang, M., Wan, Y., Zhou, D., & Cheng, J., 2007. Present-day crustal motion within the Tibetan Plateau inferred from GPS measurements, *J. Geophys. Res.*, **112**(B8).

Geman, S. & Geman, D., 1984. Stochastic relaxation, gibbs distributions, and the bayesian restoration of images, *IEEE Trans. Pattern Anal. Mach. Intell.*, **6**, 721–741.

Gerya, T., 2009. *Introduction to numerical geodynamic modelling*, Cambridge University Press.

Guttal, V. & Jayaprakash, C., 2008. Changing skewness: an early warning signal of regime shifts in ecosystems, *Ecol. Lett.*, **11**(5), 450–460.

Hatzfeld, D. & Molnar, P., 2010. Comparisons of the kinematics and deep structures of the zagros and himalaya and of the iranian and tibetan plateaus and geodynamic implications, *Rev. Geophys.*, **48**(2).

Hayes, G. P., Wald, D. J., & Johnson, R. L., 2012. Slab1.0: A three-dimensional model of global subduction zone geometries, *J. Geophys. Res.*, **117**(B1).

Hetényi, G., Cattin, R., Brunet, F., Bollinger, L., Vergne, J., Nábělek, J. L., & Diament, M., 2007. Density distribution of the India plate beneath the Tibetan plateau: geophysical and petrological constraints on the kinetics of lower-crustal eclogitization, *Earth Planet. Sci. Lett.*, **264**(1), 226–244.

Hirth, G. & Kohlstedt, D., 2003. Rheology of the upper mantle and the mantle wedge: A view from the experimentalists, in *Inside the subduction Factory*, pp. 83–105, Wiley Online Library.

Jarvis, A., Reuter, H. I., Nelson, A., & Guevara, E., 2008. Hole-filled srtm for the globe version 4, available from the CGIAR-CSI SRTM 90m Database (http://srtm.csi.cgiar.org).

Jaupart, C. & Mareschal, J.-C., 2011. *Heat generation and transport in the Earth*, Cambridge University Press.

Karato, S., 2008. *Deformation of earth materials: an introduction to the rheology of solid earth*, Cambridge University Press.

Kaus, B. J., 2010. Factors that control the angle of shear bands in geodynamic numerical models of brittle deformation, *Tectonophysics*, **484**(1), 36–47.

Kaus, B. J., Connolly, J. A., Podladchikov, Y. Y., & Schmalholz, S. M., 2005. Effect of mineral phase transitions on sedimentary basin subsidence and uplift, *Earth Planet. Sci. Lett.*, **233**(1), 213–228.

Kaus, B. J., Mühlhaus, H., & May, D. a., 2010. A stabilization algorithm for geodynamic numerical simulations with a free surface, *Phys. Earth Planet. In.*, **181**(1-2), 12–20.

Klemperer, S. L., Kennedy, B. M., Sastry, S. R., Makovsky, Y., Harinarayana, T., & Leech, M. L., 2013. Mantle fluids in the Karakoram fault: Helium isotope evidence, *Earth Planet. Sci. Lett.*, **366**, 59–70.

Kosarev, G., 1999. Seismic Evidence for a Detached Indian Lithospheric Mantle Beneath Tibet, *Science*, **283**, 1306–1309.

Laske, G., Masters, G., Ma, Z., & Pasyanos, M., 2013. Update on crust1.0 - a 1-degree global model of earth's crust, in *Geophys. Res. Abstracts*, vol. 15, p. 2658.

L'ecuyer, P., Simard, R., Chen, E. J., & Kelton, W. D., 2002. An object-oriented random-number package with many long streams and substreams, *Oper. Res.*, **50**(6), 1073–1075.

Li, C., van der Hilst, R. D., Meltzer, A. S., & Engdahl, E. R., 2008. Subduction of the Indian lithosphere beneath the Tibetan Plateau and Burma, *Earth Planet. Sci. Lett.*, **274**(1), 157–168.

Liang, S., Gan, W., Shen, C., Xiao, G., Liu, J., Chen, W., Ding, X., & Zhou, D., 2013. Three-dimensional velocity field of present-day crustal motion of the Tibetan Plateau derived from GPS measurements, *J. Geophys. Res.: Solid Earth*, **118**(10), 5722–5732.

Liu, L. & Gurnis, M., 2008. Simultaneous inversion of mantle properties and initial conditions using an adjoint of mantle convection, *J. Geophys. Res.*, **113**(B8).

Maggi, A., Jackson, J. A., McKenzie, D., & Priestley, K., 2000. Earthquake focal depths, effective elastic thickness, and the strength of the continental lithosphere, *Geology*, **28**, 495–498.

Molnar, P. & Tapponnier, P., 1975. Cenozoic tectonics of asia: effects of a continental collision, *Science*, **189**(4201), 419–426.

Moresi, L., Quenette, S., Lemiale, V., Meriaux, C., Appelbe, B., & Muhlhaus, H. B., 2007. Computational approaches to studying non-linear dynamics of the crust and mantle, *Phys. Earth Planet. In.*, **163**, 69–82.

Morokoff, W. J. & Caflisch, R. E., 1994. Quasi-random sequences and their discrepancies, *SIAM J. Sci. Comput.*, **15**(6), 1251–1279.

Mosegaard, K., 2011. Quest for consistency, symmetry, and simplicity – the legacy of albert tarantola, *Geophysics*, **76**(5), W51–W61.

Mosegaard, K. & Sambridge, M., 2002. Monte Carlo analysis of inverse problems, *Inverse problems*, **18**(3), R29–R57.

Mosegaard, K. & Tarantola, A., 1995. Monte carlo sampling of solutions to inverse problems, *J. Geophys. Res.: Solid Earth*, **100**(B7), 12431–12447.

Mühlenbein, H., Schomisch, M., & Born, J., 1991. The parallel genetic algorithm as function optimizer, *Parallel Comput.*, **17**(6), 619–632.

Nabelek, J., Hetenyi, G., Vergne, J., Sapkota, S., Kafle, B., Jiang, M., Su, H., Chen, J., Huang, B. S., & Team, t. H. C., 2009. Underplating in the Himalaya-Tibet Collision Zone Revealed by the Hi-CLIMB Experiment, *Science*, **325**(5946), 1371–1374.

Nelson, K. D., Zhao, W., Brown, L. D., Kuo, J., Che, J., Liu, X., Klemperer, S. L., Makovsky, Y., Meissner, R., Mechie, J., Kind, R., Wenzel, F., Ni, J., Nabelek, J., Leshou, C., Tan, H., Wei, W., Jones, A. G., Booker, J., Unsworth, M., Kidd, W. S. F., Hauck, M., Alsdorf, D., Ross, A., Cogan, M., Wu, C., Sandvol, E., & Edwards, M., 1996. Partially Molten Middle Crust Beneath Southern Tibet: Synthesis of Project INDEPTH Results, *Science*, **274**(5293), 1684–1688.

Niederreiter, H., 1992. *Random number generation and quasi-Monte Carlo methods*, vol. 63, SIAM.

Panasyuk, S. V. & Hager, B. H., 2000. Models of isostatic and dynamic topography, geoid anomalies, and their uncertainties, *J. Geophys. Res.: Solid Earth*, **105**(B12), 28199–28209.

Pavlis, N. K., Holmes, S. A., Kenyon, S. C., & Factor, J. K., 2012. The development and evaluation of the Earth Gravitational Model 2008 (EGM2008), *J. Geophys. Res.*, **117**(B4).

Platt, J. P. & Becker, T. W., 2010. Where is the real transform boundary in California?, *Geochem. Geophys. Geosyst.*, **11**(6).

Popov, A. A. & Sobolev, S. V., 2008. SLIM3D: A tool for three-dimensional thermomechanical modeling of lithospheric deformation with elasto-visco-plastic rheology, *Phys. Earth Planet. In.*, **171**(1), 55–75.

Press, W. H., Teukolsky, S. A., Vetterling, W. T., & Flannery, B. P., 1992. *Numerical recipes in Fortran 77: the art of scientific computing*, Cambridge University Press.

Priestley, K., Jackson, J., & McKenzie, D., 2008. Lithospheric structure and deep earthquakes beneath india, the himalaya and southern tibet, *Geophys. J. Int.*, **172**(1), 345–362.

Rai, S. S., Priestley, K., Gaur, V. K., Mitra, S., Singh, M. P., & Searle, M., 2006. Configuration of the Indian Moho beneath the NW Himalaya and Ladakh, *Geophys. Res. Lett.*, **33**(15).

Ranalli, G., 1995. *Rheology of the Earth*, Springer.

Ricard, Y. & Wuming, B., 1991. Inferring the viscosity and the 3-D density structure of the mantle from geoid, topography and plate velocities, *Geophys. J. Int.*, **105**(3), 561–571.

Ricard, Y., Vigny, C., & Froidevaux, C., 1989. Mantle heterogeneities, geoid, and plate motion: A Monte Carlo inversion, *J. Geophys. Res.: Solid Earth*, **94**(B10), 13739–13754.

Ringwood, A. E., 1994. Role of the transition zone and 660 km discontinuity in mantle dynamics, *Phys. Earth Planet. In.*, **86**(1), 5–24.

Sambridge, M., 1999a. Geophysical inversion with a neighbourhood algorithm–I. Searching a parameter space, *Geophys. J. Int.*, **138**(2), 479–494.

Sambridge, M., 1999b. Geophysical inversion with a neighbourhood algorithm–II. Appraising the ensemble, *Geophys. J. Int.*, **138**(3), 727–746.

Sambridge, M. & Mosegaard, K., 2002. Monte carlo methods in geophysical inverse problems, *Rev. Geophys.*, **40**(3), 3–1.

Schaeffer, A. J. & Lebedev, S., 2013. Global shear speed structure of the upper mantle and transition zone, *Geophys. J. Int.*, **194**, 417–449.

Scheffer, M., Bascompte, J., Brock, W. A., Brovkin, V., Carpenter, S. R., Dakos, V., Held, H., van Nes, E. H., Rietkerk, M., & Sugihara, G., 2009. Early-warning signals for critical transitions, *Nature*, **461**(7260), 53–59.

Schmalholz, S. M., Kaus, B. J., & Burg, J.-P., 2009. Stress-strength relationship in the lithosphere during continental collision, *Geology*, **37**(9), 775–778.

Schmeling, H., Babeyko, A., Enns, A., Faccenna, C., Funiciello, F., Gerya, T., Golabek, G., Grigull, S., Kaus, B., Morra, G., Schmalholz, S., & van Hunen, J., 2008. A benchmark comparison of spontaneous subduction models–Towards a free surface, *Phys. Earth Planet. In.*, **171**(1-4), 198–223.

Sobolev, S. V. & Babeyko, A. Y., 1994. Modeling of mineralogical composition, density and elastic wave velocities in anhydrous magmatic rocks, *Surv. Geophys.*, **15**(5), 515–544.

Sobolev, S. V., Zeyen, H., Granet, M., Achauer, U., Bauer, C., Werling, F., Altherr, R., & Fuchs, K., 1997. Upper mantle temperatures and lithosphere-asthenosphere system beneath the French Massif Central constrained by seismic, gravity, petrologic and thermal observations, *Tectonophysics*, **275**(1-3), 143–164.

Sobolev, S. V., Babeyko, A. Y., Koulakov, A. Y., Oncken, O., & Koulakov, I., 2006. Mechanism of the Andean orogeny: insight from numerical modeling, in *The Andes: Active Subduction Orogeny*, vol. 1, pp. 513–535, eds Oncken, O., Chong, G., Franz, G., Giese, P., Goetze, H.-J., Ramos, V. A., Strecker, M. R., & Wigger, P., Springer.

Styron, R., Taylor, M., & Okoronkwo, K., 2010. Database of active structures from the Indo-Asian collision, *Eos, Trans. Amer. Geophys. Union*, **91**(20), 181–182.

Syracuse, E. M. & Abers, G. A., 2006. Global compilation of variations in slab depth beneath arc volcanoes and implications, *Geochem. Geophys. Geosyst.*, **7**(5).

Syracuse, E. M., van Keken, P. E., & Abers, G. a., 2010. The global range of subduction zone thermal models, *Phys. Earth Planet. In.*, **183**(1-2), 73–90.

Tackley, P. J., Stevenson, D. J., Glatzmaier, G. A., & Schubert, G., 1993. Effects of an endothermic phase transition at 670 km depth in a spherical model of convection in the Earth's mantle, *Nature*, **361**(6414), 699–704.

Tarantola, A., 2005. *Inverse problem theory and methods for model parameter estimation*, SIAM.

Tarantola, A. & Valette, B., 1982a. Inverse problems= quest for information, *J. Geophys.*, **50**(3), 150–170.

Thielmann, M. & Kaus, B. J., 2012. Shear heating induced lithospheric-scale localization: Does it result in subduction?, *Earth Planet. Sci. Lett.*, **359**, 1–13.

Turcotte, D. L. & Schubert, G., 2002. *Geodynamics*, Cambridge University Press.

Vermeer, P. A. & De Borst, R., 1984. Non-Associated Plasticity for Soils, Concrete and Rock, *HERON*, **29**(3).

Vozar, J., Jones, A. G., Fullea, J., Agius, M. R., Lebedev, S., Pape, F. L., & Wei, W., 2014. Integrated geophysical-petrological modeling of lithosphere-asthenosphere boundary in central Tibet using electromagnetic and seismic data, *Geochem. Geophys. Geosyst.*, pp. 1–24.

Watts, A. B., 2001. *Isostasy and Flexure of the Lithosphere*, Cambridge University Press.

Wessel, P., Smith, W. H., Scharroo, R., Luis, J., & Wobbe, F., 2013. Generic mapping tools: Improved version released, *Eos, Trans. Amer. Geophys. Union*, **94**(45), 409–410.

Wilkinson, D. J., 2006. Parallel bayesian computation, *Statistics Textbooks and Monographs*, **184**, 477.

Wittlinger, G., Vergne, J., Tapponnier, P., Farra, V., Poupinet, G., Jiang, M., Su, H., Herquel, G., & Paul, A., 2004. Teleseismic imaging of subducting lithosphere and Moho offsets beneath western Tibet, *Earth Planet. Sci. Lett.*, **221**(1), 117–130.

Won, I. & Bevis, M., 1987. Computing the gravitational and magnetic anomalies due to a polygon: Algorithms and fortran subroutines, *Geophysics*, **52**(2), 232–238.

Zhang, P.-Z., Shen, Z., Wang, M., Gan, W., Bürgmann, R., Molnar, P., Wang, Q., Niu, Z., Sun, J., Wu, J., Hanrong, S., & Xinzhao, Y., 2004. Continuous deformation of the Tibetan Plateau from global positioning system data, *Geology*, **32**(9), 809.

Zhao, J., Yuan, X., Liu, H., Kumar, P., Pei, S., Kind, R., Zhang, Z., Teng, J., Ding, L., & Gao, X., 2010. The boundary between the Indian and Asian tectonic plates below Tibet, *Proc. Natl. Acad. Sci. U.S.A.*, **107**(25), 11229–11233.

Zubovich, A. V., Wang, X.-q., Scherba, Y. G., Schelochkov, G. G., Reilinger, R., Reigber, C., Mosienko, O. I., Molnar, P., Michajljow, W., Makarov, V. I., Li, J., Kuzikov, S. I., Herring, T. a., Hamburger, M. W., Hager, B. H., Dang, Y.-m., Bragin, V. D., & Beisenbaev, R. T., 2010. GPS velocity field for the Tien Shan and surrounding regions, *Tectonics*, **29**(6).

## APPENDIX

### *Parallel implementation of NA: NAplus*

NAplus is a revised C++ implementation of the parallel layout of the Neighbourhood algorithm (Rickwood & Sambridge, 2006; Sambridge, 1999a) that is optimized for (parallel) geodynamic forward models. A detailed description of NAplus is given in Baumann et al. (2014), but we shortly recap the main aspects and further developments here.

Geodynamic forward models can vary by an order of magnitude or more in terms of runtime depending on the largest viscosity contrast, especially for larger setups when iterative solvers are required. The runtime differences can be even larger if plasticity is part of the nonlinear rheology implementation as this requires additional inner iterations with a Picard or Newton-Raphson method (e.g. Kaus, 2010; Popov & Sobolev, 2008). For the parallel layout of the direct-search, it is thus crucial to avoid blocking and collective MPI communication mechanisms. This involves blocking sending operations (MPI_Send) as well as collective sending or reduction operations (such as MPI_Bcast, MPI_Gather, etc.). In our implementation we make use of a fully non-blocking communication scheme based on the functions MPI_Isend, MPI_Test and MPI_Recv, and a dynamic message-buffer, realised with C++ container objects. Moreover, NAplus offers a large freedom in which programming language the forward models can be implemented. Whereas in (Baumann et al., 2014) we linked parallel PETSc-supported (Balay et al., 2014) 3D forward models implemented in

standard C, we here link compiled MATLAB forward models with the inversion algorithm. Forward models implemented in Fortran have been tested as well.

*Sampling a high dimensional parameter space*

Solving a high dimensional integral by Monte Carlo sampling depends on how uniformly the (pseudo) random numbers are distributed. Typically, higher dimensional random deviates generated with pseudo random number generators form small clusters, which is why the convergence could be better if the samples would be distributed more evenly. The class of quasi random number generators that makes use of low-discrepancy series is an alternative that yields more homogeneously distributed samples. In general, the convergence rate is much faster when using quasi random deviates (e.g. Niederreiter, 1992; Morokoff & Caflisch, 1994; Caflisch, 1998). Also in terms of Monte Carlo inversion the usage of quasi random number generators can speed up the computation (Sambridge & Mosegaard, 2002). However, when it comes to higher dimensions, the sequences can correlate dramatically resulting in gaps and repetitive structures in the parameter space, although permuting the quasi-random sequences reduces the correlation effect (Caflisch, 1998). When (quasi-) random numbers are required to be present on multiple CPUs, the handling gets more complicated, because the random number seeds must be chosen more carefully.

As the sampling problem mainly affects the 'initial sampling' prior to the (main) NA sampling, we use a different strategy to keep minimum distances between the models of the initial sampling. Our strategy is to predefine a regular grid with a fixed amount of discrete values along each parameter axis. We then use the pseudo random generator after (L'ecuyer et al., 2002), which is made for parallel usage (appendix C) to randomly choose locations on the grid. By decreasing the number of possibilities per dimension, we can account for larger dimensions.

*Independent random numbers for parallel Monte Carlo based algorithms*

A crucial aspect when performing Monte Carlo type simulations or inversions is the reproducibility of the simulation or inversion results, as they depend on random numbers and their respective generators. In particular, precisely controlling the random number streams becomes important when the parallel simulation is split into several (sub-) jobs on a computer cluster. For us, the initial sampling is such a case. It can be subdivided into completely independent sub-tasks as it is a pure Monte Carlo sampling of the parameter space. Due to heterogeneous loading of the computer cluster, the queuing system of the HPC environment might privilege jobs with less CPUs as they better fit into the free capacities. Thus, we have to assign a random number seed to each sub-task to guarantee independent models. Another case is the restart of a simulation, during which we need to assure that the random number stream of the previous simulation does not overlap with the one of the restarted simulation.

We use the random number generator described in L'ecuyer et al. (2002), which is constructed in a way that a very long random number stream with a period of approximately $2^{191}$ is subdivided into subsequent streams, each with streamlength of $2^{127}$. Each stream in itself is subdivided into $2^{51}$ substreams with a periods of $2^{76}$. Every substream can be assigned to a new (restart-) invocation of the simulation, whereas the subsequent streams are distributed over the parallel processes of the simulation, e.g. all forward modelling groups. Our parallel MPI implementation of the random number generator is straight forward as it only depends on a single C++ class and associated library functions, which is provided with two source files (RngStream.cpp and RngStream.h) that are GNU licensed and can be downloaded from http://www.iro.umontreal.ca/~lecuyer.

A draft of our MPI parallel C++ implementation scheme is given as follows:

```
// Get rank and size for mpi communicator
MPI_Comm_rank(mpi_comm, &mpi_rank);
MPI_Comm_size(mpi_comm, &mpi_size);

// Create as many random number streams
// as mpi processes are available
prngstream = new RngStream[mpi_size];

// Advance the random number stream
// for each process as many times as required
// by the restart ID
// In our case the restart ID is saved in the
// restart file, so that the substream will auto-
// matically be advanced to the next substream
for(int k=0;k<restart_ID;k++)
{
  prngstream[mpi_rank].ResetNextSubstream();
}
// Retrieve random double between
// 0 and 1 (including 0 and 1) from stream
rnd = prngstream[mpi_rank].RandU01();

// Destroy the allocated RngStream array
delete [] prngstream;
```

*Benchmarking the parameter sampling in high dimensions*

To estimate how many forward models are required for a particular $n$ dimensional inverse problem, we employ the Rastrigin function for $n$ dimensional space (Mühlenbein et al., 1991) to perform a test case. The function is characterised by a high number of local minima and a global minimum at $f(\mathbf{x} = \mathbf{0}) = \mathbf{0}$ and is defined a as follows

$$f(\mathbf{x}) = 10\,n + \sum_{i=1}^{n} \left[x_i^2 - A\cos(2\pi x_i)\right], \tag{3.21}$$

where $\mathbf{x} = (x_1, \ldots, x_n)$ and $x_i \in [-5.12, 5.12]$. For each of the inverse problems described in this paper, we performed several tests, which are identical in terms of dimensions, but different in terms of tuning parameters of the NA (i.e. the resampling parameter $n_r$ and the number of initial models $n_i$) to estimate the optimal inversion parameters.

*Stopping criteria for forward models*

Statistical properties such as variance, kurtosis and skewness are often used to detect sudden transitions in dynamic systems in a broad variety of fields (e.g. Guttal & Jayaprakash, 2008; Scheffer et al., 2009). Especially the skewness, which is a measure of asymmetry of a distribution is a good indicator of regime shifts and is defined as follows

$$\gamma = \frac{E\,(x-\mu)^3}{\sigma^3}, \tag{3.22}$$

where $E$ is the expectation operator, and $\mu$ and $\sigma$ are the mean and the standard deviation of a random variable $x$ respectively. If we have a set of $n$ values, the sample skewness can be computed as

$$\gamma = \frac{\frac{1}{n}\sum_{i=1}^{n}(x_i-\bar{x})^3}{\left(\frac{1}{n-1}\sum_{i=1}^{n}(x_i-\bar{x})^2\right)^{3/2}}, \tag{3.23}$$

with $\bar{x}$ being the sample mean.

We found the skewness to be an interesting property to evaluate the state of the isostatic compensation of a geodynamic model and its dynamic topography. Randomly changing the parameters of a forward model within a certain tolerance will in many cases lead to a process of isostatic equilibration during the first stages of the forward model. As a consequence, large vertical velocities will appear, in particular if the viscous properties or the density properties of the asthenosphere and upper mantle are affected. One possibility to monitor the state of the isostatic equilibration is to compute an approximation of the dynamic topography from the pressure difference at the bottom of the domain, to which one refers to as depth of compensation (e.g. Panasyuk & Hager, 2000, although, these authors use a different code without a free surface). The pressure deviation of the average pressure,

$$\Delta P\,(x)|_{z=z_{\text{comp.}}} = P\,(x)|_{z=z_{\text{comp.}}} - \bar{P}\big|_{z=z_{\text{comp.}}} \tag{3.24}$$

results in a approximated dynamic topography

$$T_{\text{dynamic}}\,(x) = \frac{\Delta P_{\text{c.d.}}\,(x)}{\bar{\rho}\,(x)\,g}, \tag{3.25}$$

where $\bar{\rho}\,(x)$ is the average density of the model.

For a model in perfect isostatic balance, the pressure at the compensation depth should not have any lateral variations in the absence of dynamic contributions (Panasyuk & Hager, 2000). As a consequence, the dynamic topography of

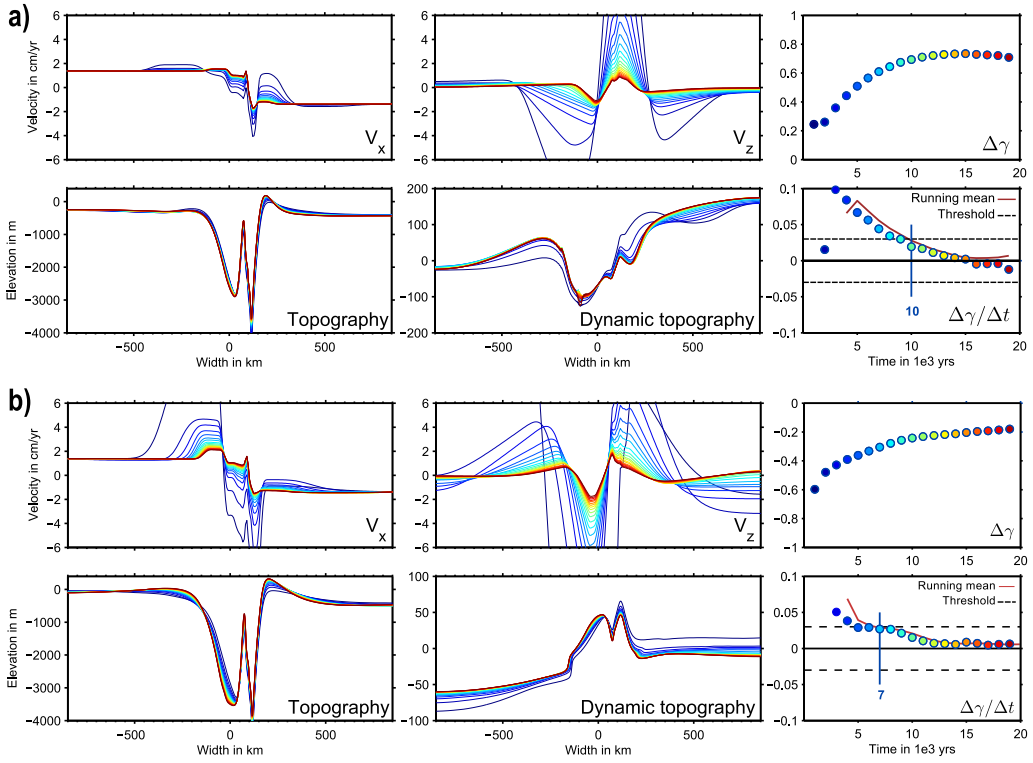


Figure 3.15: Example of monitoring the surface signals after **a)** decreasing the power-law exponent of the crust by a factor of $\Delta n = 2$, which corresponds to a change of 50% of the parameter range. **b)** Decreasing the activation volume of the asthenosphere by a factor of $\Delta V = 12.5 \cdot 10^{-6}\ m^3/mol$, which corresponds to a change of 50% of the parameter range. The color indicates the timestep after the change. We measure the skewness $\gamma$ (dimensionless number) of the dynamic topography, which is a good proxy of the state of isostatic equilibration. $\gamma$ converges very small constant rate of change, which we interpret as dynamic change only, as soon the isostatic equilibration of the model is being completed. Consequently, the change in skewness converges towards very small but constant value that is characteristic for the current dynamic regime. From empirical tests, we conclude that isostatic equilibration is completed as soon as the running average of three consecutive timesteps gives $\left({}^{\Delta\gamma}/_{\Delta t}\right) < 0.03\ \left[1/10^3 \text{yrs}\right]$.

the model is flat and its skewness (asymmetry) is zero. However, for a subduction scenario we do have dynamic effects, such that the dynamic topography is not flat after isostatic equilibration. The asymmetric shape of the dynamic topography can be characterised with a constant value of skewness. An advantage of the skewness over the variance is that the skewness is non-dimensional and does not depend on the amplitude of the signal.

Typically, the forward models with randomly modified input parameters start with a lateral imbalance in density or viscosity or topography resulting in a lateral pressure difference at the compensation depth and a motion of isostatic compensation. The question is when to stop the simulation to achieve characteristic surface observations that are not biased by signals that originate from isostatic equilibration of the model. During the isostatic equilibration

there is a strong change in dynamic topography, which also means that the skewness of the isostatic topography changes remarkably. After isostatic equilibration, the dynamic topography stays in a quasi equilibrated state of constant skewness.This means that the change in skewness is a characteristic value that we are able to monitor. The proxy can also be extended to 3D models, as the skewness can also be computed for 2D surfaces.

*Creating a reference model of intra-oceanic subduction*

To create a reference model for the synthetic inversion tests, we perform a full forward simulation of intra-oceanic subduction, starting with an initial model geometry that is 2000 km wide and 660 km deep (see Fig. 3.16a). The computational domain is discretised with linear $Q_1P_0$ elements, which are quadrilateral finite elements. We use 209 by 69 elements with a horizontal and vertical mesh refinement towards the center and the top of the model respectively. Moreover, we implement constant strain rate and shear stress free boundary conditions at the sides and bottom of the model, but have a free surface condition at the top boundary. In addition, a constant background strain rate ($\dot{\epsilon}_{BG} = -10^{-15}$ Pa s) is applied to laterally compress the model on a continuous basis and to stimulate the subduction process of oceanic plates. The thermal boundary conditions are flux-free at the lateral sides and isothermal at the top and lower boundary with 20 °C and 1350 °C respectively. The initial temperature distribution has different lithospheric ages at the left ($t_{age} = 30$ Myrs) and right ($t_{age} = 50$ Myrs) of the weak zone, which are given by a half-space cooling model (e.g. Turcotte & Schubert, 2002):

$$T(z) = (T_s - T_m) \cdot \operatorname{erfc}\left(\frac{z}{2 \cdot \sqrt{\kappa \cdot t_{age}}}\right) + T_m, \tag{3.26}$$

where $T_m$, $T_s$ and $\kappa = 10^{-6}$ m²/s are mantle, surface temperature and thermal diffusivity respectively.

The geometry of the initial model setup is illustrated in Fig. 3.16a, where the lithosphere consists of an oceanic upper crust, a lower crust - modelled as serpentinized Harzburgite - and a lithospheric mantle. To initialize the subduction process, we implemented a trapezoidal weak zone that is thinning with increasing depth. A summary of all model parameters is given in Table 3.1. Fig. 3.16b and c show the forward evolution of the subduction process, where the largest strainrates occur within the subduction channel. We stop the simulation at approximately 8.6 Myrs (Fig. 3.16d) and take the geometry and the temperature structure of this timestep as a reference model of the synthetic inversions that are described in sections 3.3.2 and 3.3.3.

*A step-wise linear approximation of the geotherm*

As oceanic lithosphere is characterised by a conductive geothermal gradient and the asthenosphere is dominantly described by an adiabatic geothermal gradient, a stepwise linear approximation for lithosphere and asthenosphere

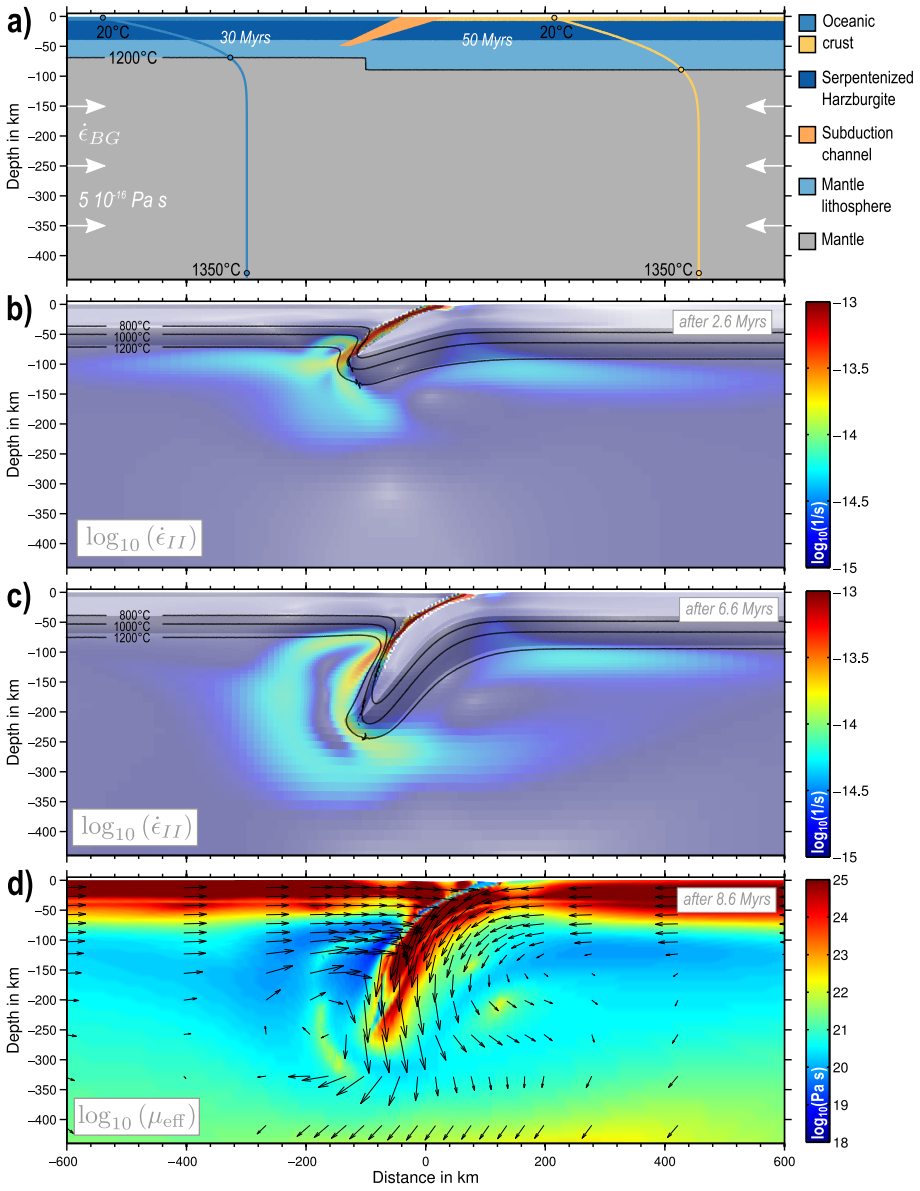


Figure 3.16: Synthetic forward modelling of oceanic subduction. **a)** The initial model geometry consists of an oceanic crust, a serpentinized harzburgite layer, a mantle lithosphere and a mantle. Moreover, a subduction channel is included to initiate subduction. The initial temperature model is derived for two different lithospheric ages of 30 Myrs and 50 Myrs. The geotherms derived from a lithospheric cooling model are shown within the limits of surface (20 °C) and mantle temperature (1350 °C). The mantle lithosphere is limited by the 1200 °C isotherm. **b)** & **c)** Forward evolution after 2.6 Myrs and 6.6 Myrs. Areas of large deformation are indicated by a large strain rate, which is overlaid on top of the lithology markers. **d)** The forward simulation is stopped at 8.6 Myrs. This time step is equivalent to the reference model that is used within the inversion process. Velocity field and effective viscosity illustrate a strong lithosphere with little internal deformation, but a characteristic nonlinear viscosity pattern in the mantle, as well as areas dominated by plastic deformation in the bending zone of the subducting plate.

is a reasonable first order approximation. However, the lithospheric geotherm usually behaves more nonlinear, which is why we prefer an approximation with at least three segments for the crust, mantle lithosphere and asthenosphere. In general a linear segment of a step-wise linear approximation of a geotherm can be described as

$$T(z) = \gamma_i \cdot z + T_{0,i}, \tag{3.27}$$

where $\gamma_i$ is the geothermal gradient, and $T_{0,i}$ the potential temperature of that segment. Due to the fact that consecutive linear segments must intersect at each interface, we can couple their expressions with the following condition:

$$\gamma_i = \frac{T_{0,i+1} - T_{0,i}}{z_{i+1}} + \gamma_{i+1}. \tag{3.28}$$

If we consider a system composed of three layers such as illustrated in Fig. 3.17 with crust, mantle lithosphere and upper mantle, we can construct a coupled system of three equations based on (eq. 3.27) and (eq. 3.28):

$$\gamma_0 = \frac{T_{0,1} - T_{0,0}}{z_1} + \gamma_1 \tag{3.29}$$

$$\gamma_1 = \frac{T_{0,2} - T_{0,1}}{z_2} + \gamma_2 \tag{3.30}$$

$$T(z_1) = T_{0,1} + \gamma_1 \cdot z_1. \tag{3.31}$$

In these equations, there are a number of variables that are well known to be stable or that at least have a relatively small variance and can be assumed to be known from a priori. Obviously, this is the surface temperature $T_{0,0}$, but also the potential mantle temperature $T_{0,2}$ and the adiabatic geothermal gradient $\gamma_2$. In addition, the Moho depth ($z_1$) is usually a well constrained parameter too. Following this approach, the step-wise linear geotherm of the three-layered system crust – mantle lithosphere – upper mantle can be parameterised with only two variables. We choose (i) the temperature at the Moho ($T(z_1)$) and (ii) the depth of the lithosphere asthenosphere boundary ($z_2$) to be free parameters and solve the system of equations (eq. 3.29-3.31) for the geothermal gradients of crust and mantle lithosphere as well as for the potential temperature of the mantle lithosphere to fully define the geotherm:

$$\gamma_1 = \frac{T_{0,2} - T(z_1) + z_2\gamma_2}{z_2 - z_1} \tag{3.32}$$

$$T_{0,1} = T(z_1) - \gamma_1 \cdot z_1 \tag{3.33}$$

$$\gamma_0 = \frac{T_{0,1} - T_{0,0}}{z_1} + \gamma_1. \tag{3.34}$$

In principle, this parameterisation is very general. Instead of using the Moho as an internal interface, we can also use the upper crust/lower crust boundary as internal separator if this better fits the model geometry, as is the case in our application in section 3.4.

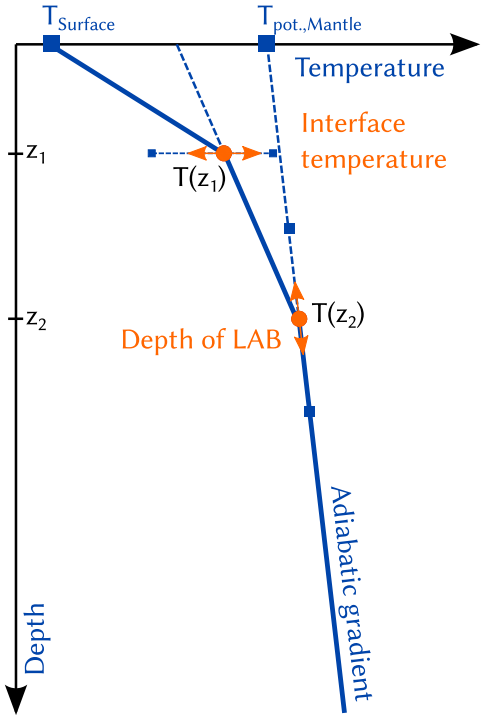


Figure 3.17: Step-wise linear approximation of a geotherm. For a given surface temperature, the potential mantle temperature, a known adiabatic gradient within the mantle, and an interface depth (upper crust/lower crust boundary or Moho), the parametrisation is only controlled by two parameters, the depth of the lithosphere asthenosphere boundary (LAB) and the temperature at the interface (Intermediate crustal or Moho temperature.

*Posterior distributions*

The posterior distributions of the synthetic and the India-Asia applications are given in terms of 1D and 2D marginal distributions. Results are illustrated with a high degree of detail. The reader is therefore referred to the electronic version of the work for an enlarged view.

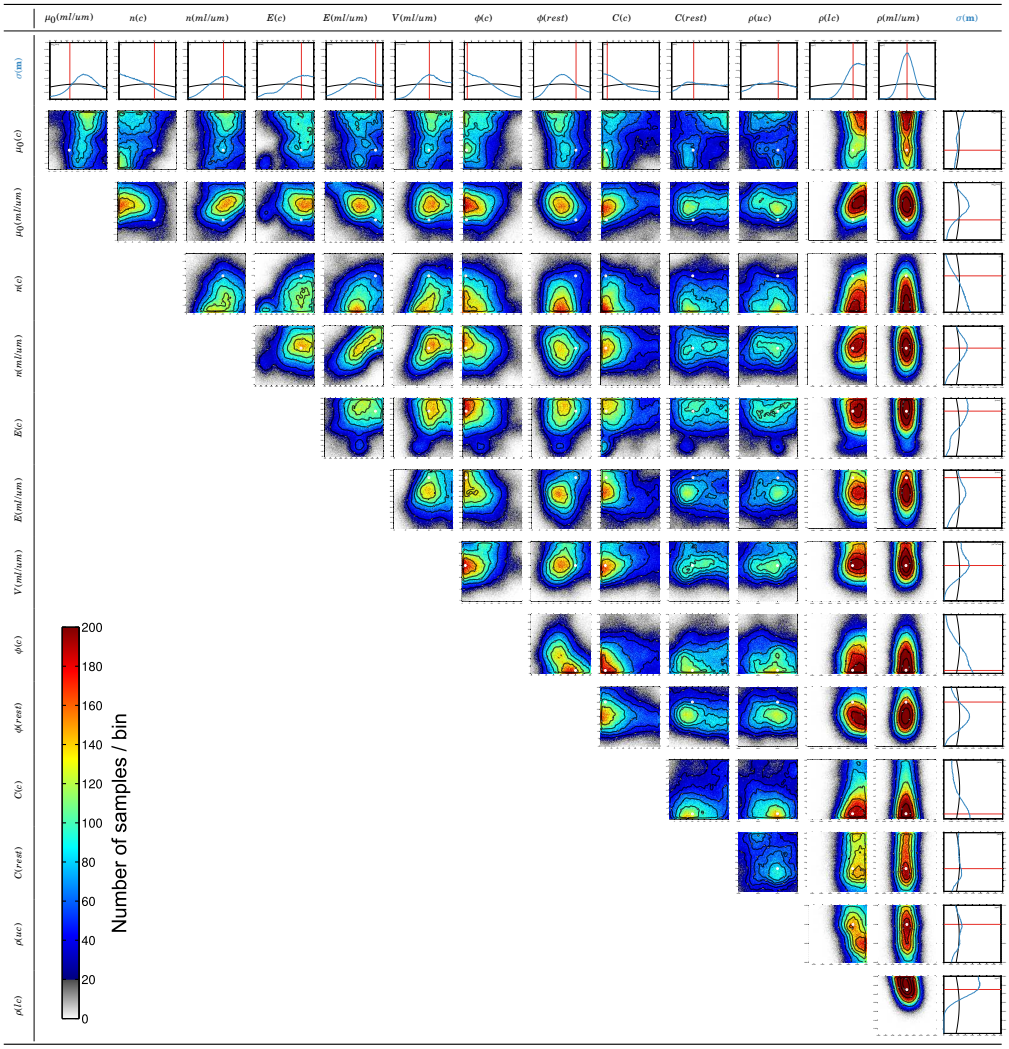


Figure 3.18: Geodynamic inversion results of the synthetic oceanic subduction scenario with full temperature knowledge described in section 3.3.2. Results are given in terms of marginal distributions of the posterior probability. Red lines and red markers show true model values.

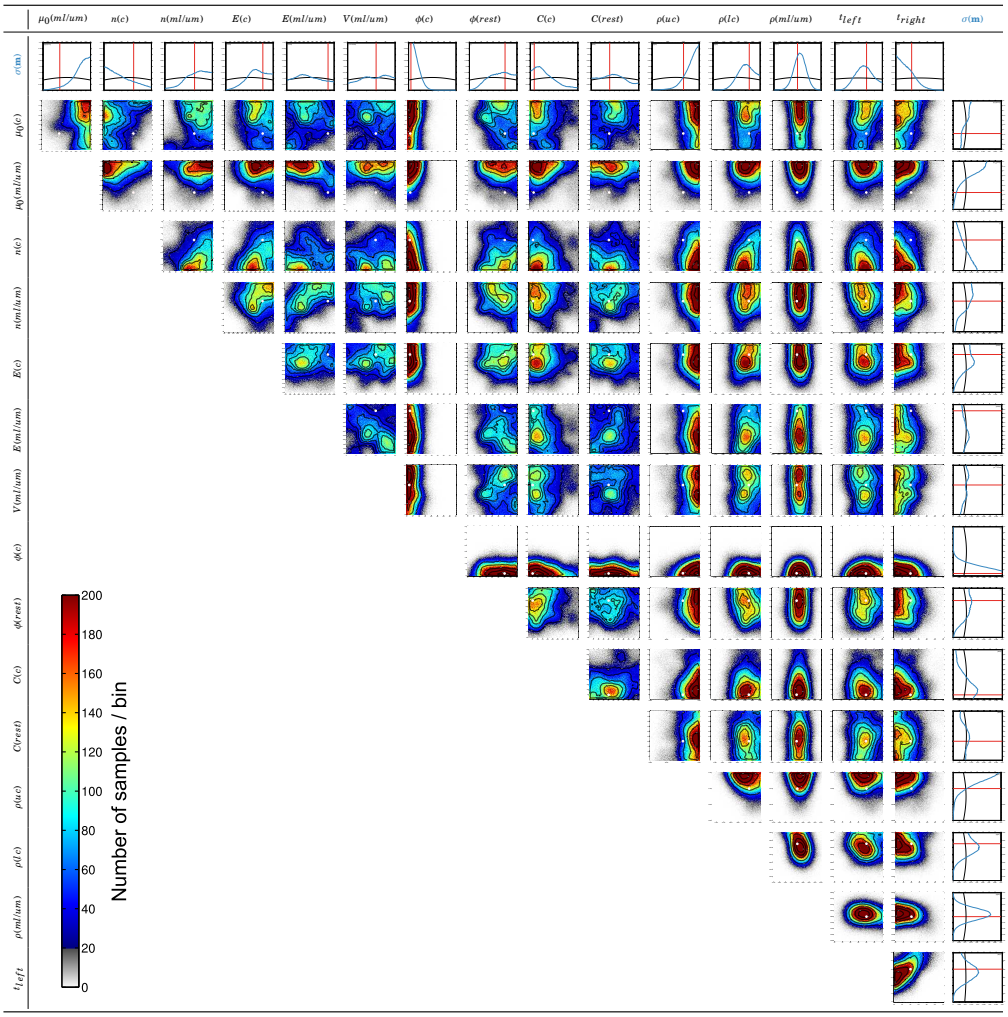


Figure 3.19: Geodynamic inversion results of the synthetic oceanic subduction scenario with parameterised temperature (section 3.3.3). Indications are similar to those in Fig. 3.18.

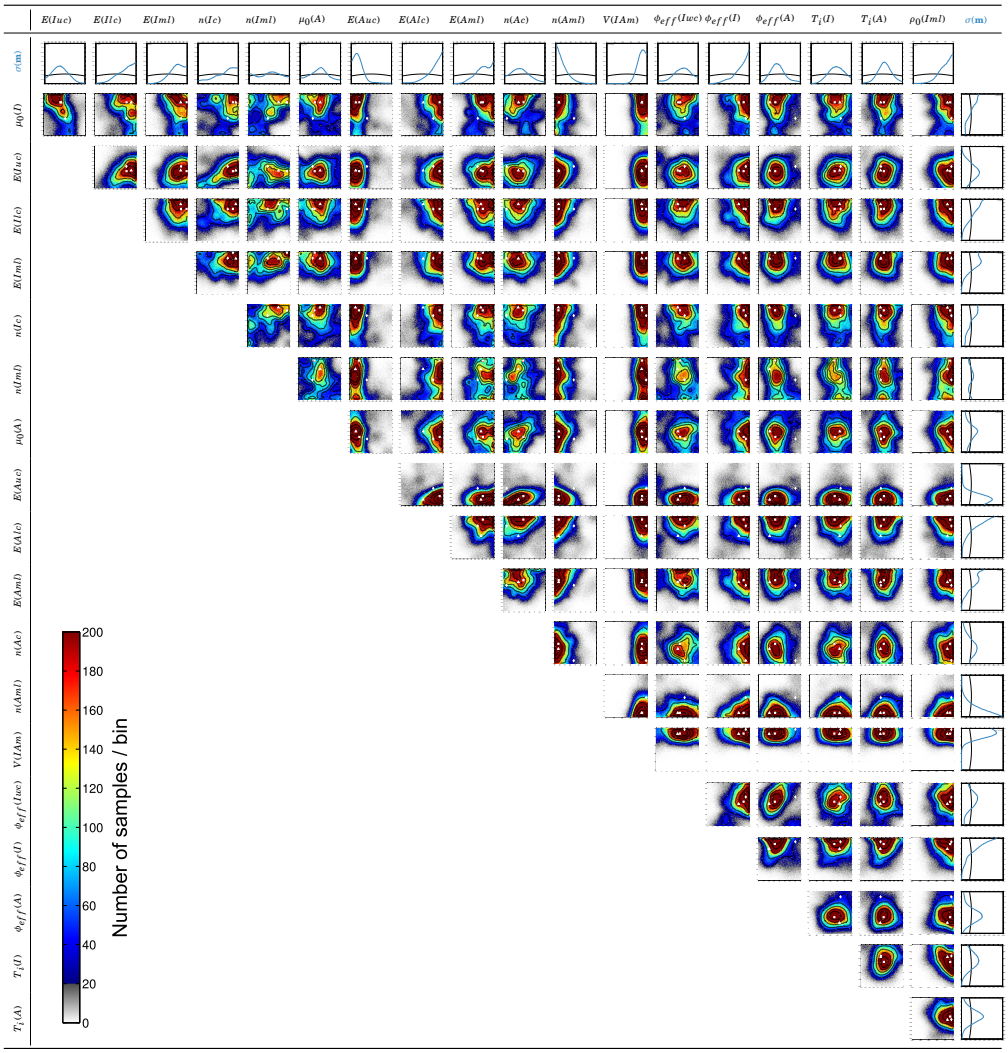


Figure 3.20: Geodynamic inversion results of the India-Asia collision scenario (section 3.4). Indications correspond to those given in Fig. 3.14.

# 4

# APPRAISAL OF GEODYNAMIC INVERSION RESULTS: A DATA MINING APPROACH

**This chapter has been submitted:**
Baumann, T. S. (submitted to Geophysical Journal International). Appraisal of geodynamic inversion results: A data mining approach.

**Abstract**

Bayesian-type inversions require many thousands or even millions of forward models, depending on how non-linear or non-unique the inverse problem is, and how many unknowns are involved. The result of such a probabilistic inversion is not a single 'best-fit' model, but rather a probability distribution that is represented by the entire model ensemble. Often, a geophysical inverse problem is non-unique, and the model distribution forms clusters of similar models that represent the observations equally well. In these cases, we would like to visually see the characteristic properties within these clusters of models, for example similar material properties, which can be different from the inversion parameters. However, even for a moderate number of model parameters, a manual appraisal for such a large number of models is not feasible, which poses the question whether it is possible to extract end-member models that represent each of the best fit regions including their uncertainties.

Here, I show how a machine learning tool can be used to determine end-member models, including their uncertainties, from a complete model ensemble that represents a posterior probability distribution. The model ensemble used here, results from a non-linear geodynamic inverse problem, where rheological properties of the lithosphere are constrained from multiple geophysical observations. It is demonstrated that by taking vertical cross-sections through the viscosity structure of each of the models, the entire model ensemble can be classified into 4 end-member model categories that have a similar viscosity structure. These classification results are helpful to explore the non-uniqueness of the inverse problem and can be used to compute typical data fits for each of the end member models. Conversely, these insights also reveal how new observational constraints could reduce the non-uniqueness. As the method is not limited to geodynamic applications, a generalised MATLAB code is provided to perform the appraisal analysis.

## INTRODUCTION

Inverse problems are usually separated into two sub tasks, (i) the estimation task, where (optimal) model parameters are estimated from the observed data,

and (ii) an appraisal part, where model uncertainties and properties are determined (e.g. Snieder & Trampert, 1999). For non-linear inverse problems, especially the latter task is challenging as no general theory exist to describe the model uncertainties (Snieder, 1999). As an numerical alternative, the class of Monte Carlo and direct-search methods is widely used to tackle the estimation part of non-linear inverse problems (e.g. Sambridge & Mosegaard, 2002). Here, the misfit is computed for a large number of forward models, which is referred to as a 'model ensemble'. In terms of appraising the model ensemble, uncertainties can be estimated in the framework of Bayesian statistics, where the full result is the posterior distribution (e.g. Tarantola, 2005). Provided that the distribution of acceptable models has a single dominant maximum, linearised concepts can be applied and Bayesian measures, such as approximated model covariance and resolution matrix can be computed (Sambridge, 1999b). Yet, posterior distributions are generally not similar to multivariate Gaussian distributions, i.e. the inversion results are non-unique, such that the posterior distribution rather resembles a conglomerate of disjoint distributions that eventually have smooth transitions. The question is, what are the discriminating properties of all acceptable models within the ensemble? And, moreover, is it possible to identify end-member representatives that help to better understand the non-uniqueness of the inversion result?

In this study, a geodynamic model ensemble (Baumann & Kaus, 2015) is used as case example to address the questions above. The previous study addressed the India-Asia collision, and performed about 1.9 million forward models to invert different geophysical surface observations to estimate non-linear rheological properties of the lithosphere. The model ensemble has typical non-linear and non-unique characteristics, such that many models with different effective viscosity structures represent the surface observations equally well. As manually discriminating these models is not feasible, the ensemble is examined with a neural network approach. Neural networks belong to the class of machine learning algorithms, which is associated with the term 'data-mining' that became increasingly popular during the last two decades when growing computer power started to produce large amounts of data, from which useful information had to be extracted into a human-usable format (e.g. Witten & Frank, 2005). In fact, this also applies to model ensembles of Monte Carlo inversions, which contain a diversity of non-obvious properties especially for high parameter dimensions. Usually one differentiates between 'supervised' and 'unsupervised' machine learning, where the first term denotes that the algorithm requires training data that comprises labelled examples similar to the target data to detect. On the other hand, 'unsupervised' algorithms can be used without a priori training and are used to discover groups of similar data, i.e. clustering purposes (e.g. Bishop, 2006). One of them is the self-organizing map algorithm by Kohonen (2001). A major advantage of SOMs is that they can be used to visualize high-dimensional data in two dimensions (Vesanto, 1999). This makes it attractive to a wide range of applications, for example in finance (e.g. Deboeck & Kohonen, 1998), genome analysis (e.g. Törönen et al., 1999), but also in industry, linguistics, bioinformatics and natural sciences (Kohonen, 2013). Liu

& Weisberg (2011) give an overview of applications in meteorology and oceanography. Applications in geosciences are often related to signal detection in seismology and volcanic tremor analysis (e.g. Köhler et al., 2009, 2010).

The paper is composed as follows. Basic principles of SOMs are shortly introduced in the following section, which also contains methodological details on an additional clustering analysis to classify the data into major categories. As the selection of characteristic model properties differs between each application, it is a crucial part of the procedure and is discussed in detail, before examining and discussing the results of the study. A short coding example that enables the reader to easily repeat the SOM analysis is enclosed in the appendix of this paper.

## METHOD

### *Self-organizing map*

The Self-organizing map (SOM) belongs to the group of unsupervised learning methods. Its original implementation resembles a gradient-decent algorithm (Kohonen, 2013) and vector quantisation algorithms (Vesanto et al., 2000; Gray, 1984) such as k-means (e.g. Jain & Dubes, 1988). The SOM consists of a set of $M_{SOM}$ neurons that are organised on a regular, low dimensional (typically 2D) grid in a N–dimensional space, where N denotes to the dimension of the input data of size $M_{data}$. Both, data ($\mathbf{x}_i$) and neurons ($\mathbf{m}_j$) are described through N–dimensional Euclidean vectors, where $\mathbf{m}_j$ are usually referred to as 'prototype vectors' with $i = 1, \dots M_{SOM}$. The total number of neurons and the aspect ratio of the SOM are usually not known in advance, but are determined during the initialisation process in a trial and error manner. According to a rule of thumb, the size is about $M_{SOM} \approx 50 \cdot M_{data}$, and the aspect ratio roughly corresponds to the relation of the two largest principal components of the input data (Kohonen, 2013).

The SOM learns the topology (characteristics) of the data in an iterative process referred to as 'training', during which the SOM behaves similar to an elastic net that folds onto 'clouds' formed by the input data (Vesanto & Alhoniemi, 2000). In this study, we make use of the MATLAB SOM toolbox by Vesanto et al. (2000) and the general procedure can be described as follows.

After an initialisation of the prototype vectors ($\mathbf{m}_i$), the 'training' starts with the selection of a random data sample ($\mathbf{x}$) and Euclidean distances between this sample and all prototype vectors are computed. The prototype vector with the minimal Euclidean distance ($\mathbf{m}_c$, i.e. $\|\mathbf{x} - \mathbf{m}_c\| = \min_i\{\|\mathbf{x} - \mathbf{m}_i\|\}$) is determined, which is also referred to as the best-matching unit (BMU). The BMU and neighbouring prototype vectors move towards the current data sample as illustrated in Fig. 4.1, and the adapted SOM after one time step is given as follows:

$$\mathbf{m}_i(t+1) = \mathbf{m}_i(t) + h_{ci}(t)\left[\mathbf{x} - \mathbf{m}_i(t)\right]. \tag{4.1}$$

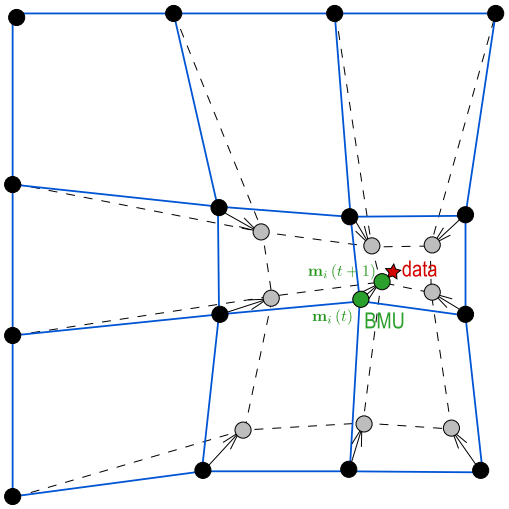


Figure 4.1: Learning process of the Self-Organizing Map after Vesanto et al. (2000). The 'best matching unit' (green), i.e. the neuron closest to the data sample, and neighbouring neurons move towards the current sample vector (red) according to eq. (4.2). Grey nodes corresponds to the adjusted SOM after a training step $t$.

$h_{ci}(t)$ denotes the neighbourhood function centred at the BMU, which defines the rate the neighbouring node locations are modified. Typically, $h_{ci}(t)$ is defined as Gaussian,

$$h_{cj}(t) = \alpha(t) \exp\left(-\frac{d_{c,i}^2}{2\sigma^2(t)}\right), \tag{4.2}$$

where $d_{c,i}$ denotes the distance between nodes $\mathbf{m}_c$ and $\mathbf{m}_i$. $\alpha(t)$ and $\sigma(t)$ are monotonically scalar functions of $t$ (Kohonen, 2013).

*Additional clustering of the SOM*

The SOM analysis is a clustering process itself, as the feature vectors are associated to their nearest neighbour prototype vectors of the SOM. How many groups or clusters exist depends on the number of nodes of the SOM. However, distances between adjacent prototype vectors are not necessarily taken into account. Therefore, similar nodes of the SOM can be grouped through additional clustering, which can be applied after the SOM learning process (Vesanto & Alhoniemi, 2000). As described in Vesanto & Alhoniemi (2000), *k*-means clustering (e.g. Jain & Dubes, 1988) is a suitable clustering approach in this respect. A disadvantage is, however, that *k*-means assumes spherical clusters and that the number of clusters has to be known a priori. A workaround is to compute a validity index. A possibility is to determine a ratio between the sum of intra-cluster distances and inter-cluster distances. This measure is referred to as Davies-Bouldin index (DB-index, Davies & Bouldin, 1979) and can be used to quantify how well a specific number of clusters is suited for the distribution of

prototype vectors. In terms of evaluating the *k*-means clustering, the DB-index minimises for an optimal number of spherical clusters.

One of the great benefits of using the SOM is the ability to visualise the high-dimensional properties of the input space directly on the SOM. This opens up the possibility of cross-validating the clustering results by visual inspection.

## DATA SET

The model ensemble that is examined in this study results from an earlier study of non-linear geodynamic inversion (Baumann & Kaus, 2015). Geodynamic inversion is a technique to constrain rheological properties of the lithosphere based on Stokes-flow models by jointly inverting geophysical surface observations. A detailed description of the technique is given in Baumann & Kaus (2015) and Baumann et al. (2014), but the key aspects are shortly recapped in this section. Moreover, the model ensemble is characterised by a set of 19 inversion parameters, but each geodynamic model provides a full range of characteristic physical properties that are linked with the inversion parameters. For example, solution variables, such as the velocity, stress or strainrate fields, and effective material properties, such as viscosity structure can be used as features to discriminate the model ensemble.

### *Geodynamic inversion of the India-Asia collision system*

In Baumann et al. (2014) and Baumann & Kaus (2015), we mainly adopted the Bayesian inversion approach of Sambridge (1999a) and Sambridge (1999b). This is a two-step procedure that is designed with (i) a direct-search method to explore the parameter space and to minimise a objective function (Sambridge, 1999a), and (ii) an appraisal method to evaluate Bayesian integrals from the direct-search model ensemble (Sambridge, 1999b). During the appraisal part, a Markov chain Monte Carlo (MCMC) method is employed to perform an 'importance-sampling' of the original model ensemble, which results in an approximate posterior distribution. The appraisal method relies on the so-called 'Neighbourhood approximation', which denotes that the objective function is interpolated with a nearest neighbour interpolation. For this reason, each MCMC-sample is automatically associated with one of the direct-search forward models, implying that the MCMC implicitly selects and weights the forward models of the direct-search part. The importance sampling with MCMC can therefore be seen as a selection process of acceptable forward models with respect to their model error.

The case study of Baumann & Kaus (2015) corresponds to a SW-NE cross section across the India-Asia collision system that transects the Himalayas, the Tibetan plateau and the Tarim region. In Fig. 4.2a, the model geometry is illustrated that was constructed from several seismological data sets and calibrated with Bouguer anomalies. We jointly inverted four kinds of geophysical observations, namely gravity anomalies, topography as well as horizontal and vertical surface velocity data, to constrain 19 unknown model parameters. These para-

meters describe the full non-linear model rheology, including the parameterised temperature and density structure of the model. Fig. 4.2b exemplifies the marginal posterior distribution of two inversion parameters, which indicates the non-unique character of the inverse problem with two distinct maxima. The model ensemble of the direct-search process contains about 1.9 million forward models. However, the importance sampling with the MCMC method revealed that only 815 of these forward models actually contribute to the posterior distribution. This means that the MCMC importance sampling works as efficient pre-selector of acceptable models in terms that they fit the surface observations within the uncertainty range. Yet, this set of 815 forward models is still too large for a manual evaluation and the question is: What are the representative model characteristics to classify all models into end-member categories?

*Constructing feature vectors from viscosity profiles*

A crucial part of the unsupervised analysis with the SOM is the construction of the input data set. The input data is composed of so-called 'feature-vectors' that store the extracted model characteristics. In general it is possible to construct feature vectors from very different data if a suitable normalisation is applied to the data before the SOM-learning process. However, selecting characteristic model features is essential for the SOM to discriminate models successfully, and it is in particular important to avoid correlated features (e.g. Kohonen, 2013; Köhler et al., 2009). This is the main reason to not use inversion parameters directly and to rather extract invariant representatives of the effective viscosity structure of the models. Other model data, such as the stress state, the density structure or the strain rate pattern can possibly be used to construct feature vectors as well, but the effective viscosity structure is also known to be most significant in geodynamic modelling as it directly affects the dynamics of the lithosphere (e.g. Baumann & Kaus, 2015). To avoid scaling problems, only markers of the viscosity structure are incorporated into the feature vectors, such that normalisation in addition to the standard $\log_{10}$-scaling of the viscosity is not required.

Features vectors for SOMs can not only consist of very different data, but can also have a very high dimension. Even images can be transformed into vectors to be analysed with SOMs. Of course, one has to pay attention that adding further components to the feature vector also increases the information content of the vector. High resolution images must not be necessary yield improved results because of a possibly higher degree of correlation (e.g. Kohonen, 2013).

For this application, the viscosity structure is partly prescribed by the geometric a priori assumptions of the geodynamic inversion, therefore the model changes laterally only very gradually. On the other hand, the power-law character of the effective viscosity can rapidly change its behaviour in vertical direction. The feature vector is therefore constructed from three viscosity profiles at characteristic locations along the cross-section (Fig. 4.2c). Profiles are taken at $x = -500\,\mathrm{km}$, $x = 200\,\mathrm{km}$ and $x = 1000\,\mathrm{km}$ for the Indian shield, Tibet, and the Tarim region respectively. In the vertical direction, the profiles are limited to a

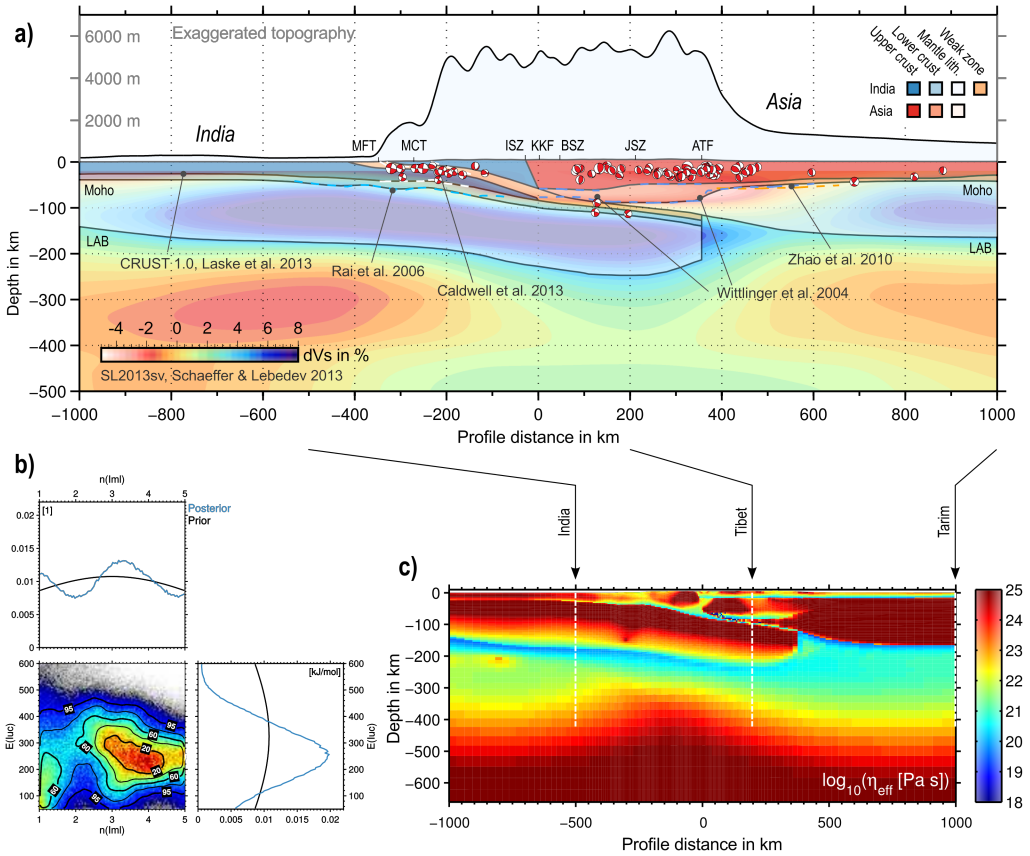


Figure 4.2: **a)** Cross section of the India Asia collision system, which is the a priori model geometry used for the geodynamic inversion. The model is constructed of many different seismological data sources (Caldwell et al., 2013; Dziewonski et al., 1981; Laske et al., 2013; Rai et al., 2006; Schaeffer & Lebedev, 2013; Wittlinger et al., 2004; Zhao et al., 2010). **b)** Marginal posterior distributions for particular parameter combination. The distribution is the result of an MCMC approach, where steps of random walks are referred to as samples. Each sample is associated to a forward model of the previous direct-search. The triangle indicates an example forward model illustrated in **c)**. Here, the model is shown in terms of viscosity structure. We use the characteristic viscosity structure to construct a feature vector of this model. It is created from three viscosity profiles at the indicated locations for India, Tibet and the Tarim regions respectively.

depth of $z \approx 400\,\mathrm{km}$ to not bias the feature vector with many viscosity properties of the upper mantle in relation to the lithosphere. Each viscosity profile has 150 viscosity values, such that the feature vector space has 450 dimensions dimensions.

## RESULTS

The SOM analysis is fully conducted with the MATLAB library provided here `http://www.cis.hut.fi/somtoolbox/` (Vesanto et al., 2000). All single steps

that are performed here can be retraced with the exemplifying MATLAB script that is provided in appendix A.

The SOM is organised on a hexagonal grid and the input data contains 815 vectors with 450 components (features) each, such that the SOM-initialisation results in a map size of $7 \times 21$ neurons. After the training process, the results can be visualized in many ways (Vesanto, 1999). Here, the results are given in Fig. 4.3. The histogram perspective in Fig. 4.3a is an obvious way of illustrating the SOM classification results. The circular markers represent the SOM-nodes (neurons) and the size of the hexagonal shapes in the background indicate the number of models (feature vectors) that are associated with each node. Colours represent the classification result that is discussed later. Independent of the colouring and based on the number of associated models, it is obvious that separated nodes exist that are offset from their adjacent nodes. An effective way of presenting these offsets of trained SOM is the unified distance matrix (Fig. 4.3b, Ultsch, 1993) that shows distance between adjacent neurons. Here, additional hexagonal fields are introduced between the nodes. Their colouring is scaled according to inter-node distances, where cold and warm colors represent small and large distances, respectively. The colouring of the nodal fields corresponds to the average distance to all adjacent nodes. The representation reveals two strictly separated parts at the left edge of the map that correlates with the histogram representation. Likewise, but less pronounced, another horizontally oriented separation is visible from the center up to the right edge of the map. The DB-index does not clearly prefer a distinct unique number of clusters, but suggests a good validation with 3-6, or 11 clusters. In fact, the lowest and second lowest DB-indices are determined for 3 and 6 clusters, respectively. Because the visual inspection of the U-matrix suggests 4 clusters, but disagrees with the corresponding $k$-means clusters, a partitioning in favour of 6 clusters is preferred, where the cluster 4-6 are manually summarised into cluster 4. This completely agrees with the inspection of the classified feature vectors in the following section.

*Classified forward models*

So far, the classification result was only shown on the SOM. In Fig. 4.4, the feature vectors are illustrated in a class-wise manner, where each column corresponds to a feature vector of three concatenated viscosity profiles. The colours and numbers in the top bar indicate the class affiliation and corresponding $k$-means clusters, respectively.

The main features of the classified groups are as follows. Class 1 (red) has a characteristic power-law viscosity behaviour within the Asian crust, and a strong upper and weak lower crust in Tibet, whereas the Indian mantle lithosphere is very strong and has no viscosity reduction with temperature. Class 2 (yellow) is related to one of the most stable clusters, which remains constant for various $k$-means clusterings of different total numbers of clusters. The reason for this is a weak Asian mantle lithosphere, which affects many components of the feature vectors. The main properties of the third class (light blue) are a

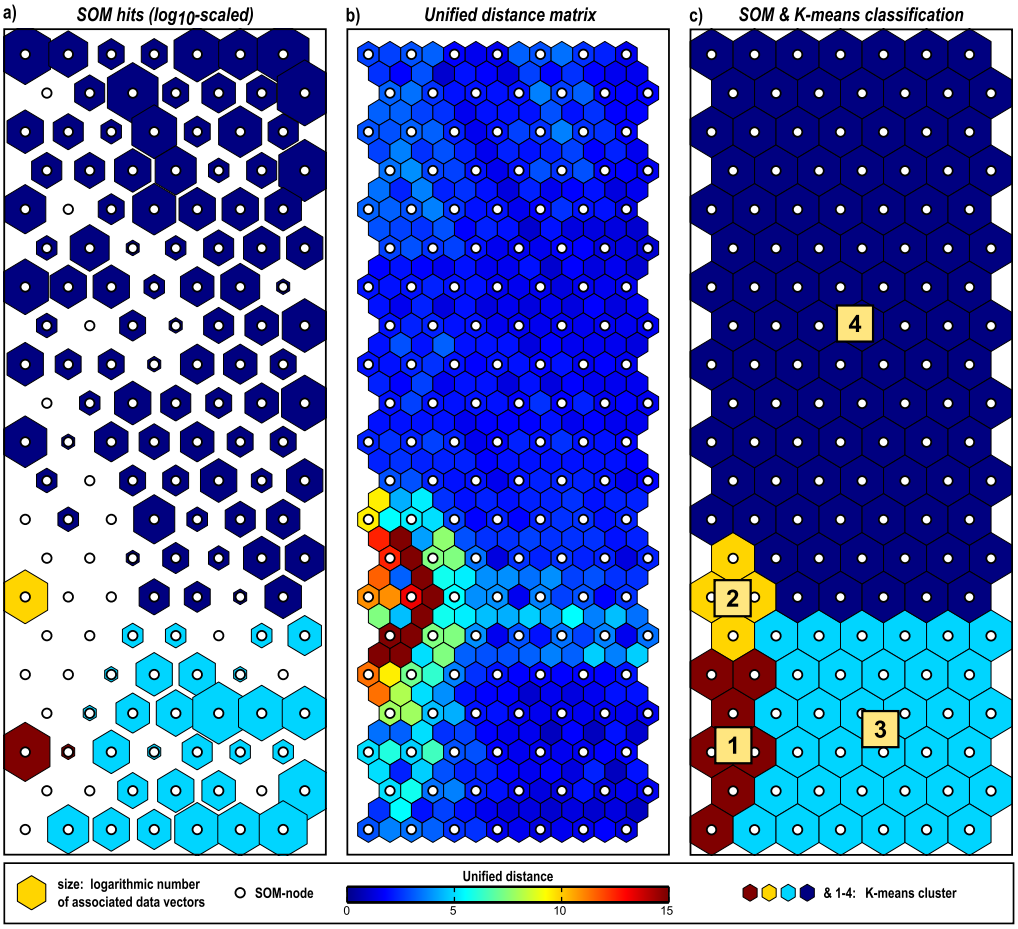


Figure 4.3: 2D visualisations of the SOM. Circular nodes indicate neurons that are arranged such that each neuron has six neighbours if not located at the boundary. **a)** SOM histogram representation shows the amount of data vectors associated with each neuron. The colouring indicates the classification result (c). The representation illustrates 'gaps' within the SOM (nodes that are not related to any data vectors), which indicates a distortion of the map and outlines cluster boundaries. This is related to **b)**, the unified distance matrix (U-matrix), which indicates inter-nodal distances. Warm colors represent large distances, and cold colors indicate short distances. Shapes that coincide with nodes correspond to averaged distances to neighbouring nodes. **c)** Additional partitive clustering (*k*-means) of SOM prototype vectors yields the final classification result, where the total number of 4 clusters is selected with respect to the U-matrix visualisation and a quantitative validation criterion (DB-index).

very strong Asian and Indian mantle lithosphere, and a rather weak crust of Tibet. The viscosity profile of the Tarim region of this class is very similar to its correspondent parts of the class 4-6 (dark blue). The classes 4 to 6 are, however, different in terms of Indian mantle lithosphere. They all show a relatively strong power-law behaviour, which supports the argument of summarising them into a single class 4, similar to what is suggested by the visual inspection of the U-matrix.

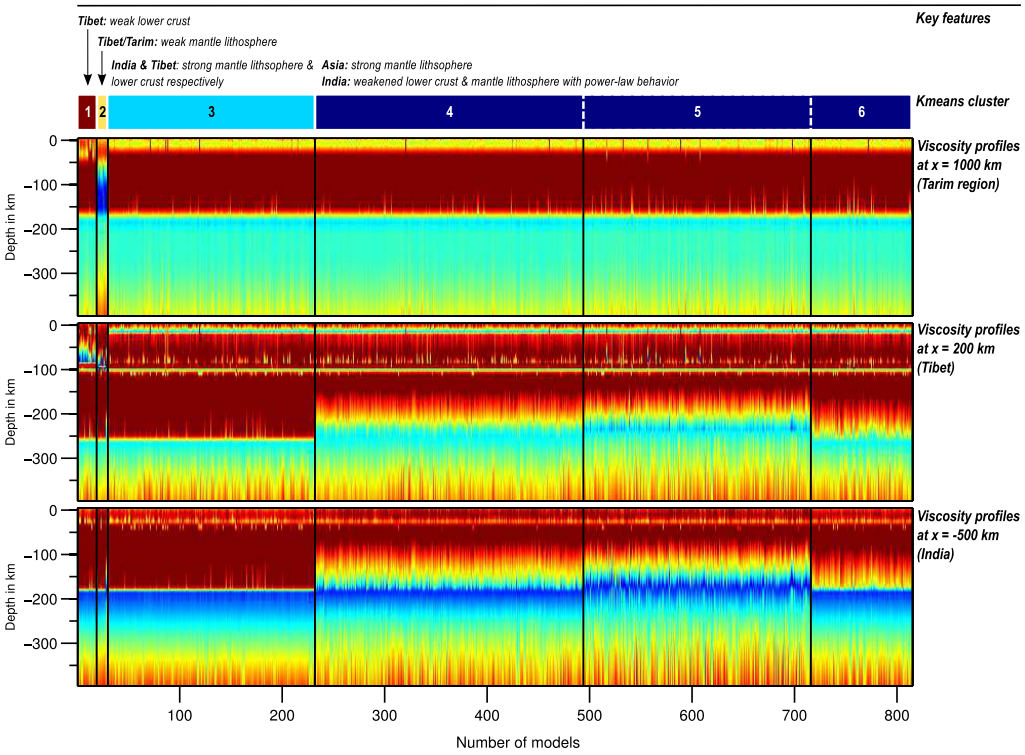


Figure 4.4: Classified feature vectors. Each feature vector is associated with a forward model that was selected during the MCMC walk. The feature vectors are constructed from three viscosity profiles of the associated forward models at $x = -500\,\text{km}$, $x = 200\,\text{km}$ and $x = 1000\,\text{km}$. They show a characteristic viscosity structure of the the Indian shield, Tibet and the Tarim region, respectively. The classification was performed with the SOM and a post-clustering of the trained SOM using $k$-means. A clustering with 6 clusters is preferred by the DB-index analysis. A visual of inspection of the U-matrix (Fig. 4.3b) suggests to summarise clusters 4 to 6 into a single class (dark blue).

*Classified regions of the parameter space*

Each forward model is linked to a certain number of MCMC-samples that directly follow the posterior distribution. A separation of the forward models into classes therefore also enables a separation of the a posteriori distribution into new distributions that correspond to the end-member model classes. This is shown as normalised marginal distributions in Fig. 4.5. The colour of the distributions represents the associated classification of the SOM and the $k$-means clustering. The normalisation is done to balance the difference in number of samples per class and to enable a reasonable comparision between the distributions. However, due to the normalisation the information on the relative importance of the respective classes is lost in this illustration. Yet, the aim of this analysis is to understand (i) the non-uniqueness of the inversion results and (ii) the properties of the end-member models. In the following paragraphs, the distributions are analysed with respect to their classification results. The analysis is led by the numeration indicated in the sub plots of Fig. 4.5.

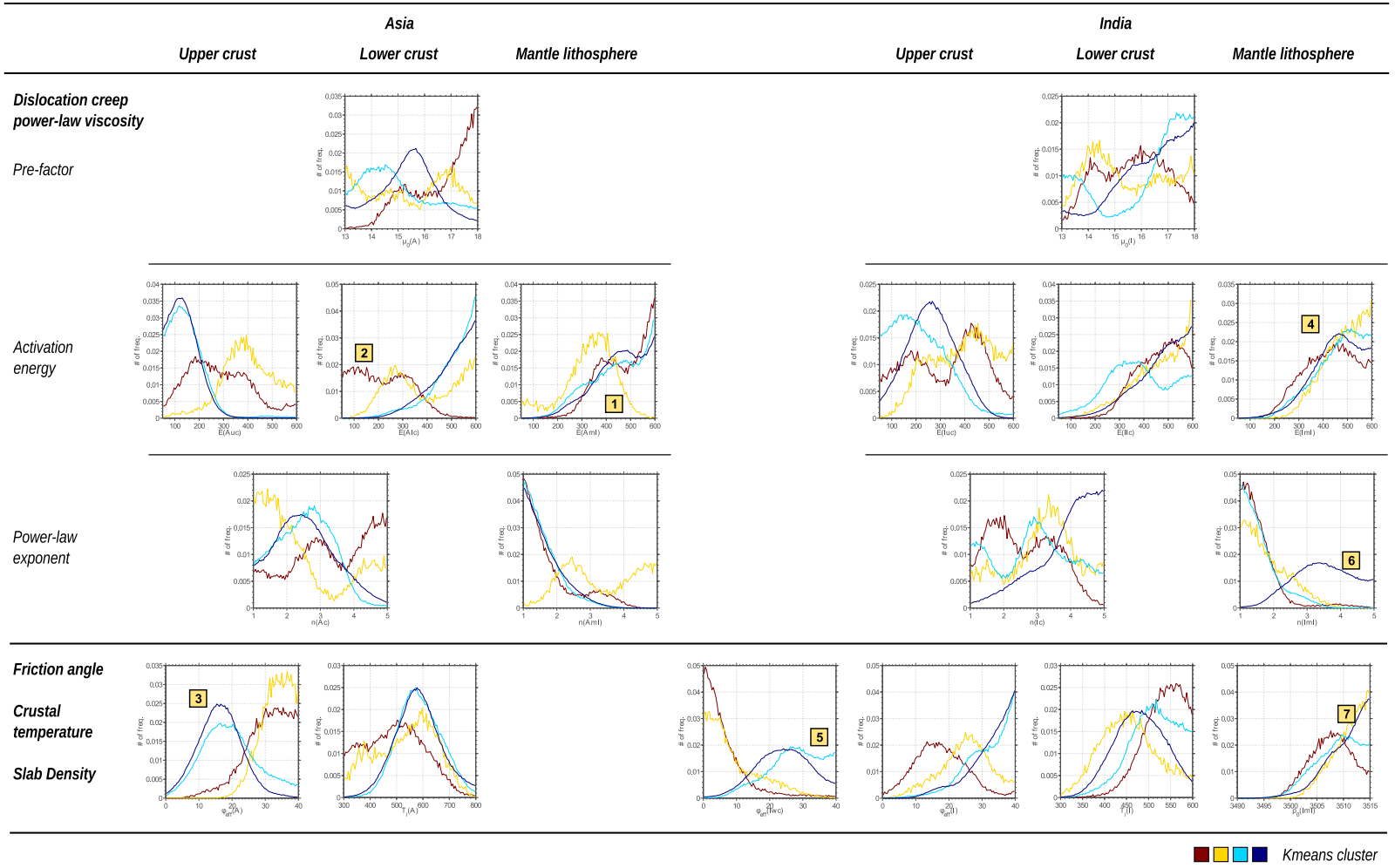


Figure 4.5: Normalized distributions of classified MCMC samples are shown for all inversion parameters. Each sample represents a step of the random walk during the appraisal stage of the inversion and is associated with a nearest neighbour forward model (voronoi cell). As the forward models can be classified, the linked MCMC samples can be classified as well. The result are classified sub-distributions for the various end-member forward models. Number indications show particular model features that are explicated in section 4.4.2

(1) The weak Asian mantle lithosphere that is seen in the viscosity structure of class 2 (yellow), corresponds to a relatively low activation energy. This has to be stabilized with a stronger upper crust, i.e. with a higher activation energy of the upper crust.

(2) Class 2 is characterized by a weak lower Tibetan crust, which is mainly caused due the low activation energy. As for case (1), the weak part must be stabilized with strong counter part, i.e. a strong mantle lithosphere.

(3) The classes 3 (light blue) and 4 (dark blue) are relatively similar with respect to the Asian part of the model: A strong mantle lithosphere and lower crust are compensated by a low viscosity upper crust and reduced friction angles. Compared to the other classes, the crustal temperature is increased, which also has a softening effect. However, the mantle lithosphere stays very strong, and is characterised by low power-law exponents.

(4) One of the most robust results of the inversion is a strong Indian mantle lithosphere. All of the clusters clearly have a high activation energy. The Indian lithosphere can be slightly weaker if the lower Asian crust is significant weak. In any case the activation energy is very likely to be above 300 kJ/mol.

(5) The friction angles of India and the weak channel are anti-correlated with the friction angle of Asia. Models with high Indian friction angles have a low friction angle for Asia and vice versa. This also means that in case of of a weak Asian lower crust or lithospheric mantle, the friction angle of the weak channel is likely to be very small ($< 15°$).

(6) In general, the Indian shield of class 4 has a significant vertical variation in effective viscosity. Obviously, this correlates with high power-law exponents for crust and mantle lithosphere.

(7) The density pre-factor of the Indian mantle lithosphere is shown to correlate with the crustal temperature: A higher density pre-factor (yellow and blue classes) corresponds to lower crustal interface temperatures, which can be explained with the effect of thermal expansion.

*Comparison of classification results with experimental data*

As the separated a posteriori distributions are now clearly associated to end-member models, a logical next step is to compare these classified distributions with constraints from laboratory experiments. For example, since the upper mantle predominantly ($\geqslant$ 60%) consists of olivine (e.g. Bürgmann & Dresen, 2008), the distributions of activation energy and power-law exponent of the Indian and Asian mantle lithosphere can be compared with experimental data of olivine. In Fig. 4.6 such a comparison is shown with experimental results from Hirth & Kohlstedt (2003). In terms of power-law exponents, most of the end-member distributions have a distinct correlation with one of the experiment-

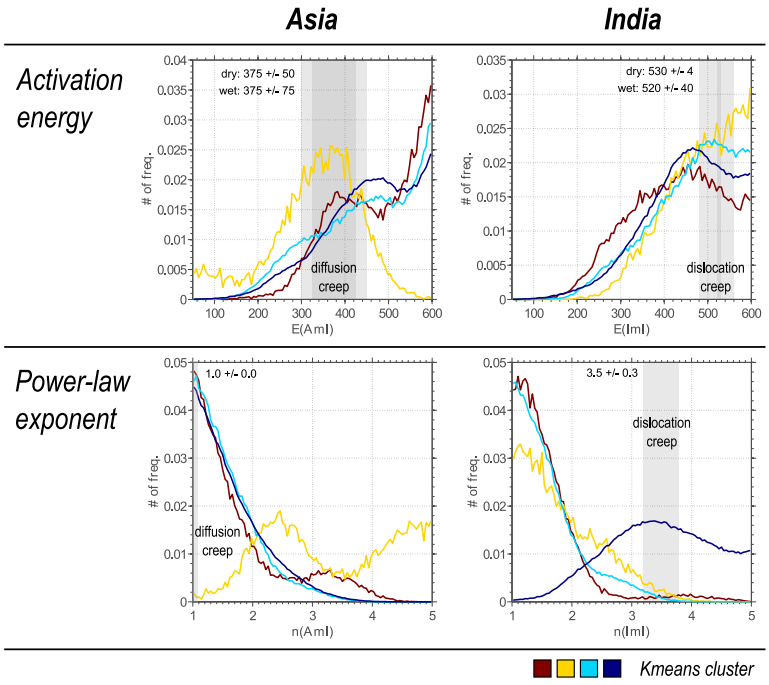


Figure 4.6: Classified posterior distributions of viscosity power-law parameters from Asian and Indian mantle lithosphere in comparison with experimental data for olivine by Hirth & Kohlstedt (2003). In particular, the class that is representing most models (class 4, dark blue) shows a distinct correlation of the Indian lithospheric mantle with dislocation creep proxies. Regarding the Asian mantle lithosphere, a good correlation with diffusion creep proxies is observed. Other end-members predominantly indicate a linear, diffusion creep dominated, deformation behaviour.

ally determined exponents. Class 4 (dark blue), which is representing most forward models, also indicates a good correlation in terms of activation energies. Whereas the Indian lithospheric mantle correlates well with experimental dislocation creep proxies, the Asian mantle lithosphere has a clear linear diffusion creep character. For other less dominant end-member models, the results are less clear, but there is a tendency of dominant linear diffusion creep deformation behaviour.

*Surface expressions of classified forward models*

In this final appraisal part of the geodynamic inversion results, the surface expressions of the classified end-member models are examined. All of the end-member models have a very similar misfit and represent the surface constraints approximately equally well within the uncertainty limits. Fig. 4.7 illustrates the model surface data for the four classes that have been identified with the clustering approach. The red signals and black dashed lines show the show the observed data and $\pm 2\sigma$ uncertainty limits, respectively. The model data is represented by the mean surface data (solid black lines) and coloured shaded areas, which show the $\pm 2\sigma$ variation of the model surface data. The topography

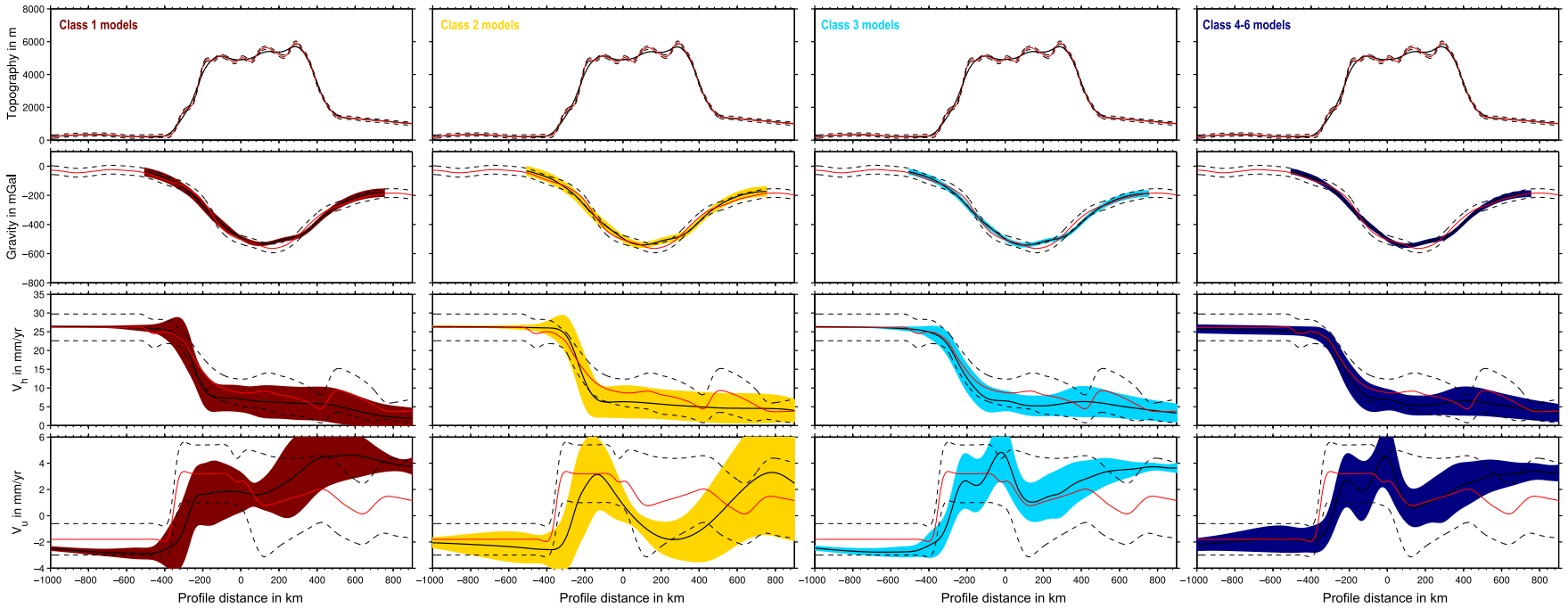


Figure 4.7: Surface expressions of classified models. The classes correspond to the classes shown in Fig. 4.4 and 4.5. The red signals are the reference signals. The black, dashed lines indicate the $\pm 2\sigma$ uncertainties of the reference signals. The black, solid line are the mean surface signals of the classified forward models and the shaded areas show the $\pm 2\sigma$ uncertainties respectively. Whereas there are almost no differences in topography and Bouguer anomaly, because the classified models already have a low misfits, the surface velocity patterns differ from each other. The largest differences are observed for the uplift velocity in Tibet and the Tarim region. The horizontal velocity pattern is fairly similar for Asia, however, a small, but significant 'peak' close to the convergence zone at $x \approx -300$ km can be observed for the model classes with either a weak lower Tibetan crust or a weak mantle lithosphere.

and the Bouguer anomaly show very little variances for the models, and all of the end-member models represent these data almost equally well, although the model variations in Bouguer anomaly for the classes 1 and 2 are slightly larger than for the classes 3 and 4. The main differences are, however, observed for the velocity fields, where also the largest uncertainties exist.

In terms of horizontal velocities, the classes 1 and 2 show an increase towards the convergence zone at $x \approx -300\,\mathrm{km}$. This 'peak'-like feature does not exist for other classes and is related with a steeper decrease, i.e. a more significant step-like drop in velocity. The horizontal velocity pattern of the Tarim region is fairly similar among all classes except class 2, where the very gradual peak followed by a gradual decrease at $x \geqslant 400\,\mathrm{km}$ is missing. This might be an effect of a strong mantle lithosphere in the Tarim region, which is missing for the class 2 models. One can speculate about a correlation with the small anomaly seen in the observed data, which could be evidence for a strong lithospheric mantle below the Tarim basin.

Regarding the uplift velocity, the most obvious difference is observed for class 2 in the Tibet and Tarim part of the profile, which corresponds to a weak mantle lithosphere of the respective models. Class 3 and 4 are more similar in this respect, as also their viscosity structure is very similar in the Tarim region. They show a characteristic double peak between $-400\,\mathrm{km} \leqslant x \leqslant 50\,\mathrm{km}$, followed by a local negative anomaly at $x \approx 200\,\mathrm{km}$ and an increase towards the end of the profile. For the Indian part, the uplift velocity differs for theses classes. On the other hand, the Indian viscosity structure of class 3 is very similar to the one of class 1 and also their uplift velocity seem to be very similar. All of the models' uplift velocities share the same strong increase north of the convergence zone and a local positive anomaly at $-300\,\mathrm{km} \leqslant x \leqslant 50\,\mathrm{km}$. This could possibly be explained with very similar densities and activation energies of the mantle lithosphere of the Indian shield, as seen in Fig. 4.5.

Because the observational uncertainties of the velocity constraints are largest, the differences of the end-member models are also mostly indicated by these fields. This also reveals that if observational uncertainties of the vertical velocity became smaller, certain end-member models could be excluded, and in fact the non-uniqueness of the inverse problem could likely be reduced.

## DISCUSSION

For non-unique inverse problems, the Bayesian approach allows a probabilistic description of the solution. The actual solution to the problem, i.e. the a posteriori distribution gives a complete, but not necessarily a comprehensive picture, in particular if many model parameters are involved and the distribution is complex. In the Earth sciences, we often think in terms of 'Earth models' to describe the solution to an inverse problem. However, a single Earth model is insufficient to describe the complete non-unique solution. This study demonstrates a way to overcome this common problem with the help of machine learning algorithms; although, it only demonstrates the results of a single application and cannot serve as a complete comparative study with multiple methods. In

the field of geophysics, there have been only very few other attempts to find common properties of model ensembles for classification purposes, for example by using statistical techniques (Vasco et al., 1993) or orthogonal function analysis (Douma et al., 1996). However, these concepts only work if the ensemble of models form a single cluster (Sambridge & Mosegaard, 2002). In machine learning, many methods exist that overcome this issue and can be used for similar type of work (e.g. Bishop, 2006). Besides dozens of SOM variants, SOM alternatives exist, for example the Generative Topographic Mapping algorithm (GTM, Bishop et al., 1996), which can be seen as a probabilistic version of the SOM, or the (growing) Neural-Gas algorithm by Fritzke (1995), which has adaptive connectivity between neurons and can even insert and remove neurons, such that multiple manifolds of different dimensions within the parameter space can be better resolved through adaptivity.

Besides all advantages of SOM variants and alternatives, the SOM provides a high degree of usability also to non-computer scientists, as only very few adjusting parameters are necessary and a user friendly MATLAB toolbox is available (Vesanto et al., 2000).

An important aspect of unsupervised learning techniques such as the SOMs, is the selection of characteristic features (Kohonen, 2013, 2001). In this geodynamical study, the viscosity structure serves as the only input quantity. This is evident as the effective viscosity field is an effective material property that summarises the impact of most of the inversion parameters (e.g. power-law exponent, activation energy, temperature) that therefore also avoids the need of additional normalisation. In general, however, the proxies of the density structure or even the characteristic solution variables, e.g. velocities or strain-rates, could be used as well. To test what features actually matter and to avoid correlated features, a feature selection has to be conducted in the first place, for example by using principle component analysis (PCA, Jolliffe, 2002; Pearson, 1901), or the SOM itself (Köhler et al., 2009).

The classification in this study is realised as a two-level approach, where the SOM clusters the model ensemble and $k$-means is used to cluster the SOM prototype vectors. Strictly speaking, $k$-means could be used to directly cluster the ensemble. However, without using the SOM visualisation techniques and with quantitative measures only, it is difficult to determine an optimal number of clusters. The additional visual validity check clearly supports the robustness of the classification result.

## CONCLUSIONS

Within geodynamics, conducting systematic modelling studies, in which we vary the input parameters automatically and perform many thousands of models, is now becoming (computationally) possible. Yet, large ensembles of models also require efficient classification methods to draw comprehensive conclusions.

Here, such a classification method is presented in the context of geodynamic modelling and in combination with a Bayesian inversion study. A two-level approach including self-organizing maps, an unsupervised machine learning tech-

nique, and partitive clustering is used to analyse and interpret the non-unique results of a Bayesian inversion with application to the rheological structure of the lithosphere within the India-Asia collision system.

The approach of performing the SOM-learning with characteristic profiles of effective model viscosity results in a reasonable model classification. It is possible to identify four end-member models that represent the major part of the non-uniqueness of the inversion results. The striking differences between the end-member models can be reduced to the existence of three model characteristics: a weak lower Tibetan crust, a weak Asian lithospheric mantle and a strong dislocation creep character of the Indian mantle lithosphere.

Evaluating the classification results in terms of surface expressions that are linked with the end-member categories, reveals that mainly the uplift rates show significant class-wise characteristics. The fact that these vertical velocity signals vary approximately within the observational uncertainty bounds suggests that reducing observational uncertainties of vertical velocities is crucial to reduce the model ambiguities. Potentially, this can help to largely improve the constraints on lithospheric rheology.

## REFERENCES

Baumann, T. S. & Kaus, B. J. P., 2015. Geodynamic inversion to constrain the non-linear rheology of the lithosphere, *Geophys. J. Int.*, **202**(2), 1289–1316.

Baumann, T. S., Kaus, B. J. P., & Popov, A. A., 2014. Constraining effective rheology through parallel joint geodynamic inversion, *Tectonophysics*.

Bishop, C. M., 2006. *Pattern recognition and machine learning*, Springer New York.

Bishop, C. M., Svensén, M., & Williams, C. K. I., 1996. GTM: A principled alternative to the self-organizing map, in *Artif. Neural Networks - ICANN 96*, pp. 165–170, Springer.

Caldwell, W. B., Klemperer, S. L., Lawrence, J. F., Rai, S. S., & Ashish, 2013. Characterizing the Main Himalayan Thrust in the Garhwal Himalaya, India with receiver function CCP stacking, *Earth Planet. Sci. Lett.*, **367**, 15–27.

Davies, D. L. & Bouldin, D. W., 1979. A cluster separation measure, *Pattern Anal. Mach. Intell. IEEE Trans.*, **1**(2), 224–227.

Deboeck, G. & Kohonen, T., 1998. *Visual explorations in finance: with self-organizing maps*, vol. 2, Springer London.

Douma, H., Snieder, R., & Lomax, A., 1996. Ensemble inference in terms of empirical orthogonal functions, *Geophys. J. Int.*, **127**(2), 363–378.

Dziewonski, A. M., Chou, T.-A., & Woodhouse, J. H., 1981. Determination of earthquake source parameters from waveform data for studies of global and regional seismicity, *J. Geophys. Res. Solid Earth*, **86**(B4), 2825–2852.

Fritzke, B., 1995. A Growing Neural Gas Learns Topologies, *Adv. Neural Inf. Process. Syst.*, **7**, 625–632.

Gray, R. M., 1984. Vector quantization, *ASSP Mag. IEEE*, **1**(2), 4–29.

Jain, A. K. & Dubes, R. C., 1988. *Algorithms for clustering data*, Prentice-Hall, Inc.

Jolliffe, I., 2002. *Principal component analysis*, Wiley Online Library.

Köhler, A., Ohrnberger, M., Scherbaum, F., Kohler, A., Ohrnberger, M., & Scherbaum, F., 2009. Unsupervised feature selection and general pattern discovery using Self-Organizing Maps for gaining insights into the nature of seismic wavefields, *Comput. Geosci.*, **35**(9), 1757–1767.

Köhler, A., Ohrnberger, M., & Scherbaum, F., 2010. Unsupervised pattern recognition in continuous seismic wavefield records using Self-Organizing Maps, *Geophys. J. Int.*, **182**(3), 1619–1630.

Kohonen, T., 2001. *Self-organizing maps*, vol. 30, Berlin: Springer, Berlin, 3rd edn.

Kohonen, T., 2013. Essentials of the self-organizing map., *Neural Netw.*, **37**, 52–65.

Laske, G., Masters, G., Ma, Z., & Pasyanos, M., 2013. Update on CRUST1.0 - A 1-degree global model of Earth's crust, in *Geophys. Res. Abstr.*, no. EGU2013-2658 in 15.

Liu, Y. & Weisberg, R. H., 2011. A review of self-organizing map applications in meteorology and oceanography, in *Self-Organizing Maps-Applications Novel Algorithm Design*, chap. 14, pp. 253–272, ed. Mwasiagi, J. I., InTech.

Pearson, K., 1901. On lines and planes of closest fit to systems of points in space, *London, Edinburgh, Dublin Philos. Mag. J. Sci.*, **2**(1), 559–572.

Rai, S. S., Priestley, K., Gaur, V. K., Mitra, S., Singh, M. P., & Searle, M., 2006. Configuration of the Indian Moho beneath the NW Himalaya and Ladakh, *Geophys. Res. Lett.*, **33**(15), L15308.

Sambridge, M., 1999a. Geophysical inversion with a neighbourhood algorithm–I. Searching a parameter space, *Geophys. J. Int.*, **138**(2), 479–494.

Sambridge, M. & Mosegaard, K., 2002. Monte Carlo methods in geophysical inverse problems, *Rev. Geophys.*, **40**(3), 1–3.

Schaeffer, A. J. & Lebedev, S., 2013. Global shear speed structure of the upper mantle and transition zone, *Geophys. J. Int.*, **194**(1), 417–449.

Snieder, R., 1999. The role of nonlinearity in inverse problems, *Inverse Probl.*, **14**(3), 387–404.

Snieder, R. & Trampert, J., 1999. Inverse problems in geophysics, in *Wavefield Inversion*, pp. 119–190, ed. Wirgin, A., Springer.

Tarantola, A., 2005. *Inverse Problem Theory and Methods for Model Parameter Estimation*, Society for Industrial & Applied Mathematics.

Törönen, P., Kolehmainen, M., Wong, G., & Castrén, E., 1999. Analysis of gene expression data using self-organizing maps, *FEBS Lett.*, **451**(2), 142–146.

Ultsch, A., 1993. Self-organizing neural networks for visualisation and classification, in *Information and Classification*, Studies in Classification, Data Analysis and Knowledge Organization, pp. 307–313, eds Opitz, O., Lausen, B., & Klar, R., Springer Berlin Heidelberg.

Vasco, D. W., Johnson, L. R., & Majer, E. L., 1993. Ensemble Inference in Geophysical Inverse Problems, *Geophys. J. Int.*, **115**(3), 711–728.

Vesanto, J., 1999. SOM-based data visualization methods, *Intell. Data Anal.*, **3**(2), 111–126.

Vesanto, J. & Alhoniemi, E., 2000. Clustering of the self-organizing map, *Neural Networks, IEEE Trans.*, **11**(3), 586–600.

Vesanto, J., Himberg, J., Alhoniemi, E., & Parhankangas, J., 2000. SOM Toolbox for Matlab 5, *Tech. Rep. A57*, **2**(0), 59.

Witten, I. H. & Frank, E., 2005. *Data Mining: Practical machine learning tools and techniques*, Morgan Kaufmann.

Wittlinger, G., Vergne, J., Tapponnier, P., Farra, V., Poupinet, G., Jiang, M., Su, H., Herquel, G., & Paul, A., 2004. Teleseismic imaging of subducting lithosphere and Moho offsets beneath western Tibet, *Earth Planet. Sci. Lett.*, **221**(1), 117–130.

Zhao, J., Yuan, X., Liu, H., Kumar, P., Pei, S., Kind, R., Zhang, Z., Teng, J., Ding, L., & Gao, X., 2010. The boundary between the Indian and Asian tectonic plates below Tibet, *Proc. Natl. Acad. Sci.*, **107**(25), 11229–11233.

## APPENDIX

### *Applying the SOM toolbox: A coding example*

The appraisal procedure in this study was performed using the SOM MATLAB toolbox by Vesanto et al. (2000). Here, the generalised work flow is illustrated as code example, which can be useful for interested readers. Descriptions of functions can be found within the toolbox documentation (Vesanto et al., 2000).

```
% (1) Construct a input data set (feature vectors) for the SOM, for
% example, viscosity profiles:
som.sD  = [Profile1(:), ..., ProfileN(:)];

% (2) Normalisation of feature vectors. This would be the place to
% normalize the feature vectors. If the feature components of the
% vectors have a different scaling this step crucial.
```

```
% som.sD = som_normalize(som.sD);

% (3) Create and initialize and train the SOM. Several options are
% available. By default, the SOM is initialised randomly.
som.sM   = som_make(som.sD);

% (4) Extract IDs of BMUs for all feature vectors. This is the first
% classification result:
som.bmus = som_bmus(som.sM,som.sD);

% (5) Visualise the SOM and create an unified-distance matrix:
um = som_umat(som.sM);
som_cplane('hexaU',som.sM.topol.msize,um(:));

% (6) Apply k-means clustering to the  SOM. Here, the k-means
% clustering is computed 19 times, for 2 to 20 clusters:
[~,som.cl,~,som.ind] = kmeans_clusters(som.sM,20);

% (7) Visualize the Davies-Bouldin index and estimate the theoretically
% best matching number of clusters:
figure('name','DB index')
plot(1:length(som.ind),ind,'o-')
[~,som.min_i] = min(som.ind);

% (8) Visualise the clustering result, assuming 4 clusters fit best, and
% create a colour map with colours:
cmap  = jet(4) ;
figure('name','SOM clusters');
som_cplane(som.sM,cmap(som.cl{4},:))
```

# 5

# THE PRESENT-DAY DYNAMICS OF THE THE INDIA-ASIA COLLISION: CONSOLIDATING STRUCTURAL AND DYNAMIC CONSTRAINTS

**This chapter has been prepared for publication:**
Baumann, T. S., Kaus, B. J., Popov, A. A., & Bauville, A. (In prep.) The present-day dynamics of the the India Asia collision: Consolidating structural and dynamic constraints.

**Abstract**

We present a 3D geodynamic model of the present-day India-Asia collision system. The model is separated into multiple tectonic blocks, for which we estimate the first order rheological properties and their impact on the dynamics of the collision system. This is done by performing systematic simulations with different rheologies to minimize the misfit to observational constraints such as the GPS-velocity field. The simulations are performed with the parallel staggered grid FD code LaMEM using a numerical resolution of at least $512 \times 512 \times 256$ cells to resolve dynamically important shear zones reasonably well. A fundamental part of this study is the reconstruction of the 3D present-day geometry of Tibet and the adjacent regions. Our interpretations of crust and mantle lithosphere geometry are jointly based on a globally available shear wave tomography and a global crustal model. We regionally refined and modified our interpretations based on seismicity distributions and focal mechanisms and incorporated regional receiver function studies to improve the accuracy of the Moho in particular. Results suggest that we can identify at least one 'best-fit' solution in terms of rheological model properties that reproduces the observed velocity field reasonably well, including the strong rotation of the GPS velocity around the eastern syntaxis of the Himalaya. We also present model co-variances to illustrate the trade-offs between the rheological model parameters, their respective uncertainties, and the model fit. The results also demonstrate that only a combination of strike-slip faults, strong cratonic blocks and weak layers (partial melting) within the crust can reproduce the observed surface deformation field.

## INTRODUCTION

The active continental collision system of India and Asia results in a large area of deformed lithosphere (e.g. Molnar & Tapponier, 1975), which is one of the main reasons why it is one of the most widely investigated regions on Earth. Especially through numerous studies of GPS velocity observations, the long-term deformation of crust and mantle lithosphere is partly examined with very

high spatial sampling densities over large areas, such as in the eastern syntaxis (e.g. Zhang et al., 2004). Although, many observations are available, basic issues remain. Whether it is the evolution of the Tibetan plateau (e.g. Royden et al., 2008; Tapponnier et al., 2001) or driving mechanisms of the collision, such as the role of ridge push and slab pull (e.g. Jagoutz et al., 2015; Van Hinsbergen et al., 2011; Capitanio et al., 2010) that are debated, all of these issues are fundamentally linked with the rheology of crust and lithosphere, which define the underlying strength profiles and, hence, the deformation mechanism of the continental collision.

Irrespective of the discussion on the rheological structure of the continental lithosphere itself (e.g. Burov & Watts, 2006; Jackson, 2002), several deformation mechanisms have been proposed over the last thirty years, which can be categorized into three end-member models. Each of them comes with rather strict model assumptions. Firstly, kinematic models with rigid blocks are proposed, where the entire deformation is accommodated by shortening along major thrust zones and strike-slip faults, favoring a mostly eastward directed extrusion of Tibet (e.g. Avouac & Tapponnier, 1993; Tapponnier et al., 1982; Tapponnier & Molnar, 1976). Contrary to this, dynamic models of viscous deformation favour a crustal thickening to accommodate the deformation (thin viscous sheet models, Houseman & England, 1986; England & Houseman, 1986; England & McKenzie, 1982) and to explain surface velocities (Vergnolle et al., 2007; Flesch et al., 2001). These models assume vertically averaged viscosities, but can incorporate lateral heterogeneities (England & Houseman, 1985) to account for local effects. However, boundaries between geological units are vertical and horizontal velocities remain constant with depth (Lechmann et al., 2014). This is the striking difference with a third category of models favouring a lower crust 'channel flow' as a key mechanism for the ongoing deformation in the upper Tibetan crust, which is decoupled from the mantle lithosphere (e.g. Beaumont et al., 2001; Clark & Royden, 2000; Royden, 1996; Royden et al., 1997; Bird, 1991). Although this mechanism seems inconsistent with centroid moment tensors of large earthquakes, which suggest mechanical coupling in south-western Tibet (Copley et al., 2011), similarities exist between observed GPS velocities and predicted deformation by 'channel flow' models in eastern Tibet, where crustal heterogeneities are taken into account (Cook & Royden, 2008). Recently, Lechmann et al. (2014) tried to avoid the shortcomings of the previous approaches by using a fully dynamic thermomechanical 3D model of the present-day India-Asia collision to estimate non-linear lithospheric rheologies. They account for major strike slip faults and rigid blocks, and incorporate other geophysical observations to confine the model geometry.

Similar to Lechmann et al. (2014), we employ a 3D mechanical Stokes-flow code (LaMEM, Kaus et al., 2016) to study a physically consistent deformation behaviour of the India-Asia collision. However, compared to their models, we employ a high resolution and couple the Stokes model with an optimisation (inversion) algorithm, which automatically optimises the model viscosity structure with respect to GPS-derived surface velocities. Our model domain is composed of multiple tectonic blocks and geological units, which results from a joint inter-

pretation of various geophysical data sets. We employ our code on 4096 CPUs and due to the high model resolution, we can account for localised deformation behaviour within strike-slip faults and thrust imitating weak zones.

The work is composed into five main parts. Firstly, we describe the numerical approach of the mechanical forward model and introduce the methods used for parameter quantification. The second part is dedicated to the 3D model construction and observational constraints of the optimisation procedure. Results are described hereafter. We separate between minimisation of the model misfit and an other section addressed for error quantification and estimation of parameter uncertainties. We discuss the results with respect to the forward model and methodological aspects and end with a conclusion of the key aspects.

## METHOD

Our methodology involves four key aspects, which are (i) to construct a realistic three dimensional present-day geometry of the India-Asia collision zone, and (ii) to comprise the geometry into a dynamic, physically consistent Stokes-flow model. Furthermore, (iii) we link the dynamic forward model with an optimisation algorithm to find best-fit viscosity model parameters with respect to the observed deformation field, and (iv) identify the key parameters and geological units of the model by estimating model uncertainties.

### *Model geometry*

#### *Data basis*

The input model geometry is based on five different seismological records. A SV-wave tomography by Schaeffer & Lebedev (2013) forms the basis of the model. We have also analysed 24 receiver function (RF) profiles in the region to collect complementary information on the depths of the Lithosphere Asthenosphere boundary (LAB) and the Moho (Zhang et al., 2014; Xu et al., 2014; Mechie & Kind, 2013; Schneider et al., 2013; Sippl et al., 2013; Zhao et al., 2010; Nábelek et al., 2009; Kumar et al., 2006; Rai et al., 2006; Schulte-Pelkum et al., 2005; Wittlinger et al., 2004; Vergne et al., 2002). Additional information was also extracted from teleseismic tomography (He et al., 2010) and seismic reflection studies (Gao et al., 2013). Locations and orientations of all seismic studies incorporated in this work are illustrated in Fig. 5.1. The Moho signals of these profiles can be seen as a refinement of the Crust 1.0 model (Laske et al., 2013), which is also included in our joint interpretation, but, because of its limited resolution ($1° \times 1°$) and averaged character, it is always reinterpreted when local information is available. For the interpretation of shear and subduction zones, seismicity distribution and focal solutions (Ekström et al., 2012; Dziewonski et al., 1981) are involved as well. Locations of strike-slip faults are transferred from literature (Tapponnier et al., 2001; Gordon & DeMets, 1989; Molnar & Tapponier, 1975). The Talas-Fergana fault is presently inactive (Feld et al., 2015;

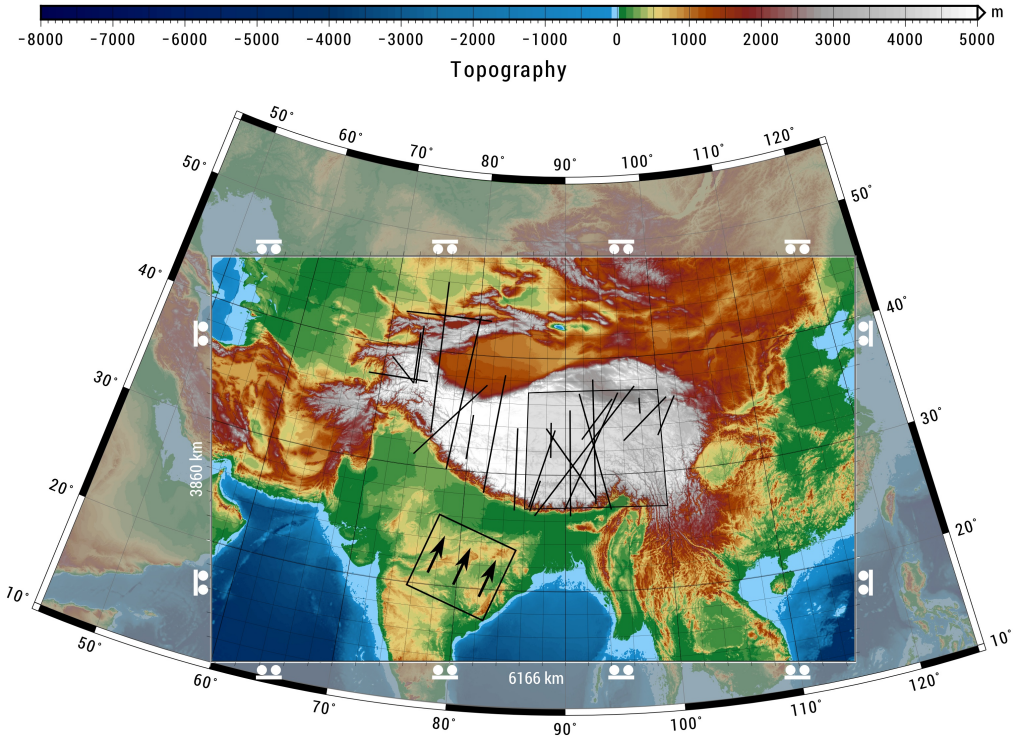


Figure 5.1: Geographical setting of the 3D model. 24 profiles of receiver function studies in the Himalaya region are indicated as black lines and with a marked area. We use these profiles in combination with the global shear wave tomography model SL2013SV (Schaeffer & Lebedev, 2013), to construct the model lithosphere. In addition, CRUST 1.0 (Laske et al., 2013) is incorporated as a reference of the Moho. Local interpretations (shear zones, subduction channels, etc.) are supported with CMT solutions, and seismicity data. The black framed box with arrows indicates an internal boundary condition, where velocities are superimposed to imitate the motion of India (38 mm/yr). White symbols mark free-slip model boundary conditions.

Ghose et al., 1998), and is therefore included for a consistency-check and also because it is in the vicinity of many GPS observation points (Fig. 5.4).

*Cross-sectional interpretation and volumetric interpolation*

To construct the model geometry, we interpret the data described in section 5.2.1.1 in horizontal slices and vertical cross-sections (every 1°) that are either oriented in South-North, or West-East direction. On each vertical section, we plot the shear wave tomography, focal solutions and other seismic events ($m_b \geqslant 5$).

For crustal heterogeneities, we found a map view interpretation most suitable as fault zones (e.g. Tapponnier et al., 2001) and traces of surface tectonics in topography (ETOPO1, Amante & Eakins, 2009) can be taken into account more easily. Horizontal interpretations lack vertical precision, therefore interpretations are conducted for various depth levels and are projected on vertical cross sections to continue the interpretation in more detail. An example is given

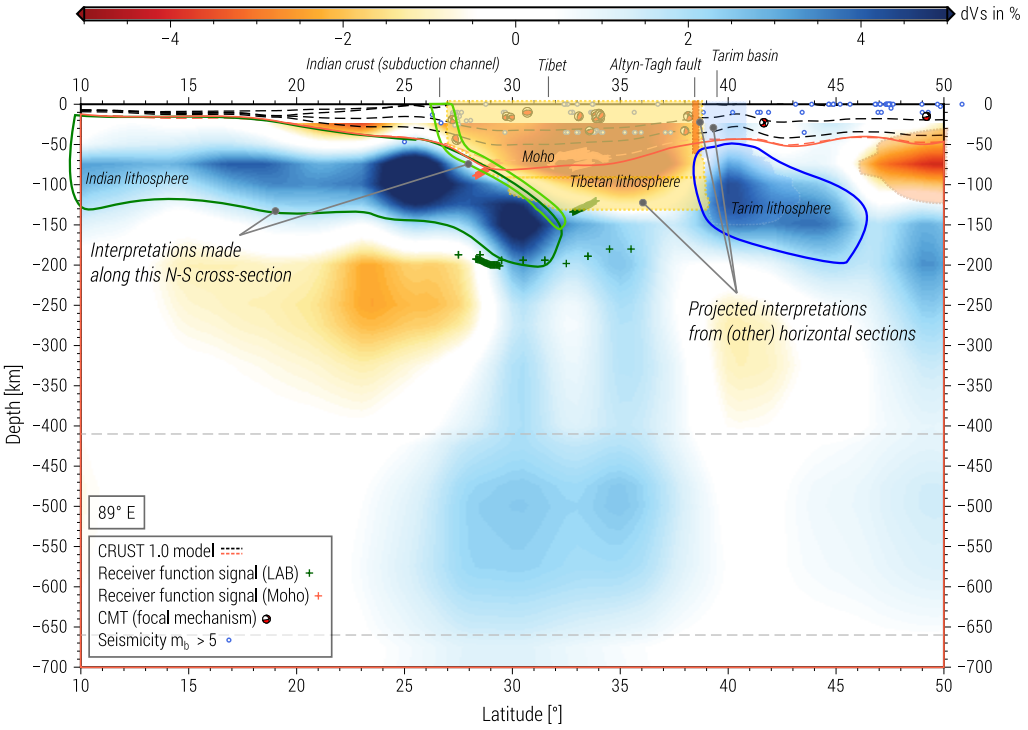


Figure 5.2: Example slice indicating the construction process of the model geometry. A south north transect along the 89° meridian is illustrated including all data that supports the interpretation procedure. Background image indicates seismic velocity anomalies of Schaeffer & Lebedev (2013). Shaded areas mark existing interpretations from different projections, here, map-view interpretations.

in Fig. 5.2, where projected (horizontal) interpretations are shown and especially lithospheric interpretations can be performed more precisely. Moreover, we adjust the Crust 1.0 Moho signal, which is used to automatically separate crustal phases from their lithospheric counterparts, which were previously interpreted as a whole, such as seen for Tibet in this example. We use the geomIO software package (Bauville & Baumann, 2015) to interpolate, summarize and re-project our interpretations on other slices. geomIO also renders 3D geometries from our joint 2D interpretations, which were all conducted in a standard vector graphics program, and allows us to look at these geometries in three dimensions with appropriate software (e.g. Paraview, www.paraview.org) to reconsider our interpretations. The final geometry interpretation is given in Fig. 5.3. We use these geometries to assign phases to markers that set the input geometry and material properties of the Stokes-flow model described in the following section.

*Geodynamic model and governing equations*

As the model geometry allows for distinct material properties for crust and mantle lithosphere within each unit, we choose a constant viscosity and solve for the viscous Stokes flow within a 3D Cartesian model domain ($x_i$, with $i =$

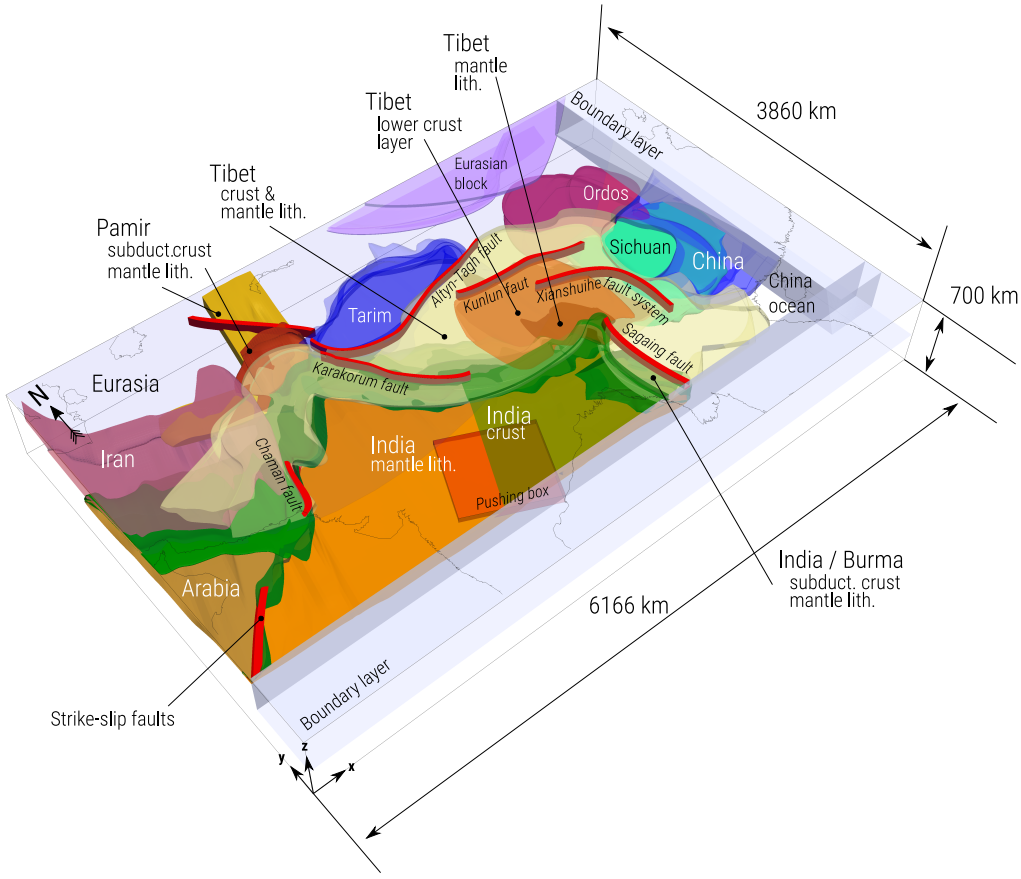


Figure 5.3: 3D volumes generated from multiple 2D interpretations on NS- EW cross sections and mapview projections. The transformation was performed with the geomIO software package (Bauville & Baumann, 2015). Each geological unit participating in the forward model can be assigned with different material properties.

1, 2, 3). This comprises the governing equations, which are the conservation of momentum (eq. 5.1) and mass (eq. 5.2) for incompressible fluids, with velocity ($v_i$) and pressure ($p_i$) as primary unknowns. Here, we give a brief abstract of the comprehensive description in Kaus et al. (2016):

$$\frac{\partial \tau_{ij}}{\partial x_j} - \frac{\partial p}{\partial x_i} + \rho g_i = 0 \tag{5.1}$$

$$\frac{\partial v_i}{\partial x_i} = 0. \tag{5.2}$$

$\tau_{ij} = \sigma_{ij} + p\,\delta_{ij}$ denotes the Cauchy stress deviator, $\rho$ density and $g_i$ gravitational acceleration. A constitutive relationship relates deviatoric stress and strainrate ($\dot{\varepsilon}_{ij}$) tensors:

$$\tau_{ij} = \frac{\tau_{II}}{\dot{\varepsilon}^{vs}_{II}}\,\dot{\varepsilon}_{ij} = 2\eta^*\dot{\varepsilon}_{ij}, \tag{5.3}$$

where $\dot{\varepsilon}_{ij} = \frac{1}{2}(\frac{\partial v_i}{\partial x_j} + \frac{\partial v_j}{\partial x_i}) - \frac{1}{3}\frac{\partial v_k}{\partial x_k}\delta_{ij}$ is a function of velocities. The subscript $_{II}$ denotes the square root of the second invariant of a corresponding tensor, e.g.

| Dir. | Number of CPUs | Number of cells | Number of c.g.[1] cells | Width [km] | Resolution [km] |
|---|---|---|---|---|---|
| x | 16 | 512 | 32 | 6166 | 8.0 (center) $<$ dx $<$ 16.1 |
| y | 16 | 512 | 32 | 3860 | 6.7 (center) $<$ dy $<$ 8.3 |
| z | 16 | 256 | 16 | 700 | 2.6 (top) $<$ dz $<$ 2.9 |

Table 5.1: Numerical model characteristics. Model resolution of adaptive FD-mesh is given in terms of minimal and maximal cell widths (dx, dy, dz). c.g.[1] denotes 'coarse grid' of the Galerkin geometric multigrid preconditioner, where 5 multigrid levels are used in total.

for the deviatoric stress $\tau_{II} = \left(\frac{1}{2}\tau_{ij}\tau_{ij}\right)^{1/2}$. $\eta^*$ describe the variable effective viscosity, which is the key variable that we optimize with respect to surface observations.

The conservation equations are discretised with a staggered grid finite difference approach (Harlow et al., 1965) and implemented into the code LaMEM (Lithosphere and Mantle Evolution Model, Kaus et al., 2016). The most important numerical characteristics are given in Tab. 5.1. Additional information on the numerical implementation and solving techniques are provided in appendix A.

*Parameter optimisation*

We optimise the model rheology (effective viscosities) with respect to the present-day surface velocity field, observed with GPS sensors (see following section 5.3). In this study, parameter optimisation is separated into a manual and an automated part. As the model geometry involves many geological units (37), the parameter space is large, and even for a simple gradient based method, the inverse problem becomes challenging through the curse of dimensionality.

Whereas in previous studies (Baumann & Kaus, 2015; Baumann et al., 2014), we were following a Bayesian strategy to tackle the inverse problem of constraining lithospheric rheology, we make use of a different, computationally cheaper, method in this paper to find first order accurate solutions that can be used as prior information for future Bayesian based projects. The Nelder-Mead downhill simplex method (NMDS, Nelder & Mead, 1965) is capable to find a local minimum of the misfit function, but it does this in a rather efficient manner. Keeping in mind that other solutions may coexist, we are still able to find one possible best-fit solution in terms of optimal model viscosities through which the observed surface velocity field can be reproduced. Assuming Gaussian error statistics, we can even evaluate the Hessian (see following subsection) to find parameter correlations and uncertainties of the involved model parameters.

*Estimating model uncertainties*

To estimate correlations and uncertainties, we approximate the Hessian in the local minimum that is found with the NMDS method. Let $f(\mathbf{m})$ be the objective function at the (local) minimum $\mathbf{m}$ to which the NMDS method has converged, then

$$\mathcal{H}(f(\mathbf{m})) = \frac{\partial^2 f}{\partial m_i \partial m_j} \tag{5.4}$$

$$\approx \frac{f(\mathbf{m}+\delta_i\mathbf{e}_i+\delta_j\mathbf{e}_j) - f(\mathbf{m}+\delta_i\mathbf{e}_i) - f(\mathbf{m}+\delta_j\mathbf{e}_j) + f(\mathbf{m})}{\delta_i\delta_j} \tag{5.5}$$

is the Hessian that can be approximated using forward finite differences (Dennis Jr. & Schnabel, 1996, p. 77 ff.). Here, $\mathbf{e}_{i,j}$ are unit vectors and $\delta_{i,j}$ are small quantities in directions $i$ and $j$ respectively. As $\mathcal{H}(f(\mathbf{m}))$ is symmetric, and provided that parameters have same units and scale (hence, $\delta_i = \delta_j$), $\frac{(d^2-3d)}{2}$ additional function evaluations are required for the approximation, where $d$ is the dimension of the parameter space. Once the approximate Hessian is found, it can be transformed into the model covariance matrix, which is proportional to the inverse of the Hessian (Menke, 2012):

$$[\mathrm{Cov}\,\mathbf{m}] = \sigma_d^2 \left[\frac{1}{2}\mathcal{H}(f(\mathbf{m}))\,|_{\mathbf{m}=\mathbf{m}_{min}}\right]^{-1}, \tag{5.6}$$

where the inverse is scaled with the data variance $\sigma_d^2$. Care must be taken according to the positive definiteness of the Hessian and local convexity of the objective function, which is the case for local minima. However, due to the approximation and numerical inaccuracies, small negative eigenvalues might occur, such that $\mathcal{H}(f(\mathbf{m}))$ must be regularized before inverting.

### OBSERVATIONAL CONSTRAINTS

We compare the model velocity field at the surface with the GPS velocity field observed during different studies (Liang et al., 2013; Zubovich et al., 2010; Gan et al., 2007; Vernant et al., 2004; Zhang et al., 2004). A fixed Eurasian frame is assumed, and the misfit between predicted and the observed velocity field is computed as weighted RMS error, i.e.:

$$\mathrm{misfit}_{RMS} = \sqrt{\frac{\sum_i w_i \cdot \left(v_{obs.,i} - v_{mod.,i}\right)^2}{\sum_i w_i}} \tag{5.7}$$

The observed velocities (Fig. 5.4) are interpolated on a rectilinear grid that corresponds to the FDSTAG-nodes of the numerical discretisation. As the velocity data is sparsely sampled, the interpolation errors can be significantly higher than the observation errors themselves. For this reason, we compute a weighted RMS error, where the weights are based on how dense the data is sampled in the local neighbourhood (Voronoi cell) of a grid point. We follow (Baumann

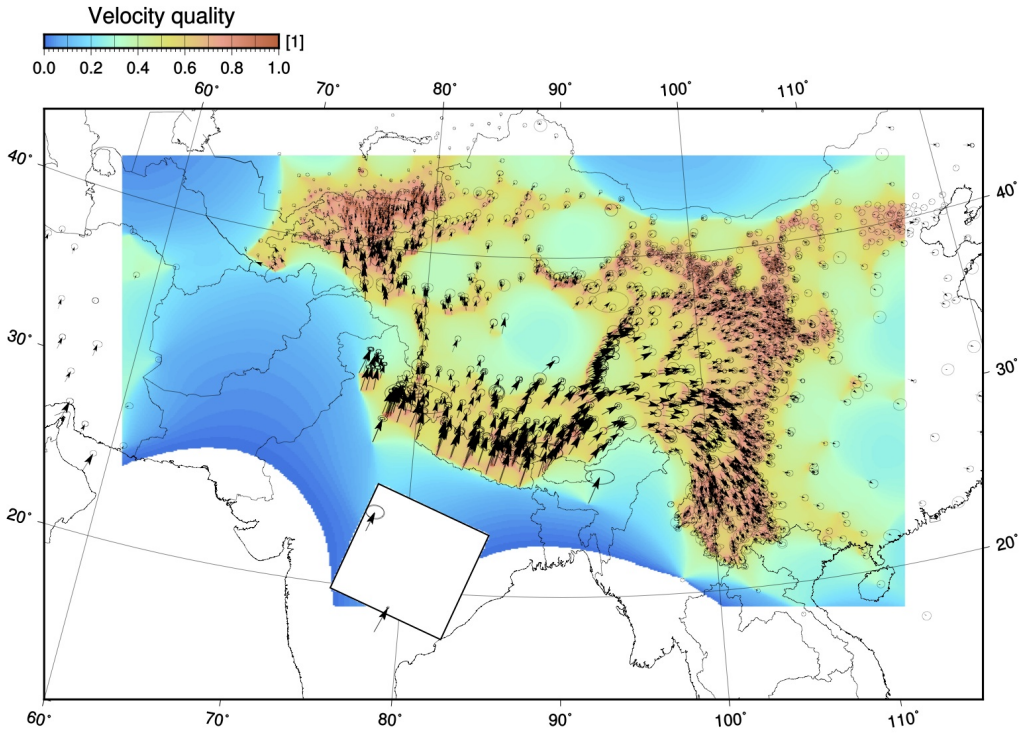


Figure 5.4: Observational constraints. GPS velocity field (black arrows) and uncertainties (ellipses) from literature (Liang et al., 2013; Zubovich et al., 2010; Gan et al., 2007; Vernant et al., 2004; Zhang et al., 2004). Observed velocities are interpolated on a rectilinear grid to match the model surface velocities. Underlying coloured map represents the quality of respective (interpolated) velocity vectors, based on the sampling density of observed data. See section 5.3 for details. Warm colours represent large weighting factors (strong constraints) and bluish colours highlight a downgrading of data quality, corresponding to a sparse data base.

et al., 2014), where the coordinates of a gridpoint are included into the Voronoi diagram of the data to determine the inverse of the corresponding Voronoi cell area, which corresponds to a local sampling density. The sampling density is logarithmised to remove notches, very small values ($< 10^{-6}$) are cut off, and the result, to which we refer to as velocity quality is normalised to a scale between 0 and 1 (see Fig. 5.4). Moreover, velocities close to the boundaries of the model are not taken into account for the misfit calculation. Corridors of 300 and 600 km at the northern and southern boundary of the domain and 400 km at the other boundaries are omitted. Velocities within the area where velocity is assigned due to internal boundary conditions are ignored too. Due to the effect of the weighting factors, large model errors in bluish regions is downgraded, the misfit of other areas with warm colors is enhanced. For example, model misfits within Afghanistan and Pakistan have a lower impact on the total error than model misfits within the eastern Himalayan syntaxis.

## RESULTS

We perform instantaneous simulations where the effective viscosity of the various geological model units is changed systematically to gradually optimise the model viscosity structure. The density structure of the model is constructed with averaged density values from a reference Earth model (PREM, Dziewonski & Anderson, 1981), but is excluded from the model optimisation in this particular study. The model evaluation is carried out according to a model misfit defined in section 5.3. This is followed by a series of independent tests before we perform an uncertainty analysis to quantify the best-fit model sensitivities.

### *Finding optimal effective viscosities*

After a manual optimisation of the model on a 'trial-and-error' basis, which is not further described here, an automatic optimisation is conducted with the NMDS optimisation method. We perform a number of consecutive optimisations with varying inversion parameters (see Fig. 5.5, 5.6). The previous best-fit result is always adopted as initial guess of subsequent optimisations. An overview of the inversion parameters is given in Tab. 5.2.

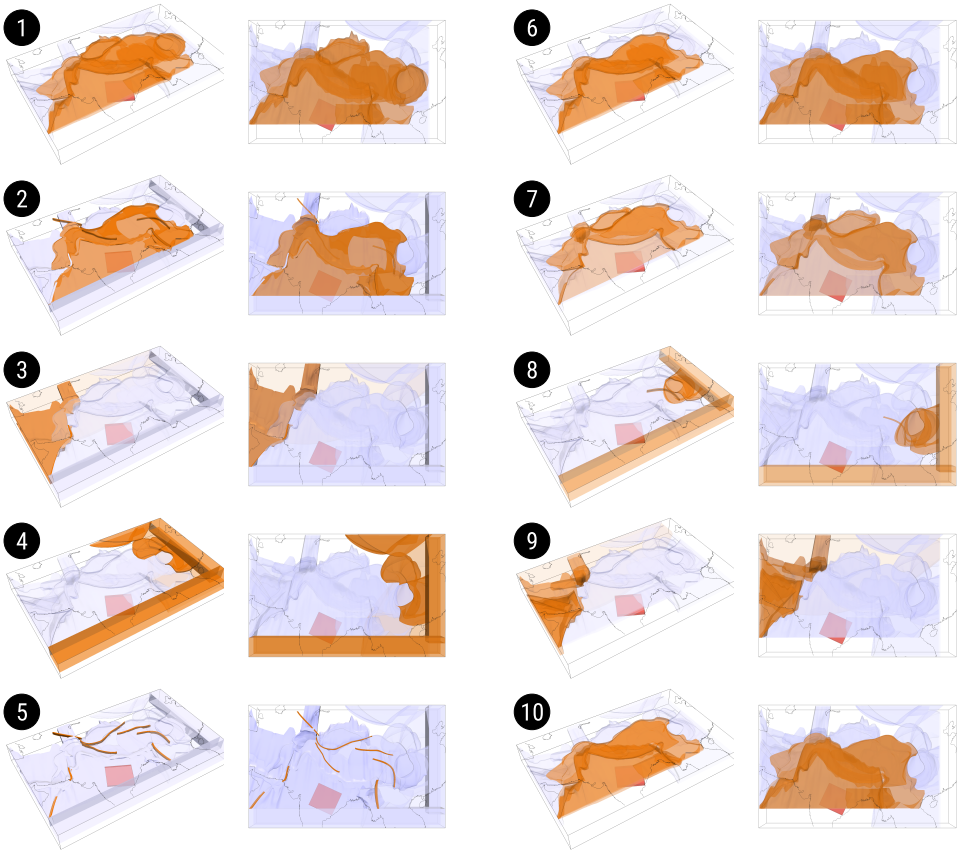


Figure 5.5: Geological units that are optimised during each separate NMDS inversion step (1-10, see Tab. 5.2). Red cuboid shows the volume where velocities are assigned as internal pushing boundary condition.

| Optimisation no. | Init. | 1 | 2 | 3 | 4 | 5 | 6 | 7 | 8 | 9 | 10 |
|---|---|---|---|---|---|---|---|---|---|---|---|
| Number of models | | 53 | 21 | 26 | 32 | 22 | 27 | 24 | 20 | 39 | 39 |
| Crust India | 22.00 | 21.75 | 21.97 | | | | 22.01 | 21.51 | | | 21.65 |
| Crust India subd. | 22.90 | 23.06 | 22.96 | | | | 22.91 | | | | 22.99 |
| Crust India subd. E | 22.48 | 22.55 | 22.57 | | | | 22.98 | | | | 22.95 |
| Lith. India subd. | 24.00 | 24.06 | | | | | 24.07 | | | | 24.01 |
| Lith. India subd. E | 23.00 | 22.85 | | | | | 23.01 | | | | 22.71 |
| Crust Tibet | 22.70 | 22.82 | 22.82 | | | | 22.64 | 22.66 | | | 22.62 |
| Lith. Tibet | 21.00 | 20.51 | | | | | 20.28 | | | | 20.18 |
| Crust Tarim | 24.00 | 24.32 | | | | | | 24.61 | | | |
| Lith. Tarim | 24.00 | 23.92 | | | | | | | | | |
| Crust Sichuan | 25.00 | 24.32 | | | | | | | 24.66 | | |
| Lith. Sichuan | 25.00 | 24.02 | | | | | | | 23.14 | | |
| Crust (lower) Tibet SE | 21.00 | 21.10 | | | | | 21.20 | | | | |
| Lith. Tibet SE | 22.00 | 21.97 | | | | | 21.82 | | | | |
| Crust China oc. | 22.70 | | | | 23.20 | | | | | | |
| Lith. China oc. | 22.70 | | | | 22.63 | | | | | | |
| Crust Eurasia block | 23.00 | | | | 23.50 | | | | | | |
| Lith. Eurasia block | 23.00 | | | | 23.50 | | | | | | |
| Crust China | 24.00 | | | | 24.05 | | | | 24.39 | | |
| Lith. China | 23.00 | | | | 23.17 | | | | 23.00 | | |
| Crust Ordos | 24.00 | | | | 24.10 | | | | | | |
| Lith. Ordos | 24.00 | | | | 23.47 | | | | | | |
| Crust Pamir subd. | 22.00 | | 21.95 | 21.10 | | | | 21.25 | | 21.24 | |
| Crust Eurasia | 23.00 | | | 22.65 | | | | | | 23.29 | |
| Lith. Eurasia | 24.00 | | | 23.91 | | | | | | 23.63 | |
| Lith. Iran | 24.00 | | | 23.66 | | | | | | 23.37 | |
| Crust Arabia oc. | 22.00 | | | 22.75 | | | | | | 22.96 | |
| Lith. Arabia oc. | 23.00 | | | 23.75 | | | | | | 24.75 | |
| Fault Altyn Tagh | 22.00 | | 22.22 | | | 23.26 | | 23.97 | | | |
| Fault Xianshuihe | 21.00 | | 20.64 | | | 19.22 | | | 19.56 | | |
| Fault Sagaing | 22.00 | | 22.22 | | | 22.31 | | | | | |
| Fault Karakorum | 22.00 | | 22.22 | | | 22.74 | | | | | |
| Fault Kunlun | 21.00 | | 21.63 | | | 20.26 | | | | | |
| Fault Chaman/OFS | 21.00 | | 22.22 | 22.60 | | 22.95 | | 21.98 | | 22.62 | |
| Fault Talas-Fergana | 21.00 | | | | | 21.91 | | | | | |
| Boundary South | 22.70 | | | | 22.77 | | | | 22.97 | | |
| Boundary East | 22.70 | | | | 22.48 | | | | 22.46 | | |
| Mantle | 21.00 | | | | | | | | | | |

Table 5.2: Model parameters and respective values during the optimisation process. Inversion parameters are effective viscosities, i. e. $\log_{10}(\eta\ [\mathrm{Pa\,s}])$. Subsets of geological units that participate at each NMDS inversion are visualized in Fig. 5.5 and the misfit progression in Fig. 5.6.

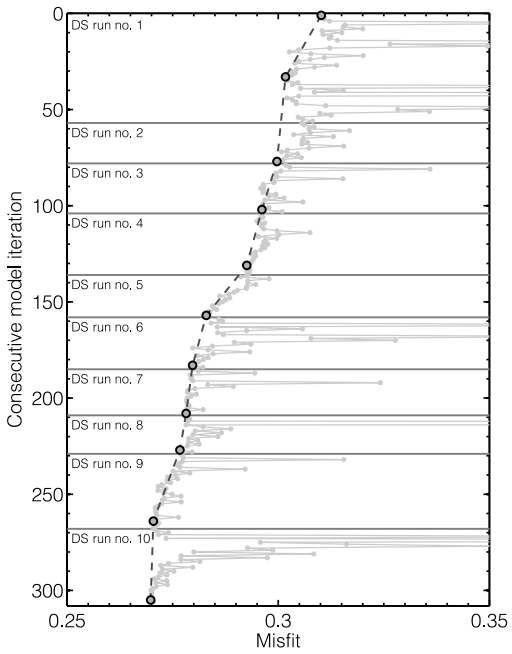


Figure 5.6: Convergence behaviour of NMDS optimisation. The gray line illustrates the model misfit with respect to a consecutive model number. In each section a separate NMDS inversion is performed for a different subset of model parameters (see Fig. 5.5). Enhanced markers indicate best-fit model of each optimisation run.

*Optimisation of the central model domain: Tibet, India, and adjacent cratonic basins*

We start with optimising the rheological structure of the central model domain (Fig. 5.5, 1), i.e. Tibet blocks (crust and mantle lithosphere) and Indian components, such as the northwards (Main Himalayan thrust) and eastwards directed subducting crust (Indo-Burman subduction zone) and their mantle lithospheric counterparts of the Indian plate. Adjacent cratonic blocks, such as the Tarim and the Sichuan basin are included as well. Tibet, in particular, is fragmented into a central and a south-eastern mantle lithosphere, which was observed to be necessary during the first manual tests. More details on this are given in appendix B. We further introduced a lower crustal phase for south-eastern Tibet additionally, to account for a potentially necessary decoupling effects in the eastern Tibet. In section 5.4.2.1, we dedicate an additional test for that. During the NMDS, the misfit first decreases quickly for the first $\approx$ 30 models, before it stagnates and even diverges. The NMDS is stopped after $\approx$ 50 models to continue with a different parameter subset (Fig. 5.6). The viscosities that have changed most compared to the initial values are the ones of Sichuan (Crust, C, and mantle lithosphere, ML) and Tibet ML, which became significantly weaker. In contrast, Tarim C viscosity increased.

*Crustal phases, convergent zones and strike slip faults*

As strike slip faults were excluded previously, we focus on the crustal viscosities of India and Tibet and effective viscosities of the six major faults (Fig. 5.3), as a correlation is expected, and keep viscosities of mantle lithosphere unchanged (Fig. 5.5, 2). The diverging behaviour of the misfit reduces and the previous best-fit model can be slightly improved (Fig. 5.6). Parameterwise, the effective viscosity of faults has changed most. Especially the viscosity of the Xianshuihe fault decreased significantly, while the strength of the others moderately increased. Initial fault viscosities are different, such that Xianshuihe and Kunlun faults are now weaker than others.

*Western model domain*

As the results of the previous optimisation still contain the largest misfits in the western syntaxis of the Himalayas, we further investigate the western part of the model domain. This includes crust and lithosphere of the Arabic plate, the Iranian lithosphere and the Chaman fault and Owen-Fracture-Zone. Most of this area is represented as Eurasian crust and mantle lithosphere, which is modelled as a single, effectively acting geological unit. Except of the Eurasian ML viscosity, all involved parameters changed notably that we interpret as a balancing behaviour.

*Eastern model domain*

In analogy to the previous part, we also optimise the eastern model adjacency and introduce the free parameters for the Chinese ocean and continental block, the Eurasian and Ordos block and two additional boundary domains that should imitate the far-field influence of various subduction systems. Parameters approximately changed by equal amounts to probably further relax the system.

*Strike slip faults - revisited*

After optimising the western and eastern part, we now optimise the faults only to test their reported significance (Avouac & Tapponnier, 1993). We observe a striking misfit reduction and a major adaptation of most of the effective fault viscosities. In particular, the Altyn-Tagh fault is noticeable, where the viscosity increased by one order of magnitude, and the Xianshuihe and Kunlun fault, which show a massive viscosity decrease. In comparison with optimisation no. 2, the trends are stable with the exception of the Kunlun fault viscosity, that increased in the first place, and then decreased by more than one order of magnitude.

*Subsequent optimisations*

We continue this procedure with five additional NMDS optimisations until the misfit decreases more and more gradually. Especially the latest optimisation

with model viscosity parameters of the model center results in no significant model improvement, while parameters are essentially unchanged.

*Best-fit model*

The best-fit model model error is shown in Fig. 5.7, and in Fig. 5.8, the difference in velocity error, before and after the NMDS inversion. The misfit is given as a weighted misfit, as weights computed from GPS sampling density are taken into account (see Fig. 5.4). Regarding the separate NMDS inversion steps, the misfit does not decrease homogeneously throughout the observed area and rather decreases for characteristic regions, depending on which of the model viscosities, the current NMDS inversion is tuned for. Overall, the improvements mainly affect regions of interest (regions with a high GPS sensor density), Tibet, Tarim, ant the eastern syntaxis with the return-flow area. However, this is on the cost of the western model domain (Pakistan, Afghanistan), where less GPS stations are available and the model misfit has more freedom to deteriorate (Fig. 5.7a). Fig. 5.7b illustrates the weighted model error. The contour lines indicate the weighting factors (see Fig. 5.4). The weighted error is more concentrated, mainly along the main thrusts, i.e. the main Himalayan thrust and the Pamir region, but also along the Xianshuihe strike-slip fault and in central Tibet. Fig. 5.8 reveals that particularly at the eastern syntaxis and in the Tarim region, the model error has massively improved (bluish colors). On the other hand, it also reveals that in some parts of the model, for example the Quaidam basin or Tien-Shan, the local misfit increased (reddish colors). At least for these example regions, introducing additional geological units will allow the model to adapt with distinct rheologies and can possibly reduce this deterioration.

For detailed insights into the characteristic surface velocity field of the eastern syntaxis, and how the predicted velocity field compares to the observations, we show this region in an enlarged representation (Fig. 5.9). Here, the predicted velocity field is interpolated on the locations of observations published by (Gan et al., 2007). The data is provided with the $2\sigma$-confidence intervals, and in almost all cases, the predicted velocities match the data taking into account the standard deviations. In Fig. 5.10, we illustrate the best-fit model in a 3D perspective. Velocity arrows at the surface are scaled according to absolute values. Label (1) indicates the area, where velocities are superimposed and label (2) highlights eastern Himalayian syntaxis, where the model is able to reproduce the characteristic 'extrusive return flow' pattern. The strainrate field is shown underneath, and indicates areas of moderate (dark blue) and strong (green and red) model deformation. Only very minor deformation is observed for cratonic blocks (Tarim, Ordos, Sichuan, label 3) and most of Eurasia. Surprisingly, we also observe only very little deformation along the Altyn-Tagh fault (label 4), which was found to have a large effective viscosity ($\log_{10}(\eta^*) = 23.97 \pm 1.08$). Taking the large standard deviation into account, it still acts as a unit with almost no internal deformation, preventing a more pronounced clockwise rotation of Tibet. However, it is strongly anti-correlated with the Tibetan crust and the Xianshuihe fault (Fig. 5.14), allowing a lower viscosity provided they have larger viscosities.

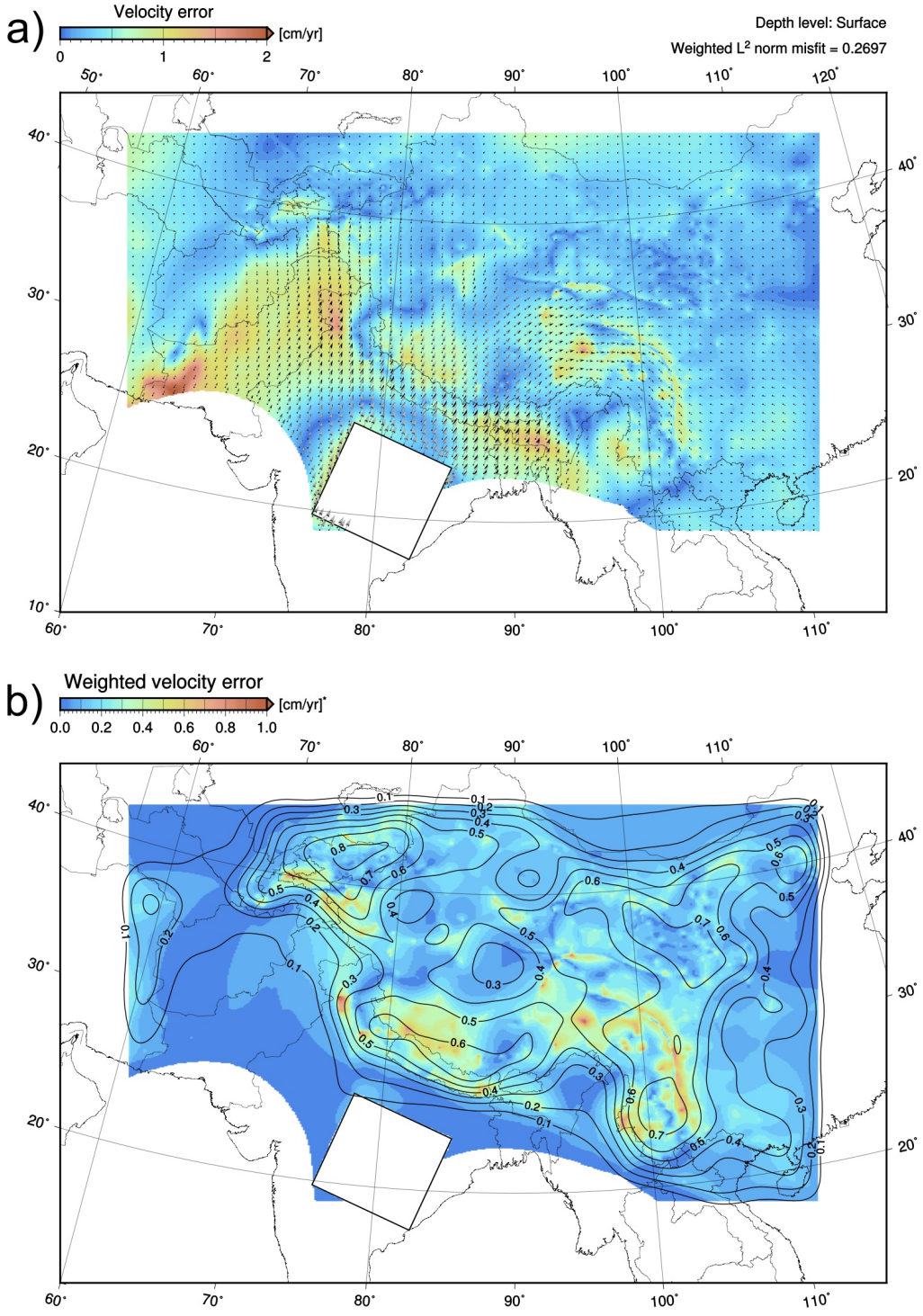


Figure 5.7: Velocity error of best-fit model. **a)** Observed (interpolated) and modelled velocity fields are illustrated with black and gray arrows respectively. Colours indicate the total velocity error in cm/yr. **b)** Weighted error that is used for optimisation. * indicates that units are scaled. Weighting factors are plotted on top as smoothed contour lines. In comparison with a), 'trusted' model regions have enhanced errors, for other regions with sparse data coverage, errors are downgraded.

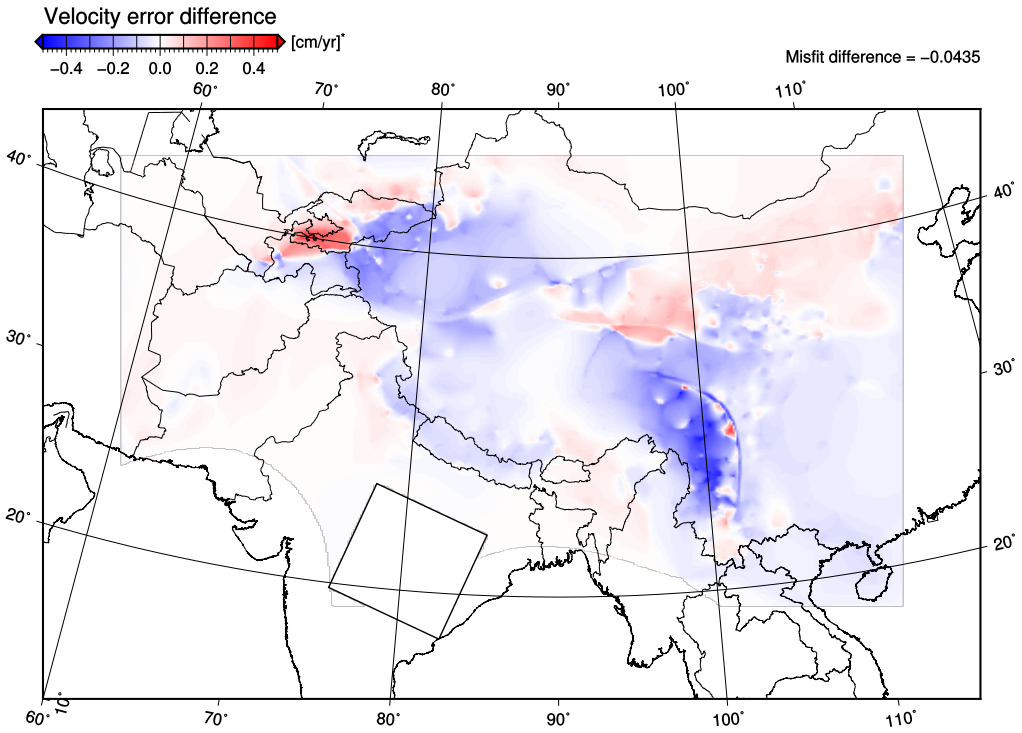


Figure 5.8: Model misfit improvement through NMDS optimisation to be compared with Fig. 5.7b. Units are scaled by weighting factors. bluish and reddish colours indicate improved and deteriorated model areas respectively.

The deformation behaviour is also seen on three transects (A-C) along characteristic collision settings. Profile B reveals that the central Tibetan crust experiences moderate deformation, and highest strain rates are localised at the surface of the underthrusting Indian shield (crustal phase). The Indian mantle lithosphere has a well constrained high viscosity ($\log_{10}(\eta^*) = 24.01 \pm 0.19$ ) and basically acts as strong indenter. This matches the fact that in this region, deep earthquakes are localised close to the Moho (Priestley et al., 2008). We also observe that the Tibetan mantle lithosphere has a particular low viscosity.

Along transect A, which crosses the Pamir region, most of the deformation is localised as well. Here, it is mainly concentrated in the southwards subducting continental crust (Crust sub. Asia) and coincides well with the deep seismicity observed here (Schneider et al., 2013; Sippl et al., 2013).

Transect C crosses eastern Tibet and a number of key features in particular. First, we see that the 'Tibet SE ML' unit, to which an extra phase has been assigned as tomographic models show anti-correlated features (appendix section B), has indeed a distinct, lower viscosity $\log_{10}(\eta^*) = 21.82 \pm 0.66$ and compared to the Indian and Asian lithosphere, it deforms noticeably ($\dot{\varepsilon}_{II} \approx 10^{-15} 1/s$). The 'Tibetan ML' is also present on this transect, indicated with a very low viscosity, which can be explained through radioactive heating from the thick Tibetan crust (McKenzie & Priestley, 2008). It is linked with the two strike slip faults, Xianshuihe and Kunlun that reach the Moho. Second, we observe a concentration of increased strainrate at the Kunlun fault down to the level of lower

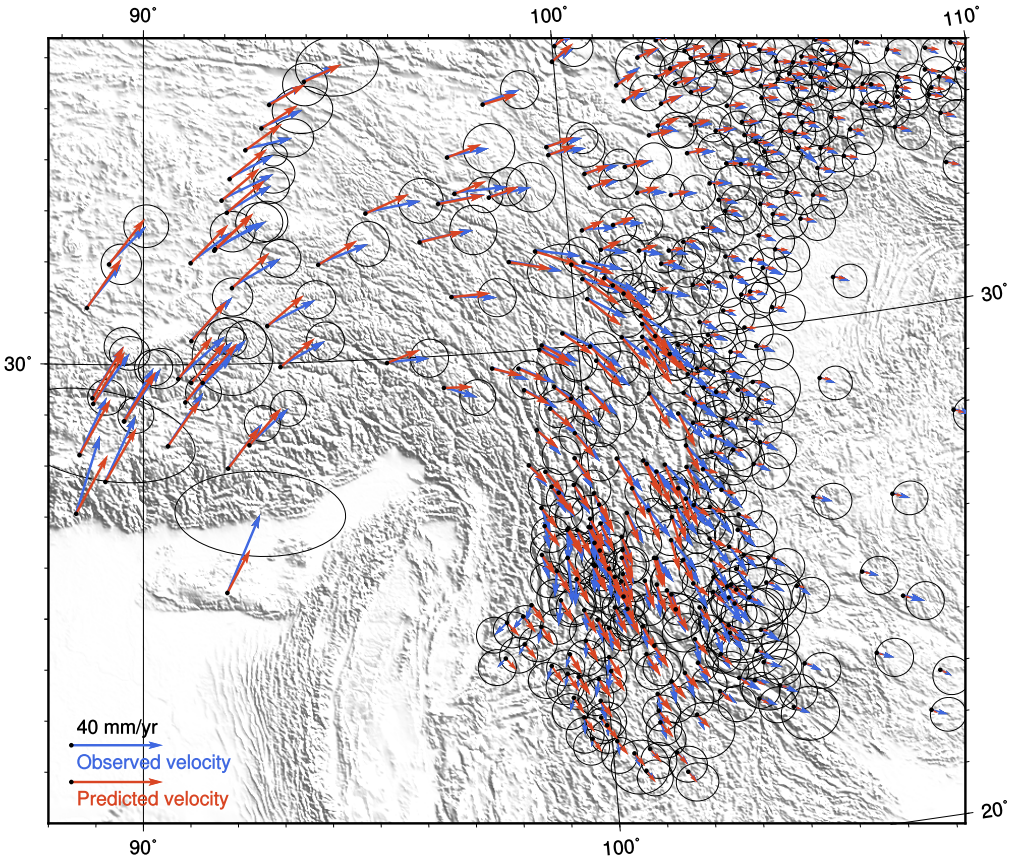


Figure 5.9: Enlarged visualisation of the velocity field in eastern Himalayien syntaxis. Observations for this plot are taken from (Gan et al., 2007). Ellipses correspond to standard deviations (95 % confidence intervals) of the data.

crust and upper mantle lithosphere. These observations agree very well with tomographic images by Ceylan et al. (2012) and Liang et al. (2012) that reveal low velocity zones concentrated along the eastern Kunlun fault at mid-lower crustal down to lithospheric depths, which Ceylan et al. (2012) interpreted as trapped strain heating caused by shearing. Moreover, this profile shows the low viscosity of the 'Tibetan lower C' unit, which can contribute to an decoupling of upper crust and mantle flow (e.g. Royden et al., 1997) in this region.

Fig. 5.11 shows the horizontal velocity components of the model in the Eastern Himalayien syntaxis and for a series of depth levels (0 to 400 km). The figure reveals a decoupled horizontal velocity field in the eastern syntaxis. Whereas at the surface, an extrusive outflow is observed, the horizontal velocity at depth resembles a large scale convection cell, approximately centred on Burma. The flow field at depth is perpendicularly directed to the eastwards subducting Indian lithosphere and is aligned with the surface deformation in Tibet.

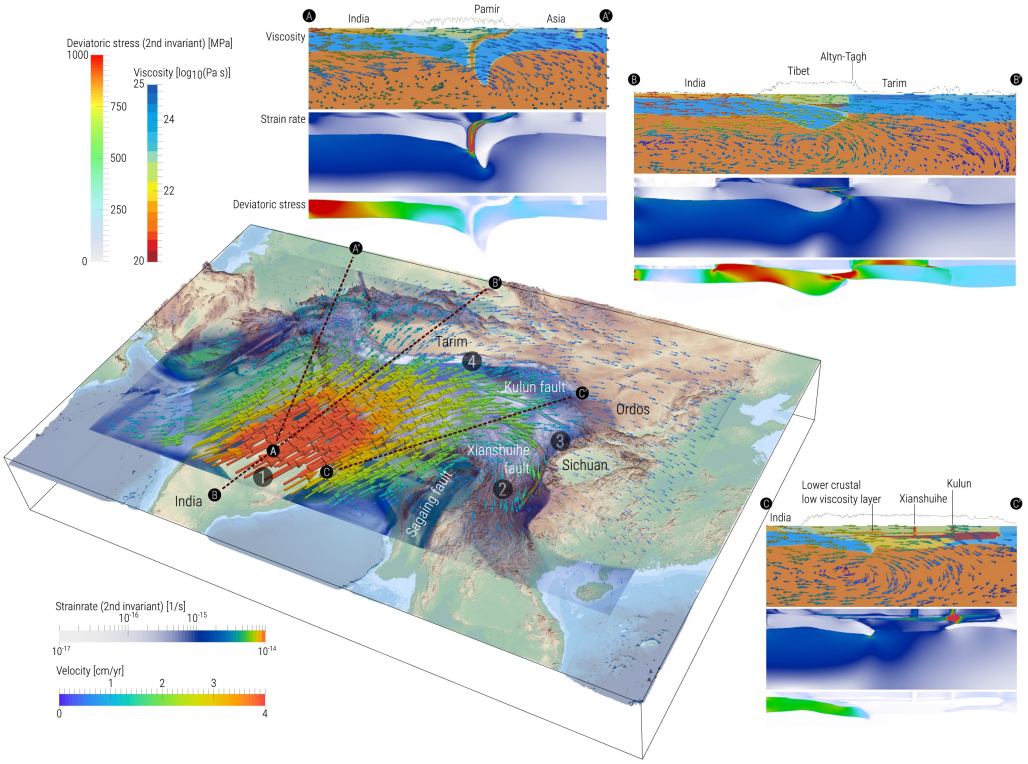


Figure 5.10: Optimised model with best-fit surface velocity field and a exaggerated topography (ETOPO1) for orientation. Three transects (A-C) are given along characteristic collision settings, where viscosity, strain rate and deviatoric stress illustrate the model dynamics. Unlike the surface velocity field, velocity arrow lengths on transects are normalised to illustrate the flow pattern. Markers 1-4 are labels for detailed description in section 5.4.1.7.

*Independent tests*

*The role of a partially molten lower crustal layer in eastern Tibet*

Seismological (e.g. Brown et al., 1996; Nelson et al., 1996; Kind et al., 1996) and magnetotelluric (Le Pape et al., 2012; Bai et al., 2010; Wei et al., 2001) studies suggest a partially molten lower crust in the south eastern syntaxis of the Tibetan plateau that is extended up to the Kunlun fault. This hypothesis is also supported by numerical models that demonstrate the importance of a low-viscosity crustal layer to establish an extrusive return flow field, which is characteristic for eastern Tibet and adjacent regions (e.g. Sternai et al., 2014; Clark & Royden, 2000; Bird, 1991). To account for these observations, we have embedded such a lower crustal layer in the model geometry (see Fig. 5.3). During the optimisation its viscosity value does not deviate much from its initial value and stays low ($\eta = 10^{21.20}$ Pa s). Yet, to estimate its total effect, we remove the volume that assigns low viscosities in this area, such that the material is replaced by the 'Tibet-crust' phase. Fig. 5.12 demonstrates the effect that this modification has on the current best-fit model. The error increase is quite significant, which is about the same order of magnitude as the error reduction of the entire NMDS

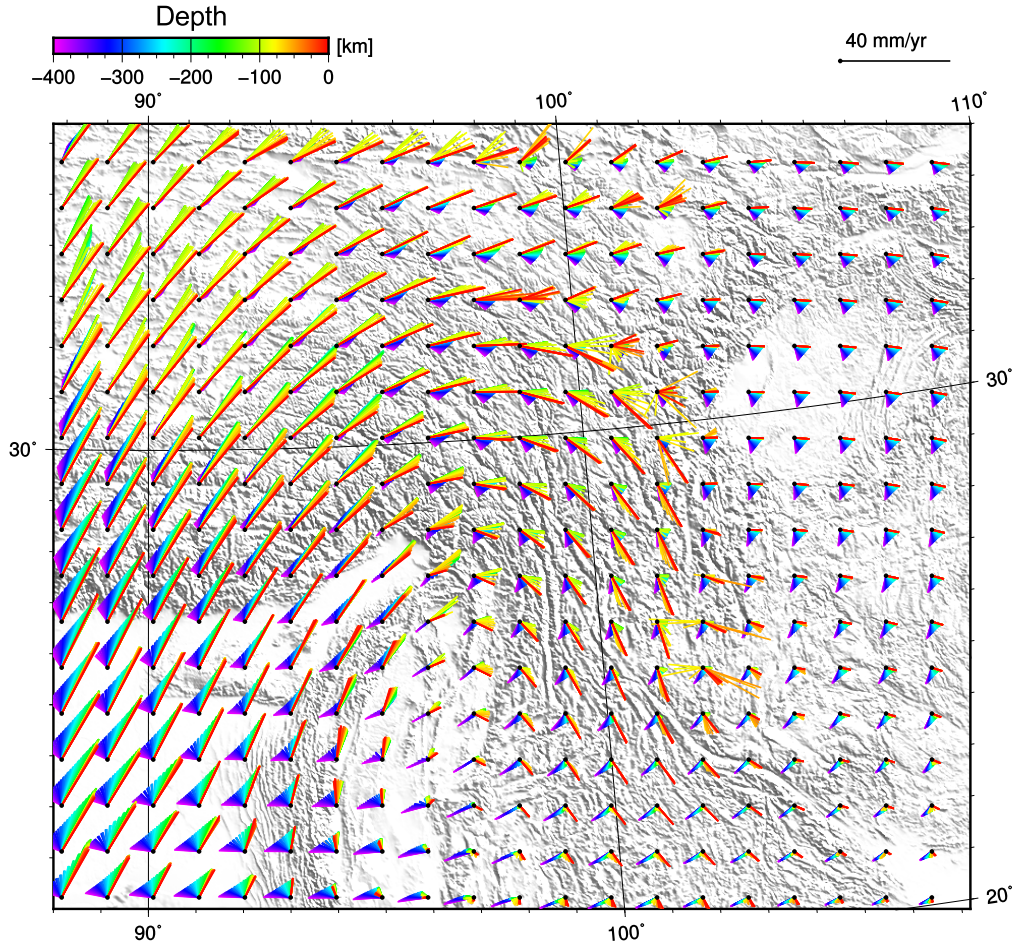


Figure 5.11: Horizontal model velocity field (directions) in eastern Himalayian syntaxis. Velocities are interpolated on a regular grid with a horizontal and vertical spacing of $\delta_h = 100\,\text{km}$ and $\delta_v = 5\,\text{km}$ respectively. Bars are oriented into flow direction. Colours indicate depth levels and bar scales express horizontal velocity magnitudes.

optimisation, but concentrated in the eastern syntaxis. Locally, the absolute error is of the order $> 0.5\,\text{cm/yr}$. This shows that a weak lower crust is required to fit the data.

*Weakening the Indian mantle lithosphere*

As a second example, we illustrate the effect of an Indian mantle lithosphere that is one order of magnitude weaker (viscosity decrease from $10^{24.01}$ to $10^{23.00}$ Pa s) in Fig. 5.13. The new viscosity is still one order of magnitude higher as the viscosity of the Tibetan (SE) mantle lithosphere. Obviously, the Indian mantle lithosphere affects a much larger area compared to the previous test with the weak lower crustal phase. Weakening the Indian ML provokes especially large errors in the central model domain (Tibet and adjacent regions), but also moderate errors at western and eastern bounds. However, some other parts,

such as the northern model boundary in fact improve their fits. The model fit is also improved for a small region in central Tibet.

*The effect of different boundary conditions*

All our simulations so far were performed in a free-slip box. The southern and eastern boundary are additionally damped with thick vertical boundary layers to mimic far field effects. The viscosities of those layers are even integrated into the inversion scheme. However, the northern and western boundary as well as the bottom boundary at 700 km depth were left untouched. We therefore perform an additional test, where the northern 'Eurasian' boundary is modified into a no-slip boundary instead, which is another reasonable choice. In the same manner, we also test a no-slip bottom boundary condition. Yet, both simulations show that the velocity-fit is not affected by these changes. The Eurasian part of the model has a high viscosity (see Tab. 5.2), which strongly attenuates the model velocities.

*Uncertainties of optimisation results*

For a particular set of model parameters we compute an approximation of the Hessian (eq. 5.5) to get an impression of the parameter uncertainties of the optimised solution. Our approach, described in section 5.2.4, can only serve as a first order approximation, simply because the number of forward solves grows quadratically when approximating the components of the Hessian with forward finite differences (eq. 5.4). This is cheaper but also less accurate than higher order approximations, such as central differences. Yet, the forward finite difference approximation for first and second derivatives are computed for 21 selected model viscosities.

As the effective viscosities vary on an exponential scale, our numerical parameter space is scaled to the range $[17.0, \ldots 25.0]$, which corresponds to the $\log_{10}$ values of the cut-off viscosities for which we can generally expect numerically stable results. According to this range, the finite difference increments are set to $\delta_i = +0.25$. The Altyn-Tagh-fault viscosity parameter is an exception in this respect, and $\delta_i = -0.25$ because its viscosity is already very high, such that a further increase results in non-convergence.

By definition, the objective function must be perfectly convex and $\mathcal{H}(f(\mathbf{m}))$ semi positive definite. In reality, the objective function $f(\mathbf{m})$ might be a lot more bumpy and probably bears trade-offs and maybe multiple local minima close to each other, such that the positive definiteness of $\mathcal{H}(f(\mathbf{m}))$ also strongly depends on the particular increments $\delta_i$. In some cases, this analysis results in slightly smaller or similar values of the objective function when increasing a parameter. To enforce the convex shape of $f(\mathbf{m})$ and the semi-positve definiteness of $\mathcal{H}(f(\mathbf{m}))$, we enforce $f(\mathbf{m}_{opt,i} + 2\delta_i \mathbf{e}_i) > f(\mathbf{m}_{opt,i} + \delta_i \mathbf{e}_i) > f(\mathbf{m}_{opt,i})$ by shifting the function values with small $\epsilon_i$ of the order $10^{-4}$. Practically, this can be done by increasing small, but negative eigenvalues of $\mathcal{H}(f(\mathbf{m}))$ by very small increments, to yield an new approximate Hessian $\mathcal{H}^*(f(\mathbf{m}))$. This process can be repeated several times (here 6 iterations) until $\mathcal{H}^*(f(\mathbf{m}))$ is semi-positive

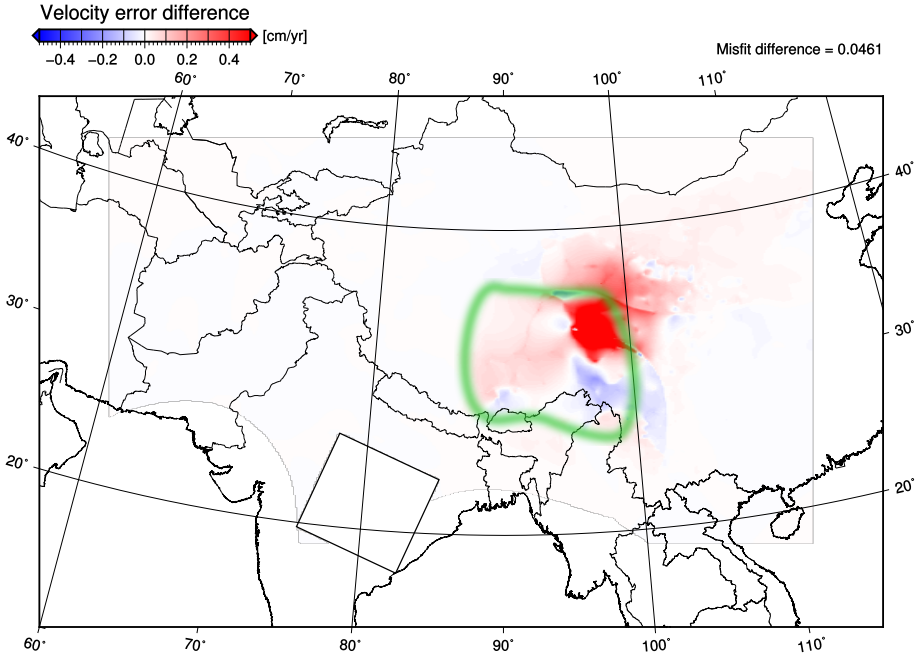


Figure 5.12: The effect of a lower crustal low viscosity (LCLV) layer in eastern Tibet is illustrated as difference in model misfit between the best-fit model and a model without a LCVC layer. The model misfit without LCLV layer is significantly increased. Green outline indicates the lateral extend the LCVC layer.

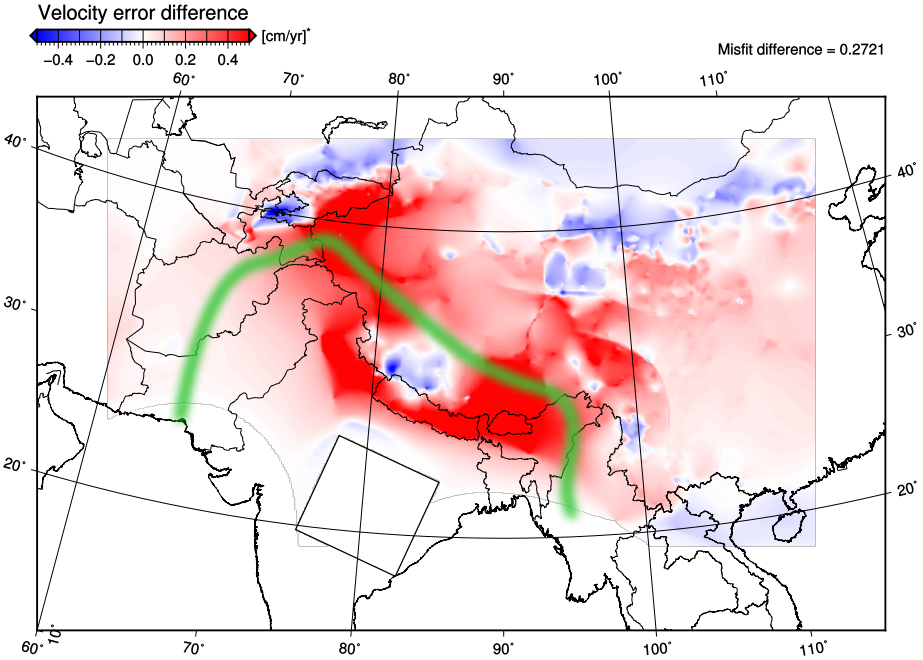


Figure 5.13: Effect of weakening the Indian mantle lithosphere by one order of magnitude (viscosity decrease from $10^{24.01}$ to $10^{23.00}$ Pa s) has a significant deteriorating effect on the model misfit, although the error in northern model boundary locally reduces. Green outline indicates the laterally most extended outline of the northwards subducting Indian mantle lithosphere.

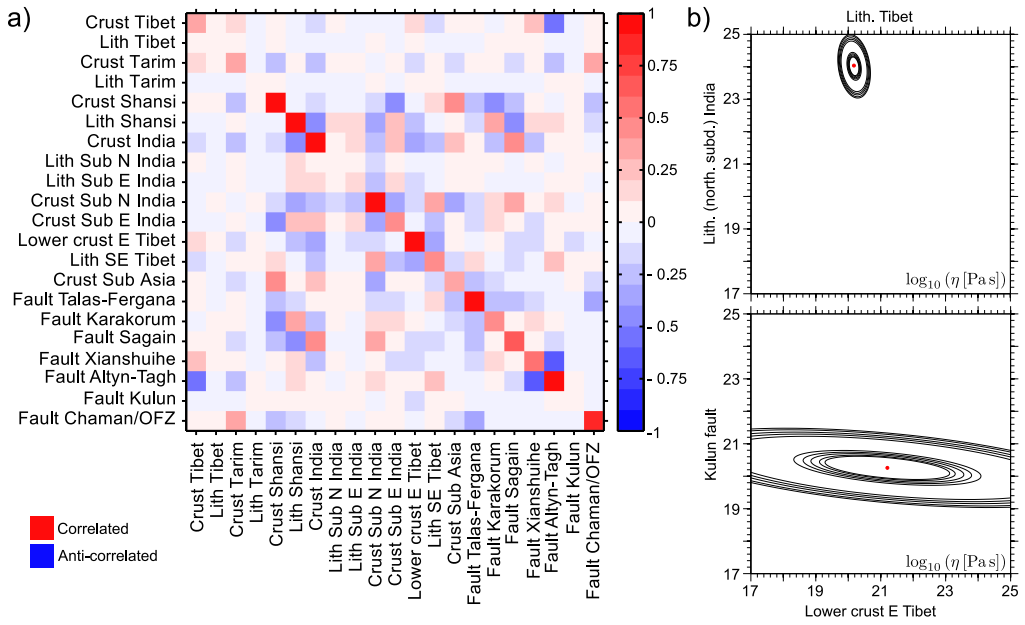


Figure 5.14: **a)** Approximated model covariance matrix for a selected subset of the parameter space. Reddish colours represent positive correlation. bluish colours indicate anti-correlated parameters. Diagonal entries show model parameter variances **b)** Two parameter correlation examples of (a) represented with Gaussian confidence intervals (0.5, 1, 2.5, 5, 10 % and 90, 95, 97.5, 99, 99.5 % ). Both examples show anti-correlated parameters. The upper case shows that viscosities of Indian and Tibetan mantle lithosphere are well constrained. We find a strong Indian shield and a weak Tibetan mantle lithosphere. Both have low correlation with other parameters as well (see a). The lower example is more specific and illustrates a stronger correlation between the a weak lower crustal layer in eastern Tibet and the Kunlun fault.

definite. According to eq. 5.6, we compute the covariance matrix, by inverting $\mathcal{H}^*(f(\mathbf{m}))$ and scaling it with the data variance, for which we assume a constant standard deviation of $\sigma = 1\,\mathrm{mm/year}$.

The model covariance is given in Fig. 5.14. Fig. 5.14a shows the colour-coded covariance matrix, where negative correlation is indicated with bluish and positive correlation with reddish colours. Standard deviations in a Gaussian sense can be computed from the diagonal of the covariance matrix, which is equivalent to model parameter variances, i.e. $\sigma_i = \sqrt{\mathrm{diag}([\mathrm{Cov}\, m_i])}$. An overview of these standard deviations is given in Tab. 5.3. Both, this listing and 5.14a reveal that the mantle lithosphere of Tibet and Tarim, the Kulun fault and that part of the Indian lithosphere that is underthrusting Tibet have small variances and covariances in particular. This is also partly the case for the eastwards subducting-Indian mantle lithosphere, referred to as Burma slab. All of these model viscosities have a significant impact on the dynamics of the model.

Our interpretation of this behaviour is as follows. The Indian lithosphere has to be strong (high viscosity) and a large convergence rate ($34 - 44\,\mathrm{mm/yr}$, Molnar & Stock, 2009) can only be observed if a weak Tibetan Mantle lithosphere is

| Name | $\log_{10}(\eta_{i,opt.} \pm \sigma_i\,[\mathrm{Pa\,s}])$ |
|---|---|
| Crust Tibet | $22.62 \pm 0.56$ |
| Lith Tibet | $20.18 \pm 0.10$ |
| Crust Tarim | $24.61 \pm 0.59$ |
| Lith Tarim | $23.92 \pm 0.01$ |
| Crust Sichuan | $24.66 \pm 1.17$ |
| Lith Sichuan | $23.14 \pm 0.99$ |
| Crust India | $21.65 \pm 0.99$ |
| Lith Sub N India | $24.01 \pm 0.19$ |
| Lith Sub E India | $22.71 \pm 0.36$ |
| Crust Sub N India | $22.99 \pm 0.95$ |
| Crust Sub E India | $22.95 \pm 0.67$ |
| Lower crust E Tibet | $21.20 \pm 1.31$ |
| Lith SE Tibet | $21.82 \pm 0.66$ |
| Crust Sub Asia | $21.24 \pm 0.62$ |
| Fault Talas-Fergana | $21.91 \pm 1.30$ |
| Fault Karakorum | $22.74 \pm 0.69$ |
| Fault Sagaing | $22.31 \pm 0.80$ |
| Fault Xianshuihe | $19.56 \pm 0.73$ |
| Fault Altyn Tagh | $23.97 \pm 1.08$ |
| Fault Kunlun | $20.26 \pm 0.24$ |
| Fault Chaman/Owen-Fracture-Zone | $22.62 \pm 0.91$ |

Table 5.3: Optimisation results and model uncertainties for selected parameters. Uncertainties result from the diagonal of the model covariance matrix given in Fig. 5.14a.

able to accommodate the strong indenter. In addition, the Tarim basin plays an important role as a strong resisting block is in agreement with earlier studies (e.g. Cook & Royden, 2008). The modelling results show that this behaviour can not easily be adopted by other tectonic blocks and there are little trade-offs with other model parameters. The Tibetan crust also does not show any correlation except with the lower crustal part in eastern Tibet that was introduced additionally (see 5.4.2.1). The Kunlun fault, and this was already qualitatively observed during the NMDS inversion plays a key role without any significant correlation with other parts of the model. The role of the Burma slab is more complicated as it is correlated with a couple of other units, such as the Sichuan basin (crust and mantle lithosphere). However, its viscosity matters because it controls the return flow in the eastern Himalayan syntaxis within the mantle.

In Fig. 5.14b, we illustrate the parameter correlation with Gaussian error ellipses for two end-member cases. In the upper example, the viscosity solution is plotted for Indian and Tibetan lithosphere, where standard deviations are relatively small and only a very moderate negative correlation exists, meaning if India would have a higher viscosity, the viscosity of the Tibetan lithosphere would decrease at the same time to accommodate the change. The other example shows a stronger correlation of the viscosities in the Tibetan lower crust and the Kunlun fault. Both have an impact on the eastern syntaxis flow field within the crust and the result shows that a stronger lower Tibetan crust would require a stronger Kunlun fault as well to explain the (clockwise rotational) dynamics. This observation is in agreement with Fig. 5.10, which shows that both units are coupled.

## DISCUSSION

### *Forward model*

The resolution of tomographic images is limited and varies significantly between P-wave and S-wave tomographies, such that the interpretation of this data remains very challenging and involves a lot of uncertainty. Here, we tried to incorporate a large number of additional, independent constraints, such as signals of LAB and Moho from receiver functions of independent studies. Yet, creating a three dimensional model structure based on such a large data set also leaves some room for personal interpretation, hence, variance. This also applies to deeper model regions, where the resolution of tomographic models noticeably decreases.

Our boundary conditions are chosen to be free-slip at all sides, which can be discussed, yet the effect was tested to not influence the inversion result. The effect of the bottom boundary is negligible because in our model, slabs do not reach very deep, close to this boundary. Of course, this must be re-assessed when the model geometry accounts for deep hanging slabs that might be visible in future with improved tomographic images. Compared to similar studies (e.g. Lechmann et al., 2014; Cook & Royden, 2008), our model does not take into account a free surface. This certainly has to be tested, how topography affects the horizontal flow field in a fully dynamic 3D model. Nevertheless, as the current model fit without topography is already reasonably good, and taking into account that deflections of the Earth's surface induced by dynamic effects is not more than 300 m (Molnar et al., 2015), we only expect a minor impact.

In our model, we add an additional internal velocity boundary, which is a defined area of prescribed velocity and direction. This approach is justified due to the fact that the Indian continent shows little internal deformation almost moves with a constant, reliably observed velocity (Molnar & Stock, 2009). However, this effect might be overestimated due to the fact that the connection between subducted cratonic Indian mantle lithosphere and even older (deeper) parts of the subducted slab is not represented in our model. A change in mech-

anism, and especially a dynamically sensitive connection of subducted Indian lithosphere and old oceanic slabs might cause changes of the best-fit rheology.

*Inversion method and challenges*

We use a steepest gradient alike inversion method that is capable to find a local solution. However, multiple solutions and trade-offs between correlated parameters are likely to coexist (Baumann & Kaus, 2015; Baumann et al., 2014). We partly overcome this issue by computing the approximate Hessian to estimate parameter uncertainties and identify correlated parameters. Hence, estimated trade-offs at least give a hint which other parameter combinations (models) are likely to give similar accurate results. However, this approach has the strong assumption that one has to be already close to the global solution. To fully over come this problem, a probabilistic sampling based approach has to be aimed for, although it might be computationally challenging without very good prior knowledge on the rheological properties and we believe that the results of this study can certainly contribute to find good prior conditions.

As inversion results are usually ambiguous, additional data constraints can be used for regularisation. Here , we only used the GPS-velocities, because we were primarily interested in reproducing the characteristic surface velocity field of Tibet and adjacent regions. However, when inverting for complex (power-law) rheologies, one has to reduce the ill-posed character of the inverse problem by including other observational data in the inversion process (Baumann & Kaus, 2015).

## CONCLUSIONS

Using a highly resolved geodynamic 3D model, we can reproduce the surface velocity field of the India-Asia collision system reasonably well and find optimal viscosities for predefined geological units. We find that only an interaction of end-member models proposed in literature, can do a reasonable job in explaining the surface deformation field.

1. Our model demonstrates that strike-slip zones within the crust are important. This confirms kinematic models favouring a brittle behaviour and a major role of strike slip faults.

2. We find that the Kunlun and Xianshuihe faults are most ‘active’, in the sense that we observed largest strain rates for them. Opposing to this, the Altyn-Tagh fault is effectively locked.

3. Lateral heterogeneities play a major role too, in agreement with thin viscous sheet models that incorporate Tarim and Sichuan basin for example. In fact, we find the lowest uncertainties for the high viscosity Tarim mantle lithosphere.

4. Models with vertically averaged viscosities can serve as a good first approximation for the observed surface deformation. However, they can-

not be a sufficient explanation, because important aspects are underestimated. Our results demonstrate the importance of vertical heterogeneities in the crust (low viscosity zones) and lithosphere (strong Indian and weak Tibetan) with acceptable standard deviations. A strong Indian mantle lithosphere indenting in a weak Tibetan mantle lithosphere also confirms our previous findings (Baumann & Kaus, 2015).

## REFERENCES

Agius, M. R. & Lebedev, S., 2013. Tibetan and Indian lithospheres in the upper mantle beneath Tibet: Evidence from broadband surface-wave dispersion, *Geochem. Geophys. Geosyst.*, **14**(10), 4260–4281.

Amante, C. & Eakins, B. W., 2009. *ETOPO1 1 arc-minute global relief model: procedures, data sources and analysis*, US Department of Commerce, National Oceanic and Atmospheric Administration, National Environmental Satellite, Data, and Information Service, National Geophysical Data Center, Marine Geology and Geophysics Division.

Avouac, J. & Tapponnier, P., 1993. Kinematic model of active deformation in central Asia, *Geophys. Res. Lett.*, **20**(10), 895.

Bai, D., Unsworth, M. J., Meju, M. a., Ma, X., Teng, J., Kong, X., Sun, Y., Sun, J., Wang, L., Jiang, C., Zhao, C., Xiao, P., Liu, M., & Others, 2010. Crustal deformation of the eastern Tibetan plateau revealed by magnetotelluric imaging, *Nat. Geosci.*, **3**(5), 358–362.

Balay, S., Abhyankar, S., Adams, M. F., Brown, J., Brune, P., Buschelman, K., Eijkhout, V., Gropp, W. D., Kaushik, D., Knepley, M. G., & Others, 2014. PETSc users manual: Technical Report ANL-95/11-Revision 3.5, *Argonne Natl. Lab.*.

Baumann, T. S. & Kaus, B. J. P., 2015. Geodynamic inversion to constrain the non-linear rheology of the lithosphere, *Geophys. J. Int.*, **202**(2), 1289–1316.

Baumann, T. S., Kaus, B. J., & Popov, A. A., 2014. Constraining effective rheology through parallel joint geodynamic inversion, *Tectonophysics*, **631**, 197–211.

Bauville, A. & Baumann, T. S., 2015. Geometry I/O: A library for geoscientists to transfer 2D interpretations into 3D geometries, https://geomio.bitbucket.org/.

Beaumont, C., Jamieson, R. a., Nguyen, M. H., & Lee, B., 2001. Himalayan tectonics explained by extrusion of a low-viscosity crustal channel coupled to focused surface denudation., *Nature*, **414**(6865), 738–742.

Bird, P., 1991. Lateral extrusion of lower crust from under high topography in the isostatic limit, *J. Geophys. Res. Solid Earth*, **96**(B6), 10275–10286.

Brown, L. D., Zhao, W., Nelson, K. D., Hauck, M., Alsdorf, D., Ross, A., Cogan, M., Clark, M., Liu, X., & Che, J., 1996. Bright spots, structure, and magmatism in southern Tibet from INDEPTH seismic reflection profiling, *Science*, **274**(5293), 1688–1690.

Burov, E. B. & Watts, A. B., 2006. The long-term strength of continental lithosphere : 'jelly sandwich' or 'crème brûlée'?, *GSA today*, **16**(1), 4–10.

Cai, M., Nonaka, A. J., Bell, J. B., Griffith, B. E., & Donev, A., 2014. Efficient variable-coefficient finite-volume Stokes solvers, *Comp. Phys.(CiCP)*, **16**, 1263–1297.

Capitanio, F. A., Morra, G., Goes, S., Weinberg, R. F., & Moresi, L., 2010. India–Asia convergence driven by the subduction of the Greater Indian continent, *Nat. Geosci.*, **3**(2), 136–139.

Ceylan, S., Ni, J., Chen, J. Y., Zhang, Q., Tilmann, F., & Sandvol, E., 2012. Fragmented Indian plate and vertically coherent deformation beneath eastern Tibet, *J. Geophys. Res.*, **117**(B11), B11303.

Clark, M. K. & Royden, L. H., 2000. Topographic ooze:Building the eastern margin of Tibet by lower crustal flow, *Geology*, **28**, 703–706.

Cook, K. L. & Royden, L. H., 2008. The role of crustal strength variations in shaping orogenic plateaus, with application to Tibet, *J. Geophys. Res. Solid Earth*, **113**(B8).

Copley, A., Avouac, J.-P., & Wernicke, B. P., 2011. Evidence for mechanical coupling and strong Indian lower crust beneath southern Tibet., *Nature*, **472**(7341), 79–81.

Dennis Jr., J. E. & Schnabel, R. B., 1996. *Numerical methods for unconstrained optimization and nonlinear equations*, vol. 16, Siam.

Dziewonski, A. M. & Anderson, D. L., 1981. Preliminary reference earth model, *Phys. Earth Planet. In.*, **25**(4), 297–356.

Dziewonski, A. M., Chou, T.-A., & Woodhouse, J. H., 1981. Determination of earthquake source parameters from waveform data for studies of global and regional seismicity, *J. Geophys. Res. Solid Earth*, **86**(B4), 2825–2852.

Ekström, G., Nettles, M., & Dziewoński, A., 2012. The global cmt project 2004–2010: centroid-moment tensors for 13,017 earthquakes, *Phys. Earth Planet. In.*, **200**, 1–9.

England, P. & Houseman, G., 1985. Role of lithospheric strength heterogeneities in the tectonics of Tibet and neighbouring regions, *Nature*, **315**(6017), 297–301.

England, P. & Houseman, G., 1986. Finite strain calculations of continental deformation: 2. Comparison with the India-Asia collision zone, *J. Geophys. Res. Solid Earth*, **91**(B3), 3664–3676.

England, P. & McKenzie, D., 1982. A thin viscous sheet model for continental deformation, *Geophys. J. Int.*, **70**(2), 295–321.

Feld, C., Haberland, C., Schurr, B., Sippl, C., Wetzel, H.-U., Roessner, S., Ickrath, M., Abdybachaev, U., & Orunbaev, S., 2015. Seismotectonic study of the Fergana Region (Southern Kyrgyzstan): distribution and kinematics of local seismicity, *Earth, Planets Sp.*, **67**(1), 40.

Flesch, L. M., Holt, E., Haines, A. J., & Holt, W. E., 2001. Dynamics of the India-Eurasia collision zone, *J. Geophys. Res. Solid Earth*, **106**(B8), 16435–16460.

Gan, W., Zhang, P., Shen, Z.-K., Niu, Z., Wang, M., Wan, Y., Zhou, D., & Cheng, J., 2007. Present-day crustal motion within the Tibetan Plateau inferred from GPS measurements, *J. Geophys. Res.*, **112**(B8), B08416.

Gao, R., Chen, C., Lu, Z., Brown, L. D., Xiong, X., Li, W., & Deng, G., 2013. New constraints on crustal structure and Moho topography in Central Tibet revealed by SinoProbe deep seismic reflection profiling, *Tectonophysics*, **606**, 160–170.

Ghose, S., Hamburger, M. W., & Ammon, C. J., 1998. Source parameters of moderate–sized earthquakes in the Tien Shan, central Asia from regional moment tensor inversion, *Geophys. Res. Lett.*, **25**(16), 3181–3184.

Gordon, R. G. & DeMets, C., 1989. Present-day motion along the Owen fracture zone and Dalrymple trough in the Arabian Sea, *J. Geophys. Res*, **94**, 5560–5570.

Harlow, F. H., Welch, J. E., & Others, 1965. Numerical calculation of time-dependent viscous incompressible flow of fluid with free surface, *Phys. fluids*, **8**(12), 2182.

He, R., Zhao, D., Gao, R., & Zheng, H., 2010. Tracing the Indian lithospheric mantle beneath central Tibetan Plateau using teleseismic tomography, *Tectonophysics*, **491**(1-4), 230–243.

Houseman, G. & England, P., 1986. Finite strain calculations of continental deformation: 1. Method and general results for convergent zones, *J. Geophys. Res. Solid Earth*, **91**(B3), 3651–3663.

Houseman, G. A., McKenzie, D. P., & Molnar, P., 1981. Convective instability of a thickened boundary layer and its relevance for the thermal evolution of continental convergent belts, *J. Geophys. Res. Solid Earth*, **86**(B7), 6115–6132.

Jackson, J., 2002. Strength of the continental lithosphere: Time to abandon the jelly sandwich?, *GSA today*, **12**(9), 4–9.

Jagoutz, O., Royden, L., Holt, A. F., & Becker, T. W., 2015. Anomalously fast convergence of India and Eurasia caused by double subduction, *Nat. Geosci.*, **8**(May).

Kaus, B. J. P., Popov, A. A., Baumann, T. S., Püsök, A. E., Bauville, A., Fernandez, N., & Collignon, M., 2016. Forward and inverse modeling of lithospheric deformation on geological timescales, in *NIC Symp. 2016-proceedings*, vol. 48, John von Neumann-Institut für Computing.

Kind, R., Ni, J., Zhao, W., Wu, J., Yuan, X., Zhao, L., Sandvol, E., Reese, C., Nabelek, J., & Hearn, T., 1996. Evidence from earthquake data for a partially molten crustal layer in southern Tibet, *Science*, **274**(5293), 1692–1694.

Kosarev, G., Kind, R., Sobolev, S., Yuan, X., Hanka, W., & Oreshin, S., 1999. Seismic Evidence for a Detached Indian Lithospheric Mantle Beneath Tibet, *Science*, **283**(5406), 1306–1309.

Kumar, P., Yuan, X., Kind, R., & Ni, J., 2006. Imaging the colliding Indian and Asian lithospheric plates beneath Tibet, *J. Geophys. Res.*, **111**(B6), B06308.

Laske, G., Masters, G., Ma, Z., & Pasyanos, M., 2013. Update on CRUST1.0 - A 1-degree global model of Earth's crust, in *Geophys. Res. Abstr.*, no. EGU2013-2658 in 15.

Le Pape, F., Jones, A. G., Vozar, J., & Wenbo, W., 2012. Penetration of crustal melt beyond the Kunlun Fault into northern Tibet, *Nat. Geosci.*, **5**(5), 330–335.

Lechmann, S. M., Schmalholz, S. M., Hetenyi, G., May, D. A., & Kaus, B. J. P., 2014. Quantifying the impact of mechanical layering and underthrusting on the dynamics of the modern India-Asia collisional system with 3-D numerical models, *J. Geophys. Res. Solid Earth*, **119**(1), 616–644.

Li, C., Van Der Hilst, R. D., Engdahl, E. R., & Burdick, S., 2008a. A new global model for P wave speed variations in Earth's mantle, *Geochem. Geophys. Geosyst.*, **9**(5).

Li, C., van der Hilst, R. D., Meltzer, A. S., & Engdahl, E. R., 2008b. Subduction of the Indian lithosphere beneath the Tibetan Plateau and Burma, *Earth Planet. Sci. Lett.*, **274**(1-2), 157–168.

Liang, S., Gan, W., Shen, C., Xiao, G., Liu, J., Chen, W., Ding, X., & Zhou, D., 2013. Three-dimensional velocity field of present-day crustal motion of the Tibetan Plateau derived from GPS measurements, *J. Geophys. Res. Solid Earth*, **118**(10), 5722–5732.

Liang, X., Sandvol, E., Chen, Y. J., Hearn, T., Ni, J., Klemperer, S., Shen, Y., & Tilmann, F., 2012. A complex Tibetan upper mantle: A fragmented Indian slab and no south-verging subduction of Eurasian lithosphere, *Earth Planet. Sci. Lett.*, **333-334**, 101–111.

McKenzie, D. & Priestley, K., 2008. The influence of lithospheric thickness variations on continental evolution, *Lithos*, **102**(1-2), 1–11.

Mechie, J. & Kind, R., 2013. A model of the crust and mantle structure down to 700km depth beneath the Lhasa to Golmud transect across the Tibetan plateau as derived from seismological data, *Tectonophysics*, **606**, 187–197.

Menke, W., 2012. *Geophysical data analysis: discrete inverse theory*, Academic press.

Molnar, P. & Stock, J. M., 2009. Slowing of India's convergence with Eurasia since 20 Ma and its implications for Tibetan mantle dynamics, *Tectonics*, **28**(3), 1–11.

Molnar, P. & Tapponier, P., 1975. Cenozoic Tectonics of Asia: Effects of a Continental Collision, *Science*, **189**(4201), 419–426.

Molnar, P., England, P. C., & Jones, C. H., 2015. Mantle dynamics, isostasy, and the support of high terrain, *J. Geophys. Res. Solid Earth*, **120**(3), 1932–1957.

Nábelek, J., Hetényi, G., Vergne, J., Sapkota, S., Kafle, B., Jiang, M., Su, H., Chen, J., & Huang, B.-S., 2009. Underplating in the Himalaya-Tibet collision zone revealed by the Hi-CLIMB experiment., *Science*, **325**(5946), 1371–4.

Nelder, J. A. & Mead, R., 1965. A simplex method for function minimization, *Comput. J.*, **7**(4), 308–313.

Nelson, K. D., Zhao, W., Brown, L. D., Kuo, J., Che, J., Liu, X., Klemperer, S. L., Makovsky, Y., Meissner, R., Mechie, J., Kind, R., Wenzel, F., Ni, J., Nabelek, J., Leshou, C., Tan, H., Wei, W., Jones, a. G., Booker, J., Unsworth, M., Kidd, W. S. F., Hauck, M., Alsdorf, D., Ross, A., Cogan, M., Wu, C., Sandvol, E., & Edwards, M., 1996. Partially Molten Middle Crust Beneath Southern Tibet: Synthesis of Project INDEPTH Results, *Science*, **274**(5293), 1684–1688.

Pandey, S., Yuan, X., Debayle, E., Priestley, K., Kind, R., Tilmann, F., & Li, X., 2014. A 3D shear-wave velocity model of the upper mantle beneath China and the surrounding areas, *Tectonophysics*, **633**, 193–210.

Priestley, K., Debayle, E., McKenzie, D., & Pilidou, S., 2006. Upper mantle structure of eastern Asia from multimode surface waveform tomography, *J. Geophys. Res.*, **111**(B10), B10304.

Priestley, K., Jackson, J., & McKenzie, D., 2008. Lithospheric structure and deep earthquakes beneath India, the Himalaya and southern Tibet, *Geophys. J. Int.*, **172**(1), 345–362.

Rai, S. S., Priestley, K., Gaur, V. K., Mitra, S., Singh, M. P., & Searle, M., 2006. Configuration of the Indian Moho beneath the NW Himalaya and Ladakh, *Geophys. Res. Lett.*, **33**(15), L15308.

Royden, L., 1996. Coupling and decoupling of crust and mantle in convergent orogens: Implications for strain partitioning in the crust, *J. Geophys. Res. Solid Earth*, **101**(B8), 17679–17705.

Royden, L. H., Burchfiel, B. C., King, R. W., Wang, E., Chen, Z., Shen, F., & Liu, Y., 1997. Surface Deformation and Lower Crustal Flow in Eastern Tibet, *Science*, **276**(5313), 788–790.

Royden, L. H., Burchfiel, B. C., Hilst, R. D. V. D., & van der Hilst, R. D., 2008. The Geological Evolution of the Tibetan Plateau, *Science*, **321**(5892), 1054–1058.

Schaeffer, A. J. & Lebedev, S., 2013. Global shear speed structure of the upper mantle and transition zone, *Geophys. J. Int.*, **194**(1), 417–449.

Schneider, F., Yuan, X., Schurr, B., Mechie, J., Sippl, C., Haberland, C., Minaev, V., Oimahmadov, I., Gadoev, M., Radjabov, N., Abdybachaev, U., Orunbaev, S., & Negmatullaev, S., 2013. Seismic imaging of subducting continental lower crust beneath the Pamir, *Earth Planet. Sci. Lett.*, **375**, 101–112.

Schulte-Pelkum, V., Monsalve, G., Sheehan, A., Pandey, M. R., Sapkota, S., Bilham, R., & Wu, F., 2005. Imaging the Indian subcontinent beneath the Himalaya., *Nature*, **435**(7046), 1222–5.

Sippl, C., Schurr, B., Tympel, J., Angiboust, S., Mechie, J., Yuan, X., Schneider, F., Sobolev, S., Ratschbacher, L., & Haberland, C., 2013. Deep burial of Asian continental crust beneath the Pamir imaged with local earthquake tomography, *Earth Planet. Sci. Lett.*, **384**, 165–177.

Sternai, P., Jolivet, L., Menant, A., & Gerya, T., 2014. Driving surface deformation by mantle flow, *Earth Planet. Sci. Lett.*, **16**, 5068.

Tapponnier, P. & Molnar, P., 1976. Slip-line field theory and large-scale continental tectonics, *Nature*, **264**(5584), 319–324.

Tapponnier, P., Peltzer, G., Le Dain, a. Y., Armijo, R., & Cobbold, P., 1982. Propagating extrusion tectonics in Asia: new insights from simple experiments with plasticine., *Geology*, **10**(12), 611–616.

Tapponnier, P., Zhiqin, X., Roger, F., Meyer, B., Arnaud, N., Wittlinger, G., & Jingsui, Y., 2001. Oblique stepwise rise and growth of the Tibet plateau., *Science*, **294**(5547), 1671–1677.

Van Hinsbergen, D. J. J., Steinberger, B., Doubrovine, P. V., & Gassmöller, R., 2011. Acceleration and deceleration of India-Asia convergence since the Cretaceous: Roles of mantle plumes and continental collision, *J. Geophys. Res. Solid Earth*, **116**(6), 1–20.

Vergne, J., Wittlinger, G., Hui, Q., Tapponnier, P., Poupinet, G., Mei, J., Herquel, G., & Paul, A., 2002. Seismic evidence for stepwise thickening of the crust across the NE Tibetan plateau, *Earth Planet. Sci. Lett.*, **203**(1), 25–33.

Vergnolle, M., Calais, E., & Dong, L., 2007. Dynamics of continental deformation in Asia, *J. Geophys. Res.*, **112**(B11), B11403.

Vernant, P., Nilforoushan, F., Hatzfeld, D., Abbassi, M. R., Vigny, C., Masson, F., Nankali, H., Martinod, J., Ashtiani, A., Bayer, R., Tavakoli, F., & Chéry, J., 2004. Present-day crustal deformation and plate kinematics in the Middle East constrained by GPS measurements in Iran and northern Oman, *Geophys. J. Int.*, **157**(1), 381–398.

Wang, H., Agrusta, R., & van Hunen, J., 2015. Advantages of a conservative velocity interpolation (cvi) scheme for particle-in-cell methods with application in geodynamic modeling, *Geochem. Geophys. Geosyst.*, **16**(6), 2015–2023.

Wei, W., Unsworth, M., Jones, A., Booker, J., Tan, H., Nelson, D., Chen, L., Li, S., Solon, K., Bedrosian, P., Jin, S., Deng, M., Ledo, J., Kay, D., & Roberts, B., 2001. Detection of widespread fluids in the Tibetan crust by magnetotelluric studies., *Science*, **292**(5517), 716–719.

Wittlinger, G., Vergne, J., Tapponnier, P., Farra, V., Poupinet, G., Jiang, M., Su, H., Herquel, G., & Paul, A., 2004. Teleseismic imaging of subducting lithosphere and Moho offsets beneath western Tibet, *Earth Planet. Sci. Lett.*, **221**(1-4), 117–130.

Xu, T., Wu, Z., Zhang, Z., Tian, X., Deng, Y., Wu, C., & Teng, J., 2014. Crustal structure across the Kunlun fault from passive source seismic profiling in East Tibet, *Tectonophysics*, **627**, 98–107.

Zhang, P.-Z., Shen, Z., Wang, M., Gan, W., Bürgmann, R., Molnar, P., Wang, Q., Niu, Z., Sun, J., Wu, J., Hanrong, S., & Xinzhao, Y., 2004. Continuous deformation of the Tibetan Plateau from global positioning system data, *Geology*, **32**(9), 809.

Zhang, Z., Wang, Y., Houseman, G. a., Xu, T., Wu, Z., Yuan, X., Chen, Y., Tian, X., Bai, Z., & Teng, J., 2014. The Moho beneath western Tibet: Shear zones and eclogitization in the lower crust, *Earth Planet. Sci. Lett.*, **408**, 370–377.

Zhao, J., Yuan, X., Liu, H., Kumar, P., Pei, S., Kind, R., Zhang, Z., Teng, J., Ding, L., & Gao, X., 2010. The boundary between the Indian and Asian tectonic plates below Tibet, *Proc. Natl. Acad. Sci.*, **107**(25), 11229–11233.

Zubovich, A. V., Wang, X.-q., Scherba, Y. G., Schelochkov, G. G., Reilinger, R., Reigber, C., Mosienko, O. I., Molnar, P., Michajljow, W., Makarov, V. I., Li, J., Kuzikov, S. I., Herring, T. a., Hamburger, M. W., Hager, B. H., Dang, Y.-m., Bragin, V. D., & Beisenbaev, R. T., 2010. GPS velocity field for the Tien Shan and surrounding regions, *Tectonics*, **29**(6).

## APPENDIX

### *Numerical formulation of the forward problem*

Here, we summarise the key aspects of the detailed description given in (Kaus et al., 2016). The conservation equations (5.1)-(5.2) are discretised with staggered grid finite differences (Harlow et al., 1965). This is a low-order and stable discretisation for (nearly) incompressible fluid flow. The implementation is parallelised using the PETSc library (Balay et al., 2014) and we make use of distributed arrays (DMDA) and iterative solvers (KSP, SNES) to gain a high scalability on massively parallel computers.

Material properties are retained with markers within the frame of a Marker And Cell (MAC) method (Harlow et al., 1965), which corresponds to material advection in an Eulerian kinematical framework. The advection scheme is implemented with a combination of a $4^{th}$-order Runge-Kutta method and a

conservative velocity interpolation to avoid artificial clustering effects of the markers (Wang et al., 2015).

In each time step iteration $k$, we solve the entire coupled system of nonlinear algebraic equations using a combination of the preconditioned Jacobian-Free Newton-Krylov (JFNK) and a line-search method, such as implemented in the PETSc SNES nonlinear solver framework (Balay et al., 2014):

$$\mathbf{A}^{-1}\mathbf{J}\left(\mathbf{x}_k\right)\delta\mathbf{x}_k = -\mathbf{A}^{-1}\mathbf{r}\left(\mathbf{x}_k\right), \quad \mathbf{x}_{k+1} = \mathbf{x}_k + \alpha\,\delta\mathbf{x}_k, \tag{5.8}$$

where $\mathbf{r}$ and $\mathbf{x}$ are the coupled residual and solution vectors, and $\delta\mathbf{x}$ the iterative correction vector, respectively. $\alpha$ indicates the line-search step length.

We use the current effective viscosity to obtain the preconditioning matrix ($\mathbf{A}$) by discretising the conservation equations (5.1-5.2).

$$\mathbf{A} = \begin{pmatrix} \mathbf{K} & \mathbf{G} \\ \mathbf{D} & \mathbf{C} \end{pmatrix}, \tag{5.9}$$

where $\mathbf{K}$ and $\mathbf{C}$ indicate the stiffness matrices of the velocity and pressure blocks, respectively. $\mathbf{G}$ denotes the pressure gradient matrix and $\mathbf{D}$ is the velocity divergence matrix.

The Jacobian ($\mathbf{J}$) is defined implicitly by a matrix-vector product approximated by finite differencing.

$$\mathbf{J}\mathbf{y} \approx \frac{\mathbf{r}\left(\mathbf{x} + h\,\mathbf{y}\right) - \mathbf{r}\left(\mathbf{x}\right)}{h}, \tag{5.10}$$

where $h$ denotes the perturbation parameter and $\mathbf{y}$ is an arbitrary vector to be multiplied with the Jacobian. We achieve optimal scalability of the linear solver by employing a multigrid method to approximately invert the Stokes block into the preconditioning matrix. The coarse grid operators for the $k$-th level are obtained algebraically via Galerkin coarsening:

$$\mathbf{A}_k = \mathbf{R}_{k+1}^{k}\,\mathbf{A}_{k+1}\,\mathbf{P}_{k}^{k+1}, \tag{5.11}$$

where custom restriction ($\mathbf{R}$) and prolongation ($\mathbf{P}$) operators suitable for the staggered grid discretization (Cai et al., 2014) are incorporated into the PETSc multigrid framework. For this study, we use a multigrid preconditioner ($\mathbf{A}$) that is implemented in a uncoupled form, where the pressure Schur complement is approximated by the inverse viscosity matrix:

$$\mathbf{A} = \begin{pmatrix} \mathbf{K} & \mathbf{G} \\ 0 & -\frac{1}{\eta^*}\mathbf{I} \end{pmatrix}. \tag{5.12}$$

*Tomographic interpretation: The upper mantle beneath the south-eastern Tibetan plateau*

The underlying tomographic model for our interpretation, SVSL2013 (Schaeffer & Lebedev, 2013) shows anomalous large S-wave velocities (Fig. 5.15a, green

framed area), which could be interpreted as cold, underthrusted Indian mantle lithosphere (Agius & Lebedev, 2013). However, comparing this with a *P*-wave tomography (Fig. 5.15b, Li et al., 2008a) of the same area, an anti-correlation between *P*- and *S*-wave reveals. This *P*-*S* discrepancy has been observed before with other S-wave tomographies (e.g. Agius & Lebedev, 2013; Li et al., 2008b; Priestley et al., 2006), and also newer *S*-wave tomography show fast propagation velocities (e.g. Pandey et al., 2014; Ceylan et al., 2012). The interpretations for this portion of mantle lithosphere are manifold and reach from delaminating Tibetan lithosphere through convective instability (Houseman et al., 1981) to underthrusted Indian mantle lithosphere (Pandey et al., 2014; Agius & Lebedev, 2013) and thickened lithosphere by continental collision (McKenzie & Priestley, 2008) or Asian, southwards dipping lithospheric mantle slabs (Tapponnier et al., 2001; Kosarev et al., 1999). In our interpretation, we followed additional receiver function measurements by Kosarev et al. (1999), which suggests an interpretation in favour of a gently southwards dipping subhorizontal lithosphere of Asian origin.

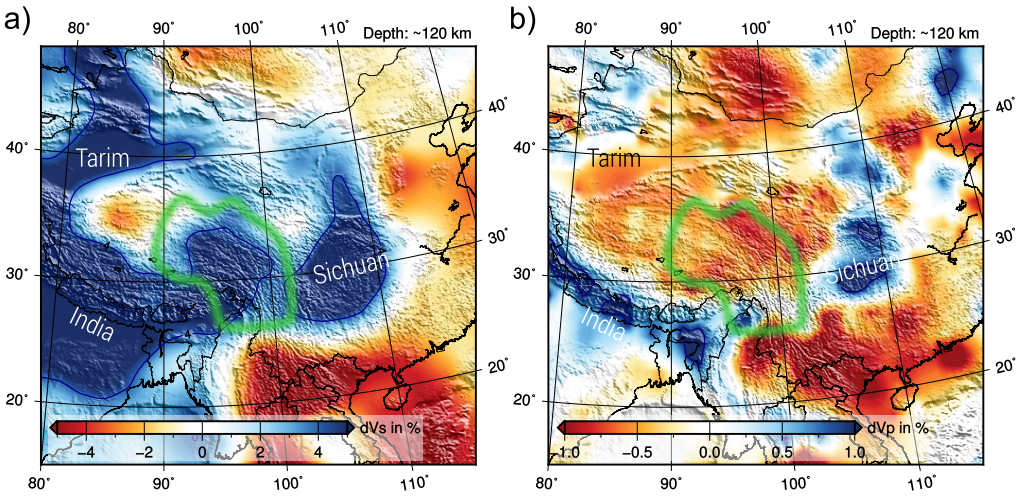


Figure 5.15: Ambiguous tomographic anomalies exist for south-eastern Tibet (green) between **a)** P- and **b)** S-wave tomographies (i.e., Li et al., 2008a; Schaeffer & Lebedev, 2013). As this area has a crucial role for the dynamics, we introduce a new geological unit ('Tibet SE lithosphere', outlined in green) to account for a possibly different rheology compared to the central Tibetan and Indian lithosphere.

# 6

# CONCLUSIONS AND OUTLOOK

## SUMMARY OF THE MAIN CONCLUSIONS

The following paragraphs summarise the central aspects and main conclusions of each chapter.

*Chapter 2 – Constraining rheology through parallel joint geodynamic inversion*

The first publication can be seen as generic feasibility test of geodynamic inversion. It contains two independent parts, a theoretical example of joint geodynamic and gravity inversion and a numerical study to test the feasibility of a Bayesian inversion approach in combination with 3D geomechanical deformation models.

The analytical test demonstrates the advantages of an inversion with physically consistent dynamic models over static models used for gravity-only inversions. Whereas the inversion of the gravity anomaly of a buried sphere at the model surface denotes a well-known, but non-unique inverse problem, we demonstrate that the inversion of the velocity anomalies at the model surface also yields non-unique results provided that the model is embedded in a dynamic context. However, the joint inversion of gravity anomaly and velocity anomaly of a rising or sinking sphere results in a unique solution because the trade-offs linked with the inversion parameters are different. Thus, we can resolve the effective viscosity of the half-space, the density contrast and the geometry of the sphere.

In the second part, we present the feasibility of our general approach: An effectively parallelised direct-search algorithm is combined with a massively parallel geomechanical 3D deformation code. We apply the code to invert for effective viscosities and densities of several layers (8 unknown parameters) in a predefined salt-tectonics model geometry and we show that we are able to identify the parameters of each geological unit including its uncertainty limits as long as they contribute to the dynamics of the forward problem.

*Chapter 3 – Geodynamic inversion to constrain the non-linear rheology of the lithosphere*

Experimental results of rock deformation suggest that, in addition to brittle deformation that is suggested for shallow parts of the lithosphere, large (and deeper) parts are dominated by non-linear deformation behaviour in the viscous regime. We use these empirical relationships established on experimental results to parameterise the rheology of lithospheric scale deformation models, and, similar to chapter 2, perform a massively parallel Bayesian joint inver-

sion of topography, gravity and surface velocities to constrain the rheological parameters. Here, experimentally determined parameter values serve as priors for the inversion. We demonstrate with synthetic tests of an intra oceanic subduction scenario that, although the parameter space increases a lot (14 unknowns) compared to the study in chapter 2, the rheology can be retrieved, but involves a higher degree of non-uniqueness. Furthermore, we test the effect of an unknown temperature distribution. The inversion therefore involves two additional unknowns to account for a parameterised model temperature. Despite using more models, and an even higher degree of non-uniqueness, the essential parts of the effective viscosity structure can be retrieved again.

The second part of the chapter covers a first application of the methodology to a real scenario and data. We considered a SW-NE cross-section through the Himalayas and the Tibetan plateau for which we constructed a structural model from many geophysical data such as seismic tomography, P- and S-receiver functions and focal mechanisms. In a first step, we performed a gravity-only inversion to identify correlated density and temperature parameters, and performed a principal component analysis to determine a reduced number of effective parameter proxies. In the second step, a full geodynamic inversion was performed with 19 unknowns and about 1.9 million forward model evaluations. Regarding the viscosity of the Indian lithospheric mantle, the results are very clear. Models with acceptable misfit contain an Indian mantle lithosphere with a high effective viscosity that acts as a strong indenter. Results for the Asian part of the model are less clear and a number of end-member models exist that can explain the data almost equally well.

*Chapter 4 – Appraisal of geodynamic inversion results: A data-mining approach*

Depending on the number of unknowns involved in a Bayesian inversion, a large number of model evaluations can be needed. In case of chapter 3, the India-Asia application involves about 1.9 million models, and all of them bear some information on the solution of the inverse problem. It can therefore be very useful to automatically extract key properties of characteristic groups of models to make the results more human-readable. Here, we analysed a subset of the entire ensemble with acceptable model misfit based on the model viscosity structure and using a combination of an unsupervised machine learning technique (Self-organizing map, SOM) and partitive clustering.

It was possible to identify four end-member model categories that represent the major part of the non-uniqueness. The striking characteristics are related to the presence of a strong dislocation creep character of the Indian mantle lithosphere, a weak lower Tibetan crust and a weak Asian lithospheric mantle. All model classes can explain the observations almost equally well within the uncertainty limits. Whereas the predicted characteristic topography and Bouguer anomaly of the end-member models are not very different from each other, the horizontal, and mainly the vertical velocity at the model surfaces show characteristic patterns. This indicates that the non-uniqueness of the inverse problem

can potentially reduced a lot by increasing the number and improving the quality of vertical velocity observations.

*Chapter 5 – The present-day dynamics of the India-Asia collision: Consolidating structural and dynamic properties*

This study is the first of its kind, where a fully dynamic, geodynamic 3D model of lithospheric scale deformation is linked with an inversion algorithm to perform a systematic parameter study. We find an optimal viscosity structure beneath Tibet and adjacent regions and provide model uncertainties for the key units of the model to explain the observed GPS-velocity field. The fit of the model predictions is particularly good for regions with a dense data coverage, for example in the Eastern Himalayan syntaxis, where the observations can be reproduced within the range of observational uncertainties.

The dynamics of the India-Asia collision is attributed to different mechanisms, and a number of end-member models has been proposed in the literature. Our results confirm that only an interaction of the proposed mechanisms can explain the observed surface deformation field. First of all, strike-slip zones play an important role. In our model, the surface deformation field cannot be reproduced without them, which is in agreement with kinematic models that favour a major role of strike slip faults. In this context, we observe largest strain rates for the Kulun and Xianshuihe faults. On the other hand, the Altyn-Tagh fault is found to be effectively locked. As reported many times, lateral heterogeneities have a large impact on the surface dynamics too. In particular, this has been tested with thin viscous sheet models. Our results also confirm these observations. For example, we find that the Tarim and Sichuan basin must have high viscosities for both, mantle lithosphere and crust, in agreement with the observed strong cratonic blocks. In other regions of the model, however, we also observe that a layered lithosphere with distinct effective viscosities for crust and mantle lithosphere is necessary to fit the surface deformation. We find that large viscosity contrasts are necessary, in particular for Tibet, where an additional layer of low viscous material, coinciding with partially molten material in the mid and lower crust, significantly improves the model fit. Furthermore, the results agree with the previous findings of chapter 3, where we showed that the Indian mantle lithosphere must have a high viscosity in order to fit the observations.

### GENERAL REMARKS AND GENERIC ISSUES OF GEODYNAMIC INVERSION ON LITHOSPHERIC SCALES

Geodynamic inversion is a promising new method to verify experimental results of lithospheric rheology. Also the fact that the model space can be analysed to understand the sensitivity of the solution to each model parameter is considered to be an important aspect in the field of lithospheric scale numerical modelling (Burov et al., 2014). Yet, a few questions remain to be addressed.

This section briefly names three generic issues of geodynamic inversion, which should be investigated in more detail in future studies.

*Temperature*

Good estimates of lithospheric temperature profiles are essential as temperature directly affects the activation energy parameter and thus viscosity (Burov, 2007). Whereas the temperature structure of oceanic lithosphere is well known and dependent on a few parameters only (half-space cooling model, e.g. Turcotte & Schubert, 2002), the temperature distribution of subducting slabs and continental lithosphere in general is much more difficult to estimate. For subducting oceanic lithosphere, it has been shown that a parameterisation adjusted to the slab surface works reasonable well, such that the effective viscosity structure can essentially be resolved (see chapter 3). For continental lithosphere, however, more advanced parameterisations need to be used that involve additional unknowns. As density is temperature dependent, gravity-only inversions can be used to pre-assess the sensitivity of single parameters and to eventually summarise groups of parameters with appropriate proxies (see chapter 3). Nevertheless, there is room for improving the temperature parameterisation depending on the geological setting. Additional constraints such as from xeonolith data and melting can eventually be included, which has to be assessed separately in each case. There are also other constraints such as heat flux observations. However, these may not be reliable enough for continental lithosphere as radioactive heat sources in the crust pollute heat flux measurements at the surface (Burov, 2007).

*Elasticity*

Another aspect that has been omitted from the inversion approach so far is the elastic deformation behaviour of the lithosphere, which can potentially have and effect in certain scenarios where the viscosities are high and the stress is not in steady state. However, this introduces certain complexities. Regarding a viscoelastic rheology, the elastic part of the strain rate $\dot{\varepsilon}_{ij}$ depends on the Jaumann derivative $\frac{D}{Dt}$ of the deviatoric stress tensor ($\dot{\varepsilon}_{ij} \propto \left(2 \cdot t_r \frac{D}{Dt} + 1\right) \tau_{ij}$) and the Maxwell relaxation time $t_r = \frac{\eta}{G}$, which denotes the ratio of viscosity $\eta$ and shear modulus G. The Jaumann derivative describes rotation and advection of the stress tensor, i.e. it contains a time derivative and thus depends on the history of the stress state (e.g. Ismail-Zadeh & Tackley, 2010). For a present-day model, the stress history is usually unknown, but can eventually be estimated to some extend such that it can be parameterised and made part of the inverse problem. In future work, this will be thoroughly tested with synthetic models.

*Geometry*

We usually have good constraints on the structural present-day geometry of the shallow parts of the lithosphere, where, predominantly due to seismolo-

gical observations, the Moho is well imaged. However, deeper parts of the lithosphere can only be resolved with techniques that make use of larger seismic wavelengths, and as a result the base of the lithosphere (LAB) is less constrained and has significant uncertainties. A parameterisation of the geometry in this model domain therefore makes sense at first glance. However, it should be noted that such a parameterisation is likely to be correlated with a parameterisation of temperature (see chapter 3). A geometry parameterisation is definitely correlated with the model densities, such that a gravity-only inversion prior to a geodynamic inversion is indispensable.

*General remarks*

It becomes obvious that as more degrees of freedom are permitted to satisfy all challenges, it all amounts to the same result: a larger parameter space. This attaches additional value to an appropriate definition of the objective (misfit) function, such that as many independent data as possible can be used to regularise and to improve the sensitivity of the objective function. Furthermore, it emphasises the importance of using the best possible approximation of the objective function with a minimum number of forward models.

### FUTURE PERSPECTIVES AND CHALLENGES OF GEODYNAMIC INVERSION

Too many model parameters imply an implicit barrier for sampling based methods and the *curse of dimensionality* prohibits a straightforward increase of inversion parameters. Two common examples are given in Fig. 6.1. Fig. 6.1a refers to a D-dimensional unit sphere (radius $r = 1$, volume $V_D \propto r^D$), where the fraction of volume of the outer shell ($r = [1 - \epsilon \dots 1]$), i.e. $V_{D,\epsilon} = \frac{V_D(1) - V_D(1-\epsilon)}{V_D(1)} = 1 - (1-\epsilon)^D$ is plotted against the thickness of the shell $\epsilon$. This demonstrates that almost the entire volume is concentrated in a thin outer shell (Bishop, 2006). As the parameter space is usually associated with a high-dimensional cuboid, much of the volume actually refers to the corners of the parameter space (Fig. 6.1b). Here, the difference in volume between a cube with unit length edges and a unit sphere is examined conceptually. As the dimension D increases, the distance from the center to a vertex of the hypercube increases with $\frac{\sqrt{D}}{2}$ whereas the volume stays constant. On the other hand, the radius of the unit sphere stays one, but the the volume decreases with increasing dimension (see Hopcroft (2008) for details). Thus, most of the volume of a hypercube in high dimensions is concentrated towards the vertices – outside of the unit sphere.

The example demonstrates that a proper guidance of the sampling is very important. One possibility is to guide the sampling according to prior distributions, which will help to focus the sampling on 'interesting regions' of the parameter space and to avoid extreme parameter combinations. The availability of good priors is indispensable, and in the context of lithospheric rheologies, should be studied in more detail. As the number of forward models is limiting the factor of each sampling approach, it is self-evident to optimise this number

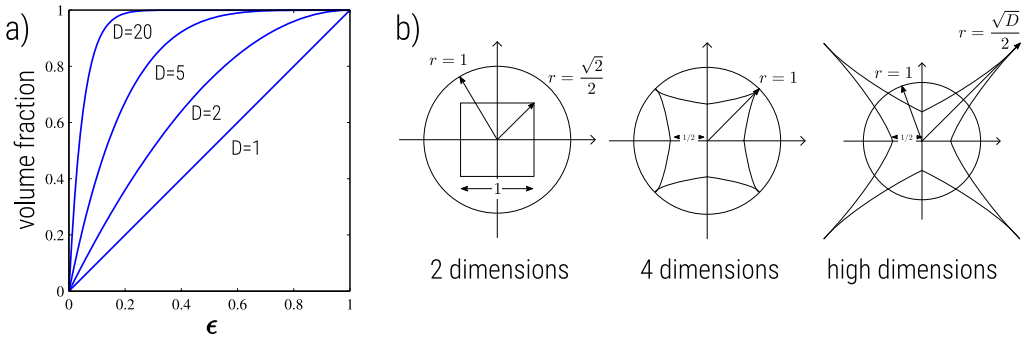


Figure 6.1: Examples of the curse of dimensionality. **a)** The fraction of volume within a thin outer shell (thickness $\epsilon$) of the unit sphere quickly increases with dimension D (Bishop, 2006). **b)** Conceptual illustration of the increase in fractional volume with D that lies between the unit hypersphere and the unit hypercube. In 2 dimensions, the cube is fully inside the sphere, in higher dimensions, however, the majority of the hypercube volume accumulates in the corners (after Hopcroft, 2008).

as much as possible. A guidance of the sampling with priors will help with the dimensionality issue, but it is an additional task to find optimal location for new forward models based on the previous model history. In this context, the concept of the Neighbourhood Algorithm (Sambridge, 1999a) provides a smart partitioning of the parameter space, where the objective function is approximated piece-wise constant, such that at least confined regions with low misfit values are proposed to insert new models. However, the proposal of new suitable model locations can be enhanced by far, if in addition to the value (misfit) of the objective function, the gradient can be evaluated.

As we usually deal with numerical solutions, the gradient of the objective function has to be approximated and is not for free. For example, finite differences can be used, which involves additional forward modelling depending on the order of the Taylor-approximation. An alternative is the adjoint method, which requires just a single solve with the transposed of the forward problem Jacobian operator to evaluate the objective function's gradient. The method is a technique developed in meteorology (Talagrand & Courtier, 1987) with increasing adoption in seismology (e.g. Fichtner et al., 2006; Tromp et al., 2004), geodynamics (Ratnaswamy et al., 2015; Worthen et al., 2014; Liu & Gurnis, 2008; Bunge et al., 2003) and ice-flow (Isaac et al., 2015; Petra et al., 2012), where it is often used in combination with a Newton method to solve inverse problems, which can be problematic as it is only capable to find a local, but not a global solution. Whereas the approach is justifiable for ice-sheet modelling, where material properties vary smoothly, the structure of the lithosphere is much more complex, such that it is at least questionable whether in lithosphere-geodynamics, an adjoint-based gradient approach is the method of choice we should ultimately aim for. A reliable solution at least requires multiple solves with different starting positions in the parameter space to verify the inversion result, otherwise it can only give an a priori solution for more comprehensive inversions.

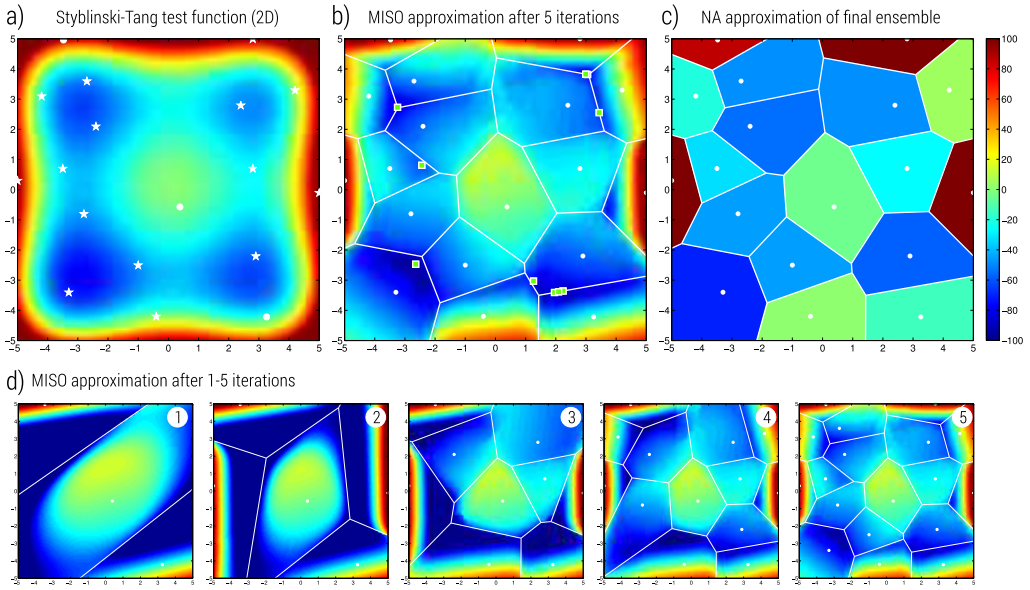


Figure 6.2: 2D benchmark of the MISO algorithm (Multivariate Inversion through Surrogate Optimisation, Baumann & Popov, in prep.). **a)** Styblinski–Tang objective function for multidimensional optimisation problems; it has exactly one global minimum at $\mathbf{x}_{min} = [-2.9035, \ldots, -2.9035]$ and three local minima in 2D (Styblinski & Tang, 1990). Filled circles and stars indicate initial models and additional models at optimal locations, respectively. **b)** MISO approximation of the objective function after 5 iterations and 18 forward models. New proposal model locations of the following iteration are indicated with green squares. **c)** Neighbourhood approximation of objective function, using the final MISO model ensemble. Low misfit regions are much larger compared to (b), thus new locations for additional forward models are less confined. Importance sampling would yield a much less accurate approximation of the likelihood function (c.f Sambridge, 1999b).

Yet, the adjoint approach itself is a low-cost method to evaluate the gradient of the objective function and can be combined with sampling based methods to improve our knowledge of the shape of the objective function with each forward model. This is a particularly valuable information in terms of geodynamics, as forward models are computationally expensive. The piece-wise constant approximation of the objective function within the concept of the Neighbourhood algorithm can be improved to a piece-wise linear or even higher order variant, provided that some sort of adjacency graph between neighbouring models exist and local interpolation, which includes the gradient information, can be applied (Alfeld, 1989). Computing adjacency graphs, for example, finding the Voronoi-neighbours, is a task of linear programming and can be solved efficiently also for high dimensions (Fukuda, 2004). However, it has to be tested how dense an adjacency graph is in very high dimensions ($> 8$), and whether this is still computable in an appropriate amount of time. Alternatively, unsupervised machine learning techniques such as Self-organizing maps (Kohonen, 2001) or Growing Neural Gas networks (Fritzke, 1995) can be used to detect

lower dimensional manifolds for which local adjacency graphs can be established.

Definitely, a higher order interpolation of the objective function (higher than piecewise constant) helps to find optimal locations for new forward models. An example is given in Fig. 6.2, where a non-unique benchmark function (Styblinski-Tang function, Fig. 6.2a, Styblinski & Tang, 1990) is well approximated with only 18 models (Fig. 6.2b) using the MISO algorithm (Multivariate Inversion through Surrogate Optimisation, Baumann & Popov, in prep.). The MISO algorithm uses a high-dimensional interpolant of the objective function to locate new samples in the parameter space. Here, the sampling started with three random samples (Fig. 6.2d, 1), and subsequent models are placed at local minima of the current approximation of the objective function (Fig. 6.2d, 2-5). The minima are found by applying a gradient based method to the surrogate (interpolant) of the objective function. As this only involves an interpolation problem, new locations can be found very efficiently. In comparison with the neighbourhood approximation of the objective function (Fig. 6.2c Sambridge, 1999b), the MISO approximation (Fig. 6.2b) is thus much more accurate, and the Neighbourhood approximation would require a much large number of models to reach a similar accuracy. This thus demonstrates how the current approach based on the Neighbourhood algorithm can potentially be improved for future applications with computationally demanding (3D) models and non-trivial rheology parameterisations that require many parameters.

## REFERENCES

Alfeld, P., 1989. Scattered data interpolation in three or more variables, *Math. Methods Comput. Aided Geom. Des.*, pp. 1–33.

Baumann, T. S. & Popov, A. A., in prep. Multivariate inversion through surrogate optimisation: The MISO algorithm.

Bishop, C. M., 2006. *Pattern recognition and machine learning*, Springer New York.

Bunge, H. P., Hagelberg, C. R., & Travis, B. J., 2003. Mantle circulation models with variational data assimilation: inferring past mantle flow and structure from plate motion histories and seismic tomography, *Geophys. J. Int.*, **152**(2), 280–301.

Burov, E., Watts, T., Podladchikov, Y., & Evans, B., 2014. Observational and modeling perspectives on the mechanical properties of the lithosphere, *Tectonophysics*, **631**, 1–3.

Burov, E. B., 2007. Crust and Lithosphere Dynamics: Plate Rheology and Mechanics, in *Treatise Geophys.*, vol. 6, chap. 3, pp. 99–151, ed. Watts, A. B., Elsevier.

Fichtner, A., Bunge, H.-P., & Igel, H., 2006. The adjoint method in seismology: I. Theory, *Phys. Earth Planet. Inter.*, **157**(1), 86–104.

Fritzke, B., 1995. A Growing Neural Gas Learns Topologies, *Adv. Neural Inf. Process. Syst.*, **7**, 625–632.

Fukuda, K., 2004. Frequently asked questions in polyhedral computation, pp. 1–30, Swiss Federal Institute of Technology Lausanne and Zurich, Switzerland.

Hopcroft, J., 2008. Lecture notes in Advanced Design and Analysis of Algorithms, pp. 1–7, Cornell University, New York.

Isaac, T., Petra, N., Stadler, G., & Ghattas, O., 2015. Scalable and efficient algorithms for the propagation of uncertainty from data through inference to prediction for large-scale problems, with application to flow of the Antarctic ice sheet, *J. Comput. Phys.*, **296**, 348–368.

Ismail-Zadeh, A. & Tackley, P., 2010. *Computational methods for geodynamics*, Cambridge University Press.

Kohonen, T., 2001. *Self-organizing maps*, vol. 30, Berlin: Springer, Berlin, 3rd edn.

Liu, L. & Gurnis, M., 2008. Simultaneous inversion of mantle properties and initial conditions using an adjoint of mantle convection, *J. Geophys. Res.*, **113**(B8), B08405.

Petra, N., Zhu, H., Stadler, G., Hughes, T. J., & Ghattas, O., 2012. An inexact Gauss–Newton method for inversion of basal sliding and rheology parameters in a nonlinear Stokes ice sheet model, *J. Glaciol.*, **58**(211), 889–903.

Ratnaswamy, V., Stadler, G., & Gurnis, M., 2015. Adjoint-based estimation of plate coupling in a non-linear mantle flow model: theory and examples, *Geophys. J. Int.*, **202**(2), 768–786.

Sambridge, M., 1999a. Geophysical inversion with a neighbourhood algorithm–I. Searching a parameter space, *Geophys. J. Int.*, **138**(2), 479–494.

Sambridge, M., 1999b. Geophysical inversion with a neighbourhood algorithm–II. Appraising the ensemble, *Geophys. J. Int.*, **138**(3), 727–746.

Styblinski, M. A. & Tang, T.-S., 1990. Experiments in nonconvex optimization: stochastic approximation with function smoothing and simulated annealing, *Neural Networks*, **3**(4), 467–483.

Talagrand, O. & Courtier, P., 1987. Variational Assimilation of Meteorological Observations With the Adjoint Vorticity Equation. I: Theory, *Q. J. R. Meteorol. Soc.*, **113**(478), 1311–1328.

Tromp, J., Tape, C., & Liu, Q., 2004. Seismic tomography, adjoint methods, time reversal and banana-doughnut kernels, *Geophys. J. Int.*, **160**(1), 195–216.

Turcotte, D. L. & Schubert, G., 2002. *Geodynamics*, Cambridge University Press.

Worthen, J., Stadler, G., Petra, N., Gurnis, M., & Ghattas, O., 2014. Towards adjoint-based inversion for rheological parameters in nonlinear viscous mantle flow, *Phys. Earth Planet. Inter.*, **234**, 23–34.